Boiling of Dilute Emulsions

A DISSERTATION
SUBMITTED TO THE FACULTY OF THE GRADUATE SCHOOL
OF THE UNIVERSITY OF MINNESOTA
BY

Matthew Lind Roesle

IN PARTIAL FULFILLMENT OF THE REQUIREMENTS
FOR THE DEGREE OF
DOCTOR OF PHILOSOPHY

Francis A. Kulacki

June 2010

Acknowledgements

I wish to express my gratitude to my adviser, Professor Frank Kulacki, for his support, guidance, and constructive criticism over the past four years. His encouragement and advice in pursuing this line of research have been invaluable.

I would like to thank Peter Zimmermann and Dave Hultman for their supervision and advice during the design and manufacture of my experimental apparatus.

I am glad to have had the opportunity to get to know my fellow students and lab-mates, including Todd Lagus, John Lutz, Bill Mohs, Keith Jackson, Jack Kalyuzhny, Dave Lunde, Aniruddha Bagchi, and others too numerous to mention. I appreciate our many fruitful discussions regarding classes, research, and life in general.

Finally, I would like to thank my parents and extended family, especially Jean and Michael, for their love and support throughout my academic career.

Dedication

This dissertation is dedicated to my parents.

Abstract

Although boiling in pure liquids has been studied thoroughly, boiling in other circumstances is less well understood. One area that has received little attention is boiling of dilute emulsions in which the dispersed component has a lower boiling point than the continuous component. These mixtures exhibit several surprising behaviors that were unknown until the 1970's. Generally, boiling of the dispersed component enhances heat transfer over a wide range of surface temperatures without transition to film boiling, but a high degree of superheat is required to initiate boiling. In single-phase convection the dispersed component has little effect on heat transfer. These behaviors appear to occur in part because few droplets in the emulsion contact nucleation sites on the heated surface. No detailed and physically consistent model of boiling in dilute emulsions exists at present.

The unusual behavior of boiling dilute emulsions makes them potentially useful for high heat flux cooling of electronics. High-power electronic devices must be maintained at temperatures below ~85 °C to operate reliably, even while generating heat fluxes of 100 W/cm^2 or more. Current research, generally focusing on single phase convection or flow boiling in small diameter channels, has not yet identified an adequate solution. An emulsion of refrigerant in water would be well-suited to this application. The emulsion retains the high specific heat and thermal conductivity of water, while boiling of the refrigerant enhances the heat transfer coefficient at temperatures below the saturation temperature of water.

To better understand boiling dilute emulsions and expand the experimental database, an experimental study of boiling heat transfer from a horizontal heated wire, including visual observations, is performed. Emulsions of pentane in water and FC-72 in water are studied. These emulsions have properties suitable for practical use in high heat flux cooling applications, unlike most emulsions that have previously been studied. The range of the experimental study is extended to include enhanced boiling of the continuous component, which has not previously been observed, in addition to boiling

of the dispersed component. In both regimes the heat transfer coefficient is enhanced compared to that of water.

Visual observations reveal the presence of large attached bubbles on the heated wire, the formation of which coincides with the inception of boiling in the heat transfer data. At very low dispersed component fractions and low temperatures, boiling of individual dispersed droplets is not observed. The large attached bubbles represent a new boiling mode that has not been reported in previous studies and is, under some circumstances, the dominant mode of boiling heat transfer.

A model of boiling dilute emulsions is developed based upon the Euler-Euler model of multiphase flows. The general balance equations as developed by Drew and Passman are applied to the present situation, thus providing a rigorous and physically consistent framework. The model contains three phases that represent the continuous component, liquid droplets of the dispersed component, and bubbles that result from boiling of individual droplets. Mass, momentum, and energy transfer between the phases are modeled based upon the behavior of and interaction between individual elements of the dispersed phases. One-dimensional simulations of a single boiling droplet in superheated liquid are also performed, and the results are used to develop the closure equations of the larger model. Droplet boiling is assumed to occur when a droplet contacts a heated surface or a vapor bubble. Collisions between droplets and bubbles and chain-boiling of closely-spaced droplets are considered.

The model is limited to the dispersed component boiling regime, and thus it does not account for phase change of the continuous component. The model also does not include the large attached bubbles revealed in the visualization experiments. However, simulations of boiling match several trends observed in the experimental data. The model thus provides a physically consistent and partially validated platform for future analytical and numerical work.

Table of Contents

List of Tables

List of Figures

Nomenclature

A	Surface area, m^2
A_0	Adjustment parameter in Eq. 2.19
A_{xc}	Cross-sectional area, m^2
Ar	Archimedes number, $(\rho_{eff} - \rho_b)g\rho_d \frac{d_b^3}{\mu_{eff}^2}$
a	Coefficient in discretized differential equations (Appendix A)
B	Pre-exponential factor in Eq. 2.4
b	Body force per unit mass, N/kg
C	Rate of heating of liquid droplet, °C/s
C_D	Drag coefficient, kg/m^3-s
C_L	Lift coefficient
C_R	Rotation coefficient
C_{sf}	Empirical constant in Eq. (5.25)
C_{TD}	Turbulent drag coefficient
C_{vm}	Virtual mass coefficient
c_p	Constant-pressure specific heat, kJ/kg-°C
c_v	Constant-volume specific heat, kJ/kg-°C
D	Viscous dissipation, W/m^3
d	Diameter, m
d_S	Sauter mean diameter, $\frac{\sum_i d_i^3}{\sum_i d_i^2}$
E	Averaged interfacial energy transfer rate, Eq. (C.23), W/m^3
e	Specific internal energy, J/kg
F	Source flow strength, m^3/s
$\mathbf{F}_{ij}$	Averaged interfacial force on phase i by phase j, N/m^3
f	Frequency, Hz

$\mathbf{g}$	Gravitational force, N/kg
h	Heat transfer coefficient, W/m^2-°C
$\mathbf{I}$	Identity matrix
I_{wire}	Electrical current, Amperes
i	Specific enthalpy, J/kg
J	Volumetric nucleation or collision rate, 1/m^{3}s
Ja	Jakob number, $\rho_f c_{p,f} \Delta T/(\rho_g i_{fg})$
K_a, K_b	Constants in Eq. (5.8)
K_T	Pseudo-turbulent factor
K_η	Collision efficiency factor
k	Thermal conductivity, W/m-°C
k_B	Boltzmann constant, 1.38065 x 10^{-23} J/K
ℓ	Eddy mixing length
L	Characteristic length, m
m	Mass, kg
$\dot{m}$	Volumetric mass transfer rate from droplet phase to bubble phase, kg/m^{3}s
N	Number density, 1/m^3
$\mathbf{n}$	Outward-pointing unit normal vector
n	Number of boiling droplets
Nu	Nusselt number, hL/k
P	Pressure, N/m^2
p	Perimeter, m
Pr	Prandtl number, ν/α
Q	Heat transfer, J
$\mathbf{q}$	Heat flux vector, W/m^2
q	Heat transfer rate, W
q”	Heat flux, W/m^2
$\dot{q}$	Volumetric heat generation rate, W/m^3
$\mathcal{R}$	Electrical resistance, Ω
$\mathbf{R}_{eff}$	Effective viscous stress (molecular plus Reynolds), m^2/s^2

$\mathbf{R}_{eff}^{C}$	Corrective stress component, m^2/s^2
$\mathbf{R}_{eff}^{D}$	Diffusive stress component, m^2/s^2
R	Droplet or bubble radius, m
R_G	Gas constant, J/kg-K
R_{cr}	Critical bubble radius, m, Eq. (2.1)
Ra	Rayleigh number, $\frac{g\beta_{film}(T_s - T_\infty)d^3}{\nu_{film}^2} Pr_{film}$
r	Radial distance, m
Re	Reynolds number, $\boldsymbol{u}d/\nu$
S	Surface area vector, m^2
S	Heat source per unit mass, W/kg
s	Prandtl number factor in Eq. 5.25
St	Stefan number, $\frac{c_{p,d}(T - T_{sat})}{i_{fg}}$
T	Temperature, K
ΔT	Temperature difference, T_∞ - T_{sat}
T	Stress tensor, N/m^2
t	Time, s
Δt	Time step size in numerical solver, s
$\boldsymbol{u}$	Characteristic fluid velocity, m/s
U	Velocity vector, m/s
$\mathbf{U}_{r,ij}$	Relative velocity vector between phases i and j, $\mathbf{U}_j$ - $\mathbf{U}_i$, m/s
u	Velocity component, m/s
u*	Turbulence characteristic velocity
V	Volume, m^3
ΔV	Voltage difference, V
v	Specific volume, m^3/kg
W	Work, J
w	Heated surface width, m

X	Continuous phase indicator
x	Position vector
x	Horizontal dimension

Greek Symbols

α	Thermal diffusivity, m^2/s
α_E	Temperature coefficient of electrical resistance of copper, 1/°C.
β	Volumetric expansion coefficient, m^3/m^3-K
Γ	Averaged interfacial mass transfer rate, Eq. (C.24), kg/m^3-s
γ	Generic diffusive flux, Eq. (C.1)
Δ	Very small value
δ	Dirac delta function
δ_t	Thermal boundary layer thickness, m
ε	Volume fraction, m^3/m^3
ζ	Generic source density, Eq. (C.1)
η	Collision efficiency
Θ	Temperature difference, $T - T_\infty$, °C
θ	Angular direction, radians
κ	Polytropic coefficient
μ	Dynamic viscosity, kg/m-s
ν	Kinematic viscosity, m^2/s
ρ	Density, kg/m^3
ρ_E	Electrical resistivity of copper, Ω-m
σ	Surface tension, N/m
τ	Characteristic time, s
ϕ	Volumetric flux, m^3/s
φ	Number of boiling droplets in a chain reaction
χ	Number of molecules in vapor bubble embryo
Ψ	Generic conserved quantity, Eq. C.1

Subscripts

+	Positive portion
-	Negative portion
0	Reference or baseline condition
b	Vapor bubble phase (emulsified component)
c	Continuous phase
coll	Collisions
cond	Condensation
cs	Current sense
D	Drag
d	Liquid droplet phase (emulsified component)
eff	Effective value for the emulsion
f	Saturated liquid
fg	Difference between saturated vapor and saturated liquid
film	Evaluated at film temperature, $(T_s + T_\infty)/2$
g	Saturated vapor
I	Interface
inertial	Inertial
init	Initial condition
i,j	Counting indices, i,j = 1, 2, 3…
L	Lift
m	Mixture
max	Maximum value
mid	At the midpoint of the heated wire
mol	Molecule
outer	Outer limit
R	Rotational
r	Radial direction
s	Surface
sat	Saturated condition

T	Turbulent quantity
TD	Turbulent dispersion
v	Vapor phase
vm	Virtual mass
w	Wall
wire	Heated wire
θ	Tangential direction (in polar coordinates)
∞	Ambient condition (at infinite distance or radius)

Superscripts and other notation

$\overline{x}$	Average value or phase property
x’	Fluctuating component of x, where $x = x' + \overline{x}$.
$\hat{\mathbf{x}}$	Unit vector
$\lvert x \rvert$	Magnitude of x
δx	Uncertainty in x
x^*	Predicted values of x in PISO algorithm
x^o	Quantity x at previous iteration
x^{Re}	Fluctuation (Reynolds) quantity
$\frac{D_i}{Dt}$	Material derivative for phase i, $\frac{\partial}{\partial t} + \mathbf{U}_i \cdot \nabla$
$\lVert \mathcal{L}[x] \rVert$	Expression arising from implicit discretization of operator $\mathcal{L}$, discretized in terms of variable x
x_F	Interpolation of cell-centered variable x to face centers
$\langle x \rangle$	Average of x over adjacent cells
$\boldsymbol{a}$	Discretized linear system of equations
$\boldsymbol{a}$:= {…}	Assignment of the discretized form of the system of linear equations in brackets { … } to $\boldsymbol{a}$
$\boldsymbol{a}_D$	Diagonal matrix coefficients of discretized linear system of equations $\boldsymbol{a}$
$\boldsymbol{a}_N$	Off-diagonal matrix coefficients of discretized linear system of equations $\boldsymbol{a}$

$\boldsymbol{a}_{\mathrm{S}}$	Source vector of discretized linear system of equations $\boldsymbol{a}$
$\boldsymbol{a}_{\mathrm{H}}$	H operator, Eq. (4.2)

1. Introduction

Boiling has long been recognized as an important heat transfer mechanism and has been intensively studied for over a century. Boiling of pure liquids is now fairly well understood, but surprising behavior is still encountered in some circumstances. One such area is boiling of dilute emulsions in which the dispersed component has a lower boiling point than the continuous component. Under these conditions, the degree of superheat required for boiling is much higher than for pure liquids, and burnout (that is, transition to film boiling) does not occur. This anomalous behavior was discovered in the 1970's (Mori, Inui, and Komotori, 1978) and has since been studied extensively by Bulanov and co-workers (Bulanov and Gasanov, 2007, 2008). Despite the experimental studies that have been performed, there is as yet no detailed understanding of how the boiling process occurs.

An emulsion is a mixture of two immiscible liquids in which one liquid (the dispersed or droplet component) forms a suspension of many small droplets in the other liquid (the continuous component). An emulsion is considered dilute when the dispersed component occupies ~5% or less of the emulsion by volume. In the emulsions considered here, the dispersed component has a lower boiling point than the continuous component. The primary purpose of this study is to understand what happens when only the dispersed component boils, although experiments are extended to higher surface temperatures to measure heat transfer when both components boil.

Superheated droplets in an emulsion exist in what is called a meta-stable state, meaning that they remain liquid despite having a temperature well above their saturation temperature. The meta-stable liquid would rapidly boil, but it must either first contact a liquid-vapor interface or experience some sort of disturbance that initiates boiling. Pure liquids are not often found in meta-stable states because the walls of the container holding the liquid contain nucleation sites – microscopic cavities, resulting from the manufacturing process, that retain gases. There is a limiting degree of superheat above which nucleation occurs spontaneously, without the presence of any nucleation sites. Theoretical predictions of this limit are generally in good agreement with experimental studies of boiling in isolated droplets. The maximum possible degree

of superheat is a function of the liquid and the ambient pressure, but is typically 100 °C or more and is also greater than the point at which boiling occurs in dilute emulsions (Bulanov and Gasanov, 2007, 2008). An understanding of the mechanisms that cause individual droplets in the emulsion to boil is crucial to understanding and predicting the overall behavior of boiling emulsions.

Bulanov and Gasanov (2008) give a possible explanation of this behavior based on chain-reaction boiling of the droplets due to the presence of impurities in the liquid. They speculate that the droplets of the low-boiling-point liquid contain floccules of nano-particles, too small to be detected or filtered out by normal means. These floccules contain some trapped atmospheric gases absorbed on their surfaces. As the liquid temperature increases the gas comes out of solution and eventually forms the nucleus for a vapor bubble, which causes the droplet to boil. The rapid expansion of a boiling droplet creates a shockwave that breaks up floccules in any nearby droplets, so that they release their trapped gases and thus cause those droplets to immediately boil as well. While this explanation agrees with much of their experimental data in a qualitative sense, the physical processes are not modeled in detail, and there are insufficient details in their papers to allow prediction of the behavior of boiling emulsions. Some experimental data for emulsions in which particles have been added to the low-boiling-point liquid are contradictory as well (Bulanov, Gasanov, and Tuchaninova, 2006).

The unusual characteristics of boiling dilute emulsions may be useful in addressing an open problem in heat transfer engineering: high heat flux cooling of electronics. High-power electronic devices, such as computer CPUs, must be maintained at temperatures below ~85 °C to operate reliably, even while producing heat fluxes as high as 100 W/cm^2 (Thome, 2006). The bulk of recent research into this problem has been in the areas of single-phase and boiling heat transfer in small-diameter channels. Often called microchannels, these channels could potentially be etched directly into the silicon substrates of CPUs, thus providing an extremely short heat conduction path for the heat generated in the electronic junctions of the CPU (Tuckerman and Pease, 1981).

Experiments performed by Tuckerman and Pease (1981) demonstrate that high heat flux cooling can be achieved using single-phase convection to water in this manner. However, at high heat flux the temperature increase along the length of the microchannel is significant. Further, high inlet pressure is required to force water through the microchannels at a sufficient rate. Both of these effects place stress on the silicon substrate. For single-phase convection in simple microchannels, tradeoffs between low temperature rise in the liquid, low pressure drop, and low temperature difference between surface and fluid are unavoidable. Various potential methods of improving on this situation have been studied, including placing structures in the microchannel (Kandlikar and Grande, 2004), electrical fields, and vibrating elements (Steinke and Kandlikar, 2004). The effect of these changes is to break up the laminar flow structure of the liquid in the microchannel, which improves heat transfer at the cost of increased pressure drop.

A separate set of problems are associated with the use of boiling heat transfer for high heat flux cooling. The most significant problem is that the heat transfer fluid of choice, water, has too high a saturation temperature to be used for cooling electronics. Other refrigerants and heat transfer liquids have lower saturation temperatures, but they also have much lower critical heat flux (CHF), typically well below 100 W/cm^2 (Wojtan, Revellin, and Thome, 2006; Zhang, Mudawar, and Hasan, 2007; Agostini et al., 2007). Similar to single-phase heat transfer, some improvement in CHF can obtained through the use of more complex geometries, such as arrays of micro-jets directed into the microchannels (Sung and Mudawar, 2009). However, changes in geometry alone produce only modest improvements in CHF, and more significant improvements have been demonstrated only by cooling the refrigerant to well below room temperature and by allowing the surface temperature to exceed 85 °C as well (Sung and Mudawar, 2009).

Boiling dilute emulsions offers an alternative to single-phase and boiling heat transfer that combines the positive characteristics of both heat transfer methods. In an emulsion of refrigerant in water, water makes up the bulk of the emulsion and gives the mixture high heat capacity and thermal conductivity. With the proper choice of

dispersed component, the droplets will boil rapidly at temperatures below 85 °C, thus agitating the water flow and breaking up its laminar flow structure (Bulanov, Skripov, Gasanov, and Baidakov, 1996). Such agitation of the water may improve heat transfer rates far more effectively than placing structures in the channel, and will do so without increasing the complexity of the channel itself.

A recent experimental study highlights the importance of the intimate contact between refrigerant and water that is achieved in emulsions. A study of mixtures of water and FC-72[1] in a flat microchannel shows that when the two fluids are not thoroughly mixed beforehand, they segregate into separate parallel streams in the microchannel. When so separated, any boiling that occurs in the FC-72 has negligible effect on the water stream, and no heat transfer enhancement is obtained over the case of a water-only flow (Roesle and Kulacki, 2008).

At present, understanding of boiling emulsions is very limited. The most detailed description of how emulsions boil is that of Bulanov and Gasanov (2008), but it still leaves many questions unanswered. The structure of the boundary layer in a boiling emulsion near a heated surface is not known. It is not known precisely where or how boiling occurs within the boundary layer. It is not known how the boiling droplets and bubbles influence each other. Also, the model of Bulanov and Gasanov is not predictive of the heat transfer rate for any given conditions.

The purpose of this study is to develop and validate via experiment a physical model of dilute emulsions undergoing boiling. The model is rooted in a detailed analysis of the behavior of a highly superheated droplet undergoing boiling. The effects of the boiling droplet on the surrounding fluid, and therefore any nearby droplets, are also considered. These boiling phenomena are linked to the overall behavior of the emulsion using the Euler-Euler approach to modeling multiphase mixtures (Rusche, 2002). The model developed here is the first to contain an internally consistent description of the mechanisms and physics of boiling dilute emulsions.

---

[1] FC-72 is a Fluorinert™ Electronic Liquid manufactured by 3M™. Its intended applications are leak testing and electronics heat transfer applications. Its notable properties include low boiling point (56.3 °C at 1 atm pressure), low solubility in water, low viscosity, and low surface tension.

Numerical simulations of boiling emulsions are performed using the model, and these simulations are compared to experimental results. The experiments examine emulsions undergoing free-convection boiling on a horizontal heated wire, and measurements of the heat transfer coefficient as well as visual observations are carried out. Although a potential application for this phenomenon is seen in heat transfer in small-diameter channels, the natural-convection experiments performed in this study offer a better opportunity to observe the detailed behavior of boiling emulsions. Experiments are performed with two combinations of fluids, FC-72 in water and pentane in water. Currently, the open literature does not contain any data on boiling emulsions of these fluid combinations. The visual observations of the heat transfer surface during boiling of these dilute emulsions, correlated with the heat transfer data, are also a new contribution to the literature base.

The following chapter describes prior work that has been accomplished in the area of boiling emulsions. The chapter also provides background information on related subjects that serve as a foundation for the work in this dissertation. The new model of boiling dilute emulsions is developed in Chapter 3, and in Chapter 4 a numerical solution procedure for the model is described. Chapter 5 describes the results of the experimental study and compares them to numerical simulations.

2. Literature review

The literature on boiling emulsions is relatively sparse and very little theoretical work on the subject exists. In this section, the literature on boiling emulsions is reviewed, as well as some related topics that are important to understanding the main subject. These topics include spontaneous nucleation in liquids and modeling of two-phase droplet and particulate flows.

2.1. Spontaneous nucleation

Spontaneous nucleation refers to the formation of vapor nuclei in a superheated liquid independent of nucleation sites on a solid surface. There are two approaches used to predict the degree of superheat necessary to cause spontaneous nucleation. One approach is based on the mechanical stability of a fluid defined by an appropriate equation of state. The other approach considers the microscopic density fluctuations present in fluids, predicted by statistical mechanics.

Spontaneous nucleation generally does not occur in engineering practice because boiling will occur at nucleation sites on a heated solid surface well before the liquid becomes sufficiently superheated to cause spontaneous nucleation. The conditions necessary for spontaneous nucleation can be produced in the laboratory, however, and some experimental studies of spontaneous nucleation that have advanced understanding of the process are discussed in the following sections. Experimental results are generally in good agreement with the theoretical predictions of the limits of superheat.

2.1.1. Thermodynamic limit of superheat

The thermodynamic limit of superheat may be predicted for a Van der Waals fluid, i.e., a fluid that obeys the Van der Waals equation of state. In Fig. 2.1, curve ABCDEF represents an isotherm for a Van der Waals fluid with temperature less than the critical temperature. The curve ABEF represents an isotherm as is commonly taught in engineering thermodynamics, where the straight segment BE represents a saturated mixture.

Consider the behavior of a Van der Waals fluid as it is slowly expanded isothermally from a compressed liquid state (state A). The fluid will proceed along the

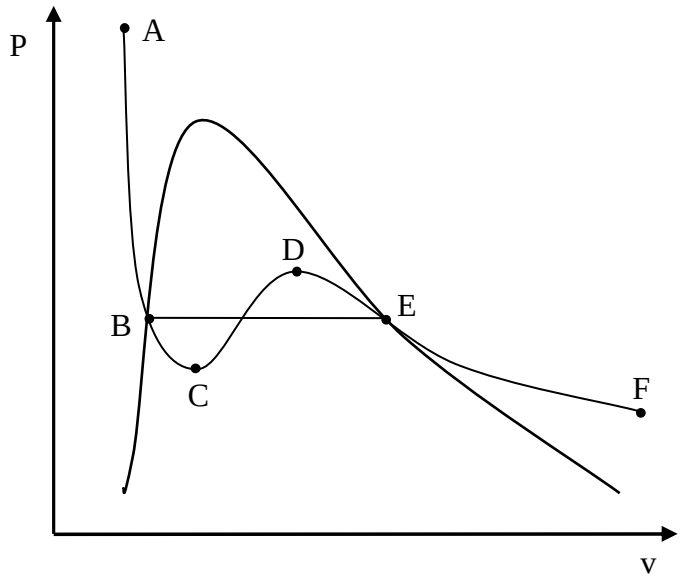

Figure 2.1. Isotherm of a Van der Waals fluid on a P-v diagram.

curve shown in Fig. 2.1 to state B, where it is saturated liquid. The expected behavior, if the liquid is expanded further, is for nucleation sites to become active on the walls of the vessel containing the fluid. The fluid will then become a saturated mixture and follow line BE. If no nucleation sites are present, however, the liquid will instead continue along the Van der Waals curve towards state C, entering the meta-stable liquid state. This process can continue only up to state C. It is impossible for a Van der Waals fluid to exist in stable equilibrium between states C and D because $\partial P/\partial v > 0$. State C, therefore, represents the thermodynamic limit of superheat. (Blander and Katz, 1975)

This approach is not limited to Van der Waals fluids; any fluid that exhibits a "Van der Waals loop" (segment CD) will have a meta-stable liquid state with an upper bound where the slope of the P-v curve crosses through zero. In fact, for most fluids the thermodynamic limit of superheat predicted using the Van der Waals equation of state is a bit too low when compared to experimental results (Blander and Katz, 1975). Other equations of state give more accurate results, although there is some difficulty in accurately modeling the state of meta-stable fluids using data from the stable liquid and vapor regions.

2.1.2. Kinetic limit of superheat

The kinetic limit of superheat is found by considering the density fluctuations that occur in all fluids. In liquids, these density fluctuations take the form of microscopic vapor bubbles, bubble embryos. Most of these bubble embryos are ephemeral and immediately collapse in on themselves due to surface tension. In a highly superheated liquid, some bubbles may pass a critical radius, R_{cr} and continue to grow. If the formation of the bubble embryo is assumed to occur isothermally,

$$P_v = P_\infty + \frac{2\sigma}{R_{cr}}. \tag{2.1}$$

At the critical radius, the vapor pressure inside a bubble embryo exactly balances the ambient pressure and surface tension. This mechanical equilibrium is unstable however. An embryo that is larger than the critical radius will grow to macroscopic size, while an embryo smaller than the critical radius will collapse. The rate at which bubble embryos grow to the critical radius depends on the reaction kinetics, where the reactions under consideration are evaporation from and condensation to the bubble wall. The kinetic limit of superheat is defined as the temperature at which the rate of bubble nucleation due to density fluctuations becomes large. The theory is described in detail by Blander and Katz (1975) and is summarized briefly as follows.

From statistical mechanics, the density of bubble embryos of a given size in a liquid is related to the number density of molecules in the liquid by,

$$N_{embryo}(\chi) = N_{mol} \exp\left(\frac{-W(\chi)}{k_B T}\right), \tag{2.2}$$

where $W(\chi)$ is the work required to form a bubble embryo containing χ molecules. At equilibrium the number of embryos of each size is constant, so the rate at which embryos grow from χ to χ+1 molecules must be independent of χ. This requirement leads to the formula for nucleation rate (Katz, Salzburg, and Reiss, 1966),

$$J = \frac{P}{(2\pi m k_B T)}\left[\int_1^{\infty} \frac{d\chi}{A(\chi)N_{embryo}(\chi)}\right]^{-1}, \tag{2.3}$$

where $A(\chi)$ is the surface area of a bubble embryo containing χ molecules, which typically can be determined by assuming that the bubble is spherical in shape and that the vapor inside behaves as an ideal gas.

Equation (2.2) can be substituted into Eq. (2.3), but an expression for the work of formation of an embryo is required before the integral in Eq. (2.3) can be solved. The work of formation is usually evaluated under the assumption that the embryo remains in mechanical equilibrium as it grows (Blander and Katz, 1975). The right-hand side of Eq. (2.1) is therefore used to describe the pressure in the embryo at all radii. Under this assumption the nucleation rate is,

$$J = N_{mol}\left[\frac{2\sigma}{\pi m B}\right]^{1/2} \exp\left[\frac{-16\pi\sigma^3}{3k_B T(P_v - P_\infty)^2}\right], \tag{2.4}$$

where B has the value 2/3 and m is the mass of a fluid molecule.

The assumption of mechanical equilibrium may not be correct under all circumstances, and several other scenarios have been examined by Kagan (1960). Kagan finds formulas for nucleation rate in which embryo growth is limited by each of four alternative factors: viscosity, inertia, rate of evaporation, and heat transfer. In each case the pre-exponential factor of J differs, but the exponent remains unchanged. For example, assuming that the embryo remains in chemical equilibrium ($P = P_v$) instead of mechanical equilibrium ($P = P_\infty + 2\sigma/r$) changes the value of the factor B from two-thirds to one. Due to the rapid rise in the exponential term with temperature, these changes in the pre-exponential factor are irrelevant for most liquids (Blander and Katz, 1975). The effects of non-ideal gas behavior in the bubble embryo are similarly negligible when considering spontaneous nucleation of a pure substance (Katz and Blander, 1973).

Table 2.1. Nucleation rates of FC-72 at atmospheric pressure (Chen et al., 2006).

T (K)	P_{sat} (kPa)	ρ_f (kg/m^3)	σ (N/m)	J ($m^{-3}s^{-1}$)
403.2	729.1	1320.9	0.0026	5.26×10^{-24}
404.2	745.0	1311.7	0.0025	1.24×10^{-14}
405.2	761.1	1302.8	0.0025	3.97×10^{-8}
406.2	777.5	1293.9	0.0024	2.26×10^{-2}
407.2	794.1	1284.9	0.0023	2.78×10^{3}
408.2	811.0	1276	0.0023	8.71×10^{7}
409.2	828.2	1267.1	0.0022	0.81×10^{10}
410.2	845.7	1258.1	0.0021	4.40×10^{12}
411.2	863.4	1249.2	0.0021	2.55×10^{15}
412.2	881.3	1240.3	0.0020	3.07×10^{18}
413.2	899.6	1232.8	0.0020	1.57×10^{21}

Unlike the thermodynamic limit of superheat, this description of spontaneous nucleation does not provide a definite temperature at which spontaneous nucleation will occur. In fact, Eq. (2.4) predicts a nonzero rate of nucleation for any superheated liquid. To define the kinetic limit of superheat from this theory, one must also specify a nucleation rate above which the liquid is considered to be boiling. In practice, values between 10^{12} and 10^{20} $m^{-3}s^{-1}$ are generally found to give good agreement with experiment (Blander and Katz, 1975; Chen et al., 2006). This range is large, but the exponential term of Eq. (2.4) changes extremely rapidly with temperature for pure liquids and so corresponds to a temperature range of less than three degrees. The terms in the denominator of the exponential, T and P_v increase with temperature, while the surface tension in the numerator decreases with temperature. As shown in Table 2.1 for the heat transfer liquid FC-72, J increases by a factor of approximately 10^3 per Kelvin. Other pure liquids have similar rates of increase in nucleation rate.

2.1.3. Experimental studies of spontaneous nucleation

Spontaneous nucleation may be produced in the laboratory, but care is required to prevent boiling at nucleation sites on solid surfaces. Nucleate boiling is avoided in a

number of ways, including using glass capillary tubes, pulsed heating, and the floating droplet method (Skripov, 1974). A drawn and annealed glass capillary tube has an exceptionally smooth surface that contains few, if any, nucleation sites. Large degrees of superheat were first studied using this method (Wismer, 1922). In the pulsed heating method an electrical heating element (such as a fine wire or a film heater) is immersed in the liquid under study. A pulse of electrical current applied to the heater causes the surface temperature to rise extremely rapidly, at a rate of 10^7 °C/s or more. Both nucleate boiling and spontaneous nucleation occur on the heater surface in the first several tens of microseconds, but the time scale is so short that the nucleate boiling does not dominate, and spontaneous nucleation may be observed (Iida, Okuyama, and Sakurai; 1994). This technique was developed by Pavlov and Skripov (1970) and allows observation of higher nucleation rates than the other methods, although the short time scales involved make observation and measurement of the phenomenon challenging. The final technique, the floating droplet method, uses conditions most similar to those found in dilute emulsions.

One of the first uses of the floating droplet method was by Moore (1959). Moore created droplets of Freon-12 in water in a heated test chamber held at high pressure, and then superheated them by slowly reducing the pressure in the chamber while holding temperature constant. An alternative approach was developed by Wakeshima and Takata (1958), in which the droplet is instead heated at constant pressure. This is accomplished by creating a column of dense, high-boiling-point liquid that is heated mostly at its top. The bottom of the column is held at a temperature below the saturation temperature of the liquid under study. Small droplets of the liquid under study are introduced at the bottom of the column, and they slowly rise into ever warmer liquid until nucleation occurs. This technique was used by several teams of researchers to measure the limits of superheat of a wide variety of liquids, generally finding close agreement with the kinetic limit of superheat (Blander and Katz, 1975; Skripov, 1974).

The effects of impurities in a liquid on its spontaneous nucleation have also been studied experimentally, mostly through the floating droplet method. Usually the liquid under study is distilled in an attempt to remove any microscopic particles suspended in

the liquid, as these are regarded as possible nucleation sites. However, various studies on the effects of suspended particles on nucleation as well as cavitation have produced contradictory results (Kenrick, Gilbert, and Wismer, 1924; Apfel, 1970; Strasberg, 1959). An elegant study by Buivid and Sussman (1978) shows that the suspended particles themselves do not cause nucleation. Instead, gas entrapped within the particles can serve as bubble nuclei. They demonstrate this mechanism by mixing particles of carbon black into pentane and then measuring the temperature at which the boiling occurs after soaking the mixture for some time at temperatures near the saturation temperature of pentane. They find that the longer the soak time of the mixture (during which the gas entrapped in the particles is driven off), the closer the boiling temperature of the droplets comes to the kinetic limit of superheat.

2.2. Continuum models of multiphase flows

Multiphase flows[2] exist in a variety of forms in nature and in many industrial processes. Some examples include the flow of sediment-laden river water, boiling liquids, sprays of liquid fuel in combustors, and the emulsions that are the subject of this study. These examples are classified as dispersed flows, because in each case one phase exists as many separate elements distributed throughout the other phase. Although the equations that govern the motion of these flows is known – the Navier-Stokes equations – it is generally impossible, or at least impractical, to solve directly for the flow field in dispersed multiphase flows because there are too many surfaces to track individually.

Given the complexity of multiphase flows, any practical model of multiphase flow must account for the interaction between phases without tracking all the interfaces between them. Doing so necessarily requires making some assumptions regarding the structure of the dispersed phase(s), and these assumptions limit the range of

[2] The terms 'phase' and 'component' deserve clarification, as their usage is not uniform across all fields of study. In this dissertation, 'component' refers to a distinct substance, while 'phase' identifies both substance and state of matter. For example, a boiling emulsion of FC-72 in water contains two components (FC-72 and water) but three phases (vapor FC-72, liquid FC-72, and liquid water).
However, in the multiphase flow modeling literature, 'phase' is often used generically and could refer to either a component or a phase, depending on how the model is applied. In this Section, phase is used in this generic sense.

applicability of any model of multiphase flows. Many models therefore exist for various types of flows and geometries and at differing levels of complexity, fidelity, and generality (Wallis, 1969), and modeling multiphase flows remains an active field of study.

Increasingly, modeling efforts in multiphase flow are directed towards the field of computational fluid dynamics (CFD), the analysis of fluid flow and related phenomena using numerical methods solved on computers. Approaches to CFD can generally be divided into one of three approaches: direct numerical simulation (DNS), Euler-Lagrange, and Euler-Euler (Rusche, 2002). These are illustrated schematically in Fig. 2.2. The DNS approach is the most computationally costly, as it requires simulating the (usually very small-scale) motion of the surfaces dividing the phases, as well as the fluids themselves. This approach is often prohibitively costly for flows of engineering interest. In the Euler-Lagrange approach, the motions of individual elements of the dispersed phase are simulated but the internal behavior of each element is not. The name Euler-Lagrange reflects the fact that the dispersed phase is simulated using a Lagrangian method (Newton's laws of motion) while the continuous phase is simulated with an Eulerian method (the Navier-Stokes equations). Finally, the Euler-Euler approach is the least computationally intensive because it dispenses with simulating individual elements of the dispersed phase at all. Instead, each phase is represented as a continuous fluid that occupies a fraction of the total volume, ε (Bouré and Delhaye, 1982, Gidaspow, 1994).

The most straightforward interpretation of the Euler-Euler approach is that all the quantities that are considered (phase fraction, velocity, temperature, and so on) are composite time- and space-averaged values. This is well-suited to CFD, in which the flow domain under consideration is split into a number of discrete volumes and the simulation proceeds by discrete time steps. While this interpretation has clear physical meaning, it leads to a number of difficulties that are discussed in detail by Hill (1998).

One limitation of composite-averaged equations is in the scale of the discrete volumes and time steps. For a volume-averaged quantity of the dispersed phase to be meaningful, the volume over which averaging takes place must be large compared to

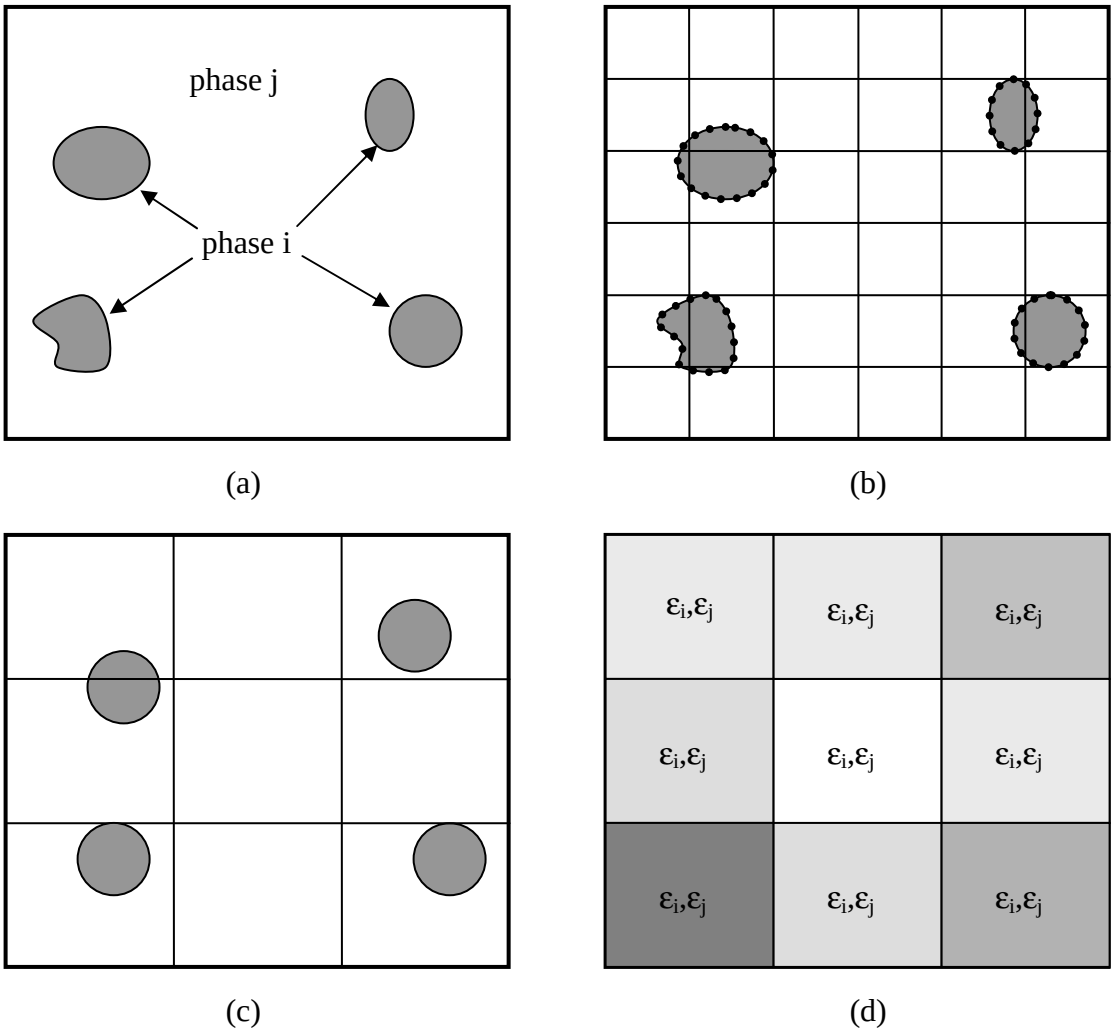

Figure 2.2. (a) Dispersed two-phase flow, (b) DNS approach where surfaces as well as fluid elements are simulated, (c) Euler-Lagrange approach where individual elements of dispersed phase are simulated, (d) Euler-Euler approach where average volume fraction of each phase is simulated.

the average spacing between elements of the dispersed phase. Similarly, for a time-averaged quantity to be meaningful, the averaging period must be long compared to the transit time of an element of the dispersed phase through the volume. On the other hand, the sizes of the discrete volumes and time steps must be small compared to the macroscopic flow features that the simulation is meant to capture. It is not always possible to satisfy both of these requirements simultaneously (Hill, 1998).

Another difficulty rises from correlation of fluctuations in the averaged quantities. Usually the composite-averaging process is accomplished by averaging over the discrete volume first and then over time. The intermediate quantity – an instantaneous, space-averaged value – fluctuates in time. A number of new terms arise in the Navier-Stokes equations due to correlations in the fluctuations of different quantities, similar to the Reynolds stress terms found in turbulent flows, and the physical meanings of the new terms are not always clear (Hill, 1998).

These difficulties may be eliminated by abandoning the composite averaging process altogether and instead using ensemble averages. This approach, also called conditional averaging, yields averaged mass, momentum, and internal energy balance equations in a single averaging operation (Drew and Passman, 1999),

$$\frac{\partial \varepsilon_i \bar{\rho}_i}{\partial t} + \nabla \cdot \left(\varepsilon_i \bar{\rho}_i \bar{\mathbf{U}}_i \right) = \Gamma_i , \tag{2.5}$$

$$\frac{\partial \varepsilon_i \bar{\rho}_i \bar{\mathbf{U}}_i}{\partial t} + \nabla \cdot \left(\varepsilon_i \bar{\rho}_i \bar{\mathbf{U}}_i \bar{\mathbf{U}}_i \right) = \nabla \cdot \left[\varepsilon_i \left(\bar{\mathbf{T}}_i + \mathbf{T}_i^{\mathrm{Re}} \right) \right] + \varepsilon_i \bar{\rho}_i \bar{\mathbf{b}}_i + \mathbf{F}_i + \mathbf{U}_{i,I} \Gamma_i , \tag{2.6}$$

$$\begin{aligned} \frac{\partial \varepsilon_i \bar{\rho}_i \bar{e}_i}{\partial t} + \nabla \cdot \left(\varepsilon_i \bar{\rho}_i \bar{\mathbf{U}}_i \bar{e}_i \right) = \varepsilon_i \bar{\mathbf{T}}_i : \nabla \bar{\mathbf{U}}_i - \nabla \cdot \left[\varepsilon_i \left(\bar{\mathbf{q}}_i + \mathbf{q}_i^{\mathrm{Re}} \right) \right] + \\ \varepsilon_i \bar{\rho}_i \bar{S}_i + \varepsilon_i D_i + E_i + e_{i,I} \Gamma_i . \end{aligned} \tag{2.7}$$

All quantities in Eqs. (2.5) through (2.7) are averaged; the over bar denoting averaging is omitted henceforth for brevity. Internal energy, e_i, and velocity, $\mathbf{U}_i$, are mass-weighted (Favré averaged). The body force is $\mathbf{b}_i$ and the volumetric heating rate is S_i. The derivation of these equations is described in more detail in Appendix C.

The volumetric rate of mass transfer to phase i through interfaces is Γ_i. The interfacial force applied to phase i from other phases is $\mathbf{F}_i$ and the interfacial internal energy transfer to phase i is E_i. Stress is decomposed into an average stress, $\mathbf{T}_i$, and the Reynolds stress, $\mathbf{T}_i^{\mathrm{Re}}$. Similarly, the heat flux is decomposed into the flux based on

average temperature gradients, $\mathbf{q}_i$, and the fluctuation heat flux, $\mathbf{q}_i^{Re}$. The internal energy equation also contains dissipation, D_i. All of these terms must be defined through either constitutive laws or other closure equations.

The fluid is generally assumed to be Newtonian so that, using Stokes' assumption,

$$\mathbf{T} = -P\mathbf{I} + \mu\left(\nabla\mathbf{U} + \nabla^T\mathbf{U} - \frac{2}{3}\mathbf{I}(\nabla\cdot\mathbf{U})\right). \tag{2.8}$$

It is further assumed that the pressure is the same in each phase. If the Reynolds stress is represented using Boussinesq's eddy viscosity hypothesis (Pope, 2000), the stress term in Eq. (2.6) is expressed,

$$\begin{aligned}\nabla\cdot\left[\varepsilon_i\left(\mathbf{T}_i + \mathbf{T}_i^{Re}\right)\right] &= -\varepsilon_i\nabla P + \nabla\cdot\left[\varepsilon_i\left(\bar{\mu}_i + \mu_{i,T}\right)\left(\nabla\mathbf{U}_i + \nabla^T\mathbf{U}_i - \frac{2}{3}\mathbf{I}(\nabla\cdot\mathbf{U}_i)\right)\right] \\ &= -\varepsilon_i\nabla P - \nabla\cdot\left(\varepsilon_i\rho_i\mathbf{R}_{eff,i}\right).\end{aligned} \tag{2.9}$$

For brevity, the effective viscous stress term is sometimes expressed as $\mathbf{R}_{eff,i}$, as shown above. The term $P\nabla\varepsilon_i$ is absorbed into a fluctuating interfacial pressure term by Hill (1998). Hill (1998) and Rusche (2002) use a k-epsilon turbulence closure model and include an additional term that is a function of the turbulent kinetic energy. On the other hand, Drew and Passman (1999) omit the $\nabla\cdot\mathbf{U}_i$ term and use different average velocities for the viscous and turbulent stresses.

The interfacial momentum transfer term in Eq. (2.6) is decomposed into several individual forces. Drew and Passman (1999) identify drag, virtual mass, lift, rotation, turbulent dispersion, and other forces. The expressions that are developed for these forces are typically based on the forces that act on a single representative element of the dispersed phase, and a correction is sometimes applied to account for interactions between the many dispersed elements present in a multiphase flow.

For flows in which the dispersed elements are small enough to be subjected to Stokes' drag, the averaged drag force is (Ishii and Zuber, 1979),

$$\mathbf{F}_D = \frac{18\varepsilon_d}{d_d^2}\mu_{eff}\left(\mathbf{U}_c - \mathbf{U}_d\right), \tag{2.10}$$

where the subscripts d and c refer to the dispersed and continuous phases respectively, d_d is the characteristic diameter of the dispersed elements, and μ_{eff} is the effective viscosity of the mixture. The effective viscosity accounts for the increased drag experienced by dispersed elements when they are not widely spaced (that is, when ε_d is not near zero). Rusche and Issa (2000) develop correction factors as functions of ε_d that may be applied to the single-element drag force for bubbly, droplet, and particulate flows.

Drew and Passman (1999) express virtual mass, lift, and rotational forces,

$$\mathbf{F}_{vm} = C_{vm}\varepsilon_d\rho_c\left(\frac{D_c\mathbf{U}_c}{Dt} - \frac{D_d\mathbf{U}_d}{Dt}\right), \tag{2.11}$$

$$\mathbf{F}_L = -C_L\varepsilon_d\rho_c\left(\mathbf{U}_c - \mathbf{U}_d\right)\times\left(\nabla\times\mathbf{U}_c\right), \tag{2.12}$$

$$\mathbf{F}_R = -C_R\varepsilon_d\rho_c\left(\mathbf{U}_c - \mathbf{U}_d\right)\times\left(\nabla\times\mathbf{U}_d\right), \tag{2.13}$$

where C_{vm} = ½ and $C_L = C_R$ = ¼. They argue that the principle of objectivity requires that $C_L + C_R = C_{vm}$, for only in that case is the sum $\mathbf{F}_{vm} + \mathbf{F}_L + \mathbf{F}_R$ frame indifferent. The three forces, taken individually, are not frame indifferent. However, many practitioners consider only the virtual mass force, or virtual mass and lift forces, and neglect the others (Behzadi, Issa, and Rusche, 2004, Gosman et al., 1992, Hill, 1998, Hao and Tao, 2003b). Further, experiments show that for dispersed mixtures, the virtual mass coefficient increases slowly with ε_d (Drew and Passman, 1999, Gosman et al., 1992) while the lift coefficient rapidly decreases towards zero with increasing

dispersed phase fraction (Behzadi, Issa, and Rusche, 2004). This discrepancy may be an indication that the form of Eqs. (2.12) and (2.13) is not correct for dispersed flow. Rusche (2002) examines other equations for lift that do not depend on shear in the average flow.

Gosman et al. (1992) and Drew and Passman (1999) both include an additional turbulent drag force, which Drew and Passman express as,

$$\mathbf{F}_{TD} = C_{TD}\frac{3}{4}\frac{\rho_c C_D}{d_d}\varepsilon_d\left|\mathbf{U}_c - \mathbf{U}_d\right|\mathbf{T}_c \cdot \nabla\varepsilon_d\,, \tag{2.14}$$

where for small particles $C_{TD} = 1$. Other interfacial forces include the Basset and Faxén forces, as well as a half-dozen additional terms that Drew and Passman (1999) list but do not name. These forces are neglected in simulations of multiphase flow. In fact, Gosman et al. (1992) find that only the drag force is significant for liquid-solid flows and drag and virtual mass forces for liquid-gas flows.

Many practitioners are concerned only with describing the flow field for non-reacting two-phase flows, so that $\Gamma_i = 0$, and the internal energy equation is not solved. One group that has used the Euler-Euler approach to successfully simulate two-phase flows with both heat and mass transfer between phases is Hao and Tao (2003a, 2003b). Hao and Tao numerically predict the melting of a packed bed of spheres in liquid flow (2003b). Additional constitutive relations are required to model heat transfer between the phases due to convection and mass transfer due to melting. They use an energy equation similar to Eq. (2.7) but expressed in terms of enthalpy rather than internal energy. They neglect the viscous dissipation and flow work terms, and use Fourier's law to express $\mathbf{q}_i$ in terms of the mean temperature gradient. Their simulations are laminar so they do not include the turbulent heat flux term. Hao and Tao do not attempt to simplify the equations further or develop an analytical solution from them. They perform simulations of a packed bed of spheres of ice in a horizontal flow of water through a channel, with conditions matching those of earlier experiments (Hao and Tao,

2003a). The results of the simulations match those of the experiment well for changes in the depth of the packed bed as well as the mass of melted ice over time.

In a separate study, Hao and Tao (2004) use an Euler-Euler model to simulate flow and heat transfer in a laminar flow of a liquid laden with particles of encapsulated phase change material (PCM). The governing equations are similar to those obtained in the previous study, although they are simpler in this case because there is no mass transfer between the encapsulated PCM and the carrier fluid. The specific enthalpy of the particle component is used to differentiate between solid, partially melted, and liquid PCM, and the bulk properties (density, specific heat) of the PCM are defined accordingly at each point. Thermal equilibrium within each PCM particle is assumed, although not between the PCM and the carrier fluid. The study simulates flow in a microchannel with a diameter of 122 μm and particle sizes between 0.24 and 10 μm. No experimental data under such conditions exist for direct comparison, but the authors find qualitative agreement between their results and experiments performed at larger scales. Further numerical simulations are made with the goal of finding optimal operating conditions for such particle-laden flows (Xing, Tao, and Hao; 2006). These simulations are performed at a larger scale so that their conditions can be matched to experiments. The authors again find reasonably good agreement with experiment, although sensitivity of both experiment and simulation to the flow inlet temperature near the melting temperature of the PCM leads to large uncertainty in the results.

Determination of the properties of each phase can be problematic. It must be kept in mind that in an Euler-Euler model of multiphase flow, a collection of discrete dispersed elements is represented as a fictitious continuous fluid. The properties of the fictitious fluid are not the same as those of the fluid that makes up the actual dispersed elements. The property for which this distinction is most important is viscosity. Many correlations exist for the effective viscosity of multiphase mixtures, but for an Euler-Euler model some method is required to split up the effective viscosity between the phases of the mixture. Xing, Tao, and Hao (2006) take the approach of setting the viscosity of the continuous phase equal to that of the pure fluid and assigning the

'excess' viscosity to the dispersed phase using a weighted average based on volume fraction[3],

$$\begin{aligned} \bar{\mu}_c &= \mu_c \\ \bar{\mu}_d &= \left(\mu_{eff} - \varepsilon_c \mu_c\right)\varepsilon_d^{-1}. \end{aligned} \tag{2.15}$$

This linear relationship between the phase viscosities is assumed by Xing et al., without justification. They find that this approach, when implemented in a numerical simulation, gives results that more closely match their experimental data than assigning a fixed value of 0.01 kg/m-s to $\bar{\mu}_d$. A more rigorous approach by Soo (1967) for suspensions of solid particles in gas results in a distribution of viscosity based on mass fractions,

$$\begin{aligned} \bar{\mu}_c &= \left(1 - \frac{\varepsilon_d \rho_d}{\varepsilon_c \rho_c}\right)\mu_{eff} \\ \bar{\mu}_d &= \frac{\varepsilon_d \rho_d}{\varepsilon_c \rho_c}\mu_{eff}. \end{aligned} \tag{2.16}$$

Regardless of the method used to assign viscosity to each phase, a suitable empirical relation must be selected to determine the effective mixture viscosity, μ_{eff}.

2.3. Boiling emulsions

Several experimental studies of the heat transfer performance of boiling emulsions have been performed over the past few decades. Emulsions are opaque due to the scattering of light at the surfaces of the droplets, and thus direct observation of the boiling process in experiments is generally impossible. Therefore little is known about

[3] An over bar on a fluid property indicates the property assigned to the phase in the Euler-Euler model. So, μ_d is the viscosity of the liquid that makes up the droplets in the emulsion, while $\bar{\mu}_d$ is the viscosity assigned to the phase that represents the droplets.

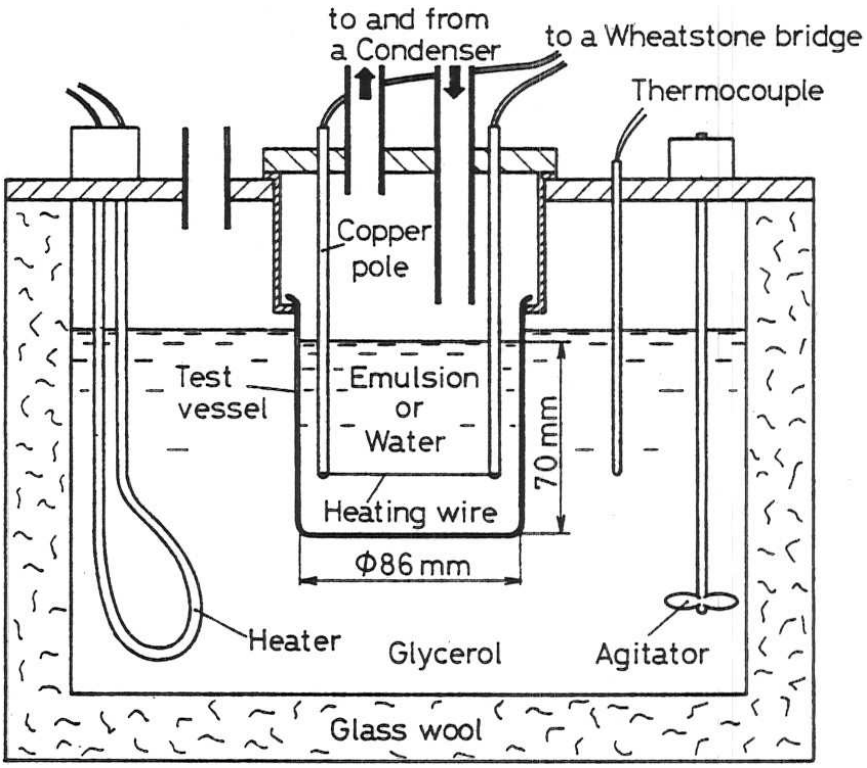

Figure 2.3. Apparatus used by Mori et al. to measure the heat transfer coefficient of boiling emulsions (Mori, Inui, and Komotori, 1978).

the detailed behavior of a boiling emulsion at the heated surface or what interactions may occur between the two components. The complex structure of the emulsion makes theoretical predictions difficult as well.

An early study of boiling emulsions by Mori, Inui, and Komotori (1978) investigates boiling emulsions of water and oil. The oils used have boiling points of at least 196 °C, so the water is the low-boiling-point liquid. Their study covers a wide range of mass fractions of water, from 10 to 95%. None of the emulsions used in this study can therefore be considered dilute emulsions. As shown in Fig. 2.3, Mori et al. measure boiling heat transfer from a thin heated wire in quiescent fluid. They use emulsifiers to produce stable emulsions with average droplet size less than 6 μm.

Mori et al. find that for oil in water emulsions a significant temperature overshoot occurs before boiling is initiated, as shown in Fig. 2.4 (a). The designation ‘oil in water’ indicates that water makes up more than half of the mixture, so that the structure

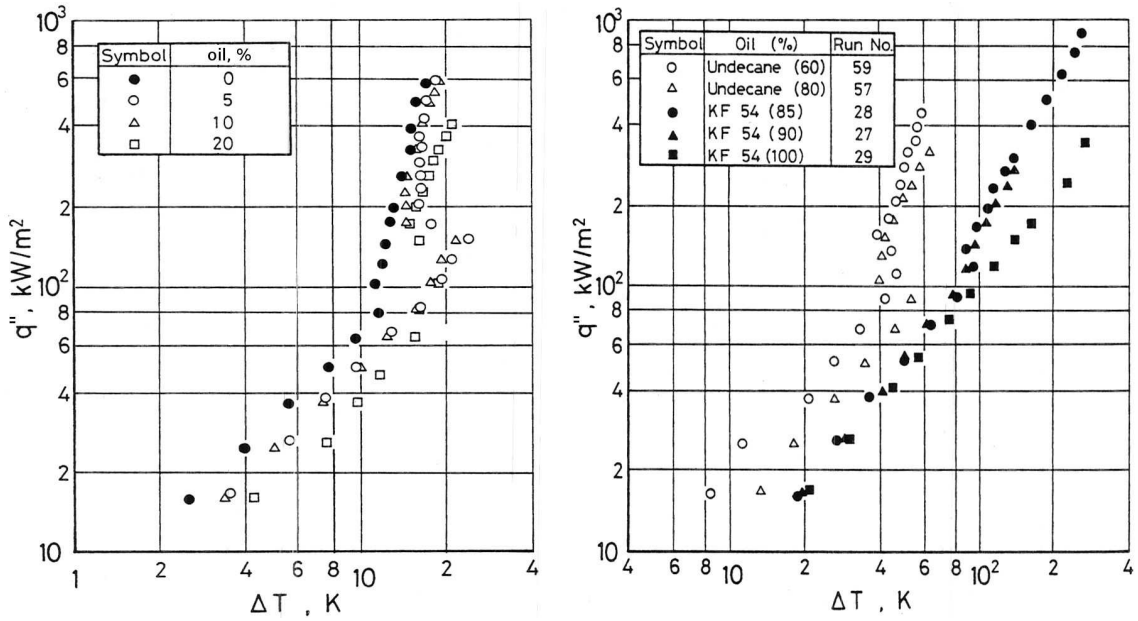

(a) (b)

Figure 2.4. Heat transfer data of Mori et al. for (a) oil in water emulsions using KF 96 synthetic oil and 1% Tween™ 80 emulsifier and (b) water in oil emulsions using Span™ 80 emulsifier. All percentages are on mass basis (Mori, Inui, and Komotori, 1978).

of the emulsion may be assumed to be droplets of oil dispersed in water. Mori et al. suggest that the large temperature overshoot is a result of partial wetting of the heated wire by the oil. Once boiling begins the oil is driven off, causing a subsequent decrease in surface temperature. They also find that, in a few cases of boiling at high heat flux, the surface temperature may suddenly increase by ~200 °C , which they speculate may be due to rewetting of the wire by oil. They find that the heat transfer coefficient of the emulsion may be better or worse than that of pure water depending on the emulsifier used, but the type of oil generally does not have any effect. The boiling heat transfer coefficient generally decreases with increasing oil concentration.

Mori et al. also study water in oil emulsions and find that some of the trends identified in oil in water emulsions continue, as seen in Fig. 2.4(b). Water in oil emulsions require higher temperature overshoots before boiling begins, typically between 50 and 100 °C, and have lower heat transfer coefficients. Unlike the oil in water cases, for water in oil emulsions the type of oil does have an effect on the heat

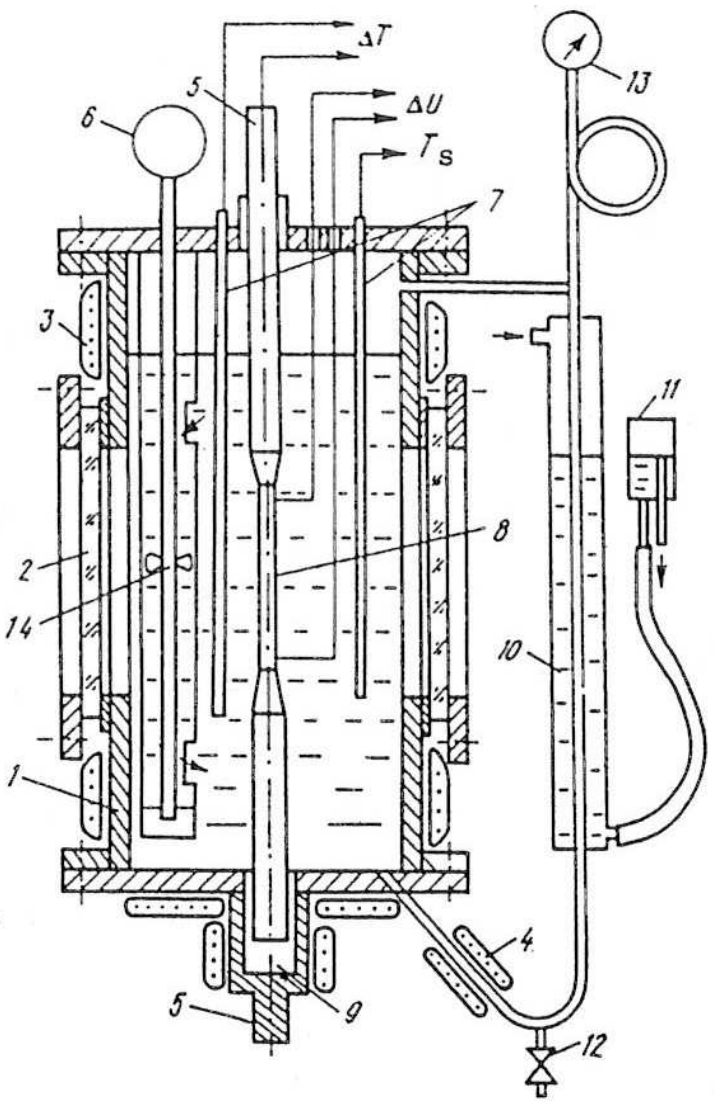

Figure 2.5. Apparatus used by Ostrovskiy. Components include (1) chamber, (2) port, (3) and (4) auxiliary heaters, (7) thermocouple sleeves, (8) heater, (10) condenser, (13) pressure gage, (14) agitator (Ostrovskiy, 1988).

transfer coefficient. Mori et al. do not speculate on the boiling mechanism of water in oil emulsions.

Some of the difficulties specific to studying boiling emulsions are illustrated by Ostrovskiy (1988). The apparatus used by Ostrovskiy to study pool boiling of emulsions is shown in Fig. 2.5. He uses emulsions of water and various other liquids with low boiling points, so that water is the high boiling point liquid. He does not use emulsifiers, and instead uses an agitator inside the apparatus to emulsify the mixture

and maintain the emulsion. He does not report the droplet sizes of the emulsions. The opacity of the mixture is used as an indicator that the mixture is emulsified. Ostrovskiy measures heat transfer from a vertical cylinder with 6.6 mm diameter and 70 mm heated length, in contrast to the heated fine wire used by Mori et al.

For emulsions of water and R-113, Ostrovskiy finds that emulsions containing 20 and 40% water have approximately the same boiling heat transfer coefficient as pure R-113. This result is similar to the findings of Mori et al. for oil in water emulsions using Tween^{TM} 80[4] emulsifier. Ostrovskiy does not note any difference in the degree of superheat required to initiate boiling. Ostrovskiy also investigates emulsions of water and butyl alcohol. Butyl alcohol is partially soluble in water, and mixing the two liquids produces two water-butyl alcohol solutions with different densities but the same saturation temperature. He finds that there is little difference in the boiling heat transfer coefficient for the less dense solution, the more dense solution, and emulsions of the two solutions.

Finally, Ostrovskiy investigated emulsions of water and benzene. The boiling heat transfer coefficients for these emulsions are shown in Fig. 2.6. An interesting feature of these boiling curves is that their slope for the emulsions is much lower than for pure liquids. These results are unlike those of other emulsions studied by Ostrovskiy, in which both the emulsions and the pure liquids showed similar dependence of heat transfer coefficient on heat flux. For these benzene and water emulsions, $h \propto (q'')^{0.3}$, which is close to the behavior of single-phase turbulent free convection ($h \propto (q'')^{0.25}$). Ostrovskiy attributes this behavior to the fact that, at the heated wall, heat is removed by convection to the water, and the water is stirred by the boiling of superheated benzene droplets in a turbulent-like manner.

However it is noteworthy that the portions of the boiling curves in Fig. 2.6 that follow the $h \propto (q'')^{0.3}$ curve all correspond to temperature differences of less than 20 °C. Ostrovskiy does not report the bulk temperature of the emulsion but it is reasonable to

[4] Tween 80 is a trademark of ICI Americas. Also known as Polysorbate 80, it is a nonionic surfactant. Span 80 (Sorbitan monooleate) is also a nonionic surfactant, and is a trademark of Croda International PLC.

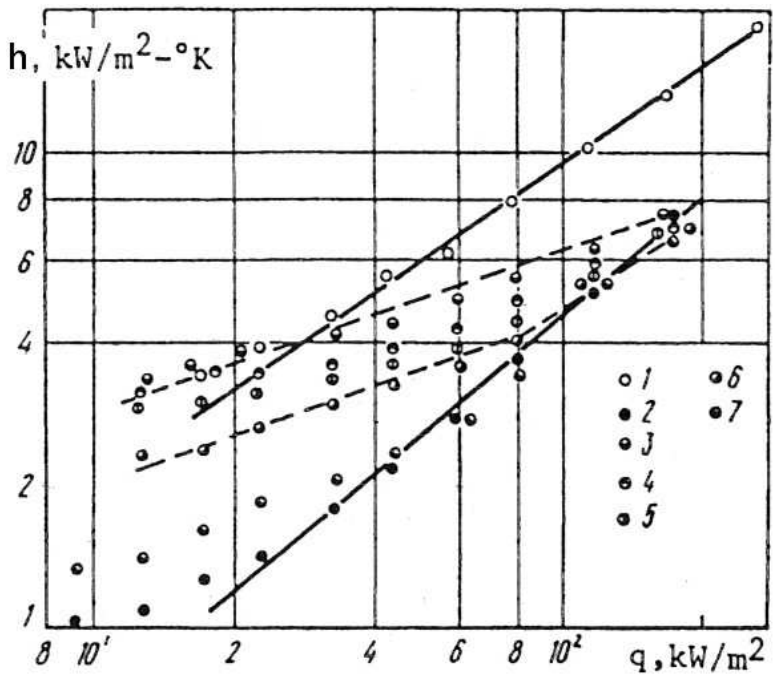

Figure 2.6. Heat transfer coefficient for boiling water-benzene emulsions. (1) water; (2) benzene; (3) to (7) 20, 40, 55, 70, and 80% benzene, respectively (Ostrovskiy, 1988).

assume that the bulk of the emulsion could not have become significantly superheated, else Ostrovskiy would have observed the "sudden foaming in the bulk" reported by Mori et al. Under this assumption, the temperature of the heated surface must be less than 20 °C above the saturation temperature of the benzene. The data of Mori et al. indicate that superheats of greater than 20 °C are often needed to initiate boiling. It is possible that the boiling curves for water-benzene emulsions reported by Ostrovskiy resemble single-phase free convection because there was not, in fact, any boiling taking place. This would also explain the increase in the slope of the boiling curves for the 55, 70, and 80% benzene emulsions at high heat flux. For all three curves, the slope of the curve changes at a temperature difference of approximately 20 °C, which is where the water in the emulsion would be expected to begin boiling as well.

That such a simple point as whether or not boiling was taking place is unclear highlights some of the difficulties of investigating boiling emulsions. The large degree of superheat required to initiate boiling means that a surface having a temperature greater than the saturation temperature of the low-boiling-point liquid is not sufficient to

ensure that boiling takes place. The opacity of emulsions generally prevents direct observation of the heated surface, unless special effort is made in the design of the test apparatus. Mori et al. watched for bubbles on the free surface of the emulsion above the heated wire to indicate boiling. It appears that the design of Ostrovskiy's apparatus did not permit similar observations.

2.3.1. Dilute emulsions

A number of experimental studies of boiling dilute emulsions have been performed by Bulanov and co-workers in the past twenty-five years (Bulanov, Skripov, and Khmyl'nin, 1984; Bulanov, Gasanov, and Turchaninova, 2006). Dilute emulsions are those in which the low boiling point liquid is the dispersed component and makes up less than ~5% of the mixture by volume. They find that very high degrees of superheat are necessary to cause boiling of the dispersed component, similar to the findings of Mori et al., and they reason that this is due to the fact that the droplets, not being in contact with the heated surface, must undergo spontaneous nucleation. They also show evidence for a boiling mode that they call chain activation of nucleation sites, in which the explosive boiling of one highly-superheated droplet causes nearby droplets to boil as well.

Early experimental studies by Bulanov et al. find that boiling dilute emulsions have several favorable characteristics. In these studies the low-boiling-point liquid is water, and is dispersed in oil that has high saturation temperature. In both pool and flow boiling it is found that the heat transfer coefficient is always higher for the emulsion than for the pure oil. In flow boiling experiments the improvement in heat transfer is found to increase with increasing mass fractions of water, up to 33% (Bulanov, Skripov, and Khmylnik; 1993), as shown in Fig. 2.7. In contrast, in pool boiling experiments the heat transfer coefficient is independent of mass fraction for fractions above 1% (Bulanov, Skripov, Gasanov, and Baidakov; 1996), as shown in Fig. 2.8. The emulsion undergoes nucleate boiling under a very wide range of surface temperatures without any sign in the heat transfer data of transition to film boiling (Fig. 2.9). Bulanov et al. speculate that film boiling cannot occur because the boiling of dispersed droplets

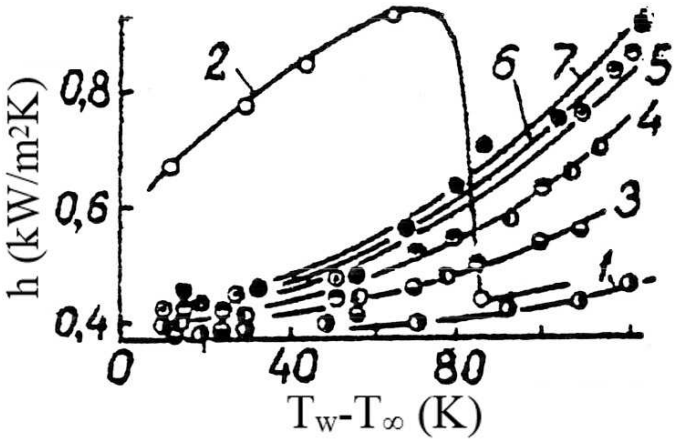

Figure 2.7. Flow boiling heat transfer coefficients for (1) oil; (2) water; and (3) – (7) water in oil emulsions of 3, 6, 12, 20, and 33% water by mass, respectively. T_∞ = 60 °C (Bulanov, Skripov, and Khmylnik, 1993).

generates insufficient vapor (Bulanov, Skripov, Gasanov, and Baidakov; 1996). The points in Fig. 2.8 corresponding to emulsions with surfactants show that the effects of surfactants are ambiguous, which is similar to the findings of Mori et al. (1978).

One unfavorable characteristic identified in dilute emulsion boiling is the high degree of superheat required to initiate boiling of the dispersed component, often 60 °C or more (Fig. 2.9). In one study, however, the water is found to boil with very little superheat (Bulanov, Skripov, and Khmyl'nin; 1984). In this case only, at low superheats the heat transfer coefficient is sometimes reduced below that of pure oil. This suggests that the suddenness of the boiling of highly-superheated droplets is essential to the heat transfer improvement, possibly because this action causes turbulence in the surrounding liquid. The authors are unable to find any reason for the abnormally early initiation of boiling in this study.

Bulanov et al. have explored several other aspects of boiling dilute emulsions, including the effects of the droplet size and the addition of surfactants and suspended particles. They find that the degree of superheat required for boiling to occur decreases with increasing droplet size in the emulsion, although once boiling is initiated the heat transfer coefficient has little dependence on the droplet size (Fig. 2.10) (Bulanov and

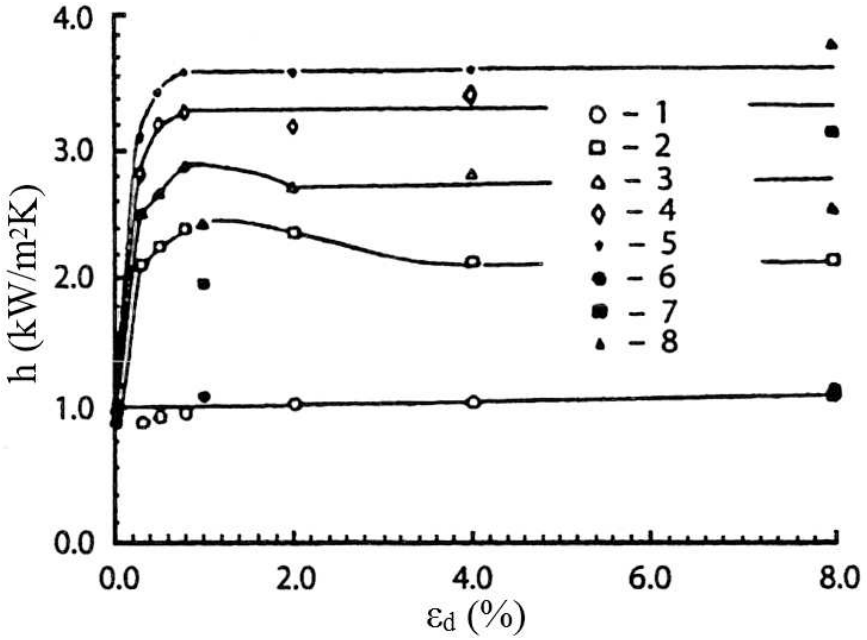

Figure 2.8. Pool boiling heat transfer coefficients for (1 - 5) water in oil emulsions at T_w = 100, 190, 205, 220, and 235 °C respectively; and (6 - 8) water in oil emulsions with emulsifier at T_w = 100, 190, and 220 °C respectively (Bulanov, Skripov, Gasanov, and Baidakov, 1996).

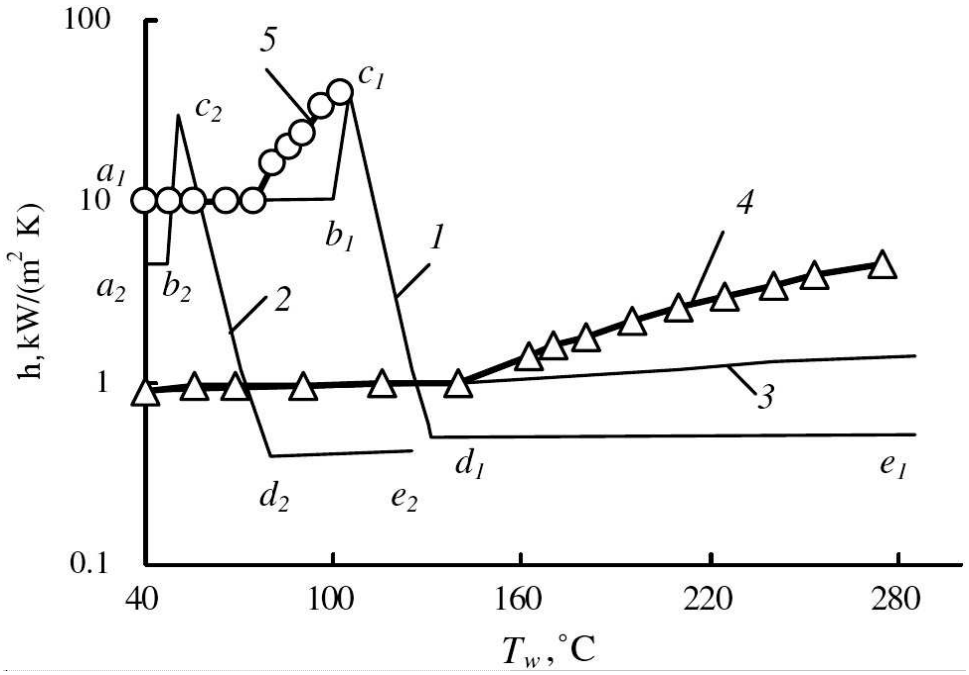

Figure 2.9. Pool boiling heat transfer coefficients for (1) water, (2) R-113, (3) transformer oil, (4) water in oil emulsion, and (5) R-113 in water emulsion (Bulanov and Gasanov, 2008).

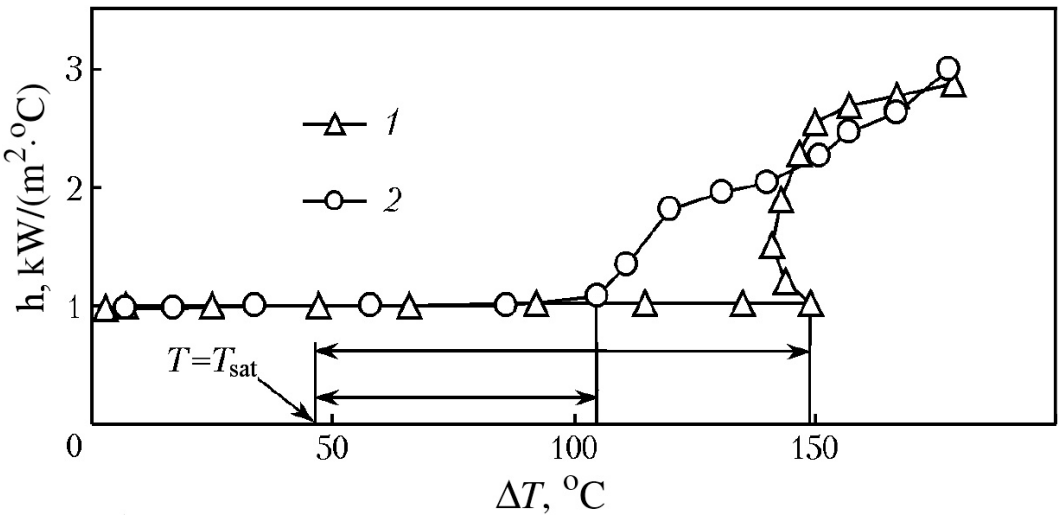

Figure 2.10. Pool boiling heat transfer coefficients for water in PES-5 oil emulsions with 1.0% water by volume, T_∞ = 60 °C, and (1) d_d = 1.5 μm and (2) d_d = 35 μm (Bulanov and Gasanov, 2006).

Gasanov, 2007). The addition of particles may advance or retard the onset of boiling, depending on the interaction of the particles with the low-boiling-point liquid and dissolved gases. In general, adding carbon particles to emulsions in which water is the low boiling point liquid reduces the boiling delay owing to the tendency of carbon particles to attract noncondensable gases (Section 2.1.3). On the other hand, carbon particles may increase the boiling delay when the low boiling point liquid is an organic substance such as pentane or ether because the carbon also absorbs the liquid (Bulanov and Gasanov, 2008). Surfactants are found to delay the onset of boiling further, as shown in Fig. 2.11. They speculate that the increased delay occurs because the surfactant coats the surface of any suspended particles as well as bubble embryos and thus interferes with nucleation. However, these explanations do not account for all of the experimental data (Bulanov, Gasanov, and Turchaninova; 2006).

Based on these experimental results, Bulanov (2001) has developed the following model of boiling dilute emulsions. He assumes that each droplet that boils does so randomly, as in spontaneous nucleation, while inside the thermal boundary layer surrounding a heated surface. Boiling does not depend on contact with the heated surface itself. When a droplet boils it rises out of the thermal boundary layer owing to

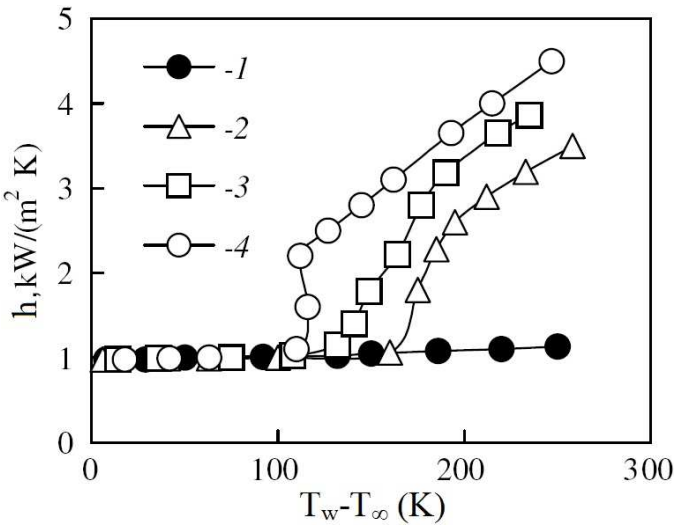

Figure 2.11. Boiling delay at T_∞ = 36 °C for (1) pure oil; and water in oil emulsions with (2) trisodiumphosphate emulsifier, (3) caustic soda emulsifier, and (4) no emulsifiers (Bulanov and Gasanov, 2008).

buoyancy, and its place is taken by more emulsion. This process is illustrated schematically in Fig. 2.12. The probability of boiling is based on the nucleation rate of the low boiling point liquid in the emulsion, J_{eff}, and the time of residence of the droplet in the thermal boundary layer. The residence time is a function of the rate at which droplets boil and the thickness of the thermal boundary layer.

Bulanov makes some contradictory assumptions regarding the temperature profile in the thermal boundary layer. For the purpose of calculating the nucleation rate, Bulanov assumes that the fluid temperature in the thermal boundary layer is uniform and equal to the heated surface temperature. For the purpose of calculating the thickness of the boundary layer, he assumes a linear temperature profile. Bulanov also assumes that the energy required to boil the droplets is provided by the liquid surrounding them, so that the temperature in the boundary layer decreases as droplets boil. These assumptions are inconsistent with each other and make a detailed examination of the behavior of the emulsion in the boundary layer impossible.

In mathematical terms, for a monodisperse emulsion in which droplets enter the boundary layer as saturated liquid and bubbles exit as saturated vapor, the heat transfer to the boiling droplets is,

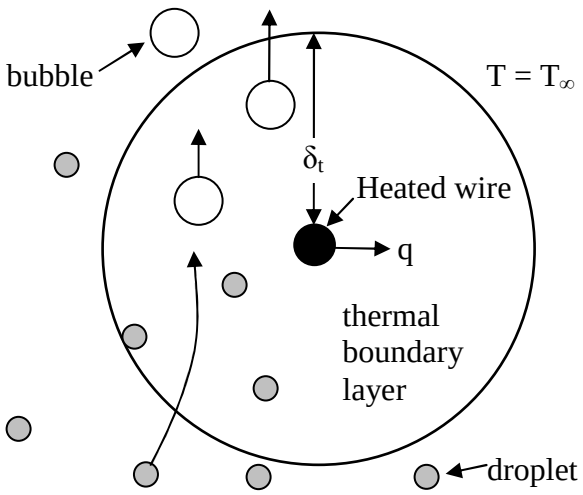

Figure 2.12. Bulanov's model of boiling emulsion.

$$Q = A\delta_t \varepsilon_d \rho_d i_{fg} \left[1 - \exp\left(-J_{eff} V_d \tau\right)\right]. \tag{2.17}$$

The expression $1 - \exp\left(-J_{eff} V_d \tau\right)$ represents the probability that a droplet boils during residence time τ in the boundary layer, where J_{eff} is the effective nucleation rate and V_d is the volume of a droplet. For a monodisperse emulsion, this probability also represents the fraction of droplets, and therefore the fraction of droplet liquid, that boils. In Eq. (2.17), δ_t is the thickness of the thermal boundary layer, A is the heated surface area, and ε_d is the volume fraction of droplets, so that $A\delta_t\varepsilon_d$ represents the total volume of droplet liquid in the boundary layer. The boiling heat transfer rate is obtained by dividing Eq. (2.17) by the droplet residence time τ. The boiling heat transfer coefficient may therefore be expressed as $h = Q/A\tau\left(T_s - T_{sat}\right)$.

Next, Bulanov equates the droplet residence time to the time required for a bubble to rise through the thermal boundary layer due to buoyancy. Assuming that the bubbles are small enough to be subjected to Stokes drag and that the surrounding liquid is motionless, the bubble rise time is,

$$\tau = \frac{\delta_t}{Ar}\frac{18 d_b \rho_d}{\mu_{eff}}, \tag{2.18}$$

where Ar is the Archimedes number of the bubble. Using this characteristic time in the equation for the heat transfer coefficient, Bulanov expresses the boiling Nusselt number as,

$$Nu = \frac{h d_b}{k_{eff}} = A_0 \frac{Ar\,Pr}{St}\varepsilon_d\left[1 - \exp\left(-J_{eff} V_d \tau\right)\right]. \tag{2.19}$$

Bulanov uses the bubble diameter as the characteristic length in the Nusselt number. The factor of 18 in Eq. (2.18) is absorbed into an adjustment parameter A_0, which must be obtained from experimental data. Bulanov calls the Prandtl number in Eq. (2.19) the "mixed" Prandtl number, as it contains both droplet and emulsion properties, $Pr = \mu_{eff} c_{p,d} / k_{eff}$.

Equations (2.18) and (2.19) cannot be solved yet because the boundary layer thickness in Eq. (2.18) is unknown. Bulanov estimates the boundary layer thickness by assuming that heat transfer through the boundary layer occurs by pure conduction, and that the temperature profile in the boundary layer is linear. Under these assumptions, the conductive heat flux through the boundary layer is $k_{eff}\left(T_s - T_{sat}\right)/\delta_t$. Bulanov sets this flux equal to the convective heat flux expressed in terms of the Nusselt number, $Nu k_{eff}\left(T_s - T_{sat}\right)/d_b$, with the result $\delta_t = d_b/Nu$. The characteristic time can therefore be expressed by,

$$\tau = \frac{18 d_b^2 \rho_d}{Ar Nu \mu_{eff}}. \tag{2.20}$$

Equations (2.19) and (2.20) can be solved iteratively for the boiling heat transfer coefficient.

Equation (2.19) indicates that the boiling heat transfer coefficient varies with the droplet volume fraction. But, as shown in Fig. 2.8, experimental data show that for pool boiling the heat transfer coefficient is independent of droplet fraction for fractions above ~1%. Bulanov explains this discrepancy by noting that when a superheated droplet boils, the energy required to vaporize the droplet comes from the surrounding liquid, so boiling droplets cause the average temperature of the emulsion to decrease. If the droplet fraction is large enough, the temperature of the emulsion will fall to the saturation temperature of the droplet liquid before all the droplets boil. For a given volume of emulsion, V, in the thermal boundary layer, the enthalpy required to vaporize all of the droplets in the volume is $Vi_{fg}\rho_d\varepsilon_d$ and the sensible enthalpy that may be used to vaporize the droplets is $V\left[c_{p,c}\rho_c(1-\varepsilon_d)+c_{p,d}\rho_d\varepsilon_d\right](T_s-T_{sat})$. The maximum droplet fraction for which all the droplets are completely vaporized, $\varepsilon_{d,0}$, can be found by equating these two enthalpies to give,

$$\varepsilon_{d,0}=\frac{c_{p,c}\rho_c(T-T_{sat})}{\rho_d i_{fg}+(c_{p,c}\rho_c-c_{p,d}\rho_d)(T-T_{sat})}. \tag{2.21}$$

Bulanov uses $\varepsilon_{d,0}$ in Eq. (2.19) in place of the actual droplet fraction except for very dilute emulsions.

This model is employed not to predict heat transfer rates, but to determine the values of the parameters A_0 and J_{eff} based on experimental data. Values found for A_0 vary between 0.046 (Bulanov, 2001) and 0.038 (Bulanov and Gasanov, 2007; 2008). The factor A_0 is generally found to have a single value for a given set of experimental data. On the other hand, the value of J_{eff} changes with temperature and other experimental parameters, as shown in Fig. 2.13. One striking result is that, according to this model, the nucleation rate for an emulsified liquid is much higher than for the liquid alone (compare curves 1 and 3 in Fig. 2.13). This difference suggests that although Bulanov's model is developed assuming that superheated droplets boil by spontaneous nucleation, some other mechanism must be responsible.

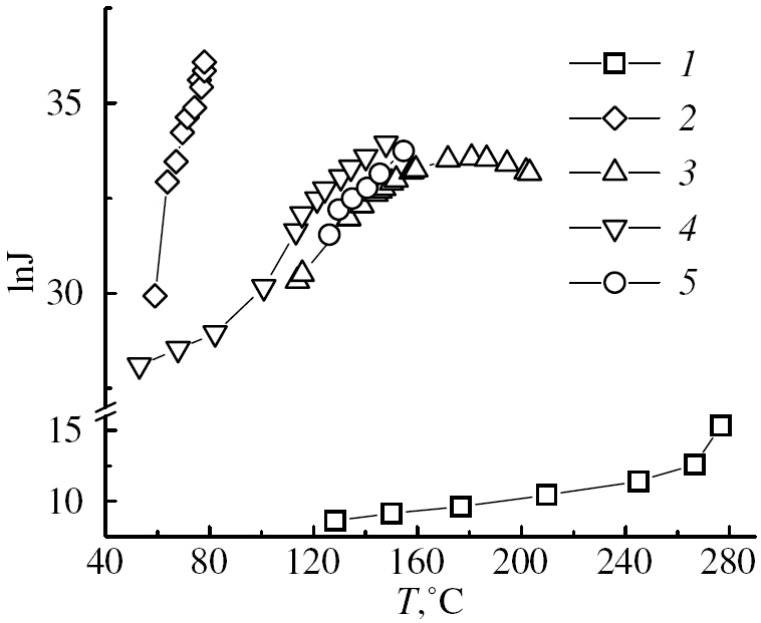

Figure 2.13. Nucleation rate J of water (1) and emulsified droplets of R-113 (2), water (3), pentane (4), and ethanol (5). (Bulanov and Gasanov, 2008)

Bulanov and Gasanov theorize that the elevated nucleation rate is due to chain activation of nucleation sites. They claim that nucleation in the droplets occurs on floccules of particles with size of the order of 100 nm. The floccules contain gases that were adsorbed from the surrounding liquid when they were at low temperature. When the droplet enters the thermal boundary layer, the gas is desorbed from the floccule and can serve as a nucleation site. When one highly superheated droplet boils, it does so explosively and generates a shockwave that travels for some distance through the surrounding liquid. If a second droplet is close enough, as the shockwave passes it causes floccules within the droplet to break up, thereby liberating some of their absorbed gas and inducing nucleation in that droplet as well. Thus a chain boiling mechanism is set up.

The experimental evidence accumulated by Bulanov and co-workers indicates that some boiling mechanism must exist aside from spontaneous nucleation, but some of the central components of their theory of chain boiling (the breakup of floccules within a droplet due to a shockwave) have so far not been shown to occur (Bulanov and Gasanov, 2005; 2007). The Bulanov model contains a number of assumptions that are

required to produce a solvable set of equations, but these assumptions also make it impossible to use the model to gain any deeper insight into the behavior of boiling emulsions. The most significant of these assumptions are that the temperature in the thermal boundary layer is uniform and that the boiling of droplets in the thermal boundary layer can be treated probabilistically.

3. A model of boiling emulsions

Understanding the behavior of boiling dilute emulsions requires consideration of heat and mass transport at multiple scales. First, the mechanism by which individual droplets boil and their behavior must be understood. Recall that the experimental work of Bulanov and co-workers shows that a boiling mechanism exists in addition to spontaneous nucleation, although their explanation in terms of the breaking up of floccules seems to be purely speculative. Second, the effects of the boiling droplets on the overall flow and heat transfer of the emulsion must be modeled.

In this section, a model of boiling emulsions is developed based on observable phenomena. Interactions between superheated droplets and their surroundings that may cause boiling are characterized. This information on the behavior of individual droplets is used to define the parameters of a model of boiling emulsions based on the Euler-Euler approach. This model is used in numerical simulations of boiling emulsions, which are partially validated by experiment.

3.1. Droplet temperature distribution

Different approaches may be taken to formulate the energy balance equations. Similar to the momentum equations (Eq. 2.6), a separate energy balance for each phase[5] may be maintained, along with additional relations for the rate of energy transfer between the phases. This approach is necessary when the rate of heat transfer between phases that are not in thermal equilibrium is important, such as in Hao and Tao's (2003a, 2003b) experiments on melting spheres of ice in water flow. On the other hand, if the phases are nearly in thermal equilibrium, it is possible to combine the individual phase energy balances into a single mixture energy balance. This approach is considerably simpler (Bouré and Delhaye, 1982).

The small size of the droplets present in emulsions suggests that the thermal disequilibrium between phases should be negligible, but a simple analysis of the temperature distribution in a droplet can be performed to verify this condition. The

[5] Recall that, in this dissertation, 'component' refers to a distinct substance, while 'phase' identifies both substance and state of matter (Section 2.2).

maximum possible temperature variation within a droplet would occur when the fluid in the droplet is stationary. In general this will not be true; shearing in the flow surrounding the droplet will induce circulation within the droplet, which will help to equalize temperatures. The worst case scenario of conductive heat transfer inside the droplet is easily analyzed. The response of a liquid droplet to external temperature changes can thus be characterized by examining the case of a droplet subjected to a uniform, steadily-rising surface temperature.

Following the solution method suggested by Arpaci (1991), the spherically symmetrical temperature field inside the droplet is,

$$T(r,t) = \sum_{n=1}^{\infty} \frac{-2C R_d^3}{r\alpha} \frac{(-1)^n}{(n\pi)^3} \exp\left[-\alpha \left(\frac{n\pi}{R_d} \right)^2 t \right] \sin\left(\frac{n\pi r}{R} \right) + \frac{C}{6\alpha}\left(r^2 - R_d^2 \right) + C t \,. \qquad (3.1)$$

The first term of Eq. (3.1) is the transient response, the second term is the steady temperature distribution in the droplet, and the last term accounts for the steadily-increasing boundary temperature. The variable C represents the rate of increase of the temperature of the surrounding fluid, and R_d is the droplet radius. This temperature distribution is illustrated in Fig. 3.1.

According to this analysis, the magnitude of the steady-state temperature variation inside a droplet varies with the square of the droplet diameter. For the very small droplets present in an emulsion, the temperature variation should also be small. The most rapid heating that a droplet would experience is when it enters the thermal boundary layer next to a heated surface. If Eq. (3.1) is applied to a representative droplet of FC-72 with diameter 10 µm, even a rapid heating rate of 100 °C/s produces a temperature difference inside the droplet of no more than 0.014 °C. This temperature difference is negligible when compared to the large degree of superheat required for boiling in emulsions, as discussed in Section 2.3. The lowest-order transient term of Eq. (3.1) decays with a time constant of 86 µs, so the steady-state temperature distribution is attained very rapidly. According to this result, therefore, it is reasonable

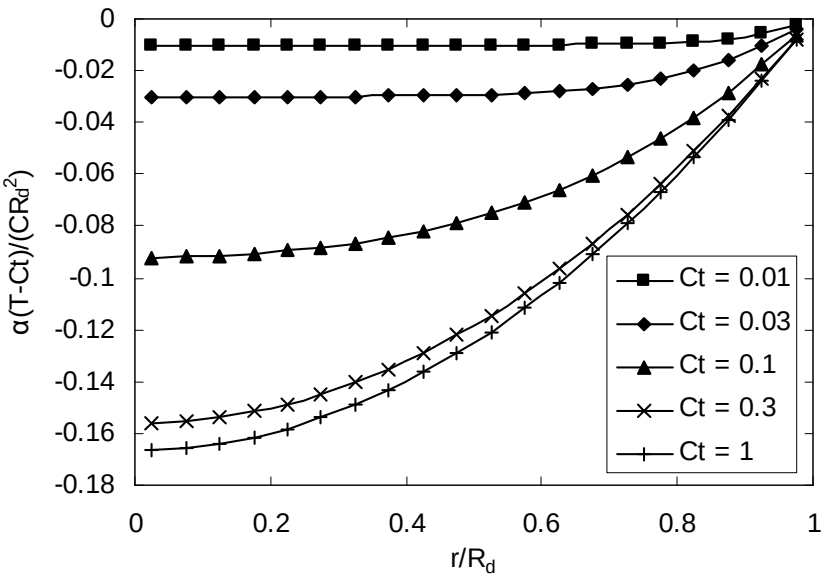

Figure 3.1. Temperature distribution within a quiescent droplet subjected to steadily-rising surface temperature (Eq. 3.1).

to use a single mixture energy balance equation rather than individual energy balances for each phase.

3.2. Balance equations

A model of boiling emulsions can be developed using the Euler-Euler approach. Because the degree of superheat required for boiling may vary widely (Bulanov, Gasanov, and Turchaninova; 2006), the phase of the dispersed component cannot be easily determined based on temperature or other macroscopic properties of the mixture. Instead, the liquid droplets and vapor bubbles must be treated as separate phases. The boiling emulsion is then modeled as a three-phase flow, where boiling and condensation of the dispersed component results in mass transfer between the droplet phase and the bubble (vapor) phase. This approach also makes it possible to tailor constitutive relations (for quantities such as viscosity or drag) to the droplet and bubble phases individually.

Conservation of mass is applied separately to each phase. The boiling of liquid droplets is modeled as transfer of mass from the droplet phase to the vapor bubble phase, denoted $\dot{m}$. The droplet and carrier liquids are immiscible so there is no mass

transfer between them. It is assumed that the temperature of the emulsion remains below the saturation temperature of the continuous liquid, so that evaporation of the carrier liquid into the bubbles is negligible. The Boussinesq approximation for buoyancy is applied, so the density for each phase is assumed to be constant except for the buoyancy term in the momentum equations. Relations for the rate of boiling are developed in the following sections, based on the detailed behavior of the liquid and vapor particles. Starting with Eq. (2.5), the mass balance for each phase is,

$$\frac{\partial \varepsilon_c}{\partial t} + \nabla \cdot \left(\varepsilon_c \mathbf{U}_c \right) = 0 , \tag{3.2}$$

$$\frac{\partial \varepsilon_b}{\partial t} + \nabla \cdot \left(\varepsilon_b \mathbf{U}_b \right) = + \frac{\dot{m}}{\rho_b} , \tag{3.3}$$

$$\frac{\partial \varepsilon_d}{\partial t} + \nabla \cdot \left(\varepsilon_d \mathbf{U}_d \right) = - \frac{\dot{m}}{\rho_d} . \tag{3.4}$$

Linear momentum is conserved for each phase individually. The momentum equation for each phase is obtained by applying the Boussinesq approximation to Eq. (2.6) and expressing the stress tensor as in Eq. (2.9). The only body force is gravity. Expressions for the interfacial force terms are developed in the following section. The notation $\mathbf{F}_{ij}$ indicates the average force exerted on phase i by phase j on a per-volume basis. Although the flow is assumed to be laminar in general, an expression for $\mu_{c,T}$ based upon the agitation of the flow by the boiling droplets is developed in the following sections as well. It is assumed that the pressure and temperature are the same in each phase.

It is also assumed that the droplet and bubble phases do not exert forces on each other directly. This assumption results from the fact that bubbles exist only within the thermal boundary layer. Outside the boundary layer, the bubbles quickly condense in the subcooled emulsion. Within the boundary layer, the droplets are superheated so that

when a droplet and bubble collide, the droplet boils. Thus collisions between bubbles and droplets result in mass transfer rather than momentum transfer between the two dispersed phases. Under these assumptions the phase momentum balances are,

$$\frac{\partial}{\partial t}\left(\varepsilon_c \mathbf{U}_c\right)+\nabla\cdot\left(\varepsilon_c \mathbf{U}_c \mathbf{U}_c\right)=\nabla\cdot\left[\frac{\varepsilon_c}{\rho_c}\left(\bar{\mu}_c+\mu_{c,T}\right)\left(\nabla\mathbf{U}_c+\nabla^T\mathbf{U}_c-\frac{2}{3}\left(\nabla\cdot\mathbf{U}_c\right)\mathbf{I}\right)\right] - \frac{\varepsilon_c}{\rho_c}\nabla P+\varepsilon_c\mathbf{g}\left[1-\beta_c\left(T-T_{c,0}\right)\right]+\frac{\mathbf{F}_{cb}}{\rho_c}+\frac{\mathbf{F}_{cd}}{\rho_c}, \tag{3.5}$$

$$\frac{\partial}{\partial t}\left(\varepsilon_b \mathbf{U}_b\right)+\nabla\cdot\left(\varepsilon_b \mathbf{U}_b \mathbf{U}_b\right)=\nabla\cdot\left[\frac{\varepsilon_b\bar{\mu}_b}{\rho_b}\left(\nabla\mathbf{U}_b+\nabla^T\mathbf{U}_b-\frac{2}{3}\left(\nabla\cdot\mathbf{U}_b\right)\mathbf{I}\right)\right] - \frac{\varepsilon_b}{\rho_b}\nabla P+\varepsilon_b\mathbf{g}\left[1-\beta_b\left(T-T_{b,0}\right)\right]+\frac{\dot{m}\mathbf{U}_b}{\rho_b}+\frac{\mathbf{F}_{bc}}{\rho_b}, \tag{3.6}$$

$$\frac{\partial}{\partial t}\left(\varepsilon_d \mathbf{U}_d\right)+\nabla\cdot\left(\varepsilon_d \mathbf{U}_d \mathbf{U}_d\right)=\nabla\cdot\left[\frac{\varepsilon_d\bar{\mu}_d}{\rho_d}\left(\nabla\mathbf{U}_d+\nabla^T\mathbf{U}_d-\frac{2}{3}\left(\nabla\cdot\mathbf{U}_d\right)\mathbf{I}\right)\right] - \frac{\varepsilon_d}{\rho_d}\nabla P+\varepsilon_d\mathbf{g}\left[1-\beta_b\left(T-T_{b,0}\right)\right]-\frac{\dot{m}\mathbf{U}_d}{\rho_d}+\frac{\mathbf{F}_{dc}}{\rho_d}. \tag{3.7}$$

The large degree of superheat required for boiling of dilute emulsions suggests that large temperature differences will be present in flows of boiling dilute emulsions. If it is assumed that fluid velocities are not very large, the contribution of kinetic energy to the conservation of energy equation becomes negligible. The internal energy equation is therefore used rather than the full energy equation. As mentioned above, the phases are assumed to be in thermal equilibrium, so a single mixture energy equation is used rather than one equation for each phase. Starting with Eq. (2.7), the dissipation and heat source terms are neglected, and the internal energy is expressed in terms of temperature (assuming constant specific heat for each phase). The phase internal energy equations are then added together to give,

$$\frac{\partial}{\partial t}\left(T\sum_i \varepsilon_i \rho_i c_{v,i}\right) + \nabla\cdot\left(T\sum_i \varepsilon_i \rho_i c_{v,i}\mathbf{U}_i\right) = \nabla\cdot\left[(k_{eff} + k_T)\nabla T\right] + \sum_i E_i + \sum_i c_{v,i} T_I \Gamma_i \quad (3.8)$$

The summations in Eq. 3.8 represent sums over all the phases in the emulsion. The symbol k_{eff} is the effective thermal conductivity of the emulsion and k_T is the turbulent thermal conductivity. The fourth term, the sum of the interfacial heat transfer into each phase, does not sum to zero due to phase change of the dispersed component. Consider, for example, the case of a droplet boiling as described in Appendix A. There is heat conduction in the droplet to the droplet-bubble interface (E_d is negative), but there is no heat conduction into the bubble. Instead, evaporation occurs ($\dot{m}$ is positive, and equal to $-E_d/i_{fg}$). In the absence of phase change, the interfacial energy transfer terms sum to zero. The fourth term may therefore be rewritten in terms of the boiling rate, $-\dot{m} i_{fg}$. The last term in Eq. (3.8) may be eliminated by rewriting the first two terms of the equation,

$$\frac{\partial T}{\partial t}\sum_i \varepsilon_i \rho_i c_{v,i} + \cdot\sum_i \varepsilon_i \rho_i c_{v,i}\mathbf{U}_i \cdot\nabla T + T\sum_i c_{v,i}\left(\rho_i \frac{\partial \varepsilon_i}{\partial t} + \rho_i \nabla\cdot(\varepsilon_i \mathbf{U}_i)\right) = \nabla\cdot\left[(k_{eff} + k_T)\nabla T\right] - \dot{m} i_{fg} + \sum_i c_{v,i} T_I \Gamma_i . \quad (3.9)$$

According to the phase continuity equation (Eq. 2.5), the expression in parentheses in the third term of Eq. (3.9) is equal to the mass transfer rate, Γ_i. It has already been assumed that the temperature is the same in each phase. It is reasonable to assume also that the temperature at the interface between phases is equal to the average temperature within the phases, so that the third and sixth terms of Eq. (3.9) cancel out. The resulting mixture internal energy equation is,

$$\frac{\partial T}{\partial t}\sum_i \varepsilon_i \rho_i c_{v,i} + \cdot\sum_i \varepsilon_i \rho_i c_{v,i}\mathbf{U}_i \cdot\nabla T = \nabla\cdot\left[\left(k_{eff} + k_T\right)\nabla T\right] - \dot{m}\, i_{fg}\,. \tag{3.10}$$

The above seven equations (Eqs. 3.2-7, 10) contain eight unknowns: ε_b, ε_c, ε_d, $\mathbf{U}_b$, $\mathbf{U}_c$, $\mathbf{U}_d$, T, and P. The requirement that the volume fractions sum to one may be used to eliminate one fraction as an independent variable, to bring the numbers of equations and unknowns into agreement. Several equations are also required to close this system of equations to define fluid properties for each phase as well as for the forces and mass transfer between the phases. These closure equations are developed in the next section.

3.3. Closure equations

3.3.1. Momentum transfer

The forces between phases in Eqs (3.5)-(3.7) must be defined. By Newton's third law of motion, $\mathbf{F}_{cd} = -\mathbf{F}_{dc}$ and $\mathbf{F}_{cb} = -\mathbf{F}_{bc}$, so only two sets of interfacial forces need to be defined. The droplets and bubbles in emulsions are sufficiently small so that the flow around them is Stokes' flow. Equation (2.10) is therefore used to define the drag force on each phase.

The small size of the droplets and bubbles in an emulsion also means that their drift velocity, relative to the carrier fluid, is very small. Examining the formulas for virtual mass, lift, and rotational forces (Eq. 2.11 – 2.13) reveals that all three forces are proportional to the difference in velocity between the dispersed and continuous phases. Because the velocity difference is very small for emulsions, these forces are negligible. The turbulent drag (Eq. 2.14) is also neglected, both because it is proportional to the velocity difference between continuous and dispersed phases and because the flow is assumed to be laminar. Therefore the interfacial force terms are,

$$\mathbf{F}_{dc} = -\mathbf{F}_{cd} = \frac{-18\varepsilon_d \mu_{eff}}{d_d^2}\left(\mathbf{U}_d - \mathbf{U}_c\right), \tag{3.11}$$

$$\mathbf{F}_{bc} = -\mathbf{F}_{cb} = \frac{-18\varepsilon_b \mu_{eff}}{d_b^2}\left(\mathbf{U}_b - \mathbf{U}_c\right). \tag{3.12}$$

3.3.2. Mass transfer

Mass transfer occurs between the bubble and droplet phases as a result of boiling and condensation. Two causes of boiling will be considered: contact between droplets and a heated surfaces and collisions between droplets and bubbles. It will be shown that spontaneous nucleation is not a significant cause of boiling in dilute emulsions. Chain boiling will be considered as well, where boiling droplets collide with other nearby droplets. Condensation of bubbles will be modeled as well.

3.3.2.1 Chain boiling

Chain boiling can occur when one boiling droplet causes adjacent droplets to boil as well. Bulanov and Gasanov (2008) also discussed chain boiling and attributed it to the production of shock waves by boiling droplets. However, as is discussed in Appendix A, there is no indication that a shock forms when a highly-superheated droplet boils. Another possible mechanism for chain boiling is simple contact between the boiling droplet and an adjacent droplet.

The probability of a liquid droplet being close enough to a boiling droplet to make contact depends on the maximum diameter achieved by the boiling droplet, the local volume fraction of liquid droplets, and the motion of the adjacent droplets. The inertial response time due to Stokes drag of a particle (Peskin, 1982) is,

$$\tau_{inertial} = \frac{2}{9}\frac{R_d^2 \rho_d}{\mu_c} \ . \tag{3.13}$$

Using this formula, the inertial response time of a typical droplet ($d_d \sim 10$ μm) in water is greater than the length of time required for a droplet to boil. Thus, the droplets that surround a boiling droplet can be assumed to be stationary during the boiling process. Any droplet whose distance from a boiling droplet, measured center-to-center, is less than R_d+R_{max} will contact the boiling droplet, where R_{max} is the maximum radius achieved by the droplet during the boiling process.

This distance limit describes a sphere of volume $4/3\pi(R_d+R_{max})^3$ centered on the boiling droplet. Clearly, if the number density of droplets in the emulsion is great

enough that several droplets are contained in this volume on average, a chain reaction that causes most of the liquid droplets in the volume to boil very rapidly can occur. Such chain reactions are probably responsible for the "sudden foaming in the bulk" reported by Mori, Inui, and Komotori (1978) that brought some of their experiments to a sudden halt. That such a phenomenon is reported only by Mori et al. is most likely due to the fact that other researchers have not carried out their heat transfer experiments with the bulk temperature of the emulsion near the saturation temperature of the low-boiling-point liquid. Because most experimenters examine heat transfer from a fine wire and use a bulk temperature significantly lower than the low-boiling-point liquid saturation temperature, there never exists a large volume of superheated emulsion. It is anticipated that under most circumstances the conditions necessary for such a chain reaction will not exist over a large volume.

Some chain boiling may occur at volume fractions lower than those necessary for the sustained chain reaction described above. From elementary probability theory, the probability that a volume V does not contain a droplet when droplets are distributed randomly is $\exp(-N_d V)$. The probability of the volume containing at least one droplet is therefore $1-\exp(-N_d V)$. If it assumed that one and only one droplet is caused to boil when at least one droplet is less than the distance R_d+R_{max} from a boiling droplet and that the distribution of droplets around a boiling droplet is independent of the number of droplets that have already boiled in the chain reaction, the probability of exactly φ droplets boiling in a chain reaction is $[1-\exp(-N_d V)]^{\varphi}\exp(-N_d V)$. The average number of droplets in such a chain reaction is then,

$$\overline{\varphi} = \sum_{\varphi=1}^{\infty} \varphi e^{-N_d V}\left(1-e^{-N_d V}\right)^{\varphi} = \frac{\left(1-e^{-N_d V}\right)}{e^{-N_d V}}. \tag{3.14}$$

The quantity $N_d V$ can be expressed in terms of the droplet volume fraction and the droplet and maximum bubble radii as,

$$N_d V = \varepsilon_d \left[\left(1 + \frac{R_{max}}{R_d} \right)^3 - 1 \right]. \quad (3.15)$$

The rates of boiling by other causes described in the following sections should be multiplied by Eq. (3.14).

3.3.2.2 Boiling by wall contact

As discussed in Section 2.3.1, dilute emulsions reach very high degrees of superheat before boiling occurs because most of the droplets suspended in the emulsion do not contact the heated surface. Because the temperature of the heated surface is significantly greater than the saturation temperature of the droplets, any droplets that do come in contact with the surface will quickly boil. Whether and how many droplets will contact a solid surface depends on the flow geometry and conditions. It should be noted that this boiling mechanism is not limited to heated surfaces: once the emulsion is highly superheated, any wetted surface that is not actively cooled will have a temperature above the saturation temperature of the droplet.

Various forces may bring droplets into contact with wetted surfaces. For example, if the droplets are not neutrally buoyant, they will tend to settle or rise and must eventually encounter the walls of the vessel that contains the emulsion. In the case of flow in a vertical duct, non-neutrally buoyant droplets may migrate towards the walls due to lift forces (Haber and Hetsroni, 1971). For droplets with sufficiently high Stokes numbers, the momentum of the droplet may carry it into contact with a wetted surface either when the flow changes direction suddenly (e.g., in the presence of an obstacle) or due to turbulent eddies (although this study will generally be limited to laminar flows).

In most cases the number of droplets contacting a heated solid surface will be very small compared to the total number of droplets, but this process will provide a constant supply of vapor bubbles to induce nucleation in other superheated droplets. When the liquid droplets are denser than the carrier liquid, any force that brings a droplet into contact with a surface will act in the opposite direction on the resulting vapor bubble, directing it back into the body of the flow. In the Euler-Euler approach to modeling multiphase flows, this behavior can be modeled by changing the boundary condition at

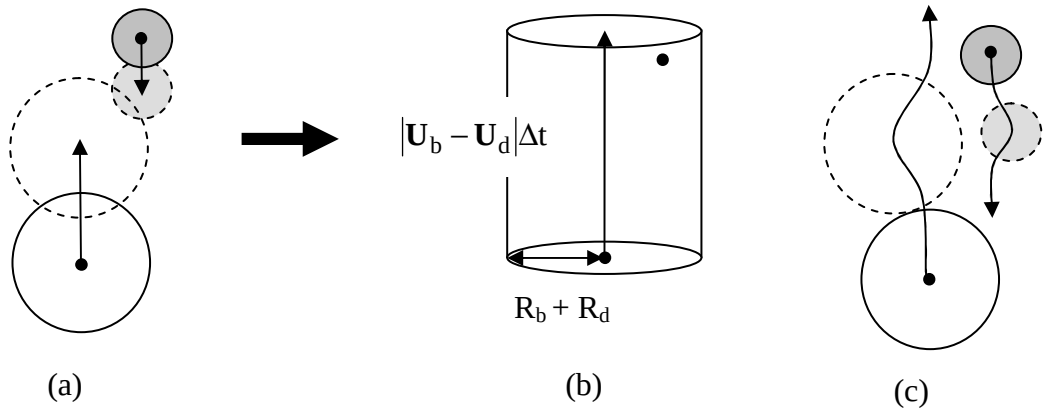

Figure 3.2. Bubble-droplet collisions. (a) Collision assuming straight-line motion (b) Volume around a bubble in which a bubble-droplet collision can occur (c) Actual motion of bubble and droplet around each other.

heated surfaces to set the mass flux of droplet phase into the surface equal to the mass flux of bubble phase departing the surface. Boiling caused by collisions between these bubbles and droplets in the body of the flow are discussed in the next section.

3.3.2.3 Collisions between droplets and bubbles

A superheated liquid droplet will boil when it contacts a liquid-vapor interface such as a vapor bubble. Such contact can occur when bubbles and droplets collide owing to their relative motion. The relative motion may arise from shearing in the carrier liquid or from differing drift velocities of the droplets and bubbles.

Calculation of the rate of collisions between bubbles and droplets is complicated by the fact that they do not travel in straight lines when passing close to each other. Instead, both droplets and bubbles tend to follow the streamlines of the surrounding liquid. Therefore, a droplet-bubble pair that may have collided had they travelled in straight lines, as shown in Fig. 3.2(a), will instead move around each other without touching, as shown in Fig. 3.2(c).

If the behavior shown in Fig. 3.2(c) is neglected, the calculation of the rate of potential collisions between bubbles and droplets is relatively straightforward. As shown in Fig. 3.2(b), in the rest frame of a droplet, nearby bubbles move with velocity $\mathbf{U}_b$-$\mathbf{U}_d$. The bubble and droplet are represented by points located at their centers. As the

bubble moves, over a time period Δt it sweeps out a cylindrical volume with radius R_b+R_d and height $\left|\mathbf{U}_b - \mathbf{U}_d\right|\Delta t$. The bubble will collide with any droplet whose center is within this volume. In a mixture with many bubbles and many droplets, the rate of potential collisions is,

$$J_{coll,0} = \frac{9\varepsilon_d\varepsilon_b\left|\mathbf{U}_d - \mathbf{U}_b\right|\left(R_d + R_b\right)^2}{16\pi R_d^3 R_b^3}. \tag{3.16}$$

Equation (3.16) does not reflect the actual rate of collisions, however, because it does not account for the tendency of bubbles and droplets to curve around each other without contact. The ratio between the number of actual collisions and the number of potential collisions given by Eq. (3.16) is known as the collision efficiency. The collision efficiency between two droplets has been studied for several decades in the context of raindrop formation in clouds. Studies of collision efficiency of bubbles and droplets suspended in liquid are not found in the literature. However, for very small droplets the Reynolds number of the flow around the droplet during steady rising or settling is close to zero so that the Stokes approximation is valid for the flow around the droplets. As long as this condition holds, and if the droplets are treated as solid spheres, the collision efficiency for two particles depends only on their relative size, and not on the properties of the surrounding fluid or the absolute scale of the particles. The portions of tables of collision efficiency developed by Pinsky, Khain, and Shapiro (2001) for droplets in clouds that fall within the Stokes flow regime ($d < 20\ \mu m$ (Beard, 1976)) may therefore be used directly. Using these data, the collision efficiency, η, for particles in the range $4 \le R_b/R_d \le 6$ may be approximated as,

$$\eta = 0.00051\left(\frac{R_b}{R_d}\right)^2 - 0.00738\left(\frac{R_b}{R_d}\right) + 0.03165. \tag{3.17}$$

It should be noted that Pinsky et al. treat their droplets as solid particles, neglecting the effects of circulation within the droplets. More accurate collision efficiencies could be calculated by considering the viscosity ratios between the particles and the surrounding fluid, but such data are not available.

Shearing of the continuous liquid will also cause particles in the flow to slide past one another. However, given the small particle diameters found in emulsions and the very small collision efficiencies of particles in Stokes flow, only extremely strong shearing motion would produce a significant number of collisions. This source of collisions may need to be considered in emulsions with larger particles or in flows of moderate velocity through small-diameter channels. In this study, however, this source of collisions will be neglected. In turbulent flows the relative effects of turbulent eddies on bubbles and droplets must also be considered carefully. This study will consider only laminar flows so that these effects may be neglected.

An equation for the rate of mass transfer due to this mechanism of boiling is required for use in the balance equations derived in Section 3.2. The rate at which droplets boil due to collisions is equal to the rate at which collisions occur multiplied by the average chain boiling length derived in Section 3.3.2.1. The rate of mass transfer may be obtained by multiplying the rate at which droplets boil by the mass of a droplet,

$$\dot{m}_{coll} = \varepsilon_b \varepsilon_d \rho_d |\mathbf{U}_d - \mathbf{U}_b| \eta \overline{\varphi} \frac{3(R_d + R_b)^2}{4 R_b^3}. \tag{3.18}$$

3.3.2.4 Spontaneous Nucleation

As described in Section 2.1, a sufficiently superheated liquid will undergo spontaneous nucleation triggered by density fluctuations in the liquid. Equation (2.4) is easily adapted to predicting the rate of nucleation of superheated droplets in an emulsion by multiplying by the volume fraction of the droplet phase. However, the experimental studies by Bulanov et al. discussed in Section 2.3.1 show that boiling in dilute emulsions occurs over a wide temperature range starting at temperatures far lower than the kinetic limit of superheat. In contrast, as Table 2.1 illustrates, the rate of

spontaneous nucleation changes very rapidly (by 10^2 - 10^3 per degree Celsius for most pure liquids). Therefore, boiling due to spontaneous nucleation is negligible except in cases where the heated surface reaches the kinetic limit of superheat. Such cases are outside the scope of this study.

The pressure fluctuations caused by a boiling droplet should be considered as well. When a droplet first begins to boil it accelerates the surrounding liquid outwards, thus increasing the pressure in the nearby liquid. The increased pressure has the effect of momentarily suppressing spontaneous nucleation in adjacent droplets, by decreasing the pressure difference in the denominator of the exponential factor in Eq. (2.4). On the other hand, when the bubble enters its final deceleration stage the pressure in the surrounding liquid is decreased and the probability of spontaneous nucleation in adjacent droplets rises. As the bubble oscillates around its equilibrium diameter the pressure in the surrounding liquid also oscillates, thus providing more time periods in which the probability of spontaneous nucleation is elevated. The magnitude of these oscillations quickly diminishes, however.

The effect of these pressure oscillations is also small. The pressure inside a boiling droplet remains positive, so the maximum possible decrease in pressure in the surrounding liquid is less than the ambient pressure. Near the kinetic limit of superheat (see Section 2.1.2), the saturation pressure of fluids changes rapidly (Blander and Katz, 1975). Therefore, for an emulsion near atmospheric pressure, the momentary decrease in pressure caused by a boiling droplet has an effect equivalent to raising the emulsion temperature by only a few degrees. As noted above, emulsions begin to boil at temperatures far lower than the kinetic limit of superheat, so this effect is also negligible. It is possible that this effect may become significant for emulsions at high pressures, but this is also outside the scope of this study.

3.3.2.5 Condensation

For emulsions in which the bulk temperature is lower than the saturation temperature of the dispersed fluid, condensation of bubbles will occur when they move out of the thermal boundary layer. Nucleation is not a concern here because the surface of the bubble provides a liquid-vapor interface upon which condensation can occur.

The rate of condensation will be limited by heat transfer from the bubble. A rough estimate of the rate of condensation may be obtained based upon the rate of heat transfer from a sphere of radius R_b. For a sphere in quiescent fluid,

$$\mathrm{Nu} = \frac{2R_b h}{k_c} = 2. \tag{3.19}$$

The heat transfer rate from a bubble at its saturation temperature is therefore,

$$q = 4\pi k_c R_b (T_{sat} - T). \tag{3.20}$$

The rate of condensation is obtained by dividing Eq. (3.20) by the latent heat of vaporization of the dispersed fluid. If it is assumed that the heat transfer rate remains constant during the collapse of the bubble, the mass transfer rate due to condensation for the emulsion is obtained by multiplying by the bubble number density,

$$\dot{m}_{cond} = \min\left[-3\varepsilon_b \frac{k_c}{i_{fg} R_b^2} (T_{sat} - T), 0 \right]. \tag{3.21}$$

Because $\dot{m}$ is defined as positive for boiling in the balance equations, the mass transfer rate due to condensation must be negative. This analysis gives only a rough estimate because it neglects the shell of droplet liquid that grows around the bubble as it collapses. For emulsions in which the two components have very different thermal conductivities (such as water and FC-72), the impact of the droplet liquid is expected to be large. The condensation process is not as critical as the boiling process, however, so this estimate is considered adequate.

3.3.3. Pseudo-turbulent effects

The relations developed in the preceding sections for mass and momentum transfer between the phases accounts for the averaged behavior of the droplets and bubbles in the emulsion. This approach neglects one potentially important effect of boiling

droplets. Some of the improved heat transfer that is observed in boiling emulsions has been attributed to agitation of the emulsion caused by boiling droplets (Bulanov, Skripov, Gasanov, and Baidakov, 1996; Ostrovskiy, 1988). The effects of this agitation can be modeled in an Euler-Euler model by borrowing a technique from turbulence modeling.

In many turbulent flows, the most significant effect of the small-scale turbulent eddies on the averaged large-scale behavior of the flow is an increase in the rate of momentum transport in the direction of the mean velocity gradient in the flow. This effect occurs because the turbulent eddies move elements of fast moving fluid into regions of slow moving fluid, and vice-versa. The effect can be modeled by introducing a turbulent kinematic viscosity, ν_T, in the equations used to model the mean flow. Similarly, the turbulent eddies also cause an increase in the rate of heat transfer in the direction of the mean temperature gradient, which can be modeled by introducing a turbulent thermal diffusivity, α_T. Experimental studies have found that for fluids with Prandtl numbers near one, the turbulent Prandtl number, $Pr_T = \alpha_T/\nu_T$, is near 0.85 (Pope, 2000; Kays, Crawford, and Weigand, 2005). It is therefore only necessary to model the turbulent viscosity, and then the turbulent thermal diffusivity can be obtained using the Reynolds analogy.

One approach to modeling the turbulent viscosity is to express it as the product of a characteristic length ℓ and a characteristic velocity u*,

$$\nu_T = u^* \ell . \tag{3.22}$$

The characteristic length represents the size of a turbulent eddy, and the characteristic velocity can be thought of as the average velocity of the eddies. In turbulent flow, determining u* and ℓ is a subtle and complex problem (Pope, 2000). On the other hand, in boiling emulsions both quantities can be related directly to the properties of the boiling droplets.

When a droplet boils it displaces the liquid around it, and it is reasonable to assume that the surrounding liquid moves radially and symmetrically outwards. If the volume

of the initial droplet is small compared to the volume of the bubble, the displacement Δr of a fluid element initially located a distance r_{init} from the center of the droplet is,

$$\Delta r = \left(r_{init}^3 + R_b^3 \right)^{1/3} - r_{init} . \tag{3.23}$$

The magnitude of the displacement therefore decreases quickly with distance from the boiling droplet. At a distance of twice the bubble radius the displacement is less than 0.1 R_b, so it is reasonable to use this distance as a cutoff – the displacement due to boiling of liquid outside of this radius is insignificant. The average displacement of the liquid in this volume may be obtained by integrating Eq. (3.23) over the volume, and the result is approximately 0.16 R_b. This displacement is directed radially outwards from the droplet, but for this pseudo-turbulent model only the component of the displacement perpendicular to the direction of a mean gradient in the flow is important. The average displacement in one dimension is half the radial displacement, so ℓ = 0.08 R_b.

The characteristic velocity can be thought of as the volume-averaged velocity of the liquid being displaced. A value for u* can be expressed as the product of the volumetric rate of droplet nucleation, the volume of displaced liquid per boiling droplet, and the average displacement of the liquid,

$$u^* = J \left(0.16 R_b \right) \left[\frac{4}{3} \pi \left(2 R_b \right)^3 \right] = 1.28 \, J \, V_b R_b . \tag{3.24}$$

An expression for the turbulent viscosity is then obtained by substituting these values for u* and ℓ into Eq. (3.22). The result is,

$$\nu_T = 0.1 J \, V_b \, {R_b}^2 . \tag{3.25}$$

For use in an Eq. (3.5), the nucleation rate in Eq. (3.25) can be expressed in terms of the rate of mass transfer between the droplet and bubble phases,

$$\mu_{c,T} = 0.1\dot{m}\frac{\rho_c}{\rho_b}R_b{}^2. \tag{3.26}$$

As discussed above, the Reynolds analogy may be used to obtain a turbulent thermal conductivity from Eq. (3.26),

$$k_T = 0.1\dot{m}c_{p,c}\frac{\rho_c}{\rho_b}R_b{}^2. \tag{3.27}$$

This model accounts for the net displacement outwards of the continuous liquid when isolated droplets boil. However, the analysis in Appendix A shows that when a droplet boils the bubble initially grows to a radius significantly larger than its equilibrium size and then oscillates for some time through radial expansion and contraction. These repeated displacements of the surrounding liquid may result in a much larger effect than the single outwards displacement modeled here. However, the precise effects of the oscillating bubble on the surrounding liquid are not known, especially when several droplets boil in proximity to each other or in regions where there is strong shearing of the continuous liquid. If the agitation of the surrounding liquid is not precisely equal to Eq. (3.26) and (3.27), it is reasonable to model the effects as at least being proportional to these equations.

3.3.4. Effective viscosity

Equations (3.5-7) require an effective viscosity to be assigned to each phase, which is generally not equal to the viscosity of the fluid that constitutes that phase. As described in Section 2.2, there does not appear to be any consensus in the literature as to how this problem should be approached. In this study a two step process is adopted, in which an effective viscosity for the mixture is calculated and then is distributed to the phases of the mixture.

It is worthwhile to start by considering the desired asymptotic behavior of the correlations for effective viscosity. First, when only one phase is present the effective viscosity should be equal to that of the fluid, that is, $\bar{\mu}_i \to \mu_i$ as $\varepsilon_i \to 1$. It is important that each phase exhibit this behavior because, even though the emulsions to be studied are dilute, the volume fraction of the bubble phase may be much higher than the average volume fraction of the droplet phase where boiling occurs. The volume fraction of the droplet phase may also become large locally in cases such as droplets settling onto a horizontal surface.

At the other extreme, the effective viscosity of a phase should go to zero as its volume fraction approaches zero. Recall that the effective viscosity of a dispersed phase represents its ability to transmit stress through interactions between elements of the dispersed phase, independent of interactions between the dispersed phase and the continuous phase. When the volume fraction of the dispersed phase is small, the elements of the dispersed phase are widely separated and should have very little direct interaction with each other.

None of the strategies for assigning effective viscosity to each phase described in Section 2.2 exhibit these asymptotic behaviors. In the absence of theoretical arguments for any particular weighting of viscosities between the phases, in this study the mixture viscosity is weighted by the local volume fraction of each phase,

$$\bar{\mu}_b = \varepsilon_b \mu_{eff} , \tag{3.28a}$$

$$\bar{\mu}_c = \varepsilon_c \mu_{eff} , \tag{3.28b}$$

$$\bar{\mu}_d = \varepsilon_d \mu_{eff} . \tag{3.28c}$$

This method of assigning effective viscosity ensures that $\bar{\mu}_i \to 0$ as $\varepsilon_i \to 0$.

A correlation for the effective viscosity of the mixture is required. The correlation should be as simple as possible so that it can be used in numerical simulations and it

must be valid for a wide range of phase fractions of the dispersed phase. The latter requirement rules out most theoretical correlations, such as the one developed by Taylor (1932), because they are generally valid only for dilute mixtures. Many empirical correlations exist for effective viscosity of liquid-vapor mixtures under various conditions. One correlation that has been shown experimentally to be valid for bubbly flow and that has the correct asymptotic behavior for dilute mixtures is that of Beattie and Whalley (1982),

$$\mu_{eff} = \mu_c(1-\varepsilon_b)(1+2.5\varepsilon_b)+\mu_b\varepsilon_b . \tag{3.29}$$

It is assumed that this correlation can be expanded to include two dispersed phases linearly,

$$\mu_{eff} = \mu_c\varepsilon_c[1+2.5(\varepsilon_b+\varepsilon_d)]+\mu_b\varepsilon_b+\mu_d\varepsilon_d . \tag{3.30}$$

3.3.5. Effective thermal conductivity

The effective thermal conductivity of the mixture must also be defined. The use of a single energy equation for the mixture obviates assigning conductivities to each phase individually. A similar difficulty is encountered here as in the determination of effective viscosities: a simple theoretical model exists (here, in the form of Maxwell's effective medium theory), but it is applicable only to cases when the volume fraction of the dispersed phase is small (Maxwell, 1904). Correlations that are valid for higher fractions exist, both theoretical and empirical, but all are much more complicated. However, the more complex correlations generally fall close to the results of the effective medium theory even at moderate fractions (Buyevich, 1992), so it will be assumed here that the effective medium theory holds. It is further assumed that the effects of the bubble phase and the droplet phase are additive. A correlation for the mixture effective thermal conductivity is therefore,

$$k_{eff} = k_c + \frac{3\varepsilon_d (k_d - k_c)}{\varepsilon_d + \frac{\varepsilon_c k_d}{k_c} + 2} + \frac{3\varepsilon_b (k_b - k_c)}{\varepsilon_b + \frac{\varepsilon_c k_b}{k_c} + 2}. \quad (3.31)$$

4. Numerical model

The model of boiling emulsions described in the preceding chapter is implemented in a numerical solver so that simulations of boiling emulsions may be performed. The numerical approach borrows heavily from Rusche (2002), as adapted to multiple dispersed phases by Silva and Lage (2007), and the interested reader is encouraged to consult that source for further details of the numerical method.

The numerical solver uses the finite volume numerical method implemented using the OpenFOAM^{TM} (Field Operation and Manipulation) computational fluid dynamics (CFD) package. OpenFOAM^{TM} is a free CFD package written in C++ and distributed under the GNU General Public License (GPU). It provides a library of routines for manipulating volumetric fields and setting up and solving partial differential equations using the finite volume approach. Details about the operation of OpenFOAM^{TM} and its numerical implementation of vector and differential operators may be found in the User Guide (2009) and Programmer's Guide (2009).

This chapter describes the numerical solution procedure of the model developed in the previous chapter. Coupling between pressure and velocity is handled with the Pressure Implicit with Splitting of Operators (PISO) algorithm. The PISO algorithm is a predictor-corrector type procedure in which, at each time step, a prediction is made for the new velocity field and then the new pressure field is solved such that continuity is enforced. The phase volume fraction, velocity, and temperature equations are linked nonlinearly through the mass transfer rate as well as buoyancy, so each time step consists of an outer loop in which the volume fraction, velocity, and temperature fields are solved iteratively as well as inner loops for the volume fraction and velocity fields.

4.1. Finite Volume Nomenclature

It is necessary to introduce quite a bit of new nomenclature to describe how the equations developed in the previous chapter are discretized and solved. First, one must recognize that in the finite volume approach the solution domain is split into a series of cells separated by faces. The dependent variables of chapter 3 ($\mathbf{U}_i$, ε_i, T) are considered cell-centered variables, meaning that they are defined at the center of each cell in the

domain. One can also have face-centered variables, which are defined at the center of each face in the domain. A cell-centered variable can be interpolated to the face centers, which is indicated with the subscript F. One important face-centered variable used in the following solution procedure is the phase volumetric flux ϕ_i. The volumetric flux is defined as $\phi_i = \mathbf{S} \cdot (\mathbf{U}_i)_F$, that is, the dot product of the cell face area vector and the phase velocity extrapolated to the cell faces.

Averaging of a variable over several neighboring cells is denoted with angular brackets, with a subscript indicating the pattern of cells over which averaging takes place. For example, $\langle \varepsilon_i \rangle_\nabla$ is the average of ε_i over the same cells used for computing the gradient. This operation is important in dealing with the term $\nabla\varepsilon_i / \varepsilon_i$, which appears in the phase-intensive momentum equation below. In general, $\nabla\varepsilon_i$ should become small as $\varepsilon_i \to 0$. However the case can arise in which ε_i is zero in a cell but not in a neighbor cell. In such a case it is not possible to divide by the value of ε_i in the cell in question, but the average value $\langle \varepsilon_i \rangle_\nabla$ is guaranteed to be nonzero when $\nabla\varepsilon_i$ is nonzero (recognizing also that ε_i is non-negative). Ruche (2002) adds an additional stabilizing factor, $\dfrac{\nabla\varepsilon_i}{\langle \varepsilon_i \rangle_\nabla + \Delta}$.

The mass, momentum, and energy balance equations are treated implicitly in time, so the result of discretizing each balance equation is a system of algebraic equations that must be solved simultaneously. Implicit discretization is denoted $\|\mathcal{L}[x]\|$, where the operator $\mathcal{L}$ is discretized implicitly in terms of the variable x. (Terms without the double brackets are discretized explicitly.) All terms in an equation that are treated implicitly must be discretized in terms of the same variable. Systems of equations resulting from implicit discretization are denoted with script variables. For example, the generic balance equation (Eq. C.1) may be discretized implicitly in its first two terms as,

$$\boldsymbol{a} := \left\{ \left\| \frac{\partial \rho [\Psi]}{\partial t} \right\| + \left\| \nabla \cdot \left(\rho \mathbf{U} [\Psi]_F \right) \right\| = \nabla \cdot \boldsymbol{\gamma} + \rho \zeta \right\}. \tag{4.1}$$

Here, $\boldsymbol{a}$ is the system of linear algebraic equations representing the discretized balance equation. In this example, in the absence of a specific model for $\boldsymbol{\gamma}$, the diffusion term must be discretized explicitly. A number of operators may now be defined to refer to specific features of the system of equations (Rusche, 2002). Some important ones are $\boldsymbol{a}_D$ and $\boldsymbol{a}_N$ for the diagonal and off diagonal components of the matrix coefficients respectively. The source vector is denoted by $\boldsymbol{a}_S$. Finally, the H operator is defined,

$$\boldsymbol{a}_H \equiv \boldsymbol{a}_S - \boldsymbol{a}_N \Psi , \tag{4.2}$$

where Ψ is the dependent variable of the discretized equations.

4.2. Momentum equations

4.2.1. Phase-intensive momentum equation

As the volume fraction of a phase becomes small, the phase momentum equations (Eq. 3.5-3.7) become singular. The solution adopted by Rusche (2002) is to divide the momentum equation by the phase volume fraction, which gives the phase-intensive momentum equation. For brevity, it is helpful to briefly return to the generic phase momentum equation of Chapter 2 (Eq. 2.6) and represent the viscous stress term simply with $\mathbf{R}_{\text{eff,i}}$, as in Eq. (2.9). The momentum equation is first divided through by density (which is assumed constant) and the first three terms are expanded,

$$\begin{aligned} \mathbf{U}_i \left[\frac{\partial \varepsilon_i}{\partial t} + \nabla \cdot \left(\varepsilon_i \mathbf{U}_i \right) \right] + \varepsilon_i \left[\frac{\partial \mathbf{U}_i}{\partial t} + \mathbf{U}_i \cdot \nabla \mathbf{U}_i \right] + \frac{\varepsilon_i}{\rho_i} \nabla \cdot \mathbf{R}_{\text{eff},i} + \mathbf{R}_{\text{eff},i} \cdot \frac{\nabla \varepsilon_i}{\rho_i} = \\ - \varepsilon_i \nabla P + \varepsilon_i \mathbf{b}_i + \frac{\mathbf{F}_i}{\rho_i} + \frac{1}{\rho_i} \mathbf{U}_{i,I} \Gamma_i . \end{aligned} \tag{4.3}$$

According to the phase mass balance equation (Eq. 2.5), the first term of Eq. (4.3) is equal to $\mathbf{U}_i\Gamma_i/\rho_i$. It is assumed that the average phase velocity, $\mathbf{U}_i$, is equal to the average velocity of fluid entering the phase across an interface, $\mathbf{U}_{i,I}$, so that the first term and last term of Eq. (4.3) are equal and cancel out. Then dividing through by the phase volume fraction, one obtains the phase intensive momentum equation,

$$\frac{\partial \mathbf{U}_i}{\partial t} + \mathbf{U}_i \cdot \nabla \mathbf{U}_i + \nabla \cdot \mathbf{R}_{\text{eff},i} + \mathbf{R}_{\text{eff},i} \cdot \frac{\nabla \varepsilon_i}{\varepsilon_i} = -\frac{\nabla P}{\rho_i} + \mathbf{g}\left[1 - \beta_i\left(T - T_{i,0}\right)\right] + \frac{\mathbf{F}_i}{\varepsilon_i \rho_i}. \tag{4.4}$$

Here the generic body force $\mathbf{b}_i$ has been replaced with the gravitational force as in Eqs. (3.5-7). Equation (4.4) contains two terms that contain the phase volume fraction in the denominator. The fourth term should always be finite because $\nabla\varepsilon_i \to 0$ as $\varepsilon_i \to 0$, and the term is discretized as described in Section 4.1 to avoid division by zero in the numerical algorithm. The final term does not present a problem for the dispersed phases because, according to Eqs. (3.11-12), the interfacial force term for each dispersed phase goes to zero as the volume fraction of the phase goes to zero. However, if the volume fraction of the continuous phase can become small at any location during a simulation careful treatment of the interfacial force terms for the continuous phase is required. A method for handling such a situation is described in a later section.

4.2.2. Discretization of the momentum equation

Rusche (2002) splits the effective phase stress into a diffusive component and a correction,

$$\mathbf{R}^{D}_{\text{eff},i} = -\nu_{\text{eff},i} \nabla \mathbf{U}_i \tag{4.5a}$$

$$\mathbf{R}^{C}_{\text{eff},i} = -\nu_{\text{eff},i}\left(\nabla^T \mathbf{U}_i - \frac{2}{3}\mathbf{I}\left(\nabla \cdot \mathbf{U}_i\right)\right), \tag{4.5b}$$

so that $\mathbf{R}_{\text{eff}}^{\text{D}} + \mathbf{R}_{\text{eff}}^{\text{C}} = \mathbf{R}_{\text{eff}}$, in accordance with the definition of the effective stress in Eq. (2.9). Rusche then discretizes the left hand side of Eq. (4.4) as,

$$\begin{aligned}\mathcal{I}_i = &\left\| \frac{\partial [\mathbf{U}_i]}{\partial t} \right\| + \left\| \nabla \cdot \left(\phi_i [\mathbf{U}_i]_F \right) \right\| + \left\| \nabla \cdot \left(\nu_{iF} \frac{\nabla \varepsilon_i}{\varepsilon_{iF} + \Delta} [\mathbf{U}_i]_F \right) \right\| - \left\| [\mathbf{U}_i] \nabla \cdot \phi_i \right\| \\ &+ \left\| [\mathbf{U}_i] \nabla \cdot \left(\nu_{iF} \frac{\nabla \varepsilon_i}{\varepsilon_{iF} + \Delta} \right) \right\| - \left\| \nabla \cdot \left((\nu_i)_F \nabla [\mathbf{U}_i] \right) \right\| + \nabla \cdot \mathbf{R}_{\text{eff},i}^{\text{C}} + \frac{\nabla \varepsilon_i}{\langle \varepsilon_i \rangle_\nabla + \Delta} \cdot \mathbf{R}_{\text{eff}}^{\text{C}} .\end{aligned} \tag{4.6}$$

Next, interfacial momentum transfer is considered. Rusche (2002) discusses methods for discretizing lift, drag, and virtual mass forces. In this study, only drag forces are considered and the same semi-implicit method is used. The drag force applied to phase i by phase j is,

$$\mathbf{F}_{ij} = \frac{18 \varepsilon \mu_{\text{eff}}}{d^2} \left(\mathbf{U}_j - \left\| [\mathbf{U}_i] \right\| \right). \tag{4.7}$$

The phase volume fraction and diameter in Eq. (4.7) are those of the dispersed phase. The implicit portion of the drag force is combined with Eq. (4.6),

$$\mathcal{A}_b := \left\{ \mathcal{I}_b = -\left\| \frac{18 \mu_{\text{eff}}}{d_b^2 \rho_b} [\mathbf{U}_b] \right\| \right\}, \tag{4.8a}$$

$$\mathcal{A}_c := \left\{ \mathcal{I}_c = -\left\| \frac{18 \varepsilon_b \mu_{\text{eff}}}{d_b^2 \varepsilon_c \rho_c} [\mathbf{U}_c] \right\| - \left\| \frac{18 \varepsilon_d \mu_{\text{eff}}}{d_d^2 \varepsilon_c \rho_c} [\mathbf{U}_c] \right\| \right\}, \tag{4.8b}$$

$$\mathcal{A}_d := \left\{ \mathcal{I}_d = -\left\| \frac{18 \mu_{\text{eff}}}{d_d^2 \rho_d} [\mathbf{U}_d] \right\| \right\}. \tag{4.8c}$$

The complete phase momentum equation can then be expressed in semi-discretized form,

$$(a_i)_D \mathbf{U}_i = (a_i)_H - \frac{\nabla P}{\rho_i} + \mathbf{g}\left[1 - \beta_i\left(T - T_{i,0}\right)\right] + \frac{18\varepsilon\mu_{eff}}{d^2\varepsilon_i\rho_i}\mathbf{U}_j . \tag{4.9}$$

Equations (4.8) and (4.9) are equivalent to the phase momentum balance equations given in Chapter 3, Eqs. (3.5-7), with the addition of the momentum transfer closure equations, Eqs. (3.11) and (3.12).

4.2.3. PISO Algorithm

Equation (4.9) is not solved directly. Instead, it is used to define predictor and corrector equations for the face volumetric flux, which are used in the PISO algorithm to obtain the velocity and pressure fields. The use of face flux as the primary variable in the PISO loop eliminates the need for a staggered grid to avoid checker boarding of pressure (Patankar, 1980; Rusche, 2002). First, Eq. (4.9) is solved for the phase velocity,

$$\mathbf{U}_i = \frac{(a_i)_H}{(a_i)_D} - \frac{\nabla P}{\rho_i (a_i)_D} + \frac{\mathbf{g}\left[1 - \beta_i\left(T - T_{ref,i}\right)\right]}{(a_i)_D} + \frac{18\varepsilon\mu_{eff}\mathbf{U}_j}{d^2\varepsilon_i\rho_i(a_i)_D} . \tag{4.10}$$

Recalling the definition of volumetric face flux from Section 4.1, the equation for face flux can be obtained from Eq. (4.10) by interpolating each term on the right hand side of the equation to the face centers and taking the dot product of each term with the face area vector, **S**. The left hand side of Eq. (4.10) is thus the phase volumetric flux, per the definition given in Section 4.1. The first term on the right hand side is interpolated to the face centers and is not manipulated further. The flux predictor equation omits the pressure term, which will be reintroduced in the flux corrector equation. In the third term on the right hand side the gravity vector, being constant, requires no interpolation. In the last term of Eq. (4.10) the phase velocity is also converted to a phase volumetric flux. Thus the flux predictor equation for each phase is,

$$\phi_b^* = \left(\frac{(\alpha_b)_H}{(\alpha_b)_D}\right)_F \cdot \mathbf{S} + \left(\frac{\left[1-\beta_b\left(T-T_{ref,b}\right)\right]}{(\alpha_b)_D}\right)_F \mathbf{g}\cdot\mathbf{S} + \left(\frac{18\mu_{eff}}{d_b^2\rho_b(\alpha_b)_D}\right)_F \phi_c\,, \tag{4.11a}$$

$$\phi_c^* = \left(\frac{(\alpha_c)_H}{(\alpha_c)_D}\right)_F \cdot \mathbf{S} + \left(\frac{\left[1-\beta_c\left(T-T_{ref,c}\right)\right]}{(\alpha_c)_D}\right)_F \mathbf{g}\cdot\mathbf{S} + \left(\frac{18\varepsilon_b\mu_{eff}}{d_b^2\varepsilon_c\rho_c(\alpha_c)_D}\right)_F \phi_b + \left(\frac{18\varepsilon_d\mu_{eff}}{d_d^2\varepsilon_c\rho_c(\alpha_c)_D}\right)_F \phi_d\,, \tag{4.11b}$$

$$\phi_d^* = \left(\frac{(\alpha_d)_H}{(\alpha_d)_D}\right)_F \cdot \mathbf{S} + \left(\frac{\left[1-\beta_d\left(T-T_{ref,d}\right)\right]}{(\alpha_d)_D}\right)_F \mathbf{g}\cdot\mathbf{S} + \left(\frac{18\mu_{eff}}{d_d^2\rho_d(\alpha_d)_D}\right)_F \phi_d\,. \tag{4.11c}$$

The flux corrector equation has the same form for each phase,

$$\phi_i = \phi_i^* - \left(\frac{1}{\rho_i(\alpha_i)_D}\right)_F \nabla P\cdot\mathbf{S}\,. \tag{4.12}$$

The pressure field is used to enforce continuity in the PISO algorithm, so the pressure equation stems from the continuity equation. The multiphase model used in this study assumes that the pressure is the same in each phase, so the mixture continuity equation is used, which is obtained by summing Eq. (3.2-4),

$$\nabla\cdot\left(\varepsilon_b\mathbf{U}_b + \varepsilon_c\mathbf{U}_c + \varepsilon_d\mathbf{U}_d\right) = \dot{m}\left(\frac{1}{\rho_b} - \frac{1}{\rho_d}\right). \tag{4.13}$$

The left hand side of Eq. (4.13) is interpolated to the face centers and the velocities are expressed in terms of the face volume fluxes,

$$\nabla \cdot \left(\varepsilon_{bF} \phi_b + \varepsilon_{cF} \phi_c + \varepsilon_{dF} \phi_d \right) = \dot{m} \left(\frac{1}{\rho_b} - \frac{1}{\rho_d} \right). \tag{4.14}$$

Next, Eq. (4.12) is substituted in for each phase flux and the equation is rearranged to,

$$\left\| \nabla \cdot \left(\left(\frac{\varepsilon_{bF}}{\rho_b} \frac{1}{\left(\left(a_b \right)_D \right)_F} + \frac{\varepsilon_{cF}}{\rho_c} \frac{1}{\left(\left(a_c \right)_D \right)_F} + \frac{\varepsilon_{dF}}{\rho_d} \frac{1}{\left(\left(a_d \right)_D \right)_F} \right) \nabla [P] \right) \right\| = \nabla \cdot \left(\varepsilon_{bF} \phi_b^* + \varepsilon_{cF} \phi_c^* + \varepsilon_{dF} \phi_d^* \right) - \dot{m} \left(\frac{1}{\rho_b} - \frac{1}{\rho_d} \right) \tag{4.15}$$

This equation can be solved for the pressure field after the face fluxes are predicted using Eq. (4.11). Finally, the updated velocity field is reconstructed from the corrected face fluxes.

4.3. Phase continuity equations

The individual phase continuity equations (Eq. 3.2-4) are solved to update the phase volume fractions at each time step. Rusche (2002) discusses several methods of solving the phase continuity equations for a two-phase mixture. He notes that the most important feature of the solution procedure is that it produces results that are bounded and conservative. The method preferred by Rusche is one that accounts for coupling between the phases using the relative velocity of the two phases, which also improves the efficiency of the solution. This method is expanded to mixtures with multiple dispersed phases by Silva and Lage (2007), and their method is used in this study. The essential features of the method are as follows.

First, the mixture velocity is defined as the volumetric average of the phase velocities,

$$\mathbf{U}_m = \sum_i \varepsilon_i \mathbf{U}_i \,, \tag{4.16}$$

and the relative velocity is defined as,

$$\mathbf{U}_{r,ij} = \mathbf{U}_i - \mathbf{U}_j \,. \tag{4.17}$$

The velocity of a phase can then be written as,

$$\mathbf{U}_i = \mathbf{U}_m + \sum_{j \neq i} \varepsilon_j \mathbf{U}_{r,ij} \,. \tag{4.18}$$

Substituting Eq. (4.18) into the incompressible version of the phase continuity equation (Eq. 2.5) yields,

$$\frac{\partial \varepsilon_i}{\partial t} + \nabla \cdot \left(\mathbf{U}_m \varepsilon_i \right) + \nabla \cdot \left(\sum_{j \neq i} \varepsilon_j \mathbf{U}_{r,ij} \varepsilon_i \right) = \frac{\Gamma_i}{\rho_i} \,. \tag{4.19}$$

This equation is discretized as,

$$\left\| \frac{\partial [\varepsilon_i]}{\partial t} \right\| + \left\| \nabla \cdot \left(\phi_m [\varepsilon_i] \right) \right\| + \left\| \nabla \cdot \left(\sum_{j \neq i} \varepsilon_j \phi_{r,ij} [\varepsilon_i] \right) \right\| = \left\| \frac{\Gamma_{i,+}}{\rho_i} \left(\frac{[\varepsilon_i] - 1}{1 - \varepsilon_i^o - \Delta} \right) \right\| + \left\| \frac{\Gamma_{i,-}}{\rho_i} \left(\frac{[\varepsilon_i]}{\varepsilon_i^o + \Delta} \right) \right\| . \tag{4.20}$$

The mass transfer term in Eq. (4.20) is discretized as recommended by Patankar (1980) to ensure that the result remain bounded between 0 and 1.

In practice, Eq. (4.20) need only be solved for the dispersed phases,

$$\left\|\frac{\partial[\varepsilon_b]}{\partial t}\right\| + \left\|\nabla\cdot\left(\phi_m[\varepsilon_b]\right)\right\| + \left\|\nabla\cdot\left(\varepsilon_c\phi_{r,bc}[\varepsilon_b] + \varepsilon_d\phi_{r,bd}[\varepsilon_b]\right)\right\| = \left\|\frac{\dot{m}_+}{\rho_b}\left(\frac{[\varepsilon_b]-1}{1-\varepsilon_b^o-\Delta}\right)\right\| + \left\|\frac{\dot{m}_-}{\rho_b}\left(\frac{[\varepsilon_b]}{\varepsilon_b^o+\Delta}\right)\right\|, \tag{4.21a}$$

$$\left\|\frac{\partial[\varepsilon_d]}{\partial t}\right\| + \left\|\nabla\cdot\left(\phi_m[\varepsilon_d]\right)\right\| + \left\|\nabla\cdot\left(\varepsilon_b\phi_{r,db}[\varepsilon_d] + \varepsilon_c\phi_{r,dc}[\varepsilon_d]\right)\right\| = \left\|\frac{-\dot{m}_-}{\rho_d}\left(\frac{[\varepsilon_d]-1}{1-\varepsilon_d^o-\Delta}\right)\right\| + \left\|\frac{-\dot{m}_+}{\rho_d}\left(\frac{[\varepsilon_d]}{\varepsilon_d^o+\Delta}\right)\right\|. \tag{4.21b}$$

The volume fraction of the continuous phase is determined by the requirement that the volume fractions add to one at every point,

$$\varepsilon_c = 1-\varepsilon_b-\varepsilon_d\,. \tag{4.22}$$

Equation (4.21) is nonlinear, so the set of phase continuity equations must be solved iteratively to achieve a converged solution.

4.4. Internal energy equation and phase change

The internal energy equation (Eq. 3.10) is discretized in a straightforward manner. The second term is expanded so that all spatial derivatives are expressed as divergences,

$$\left\|\sum_i \varepsilon_i\rho_i c_{v,i}\frac{\partial[T]}{\partial t}\right\| + \left\|\sum_i \rho_i c_{v,i}\nabla\cdot\left(\varepsilon_{iF}\phi_i[T]\right)\right\| - \left\|\sum_i \rho_i c_{v,i}[T]\nabla\cdot\left(\varepsilon_{iF}\phi_i\right)\right\| = \left\|\nabla\cdot\left(\left(k_{eff}+k_T\right)\nabla[T]\right)\right\| - \dot{m}\,e_{fg}\,. \tag{4.23}$$

The mass transfer rates are calculated using Eqs. (3.18) and (3.21). Equation (3.18) is applied only where $T > T_{sat}$ for the dispersed component and is limited to less than

$\varepsilon_d^o \rho_d / \Delta t$, which is the boiling rate that would consume all of the droplets within a single time step. Similarly, the condensation rate is limited to $\varepsilon_b^o \rho_b / \Delta t$. Boiling at the heated surface is handled as described in Section 3.3.2.2. The convection and buoyant forces that would bring droplets into contact with the heated surface are already included in the numerical model. Accordingly, the rate at which droplets contact the heated surface is determined using the cell-centered droplet velocity and volume fraction in the cells adjacent to the heated surface. For each cell adjacent to the heated surface,

$$\dot{m}_w = \frac{\rho_d \varepsilon_d \mathbf{U}_d \cdot \mathbf{S}_w}{V}, \tag{4.24}$$

where V is the volume of the cell. Thus boiling due to wall contact is not implemented as a true boundary condition in the finite volume numerical method. Implementation of such a boundary condition would pose significant difficulties, since the boundary condition would couple the ε_b, ε_d, $\mathbf{U}_b$, and $\mathbf{U}_d$ fields.

4.5. Solution procedure

The pressure, volume fraction, and temperature equations are coupled in a nonlinear fashion by the boiling and condensation of the dispersed component. Thus it is necessary to perform several iterations of the balance equations at each time step. Iterations are performed until the mass transfer rates reach convergence, as determined by a mixed absolute and relative tolerance similar to that used by Silva and Lage (2007),

$$\max\left[\frac{\left|\dot{m} - \dot{m}^o\right|}{1^{\,kg/m^3 s} + \left|\dot{m}\right|}\right] < 0.01. \tag{4.25}$$

Outer loop: Repeat until Eq. (4.25) is satisfied.

1. Phase volume fraction loop – repeat twice
   a. Solve the dispersed phase volume fraction equations (Eq. 4.21)
   b. Find the continuous phase volume fraction (Eq. 4.22)
2. Calculate the phase viscosities (Eqs. 3.28, 3.30)
3. Construct the a_i equations (Eqs. 4.8)
4. Solve the temperature equation (Eq. 4.23)
5. PISO loop – repeat twice
   a. Predict the phase fluxes (Eq. 4.11)
   b. Solve the pressure equation (Eq. 4.15)
   c. Correct the phase fluxes (Eq. 4.12)
   d. Reconstruct velocities
6. Calculate mass transfer rates (Eqs. 3.18, 3.21, 4.24)

Figure 4.1. Numerical solution procedure.

It is found that convergence is achieved more quickly when the mass transfer rates are under relaxed with an under relaxation factor of 0.25. The solution procedure for each time step is shown in Fig. 4.1.

4.6. Drag at high dispersed phase volume fractions

The model of boiling emulsions developed in Chapter 3 includes the assumptions that the emulsion is dilute and that the two dispersed phases do not impose forces on each other directly. However, even in a dilute emulsion there may be regions where the local volume fraction of one of the dispersed phases approaches one. For example, when $\rho_d > \rho_c$ the droplets will tend to settle onto horizontal surfaces and accumulate there. When such an occurrence is possible it is important that the numerical code handle it gracefully.

The most basic requirement for the numerical code at high dispersed phase fractions is stability. The code should continue to function as the volume fraction of a dispersed phase approaches one. Clearly the model described in the previous sections of this Chapter fails this requirement. Equations (4.8b) and (4.11b) contain the continuous

phase volume fraction in the denominator and so become undefined as $\varepsilon_c \to 0$. The offending terms arise from the drag forces on the dispersed phases. The interfacial forces, then, must be handled differently at high dispersed phase fractions so that the phase volume fraction does not appear in the denominator of any term.

A more ambitious goal is that the model should reflect the physical phenomena that occur at large dispersed phase fractions. For example, liquid-vapor two-phase flow undergoes a series of phase transitions as the volume fraction of the vapor phase increases. As described by Wallis (1969), bubbly flow at low vapor fraction gives way to churn flow in the range $0.1 < \varepsilon_b < 0.3$, and annular flow or droplet flow is generally observed at very high vapor fractions. These transitions are strongly affected by the presence of impurities in the system. In fact, the addition of a foaming agent to a liquid-vapor system can cause bubbly flow to persist even for vapor fractions near one. The resulting foam also exhibits significant non-Newtonian behavior. Modeling such phase transitions is well beyond the scope of this study and in fact no general model exists for predicting the structure of multiphase flow under different conditions.

Rusche (2002) describes a modeling approach for two-phase flows at large dispersed phase volume fraction that models a single phase transition at a defined dispersed phase fraction. He introduces a continuous phase indicator function X_i that is defined such that $X_i \to 1$ as $\varepsilon_i \to 1$ and $X_i \to 0$ as $\varepsilon_i \to 0$. The drag force between the phases i and j of a two-phase mixture can be expressed as,

$$\mathbf{F}_{ij} = 18\mu_{eff}\mathbf{U}_{r,ij}\left(X_i \frac{\varepsilon_j}{d_j^2} + X_j \frac{\varepsilon_i}{d_i^2}\right). \tag{4.26}$$

In a two phase mixture, $\varepsilon_j = 1 - \varepsilon_i$ and $X_j = 1 - X_i$. In the limit of $\varepsilon_i \to 1$ or $\varepsilon_j \to 1$, Eq. (4.26) becomes equal to Eq. (2.10). Use of this equation requires that a characteristic diameter be defined even for the nominally continuous phase. Rusche (2002) notes that the simplest definition of the continuous phase indicator function, $X_i = \varepsilon_i$, can lead to significant errors in the terminal velocity of the dispersed phase elements when the

characteristic diameters differ greatly. Rusche avoids this possibility by using a stronger function of the phase fraction,

$$X_i = \frac{1+\tanh\left[20\left(\varepsilon_i - 0.5\right)\right]}{2}. \tag{4.27}$$

This approach is easily extended to mixtures of more than two phases. Equation (4.26) can be applied directly to each pair of phases in the mixture. Defining a complex equation such as Eq. (4.27) for the continuous phase indicator function becomes more problematic, however. If the relation $X_i = \varepsilon_i^2$ is adopted, the drag force between each pair of phases in boiling emulsions is,

$$\mathbf{F}_{bc} = 18\varepsilon_b\varepsilon_c\mu_{eff}\mathbf{U}_{r,bc}\left(\frac{\varepsilon_b}{d_c^2}+\frac{\varepsilon_c}{d_b^2}\right), \tag{4.28a}$$

$$\mathbf{F}_{bd} = 18\varepsilon_b\varepsilon_d\mu_{eff}\mathbf{U}_{r,bd}\left(\frac{\varepsilon_b}{d_d^2}+\frac{\varepsilon_d}{d_b^2}\right), \tag{4.28b}$$

$$\mathbf{F}_{cd} = 18\varepsilon_c\varepsilon_d\mu_{eff}\mathbf{U}_{r,cd}\left(\frac{\varepsilon_c}{d_d^2}+\frac{\varepsilon_d}{d_c^2}\right). \tag{4.28c}$$

These equations can be used in place of Eq. (2.10) in Eq. (4.8) and (4.11) to prevent the simulation from becoming unstable if $\varepsilon_c \to 0$. It is noteworthy that this approach allows the bubble and droplet phases to exert drag forces on each other directly, which as explained in Chapter 3, should not occur. However, as long as the volume fraction of both dispersed phases remains small, the force between them will be small compared to the force exerted by either dispersed phase on the continuous phase.

4.7. Results

Results of simulations performed using this procedure are presented in the following chapter along with experimental results.

5. Experimental apparatus and results

Experiments have been carried out to investigate the behavior of dilute emulsions boiling on a small diameter heated wire. The emulsions used in these experiments consist of FC-72 in water. The primary objective is to measure the heat transfer coefficient at different temperatures for a still pool of dilute emulsion boiling on the wire. At very low droplet volume fractions, visual observation of the boiling droplets is also possible. These data are to provide validation of the theoretical model.

5.1. Apparatus

The test cell consists of a chamber constructed of clear acrylic with a fine copper wire stretched between two bus bars located near its center (Fig. 5.1). The wire has length 100 mm and diameter 101 μm (38 AWG copper wire) and is heated by electrical current, which is adjusted to vary the surface temperature of the wire. The wire thus has $L/d \approx 1000$. The acrylic chamber permits observation of the emulsion for visualization experiments. The bus bar assembly is not fastened to the test cell, but is instead supported by crossbars that rest on the top of the test cell. Mechanical drawings of the apparatus are provided in Appendix B.

The test cell has 25.4 mm length, 203 mm width, and 203 mm depth, allowing it to hold ~ 1 ℓ of emulsion. The length of the cell is short so that observation through the length of the cell is possible for very dilute emulsions. The sides of the cell are solvent bonded together. The base is fastened to the sides with eight bolts and a gasket is used to prevent leaks through the joint. This design permits easy access to the interior of the test cell for cleaning. Because experiments are fairly short in duration (less than ten minutes) and the total energy dissipated by the wire during each experiment is small, no additional equipment is needed to maintain the emulsion at a constant bulk temperature during the experiment.

The voltage difference across the wire and current through the wire are measured, from which the heat generation rate in the wire and the resistance of the wire are calculated. Measurements are recorded once per second during each experiment using a

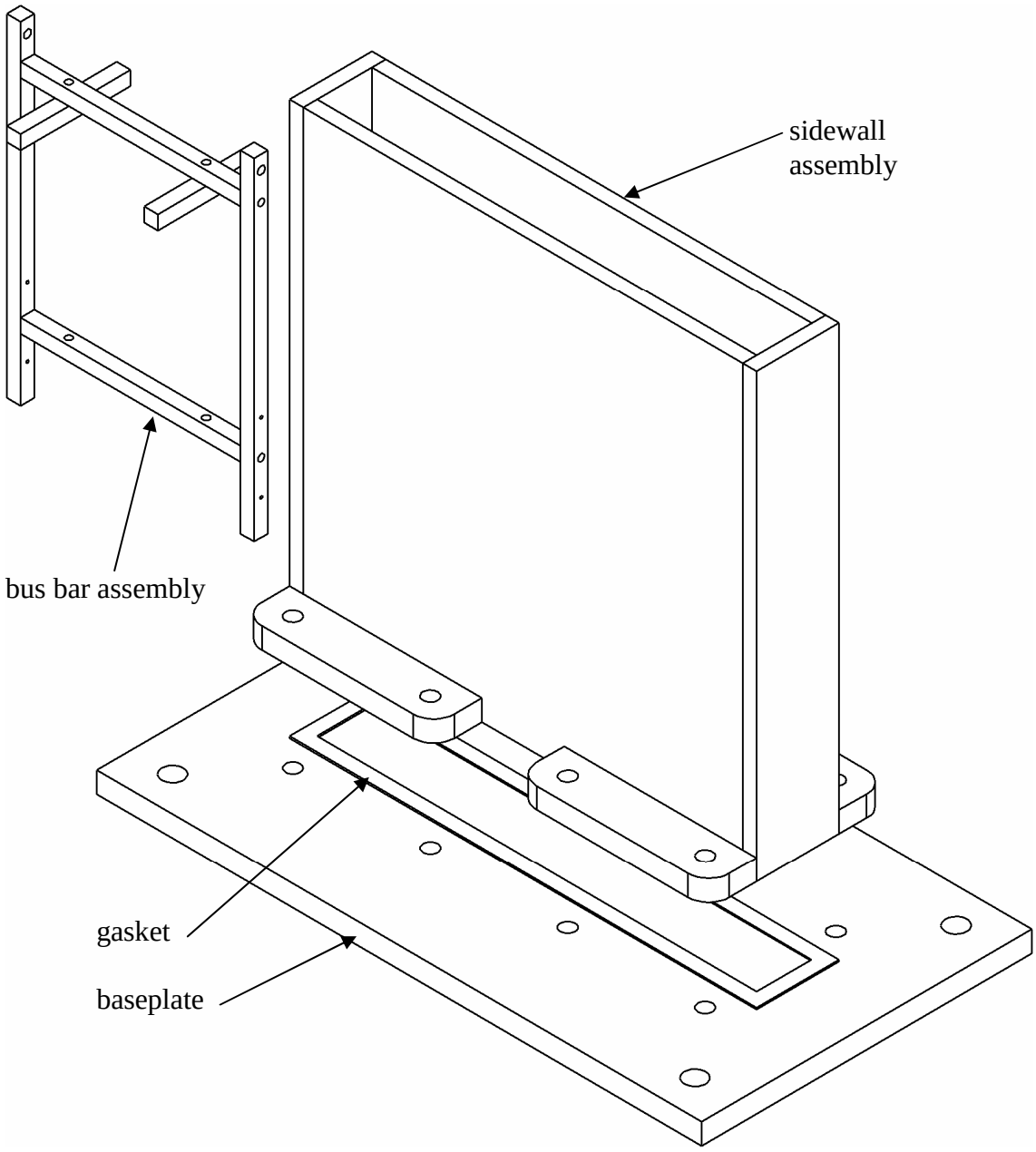

Figure 5.1. Test cell.

digital data acquisition system. The bulk temperature of the emulsion is also measured directly at the beginning of each experiment.

The schematic diagram and parts list for the power supply are provided in Appendix B. The potentiometer of the power supply is adjusted to alter the electrical current delivered to the heated wire. The current also passes through a current sense resistor,

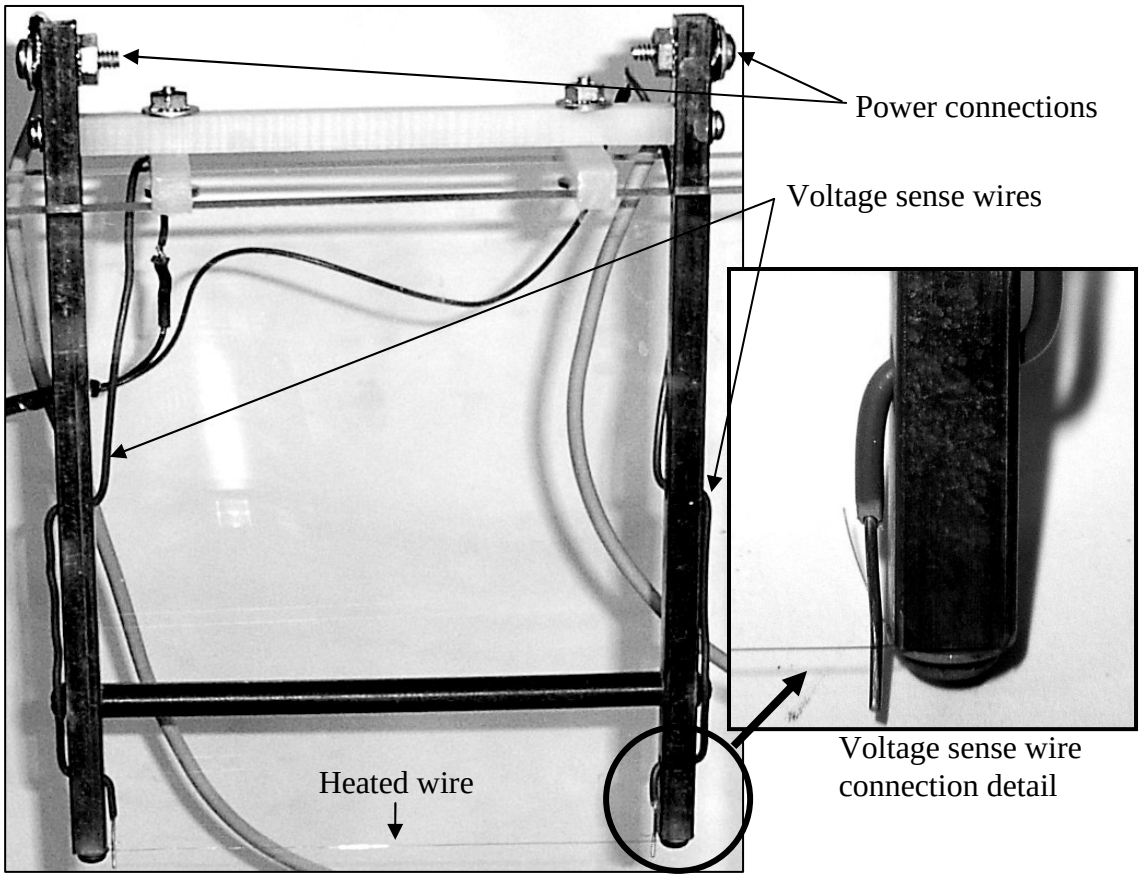

Figure 5.2. Bus bar assembly details.

and the voltage difference across this resistor is measured to determine the current passing through the wire. The voltage difference across the heated wire is measured using sense wires that contact the heated wire adjacent to the bus bars (Fig. 5.2). This approach avoids the confounding effects of resistance in the junction between the heated wire and the bus bars and in the bus bars themselves. These two voltage differences (across the heated wire and across the current sense resistor) are measured sequentially by an electronic data acquisition system once per second. Because the two voltages are not measured simultaneously, if the current is being adjusted while the measurements are made an inaccurate picture of the wire's state may be obtained. This effect is most significant at lower currents, where it is found necessary to adjust the electrical current and then wait for a few seconds for the system to reach steady state so that accurate measurements can be made. At currents higher than approximately three

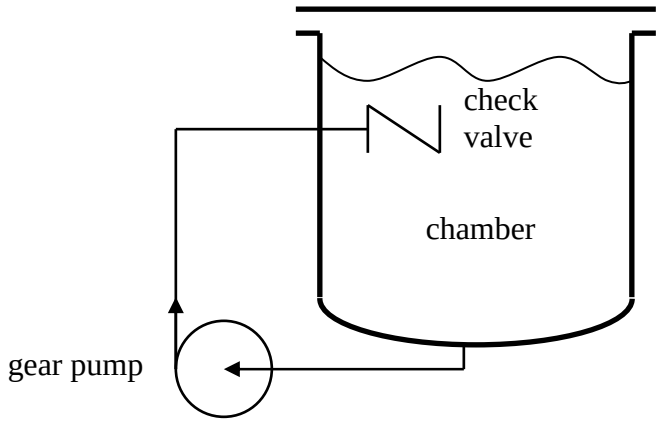

Figure 5.3. Apparatus for preparation of the emulsion.

Amperes it is possible to make a slow continuous adjustment of the current without affecting the accuracy of the measurements.

5.2. Emulsion preparation

Emulsions of FC-72 in water are prepared in a separate apparatus in batches of ~1.5 ℓ. For each batch of emulsion, the water is first degassed and brought to the desired bulk temperature for the experiment. The FC-72 is then added and emulsified in the water. The emulsion is transferred to the test cell immediately after preparation.

The apparatus used for preparing the emulsions (Fig. 5.3) consists of a chamber that holds ~1.5 ℓ of liquid and a flow loop terminating at a check valve inside the chamber. A gear pump is used to draw liquid from the chamber and return it through the check valve. The jet of liquid exiting the check valve breaks up the FC-72 into fine droplets. The inlet of the flow loop is placed at the lowest point in the chamber so that any non-emulsified FC-72 that settles to the bottom will be taken up into the flow loop.

The emulsion must be degassed to prevent air bubbles from forming on the heated surface and interfering with convection from the surface. Because FC-72 is more volatile than water, the water must be degassed before the FC-72 is introduced. Slightly more than 1.5 ℓ of distilled water is boiled for at least thirty minutes. After boiling, the water is cooled to the desired temperature with a heat exchanger. The FC-72 is not degassed separately.

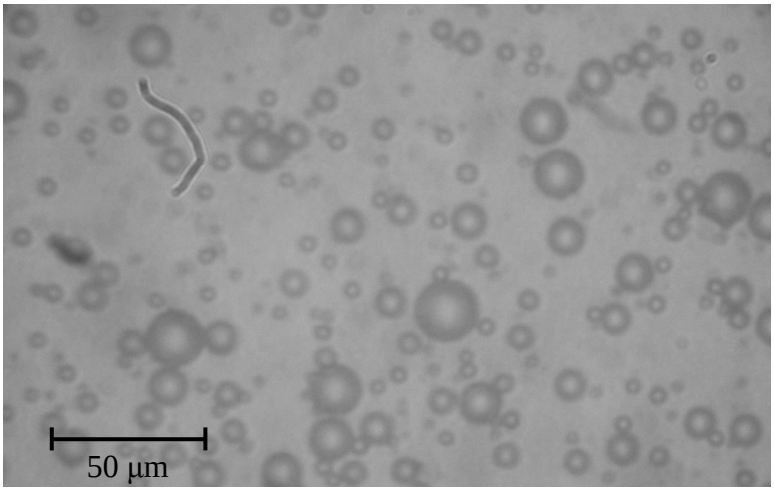

(a)

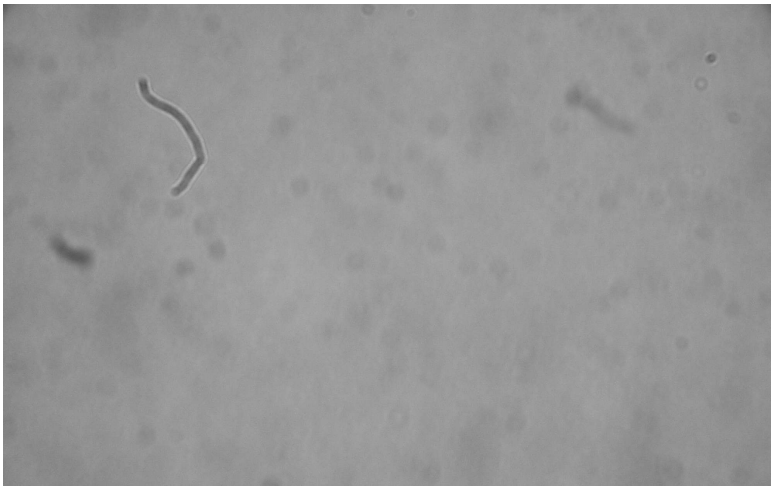
(b)

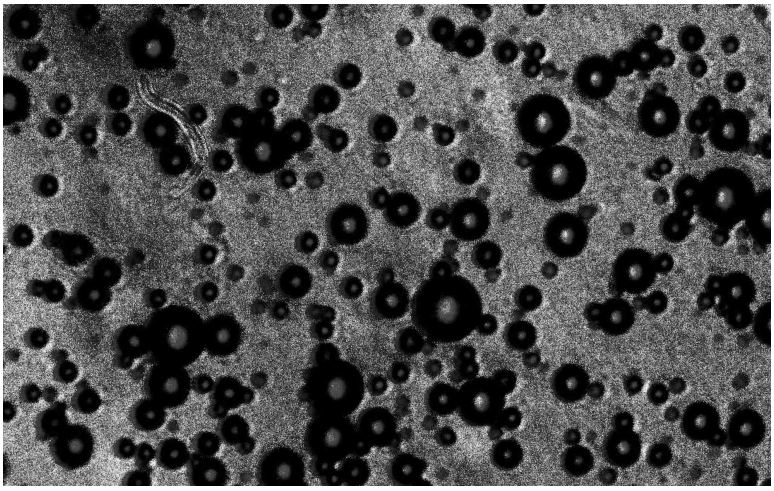
(c)

Figure 5.4. Photomicrograph of (a) emulsion, (b) no slide, and (c) difference between (a) and (b) with contrast enhanced. Emulsion is 1% FC-72 by volume.

After degassing, 1.5 ℓ of water is transferred to the chamber and FC-72 is added to produce a mixture of the desired volume fraction. The pump is turned on and run for five minutes. Because FC-72 is denser than water, any FC-72 that is not emulsified tends to settle to the bottom of the chamber, where it is drawn in by the inlet to the flow loop. The turbulent jet formed by the check valve breaks the FC-72 up into fine droplets. After two minutes the emulsion is transferred to the test chamber.

After performing tests with emulsions of FC-72 in water, additional experiments were performed with emulsions of pentane in water. The preparation of these emulsions is slightly different. Because pentane is less dense than water, the check valve is moved to the bottom of the chamber in Fig. 5.3 and the intake of the flow loop is moved near the top. After turning on the pump the pentane is introduced directly into the intake. The pump is run only long enough to give the emulsion a uniform appearance, typically ~20 s.

5.2.1. Droplet size

The diameter of droplets of FC-72 produced by this method fall in the range $4 \leq d_d \leq 22$ μm, with the majority of the droplets having $d_d = 6$ μm. These diameters were measured from photographs of samples of the emulsion taken through a microscope. To eliminate the possibility of counting dust on the lenses of the microscope as droplets, photomicrographs were taken in pairs, one with the slide containing a sample of the emulsion in place, and one with the slide removed. The second photomicrograph is subtracted from the first and the contrast of the resulting image is increased for clarity. This process is illustrated in Fig. 5.4.

Next, the diameters of the droplets in each photomicrograph are measured. A histogram of droplet diameters (Fig 5.5) shows that although most droplets have $5 < d_d < 6$ μm, a few are as large as 22 μm. The numerical average of the droplet diameters in Fig. 5.3 is 7.9 μm and the Sauter mean diameter is 11.8 μm. The model developed in Chapter 3 includes the assumption that the droplets are monodisperse, which is clearly not a good assumption for emulsions produced by this method. The distribution of d_d does not change significantly for different volume fractions of FC-72. The diameter is also not found to be a function of the mixing time.

5.3. Experimental conditions

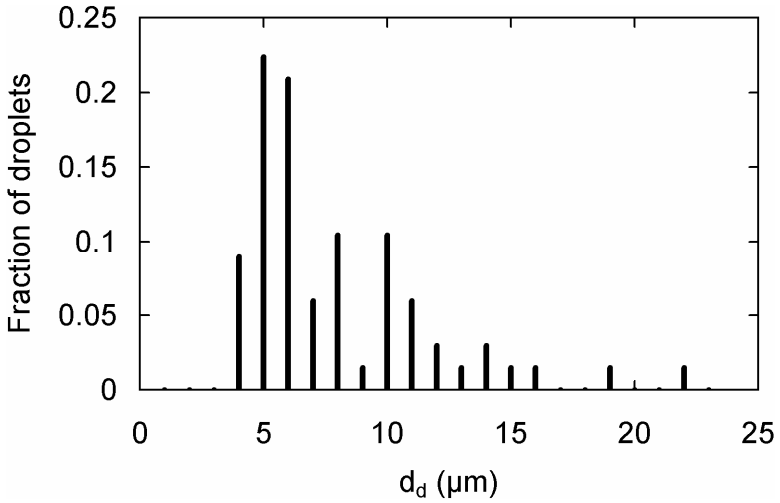

Figure 5.5. Histogram of droplet diameter for emulsion in Fig. 5.3.

Many factors can influence the boiling heat transfer rate to emulsions of FC-72 in water and it is not the goal of this study to investigate all of them. The experimental study is intended to investigate just three factors: surface temperature, volume fraction of the dispersed component, and degree of subcooling of the bulk of the emulsion. Other factors that have been shown to influence heat transfer include the droplet size distribution, flow geometry, and the presence of surfactants and other impurities in the emulsion. These parameters are held constant in the current study.

Experiments are performed at two nominal bulk temperatures of the emulsion, 25 and 44 °C (31 and 12 °C of subcooling of the FC-72, respectively). Experiments with pentane in water were performed at the 25 °C bulk temperature only. The working fluids that are investigated are water and emulsions of 0.1, 0.2, 0.5, and 1.0% disperse component volume fraction. Previous experiments have shown that for pool boiling of emulsions, the heat transfer coefficient depends on the dispersed component volume fraction up to ~1% (Bulanov et al., 1996). The emulsions are all made using distilled water and without introducing any surfactants. In each experiment the heat flux from the heated wire is adjusted from nearly zero to ~2 MW/m^2, which is the limit of the apparatus. For the pentane in water experiments the heat flux range was increased to ~7 MW/m^2. These ranges of heat fluxes encompasses natural convection from the wire

when no boiling takes place as well as a significant portion of the boiling curve. The apparatus cannot deliver sufficient power to cause transition film boiling under the conditions of these experiments.

5.4. Data reduction

The two measured voltage differences (across the heated wire and across the current sense resistor) are used to determine the temperature of the wire and the heat transfer coefficient to the emulsion surrounding it. The analysis of the data requires several steps.

First, the electrical current through the wire is calculated from the voltage difference across the current sense resistor using Ohm's law,

$$I_{wire} = \frac{\Delta V_{cs}}{\mathcal{R}_{cs}}. \tag{5.1}$$

With both the current through and voltage difference across the wire known, the resistance of the wire may also be calculated using Ohm's law,

$$\mathcal{R}_{wire} = \frac{\Delta V_{wire}}{I_{wire}} = \frac{\Delta V_{wire}\mathcal{R}_{cs}}{\Delta V_{cs}}. \tag{5.2}$$

The electrical resistivity of copper, ρ_E, is known to vary essentially linearly with temperature over a wide temperature range. Based on data from Lide (2010), between 20 °C and 127 °C the resistivity of copper increases by a factor of $\alpha_E = 0.004032\ °C^{-1}$, referenced to 20 °C,

$$\rho_E = \rho_{E,0}\left[1 + \alpha_E\left(T - 20\,°C\right)\right]. \tag{5.3}$$

The electrical resistance of the wire is a linear function of the resistivity, $\mathcal{R} = \rho_E L/A_{xc}$, so the wire resistance increases with temperature at the same rate as the resistivity. In

this study, the wire resistance is known (Eq. 5.2) and can therefore be used to calculate the temperature of the heated wire,

$$T_{wire} = 20\,°C + \left(\frac{1}{\alpha_E}\right)\left(\frac{\mathcal{R}_{wire}}{\mathcal{R}_{wire,0}} - 1\right) = 20\,°C + \left(\frac{1}{\alpha_E}\right)\left(\frac{\Delta V_{wire}\mathcal{R}_{cs}}{\Delta V_{cs}\mathcal{R}_{wire,0}} - 1\right). \tag{5.4}$$

The reference wire resistance, $\mathcal{R}_{wire,0}$, can be calculated based on the dimensions of the wire, but variations in manufacturing and handling of the wire cause small deviations of the resistance from the expected value. The direct measurement of the bulk temperature of the emulsion made at the beginning of each experiment can be used to account for these deviations. At the beginning of each experiment a direct measurement of the wire resistance is made at low current ($I_{wire} \approx 0.1$ A) where $T_{wire} \approx T_\infty$. The value of $\mathcal{R}_{wire,0}$ used for each experiment is adjusted to bring the two temperature measurements into agreement. Typical adjustments are no more than 0.5% of $\mathcal{R}_{wire}$.

The power dissipated by the wire is simply the product of the voltage difference across the wire and the current through it,

$$q'' = \frac{I_{wire}\Delta V_{wire}}{A_{wire}} = \frac{\Delta V_{wire}}{A_{wire}}\frac{\Delta V_{cs}}{\mathcal{R}_{cs}}. \tag{5.5}$$

The wire surface area A_{wire} in Eq. (5.5) is calculated using the length of wire between the points at which the voltage sense wires contact the heated wire, not between the bus bars. This length is 99 mm, approximately one millimeter shorter than the distance between the bus bars. The average heat transfer coefficient for the heated wire is calculated using Newton's law of cooling and the results of Eqs. (5.4) and (5.5),

$$h = \frac{q''}{A_{wire}\left(T_{wire} - T_\infty\right)}. \tag{5.6}$$

5.4.1. Non-uniform wire temperature correction

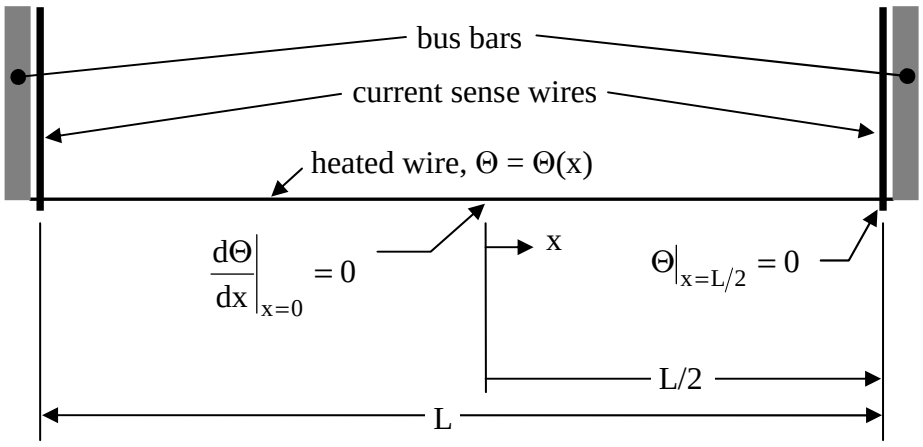

Figure 5.6. Coordinate system and boundary conditions for analysis in Section 5.4.1.

The foregoing discussion assumes that the heated wire has a uniform temperature. While this assumption is valid across the wire's cross section, the wire temperature does vary along its length. The bus bars and voltage sense wires act as heat sinks that hold the temperature of the heated wire equal to T_∞ at its ends. The wire resistance calculated in Eq. (5.2) applies to the whole heated wire, including the ends. Thus, the wire temperature calculated using Eq. (5.4) is the average temperature for the whole wire, including the ends. Under the conditions of this study, the bus bars influence the temperature of only a small fraction of the wire's length, while the middle portion of the wire has nearly uniform temperature. The temperature at the midpoint of the wire is slightly higher than the average temperature calculated above (Eq. 5.4) and is calculated as described below. The heat transfer coefficient is then calculated using the local wire temperature and the local heat flux at the midpoint of the wire. The coordinate system for the following analysis is defined in Fig. 5.6.

An energy balance applied to a cross sectional slice of the wire yields the following governing equation for temperature,

$$\frac{d^2\Theta}{dx^2} = -\frac{\dot{q}}{k_{wire}} + \frac{4h}{d_{wire}k_{wire}}\Theta, \tag{5.7}$$

where Θ is the temperature rise above ambient, $\Theta = T - T_\infty$. It is assumed that the wire is at steady state and that radiation losses are negligible. The coordinate system and boundary conditions for this equation are defined in Fig. (5.6). The heat generation rate in the wire varies linearly with the resistivity, which also varies with temperature. The heat generation rate may be expressed in terms of the current density, I/A, and the electrical resistivity, ρ_E,

$$\begin{aligned}\frac{d^2\Theta}{dx^2} &= -\frac{I_{wire}^2 \rho_{E,0}}{kA_{xc}^2}\left[1+\alpha_E(\Theta-\Theta_0)\right]+\frac{4h}{d_{wire}k_{wire}}\Theta \\ &= -K_a + K_b^2\Theta\end{aligned}, \tag{5.8}$$

where the constants K_a and K_b are,

$$K_a = \frac{I_{wire}^2 \rho_{E,0}}{kA_{xc}^2}(1-\alpha_E\Theta_0), \tag{5.9a}$$

$$K_b = \left(\frac{4h}{d_{wire}k_{wire}} - \frac{I_{wire}^2 \rho_{E,0}\alpha_E}{kA_{xc}^2}\right)^{1/2}. \tag{5.9b}$$

This formulation assumes that only the electrical resistivity is a function of temperature; the thermal conductivity of the wire, dimensions of the wire, and heat transfer coefficient are constant.

The solution to Eq. (5.8) is,

$$\Theta = \frac{K_a}{K_b^2}\left(1-\frac{\cosh(K_b x)}{\cosh(\frac{1}{2}K_b L)}\right). \tag{5.10}$$

Under the conditions of this study K_bL is fairly large (greater than ten) so most of the wire has nearly uniform temperature,

$$\Theta_{mid} = \frac{K_a}{K_b^2}. \tag{5.11}$$

The cooler ends of the wire cause the measured wire resistance to be somewhat lower than if the entire wire were at Θ_{mid}. The resistance of the wire can be obtained by integration,

$$\mathcal{R} = 2\int_0^{L/2} \frac{\rho_E}{A_{xc}}\,dx\,. \tag{5.12}$$

When the equations for copper resistivity (Eq. 5.3) and wire temperature (Eq. 5.10) are substituted into this equation the result is,

$$\mathcal{R} = \frac{L\rho_{E,0}}{A_{xc}}\left(1-\alpha_E\Theta_0+\alpha_E\Theta_{mid}\right) - \frac{2\rho_{E,0}\alpha_E}{A_{xc}}\int_0^{L/2}\frac{\cosh(K_bx)}{\cosh\left(\frac{1}{2}K_bL\right)}\,dx\,, \tag{5.13}$$

which simplifies to,

$$\mathcal{R} = \mathcal{R}_0\left(1+\alpha_E\left(\Theta_{mid}-\Theta_0\right)\right) - \mathcal{R}_0\,\frac{2}{K_bL}\,\alpha_E\,\tanh\left(\tfrac{1}{2}K_bL\right). \tag{5.14}$$

As noted before, under the conditions of this study K_bL is large, so $\tanh(0.5K_bL) \approx 1$. The resistance of the wire is therefore,

$$\mathcal{R} = \mathcal{R}_0\left(1+\alpha_E\left(\Theta_{mid}\left(1-\frac{2}{K_bL}\right)-\Theta_0\right)\right). \tag{5.15}$$

This equation can be combined with the definition of the average wire temperature (Eq. 5.4) to obtain an expression for the wire midpoint temperature,

$$T_{mid} = \left(1-\frac{2}{LK_b}\right)^{-1}\left[T_{wire}-T_\infty\right]+T_\infty. \tag{5.16}$$

Far away from the ends of the wire there is negligible axial heat conduction through the wire, so the local heat flux is a function only of the local heat generation. The heat generation, in turn, is a function of the current through the wire and the local resistivity, given by Eq. (5.3). The heat flux at the midpoint of the wire is,

$$q''_{mid} = \frac{I^2_{wire}}{A_{wire}}\mathcal{R}_{wire,0}\left[1+\alpha_E\left(T_{mid}-T_\infty\right)\right], \tag{5.17}$$

and the heat transfer coefficient at the midpoint of the wire is,

$$h_{mid} = \frac{q''_{mid}}{T_{mid}-T_\infty}. \tag{5.18}$$

This analysis assumes that h is uniform over the wire surface, but in fact the heat transfer coefficient is a function of the wire temperature. The reduced value of h near the wire ends results in a smaller region of reduced temperature than predicted by Eq. (5.10). The correction in Eq. (5.16) is therefore too large, and the heat flux predicted by Eq. (5.17) is too small. These errors oppose each other in Eq. (5.18).

5.5. Uncertainty analysis and calibration

Table 5.1. Measurement uncertainties.

Quantity	Uncertainty	
$\mathcal{R}_{cs}$	0.15%	
ΔV_{cs}	0.005% + 4 μV	
ΔV_{wire}	0.005% + 4 μV,	$\Delta V_{wire} < 0.12$ V
	0.004% + 7 μV,	$0.12 < \Delta V_{wire} < 1.2$ V
	0.0035% + 50 μV,	$1.2 \text{ V} < \Delta V_{wire} < 12$ V
T_∞	0.5 °C	
$\mathcal{R}_{wire,0}$	0.21%	
I_{wire} (direct measurement)	0.05% + 2 μA,	I < 12 mA
	0.05% + 5 μA,	12 mA < I < 120 mA
	0.1% + 100 μA,	120 mA < I < 1 A

Measurement uncertainties are listed in Table 5.1. Uncertainties in T_{wire}, T_{mid}, q''_{mid}, and h_{mid} are determined from the measurement uncertainties using calculus and the principle of superposition of errors (Topping, 1962). In general, for a variable Q that is a function of several variables, Q = Q(a, b, c, …), the square of the uncertainty in Q is the sum of the square of the uncertainties due to each independent variable,

$$\delta Q = \left[\left(\frac{\partial Q}{\partial a} \delta a \right)^2 + \left(\frac{\partial Q}{\partial b} \delta b \right)^2 + \left(\frac{\partial Q}{\partial c} \delta c \right)^2 + \cdots \right]^{0.5}, \tag{5.19}$$

where δa denotes the uncertainty in a. This procedure is applied to Eq. (5.4), (5.16), (5.17), and (5.18). The relative uncertainty of the measured voltages is quite small and so may be safely neglected. The uncertainty in T_{wire} is,

$$\delta T_{wire} = \left(\frac{1}{\alpha_E} + T_{wire} - 20\,°C \right) \left[\left(\frac{\delta \mathcal{R}_{cs}}{\mathcal{R}_{cs}} \right)^2 + \left(\frac{\delta \mathcal{R}_{wire,0}}{\mathcal{R}_{wire,0}} \right)^2 \right]^{0.5}, \tag{5.20}$$

the uncertainty in q"$_{mid}$ is,

$$\delta q''_{mid} = q''_{mid}\left\{\left(2\frac{\delta \mathcal{R}_{cs}}{\mathcal{R}_{cs}}\right)^2 + \left(\frac{\delta \mathcal{R}_{w}}{\mathcal{R}_{w}}\right)^2 + \frac{\alpha_E^2\left(\delta T_{mid}^2 + \delta T_{\infty}^2\right)}{\left[1+\alpha_E\left(T_{mid}-T_{\infty}\right)\right]^2}\right\}^{0.5}, \tag{5.21}$$

and the uncertainty in h_{mid} is,

$$\delta h_{mid} = h_{mid}\left[\left(\frac{\delta q''_{mid}}{q''_{mid}}\right)^2 + \left(\frac{\delta T_{mid}}{T_{mid}-T_{\infty}}\right)^2 + \left(\frac{\delta T_{\infty}}{T_{mid}-T_{\infty}}\right)^2\right]^{0.5}. \tag{5.22}$$

Evaluating the uncertainty in T_{mid} (Eq. 5.16) is more difficult because errors arise from the assumptions made in the analysis rather than measurement uncertainties. It is assumed that error in the analysis leading up to Eq. (5.16) may be as large as half the difference between T_{wire} and T_{mid}. The uncertainty in the wire midpoint temperature is therefore,

$$\delta T_{mid} = \left(\frac{K_b L}{K_b L - 2}\right)\left[\left(\frac{2\delta T_{\infty}}{K_b L}\right)^2 + \delta T_{wire}^2 + \left(\frac{T_{mid}-T_{\infty}}{K_b L}\right)^2\right]^{0.5}. \tag{5.23}$$

Under most circumstances, $0.8 < \delta T_{wire} < 2.2$ °C. The uncertainty in the wire temperature becomes significantly larger only at very low current, when the voltage difference across the current sense resistor is very small. The uncertainty in the heat transfer coefficient is also small except at low power. For $(T_{wire} - T_{\infty}) > 10$ °C the uncertainty in h is less than 10%, and falls to less than 3% for $(T_{wire} - T_{\infty}) > 40$ °C. At larger temperature differences the greatest contribution to uncertainty in h is uncertainty in the conduction to the ends of the wire.

5.5.1. Calibration

Electrical measurements are performed using an Agilent 34970A data acquisition unit. The instrument is capable of making very accurate voltage measurements and accurate current measurements. However, the current measurement function is limited to currents of 1 A or less, which is too low to use directly in this study. The current through the heated wire must therefore be calculated from the voltage difference across an external current sense resistor. The current and voltage measurement functions of the data acquisition unit are used to measure accurately the resistance of the current sense resistor. The resistance of the heated wire may also be accurately measured at the beginning of each experiment.

The current sense resistor has a nominal resistance of 5 mΩ and a tolerance of 1%. Such a large uncertainty applied to Eq. (5.20) would result in an uncertainty in the wire temperature of several degrees, which is unacceptably high. Because $\mathcal{R}_{cs}$ is so small, as large a current as possible must be passed through it to avoid a large relative uncertainty in the voltage measurement. A circuit is constructed that passes current from a stable 5V power supply through a power resistor, a data acquisition unit in current measurement mode, and the current sense resistor in series. The power resistor is used to limit the current through the resistor to ~1 A. A second data acquisition unit is used to measure the voltage across the current sense resistor. The current is measured to be 866.16 ± 0.97 mA and ΔV_{cs} is measured to be 4.3296 ± 0.0042 mV simultaneously. By Ohm's law, then, $\mathcal{R}_{cs}$ = 4.9986 ± 0.0074 mΩ.

It is important that two separate data acquisition units are used to perform the voltage and current measurements simultaneously, even though a single Agilent 34970A is capable of performing multiple measurements in sequence. The path taken by the current to be measured through the data acquisition unit changes when the unit switches between voltage and current measurements. The resistance of the circuit therefore changes in an unpredictable manner when a single data acquisition unit is used to make both current and voltage measurements. Using two data acquisition units avoids this problem, and also avoids the effects of any drift in the voltage of the power supply or the value of the power resistor.

The same procedure is also used to measure the resistance of the heated wire accurately at the beginning of each experiment. Because the resistance of the heated wire is much greater than that of the current sense resistor, the best accuracy is achieved when the current through the wire is ~ 100 mA. At this lower current the most accurate current measurement range of the data acquisition unit can be used without sacrificing accuracy in the voltage measurement across the heated wire. Typical relative uncertainty in $\mathcal{R}_0$ measured in this manner is 0.21%.

5.6. Results

5.6.1. Water

Before performing experiments with emulsions, the free convection heat transfer to water is measured. These experiments provide a base-line for comparison to the emulsion results and confirm that the apparatus behaves as expected. These experiments are performed with distilled water that was degassed using the procedure described in the previous section.

Morgan (1975) examines 64 previous studies of natural convection heat transfer from horizontal circular cylinders and suggests the following correlations,

$$\mathrm{Nu}_{\mathrm{film}} = 0.675\mathrm{Ra}^{0.058}, \quad 10^{-10} < \mathrm{Ra} < 10^{-2}, \tag{5.24a}$$

$$\mathrm{Nu}_{\mathrm{film}} = 1.02\mathrm{Ra}^{0.148}, \quad 10^{-2} < \mathrm{Ra} < 10^{2}. \tag{5.24b}$$

The characteristic length in the Nusselt and Rayleigh numbers in Eq. (5.24) is the diameter of the heated cylinder. All fluid properties in Eq. (5.24) are evaluated at the film temperature. Most experiments in this study fall into the Rayleigh number range of Eq. (5.24b). Morgan estimates that the uncertainty of these correlations is ~5%.

The boiling portion of the experimental data can be compared to the correlation developed by Rohsenow (1952),

$$\frac{c_p\left(T_{mid}-T_{sat}\right)}{i_{fg}\,Pr^s}=C_{sf}\left(\frac{q''}{\mu_f i_{fg}}\right)^{1/3}\left(\frac{\sigma}{g\left(\rho_f-\rho_g\right)}\right)^{1/6}, \tag{5.25}$$

where for copper surfaces in water C_{sf} = 0.013 and the power of the Prandtl number, s, is one. Although this correlation was developed for saturated boiling, the effect of subcooling is small during nucleate boiling (Lienhard and Lienhard, 2008). However, even for saturated boiling, Eq. (5.25) typically has ~25% error in ($T_{wire} - T_{sat}$) (Lienhard and Lienhard, 2008).

The measured heat transfer coefficient for water is shown in Fig. 5.7 for two bulk water temperatures, 23.2 °C and 43.4 °C. In both cases the agreement between the experimental data for single-phase free convection and Eq. (5.24b) is good. For the T_∞ = 23.2 °C case, the difference between Eq. (5.24b) and the experimental data is less than 10% at all temperatures, and the difference between the two generally decreases with temperature. For the T_∞ = 43.4 °C case, the experimental data is as much as 20% than Eq. (5.24b) for T_{wire} < 50 °C, although the experiment and correlation are within 5% for T_{wire} > 90 °C. This deviation may be due to heat loss to the walls of the test cell causing a slight decrease in T_∞ between the time at which T_∞ was measured and the experimental run (which was approximately one minute). The boiling heat transfer data also agree fairly well with Eq. (5.25), taking into account the large uncertainty associated with the correlation and the unsteadiness of the wire temperature.

In both cases, superheat of ~40 °C is required to initiate boiling, and no significant difference in the degree of superheat required is seen between the two cases. Within four to five seconds of the onset of boiling the wire temperature drops by ten to fifteen degrees Celsius. The wire temperature remains essentially constant as the heat flux at the wire surface is increased further. In neither case is transition to film boiling observed, even though the heat flux at the wire surface approaches 2 MW/m^2.

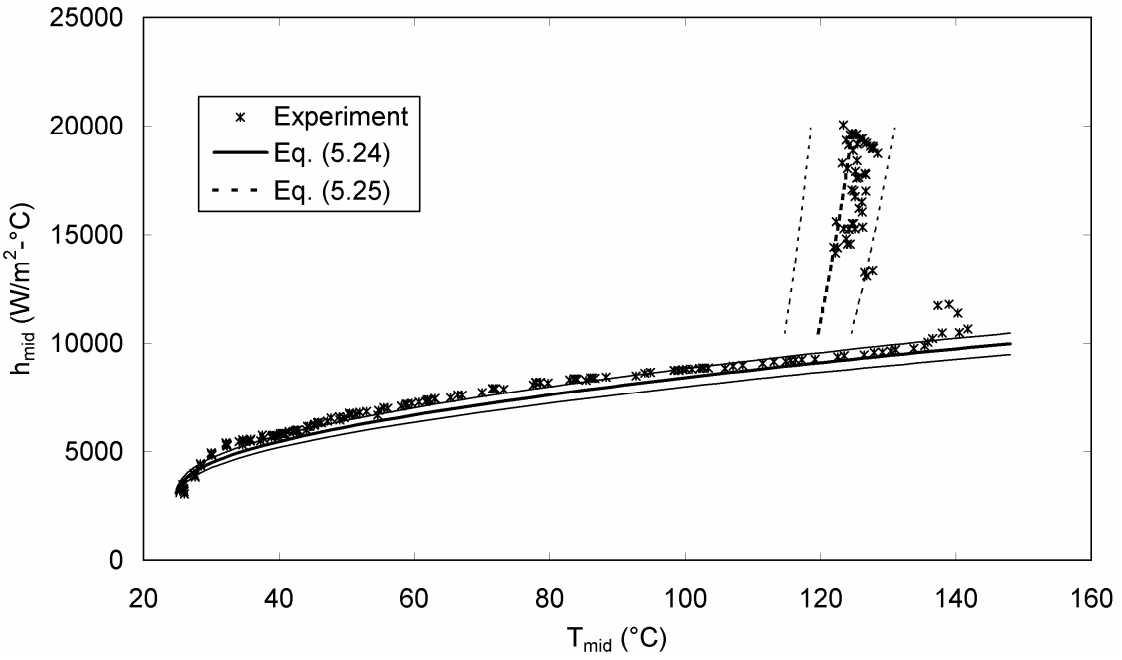

(a)

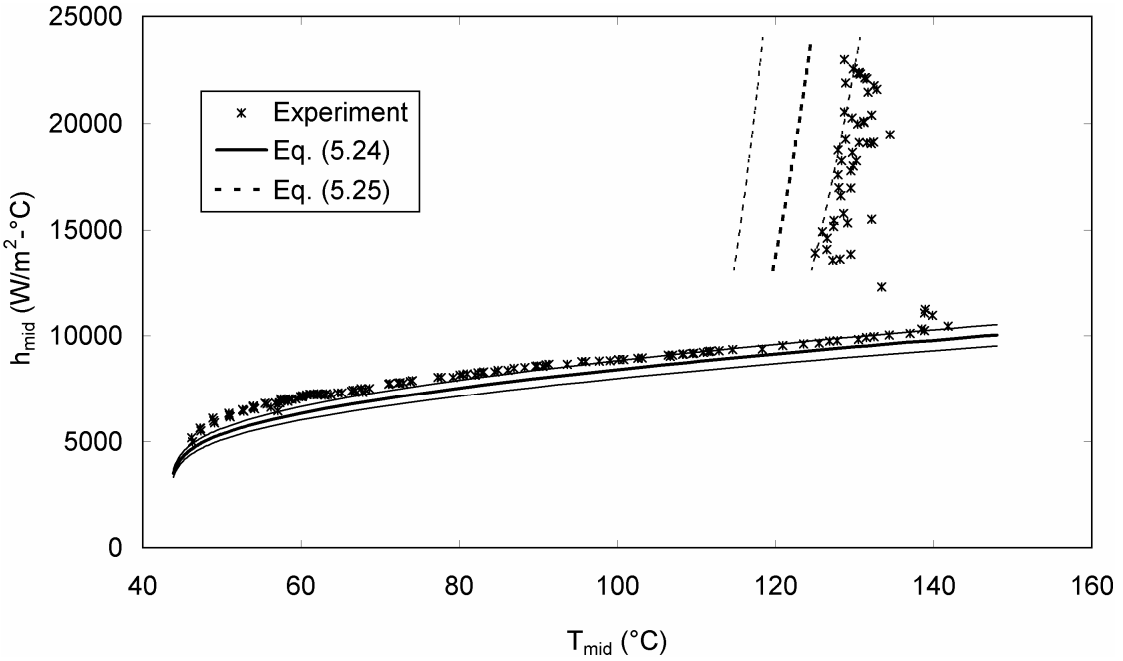

(b)

Figure 5.7. Free convection heat transfer coefficient from heated wire to water, (a) T_∞ = 24.2 °C, (b) T_∞ = 43.4 °C. Light-weight lines indicate uncertainty limits of the correlations.

5.6.2. FC-72 in water emulsions

Heat transfer coefficients for the heated wire in dilute emulsions of FC-72 in water are shown in Fig. 5.8. Equations (5.24) and (5.25) are included for comparison. The correlations are computed for water. Boiling curves for pure FC-72 are not included because the expected critical heat flux of pure FC-72 is much lower than the heat fluxes used in these experiments. Due to the lower wire temperatures in the boiling emulsion experiments, the uncertainty in the wire temperature is somewhat smaller than in the water experiments, $\delta T_{wire} < 1.4$ °C.

Several notable trends are observed in the experimental data. First, the single-phase heat transfer coefficient is lower than for water, and the divergence from Eq. (5.24) grows larger with increasing FC-72 volume fraction and with increasing ΔT. On the other hand, boiling heat transfer is enhanced compared to water (Eq. 5.25) and improves with increasing FC-72 volume fraction. A very large degree of superheat, relative to the saturation temperature of FC-72, is required before boiling occurs and, similar to the water experiments, a decrease in wire temperature is observed after boiling begins for experiments at low FC-72 volume fraction. However, unlike the water experiments the temperature drop does not occur immediately, but instead decreases gradually as the heat flux is increased. Although the wire temperatures become greater than the saturation temperature of water, no significant change in the heat transfer data is observed near or above 100 °C that would indicate that water suddenly begins participating in the boiling process. Finally, the wire temperature shows much less unsteadiness during boiling than in the water experiments.

The experiments performed at 0.1 % FC-72 volume fraction appear to be anomalous in several ways. The degree of superheat required for boiling to begin for the low T_∞ case is the highest observed in any of the FC-72 experiments. It is also much higher than for the high T_∞ case, which is opposite the trend observed at other FC-72 volume fractions. Boiling in the high T_∞ case occurs at a lower temperature than all other experiments, but at high heat flux the surface temperature suddenly increases to near that of boiling water.

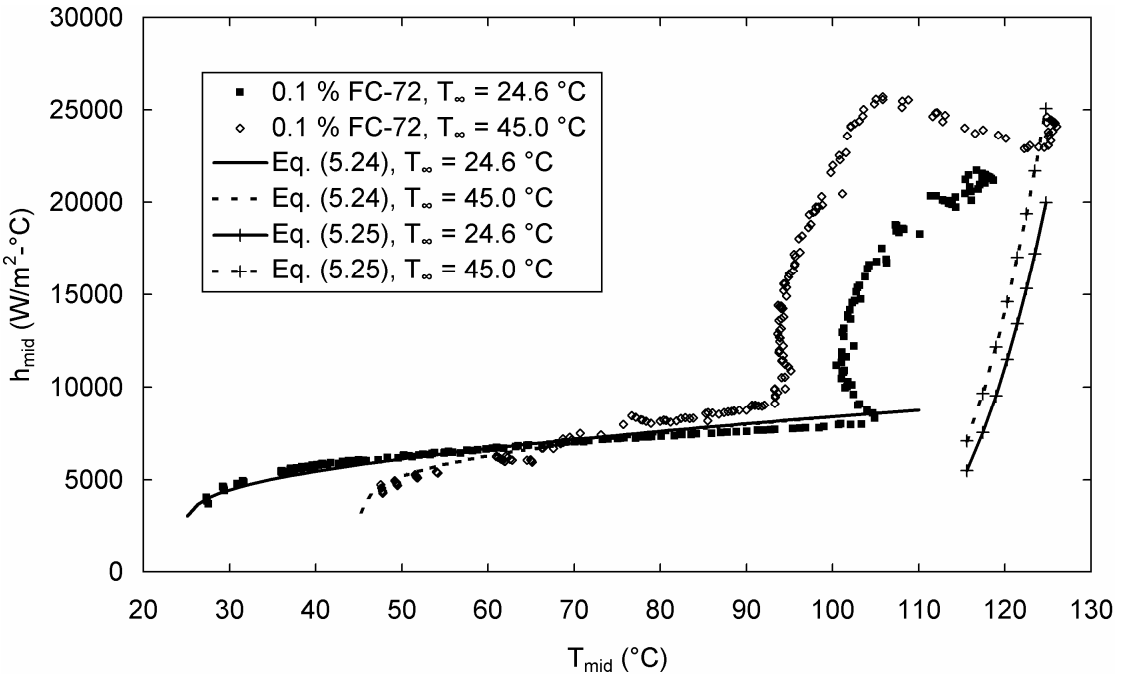

(a)

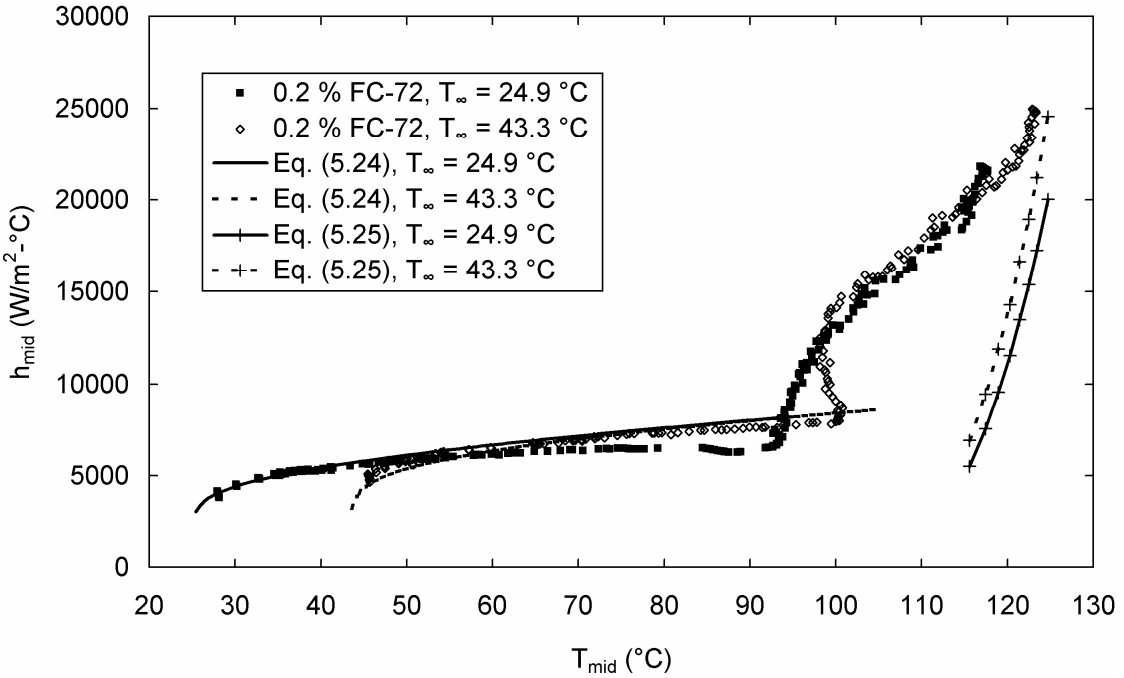

(b)

Figure 5.8. Free convection heat transfer coefficient for heated horizontal wire in emulsions of FC-72 in water with (a) 0.1%, (b) 0.2%, (c) 0.5%, and (d) 1.0% FC-72 by volume.

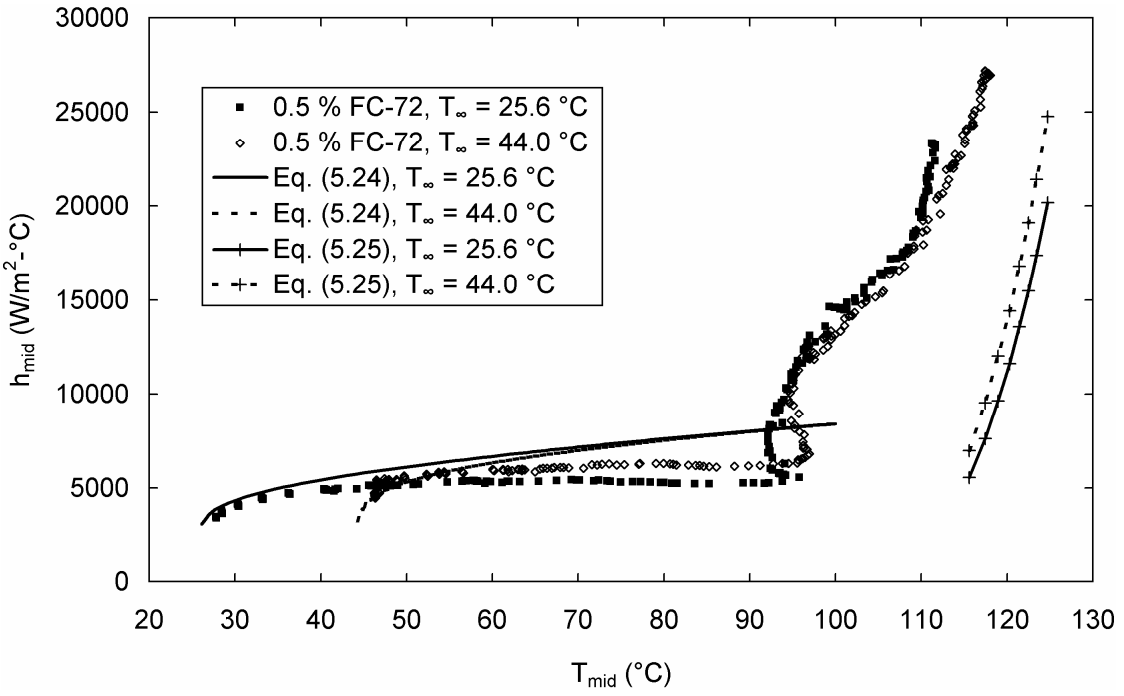

(c)

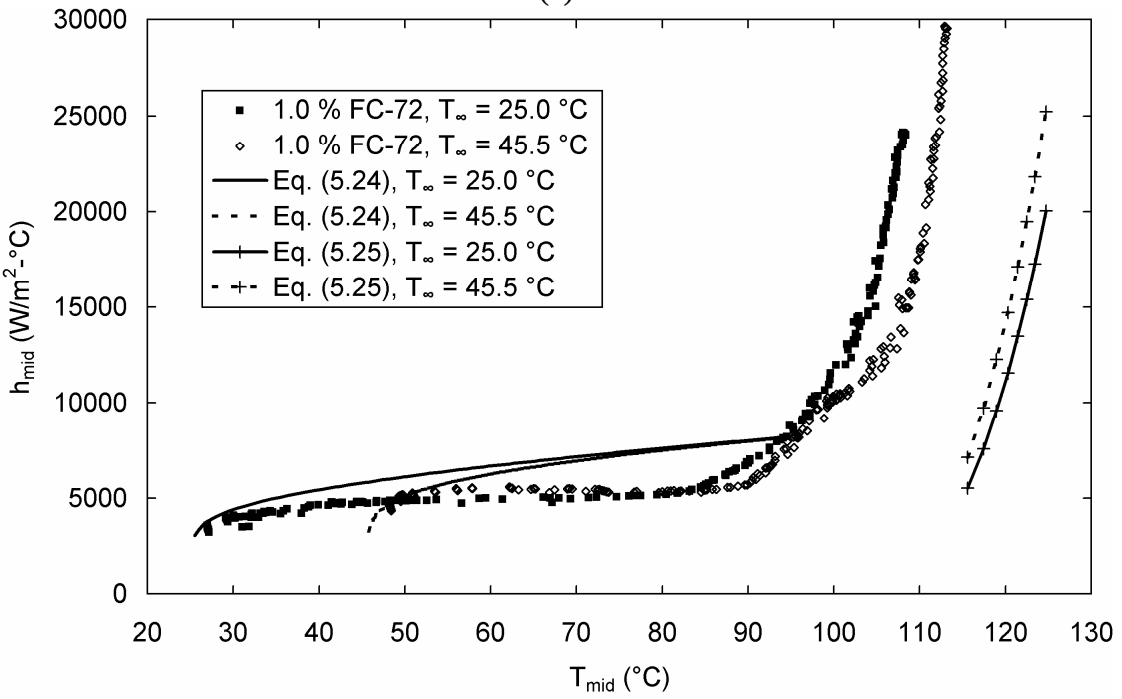

(d)

Figure 5.8. continued.

5.6.3. Pentane in water emulsions

It was observed in the FC-72 in water emulsion experiments that the wire temperature must be close to 100 °C before boiling of the emulsion occurs. Much of the boiling curves in Fig. 5.8 then lie above the saturation temperature of water, and it is somewhat unclear to what extent the water participates in boiling. To address this question a second set of experiments was performed using emulsions of pentane in water. Pentane has a saturation temperature of 35.9 °C at atmospheric pressure, approximately twenty degrees cooler than FC-72. Emulsions of pentane in water should therefore boil at a lower temperature as well, so that behavior that is unambiguously due to the boiling of the pentane alone can be observed.

A new power supply was used for the pentane in water emulsion experiments. The new supply provided a higher voltage than the original (12V rather than 5V), which enabled this set of experiments to proceed to higher surface heat flux than the water and FC-72 in water experiments (7.5 MW/m^2 vs. 2 MW/m^2). In some experiments the critical heat flux was still not achieved.

Figure 5.9 shows the boiling curves for pentane in water emulsions with four different volume fractions of pentane. As expected, boiling begins at surface temperatures between 75 and 90 °C, approximately twenty degrees lower than for the FC-72 in water emulsions. Just as in the FC-72 in water emulsions, the heat transfer coefficient for single phase free convection decreases with increasing pentane volume fraction. In all cases boiling occurs at a lower temperature than in water, and at high heat flux (~5 MW/m^2) the wire temperatures for the 0.1, 0.2, and 0.5% pentane emulsions approach the same curve, approximately 15 °C below the temperature predicted by Eq. (5.25). This behavior is not observed in the 1% pentane experiment because burnout of the wire occurs at a heat flux of 4 MW/m^2. For the 0.5% pentane experiment burnout occurs at 6.2 MW/m^2, and for the 0.2% pentane experiment it occurs at 7.2 MW/m^2. In the 0.1% pentane experiment a maximum heat flux of 7.7 MW/m^2 is achieved (at the maximum current that the power supply can provide) without reaching the critical heat flux. There is a clear trend towards decreasing critical heat flux with increasing pentane volume fraction.

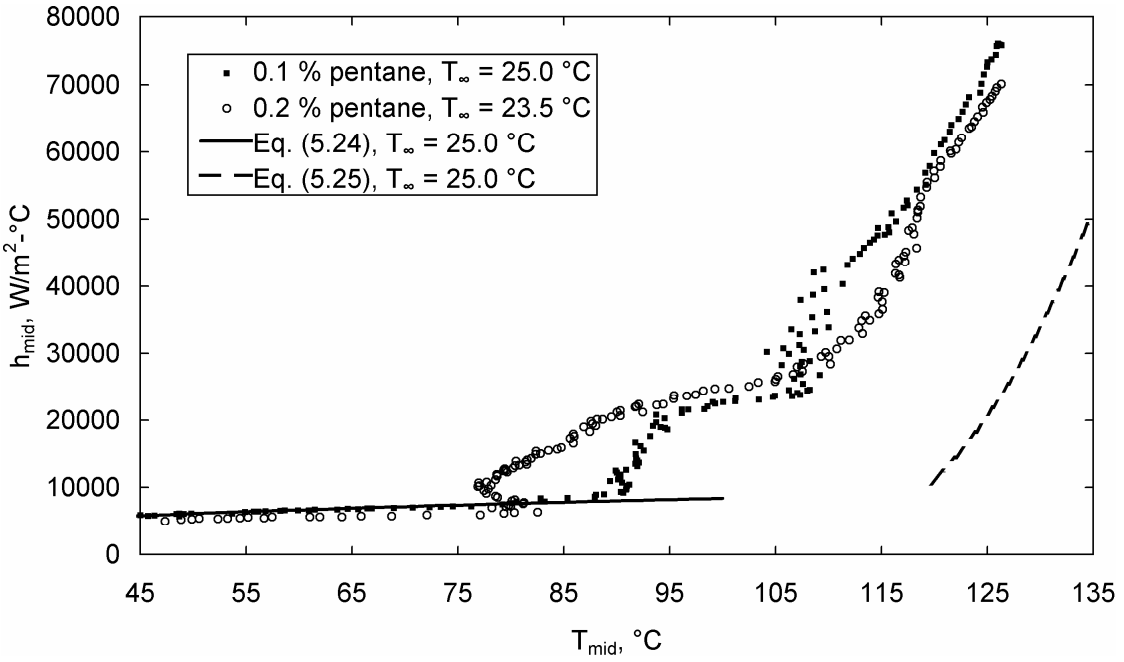

(a)

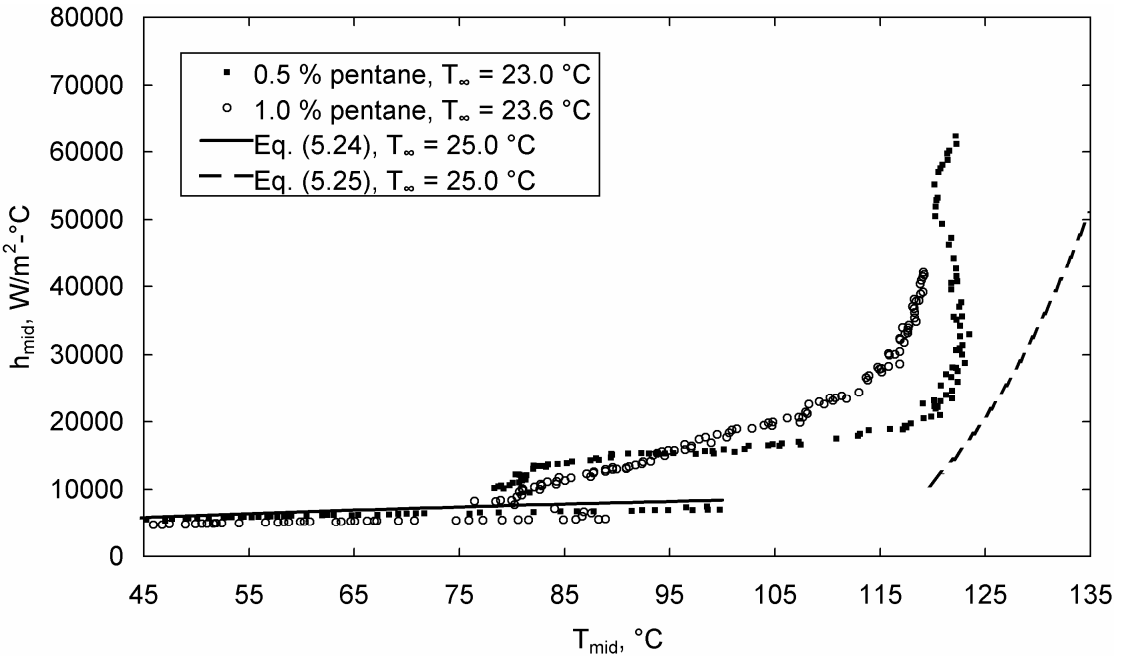

(b)

Figure 5.9. Free convection heat transfer coefficient for heated horizontal wire in emulsion of pentane in water with (a) 0.1% and 0.2%, and (b) 0.5% and 1.0% pentane by volume. Eq. (5.24) and (5.25) computed using values for water.

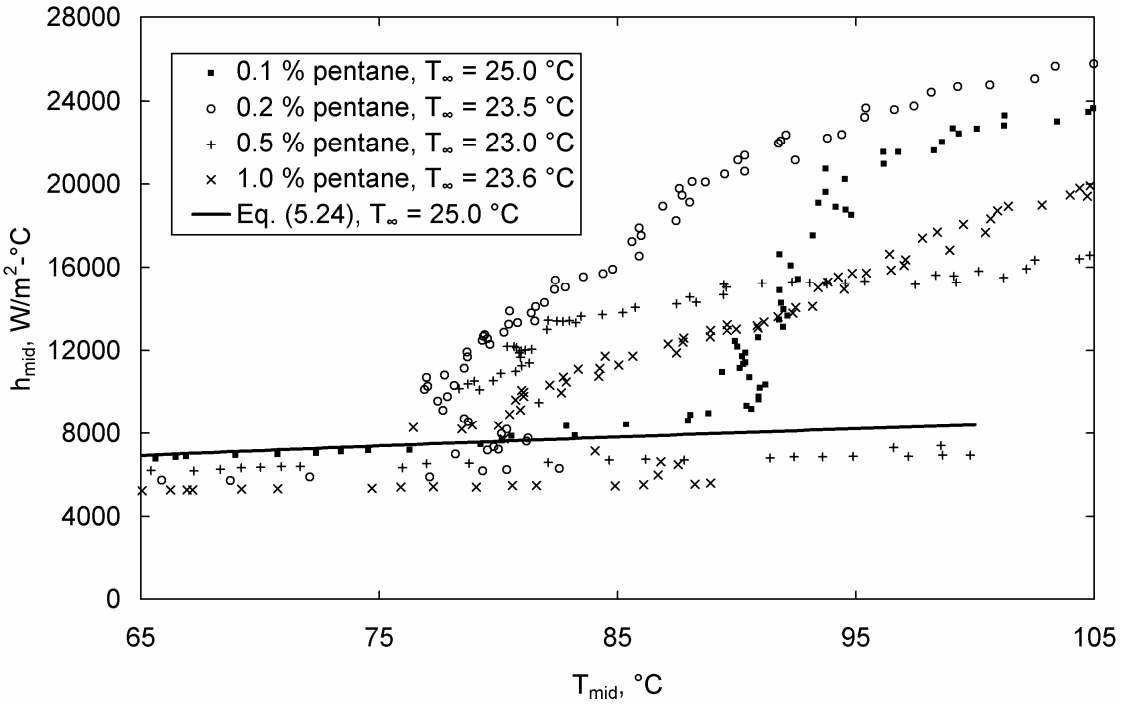

Figure 5.10. Boiling heat transfer coefficient for heated horizontal wire in emulsion of pentane in water. Eq. (5.24) computed using properties of water.

For the 0.2, 0.5, and 1.0% pentane experiments, a temperature overshoot is observed before boiling begins. For the 0.2% case, after boiling begins the wire temperature decreases gradually as heat flux increases, which is similar to the behavior of the FC-72 in water emulsions. For the 0.5 and 1.0% cases the temperature overshoot is larger and the decrease in temperature when boiling begins is abrupt, which is closer to the behavior observed in the water experiments. The temperature overshoot in the 0.5% cases is especially large, and it appears that the wire surface temperature reaching the saturation temperature of water is the trigger that initiates boiling of the pentane.

If the portions of Fig. 5.9 in which only pentane boils are examined more closely (Fig. 5.10), some similarities to the experimental data of Bulanov et al. become apparent. The boiling heat transfer coefficient increases linearly with surface temperature or exhibits some downward curvature, similar to Figs. 2.10 and 2.11. The data in this study has more scatter between adjacent data points in each experiment than that of Bulanov et al. However, in this study many more data points are reported as well. It may be that each data point in Figs. 2.7 – 11 represents an averaged value of a

sequence of several individual measurements. Unlike Fig. 2.8, in this study there is no clear trend in heat transfer coefficient vs. pentane volume fraction. Of course, the fluid combinations used in this study are different from those investigated by Bulanov et al., and other experimental conditions differ as well, so identical results are not expected.

5.7. Visualization

In addition to the experiments described in the previous section, a series of experiments were performed while recording images of the heated wire using a digital video camera. The camera used was model number EO-1312M manufactured by Edmund Optics with a Navitar Zoom 7000 macro zoom lens. With this combination a minimum resolution of 4.5 μm per pixel can be achieved.

The EO-1312M camera is not meant for use as a high-speed camera. The camera records images at 30 frames per second. Although the exposure time of the image sensor in the camera can be set as low as 20 μs, the sensor achieves this exposure time with an electronic rolling shutter. A rolling shutter means that the entire image sensor does not record an image at the same time. Instead, a certain number of rows of pixels in the sensor are exposed ahead of the row currently being read out of the sensor. The exposed area rolls down the sensor as rows of pixels are progressively read out of the sensor and transmitted to the attached computer. At the fastest possible pixel clock, which was used in this study, one row of pixels is read every 20 μs, so the exposure time can be set in multiples of 20 μs. Exposure times were chosen to be as short as possible while still allowing the image sensor to collect enough light to resolve features in the flow, and were typically between 100 and 400 μs. The rolling shutter leads to image artifacts when fast-moving objects are recorded. These artifacts will be discussed in further detail when they are encountered in the following sections.

These limitations of the camera system – the limited resolution and the rolling shutter – also somewhat limit the utility of the camera in this application. The camera is unable to resolve individual droplets or their boiling, so direct visual evidence of the boiling model presented in Chapter 3 is not easily obtained. However, the camera is capable of capturing larger and slower-moving features, which are discussed in the following sections.

5.7.1. Boiling water

In Fig. 5.11 several images of the heated wire are presented that were recorded during a boiling water experiment. The boiling curve for the same experiment is shown in Fig. 5.12 and the points at which the images were recorded are noted. For this experiment there was little contrast between bubbles in the field of view and the dark background, so the contrast of the images in Fig. 5.11 was enhanced. The increased contrast causes the grainy appearance of some images and lack of detail in the wire itself, which was bright enough to wash out the sensor. The small bright circle at the center of each bubble is a reflection of the light source.

The heat transfer behavior of the heated wire in this experiment is quite similar to the other water experiments reported in Section 5.6.1. As before, the heat transfer coefficient in the single phase region is slightly higher than predicted by Eq. (5.24) and the boiling heat transfer coefficient is quite close to Eq. (5.25). The only notable difference is that a smaller degree of superheat is required before boiling begins. In this experiment the wire reaches only 125 °C before boiling begins, rather than 140 °C as observed in the earlier experiments. The reason for this difference may be that the water used in this experiment was handled somewhat more after being degassed and before the experiment began. The water, therefore, may have reabsorbed some air before the experiment, and this may have promoted nucleation on the wire due to desorption of the air on the wire surface.

The first sign of boiling in the heat transfer data is a sudden increase in the heat transfer coefficient above the value predicted by Eq. 5.24, which corresponds to the sudden appearance of bubbles on the heated wire (Fig 5.11b). Before this point there is no visible activity on the heated wire (Fig. 5.11a). The bubbles initially remain attached to the heated wire and are steady. As the heat flux dissipated by the wire increases, the bubbles grow larger and some begin to detach from the wire (Fig. 5.11c). The bubbles depart from the wire with increasing frequency with increasing heat flux.

At higher heat flux (> 1.7 MW/m^2) the vapor bubbles grow quickly enough that some artifacts become visible in the images. In Fig. 5.11d, a portion of a bubble is visible that formed while the image was being recorded. In this experiment, the camera

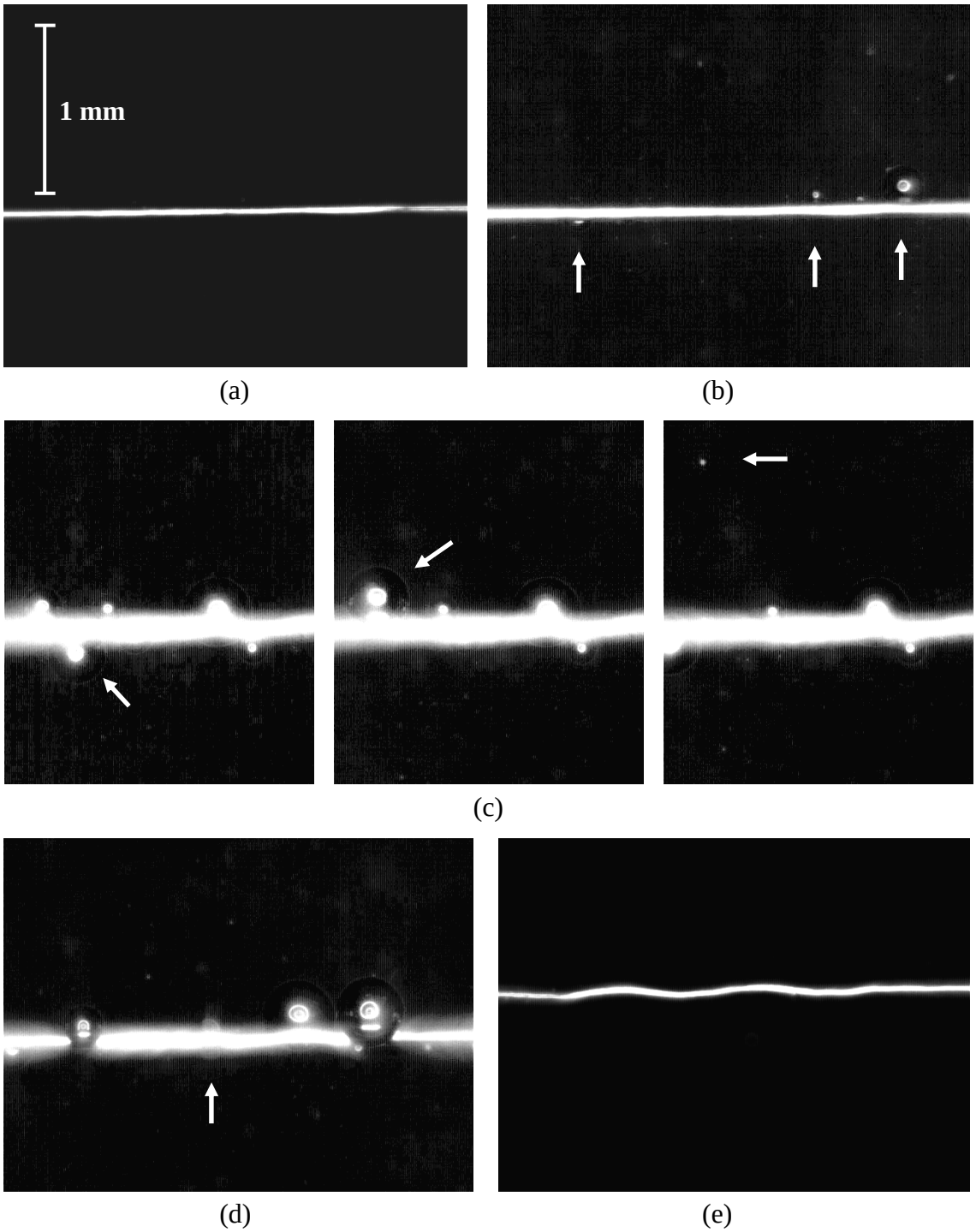

Figure 5.11. Images of heated wire during boiling in water. (a), wire in single-phase region. (b), wire at onset of boiling, arrows denote bubbles attached to wire. (c), sequence of three frames showing bubble departure near left edge of frame. (d) and (e), image artifacts caused by rapid bubble motion and vibration of wire.

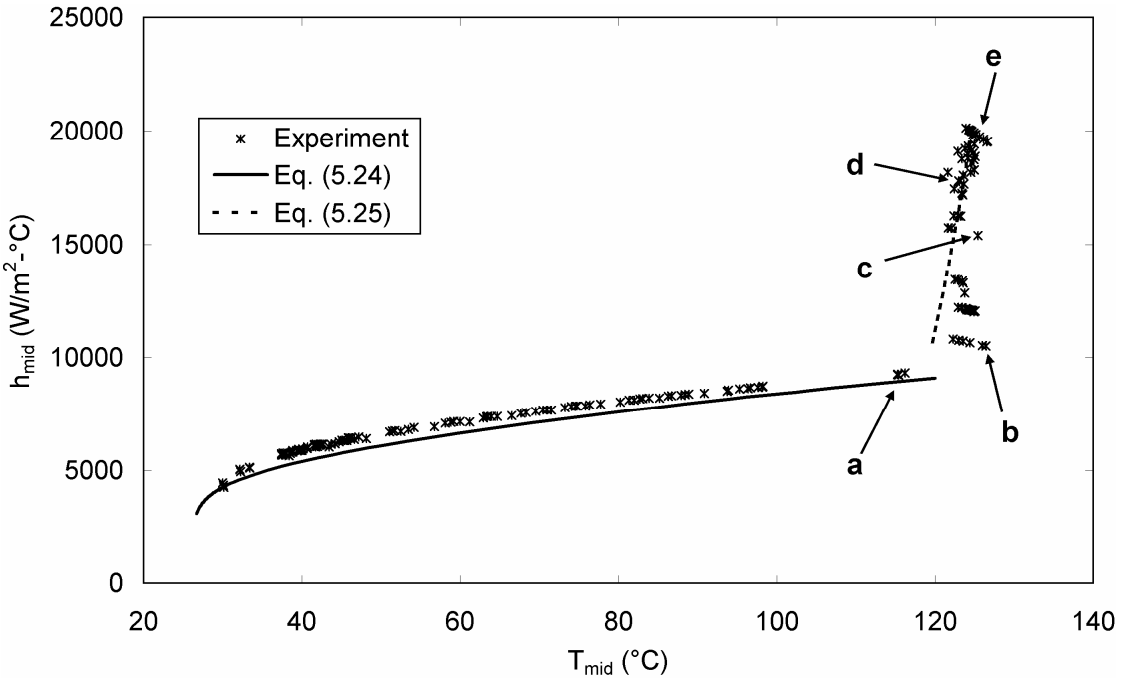

Figure 5.12. Free convection heat transfer coefficient from heated wire to water, T_∞ = 26.2 °C. Letters denote images in Fig. 5.11.

was oriented such that the image sensor scanned rows of pixels left-to-right. Similar artifacts show in most other images. As heat flux approaches 2 MW/m^2 the wire begins to vibrate intermittently, probably due to the rapid growth of bubbles on the wire and their subsequent collapse after they travel into the sub-cooled liquid outside the thermal boundary layer. The vibration of the wire manifests as waviness in the recorded images (Fig. 5.11e). The wire vibrates at approximately 270 Hz with a maximum magnitude of ~45 μm. The vibration does not have any apparent effect on the heat transfer from the wire.

5.7.2. FC-72 in water emulsion, 0.1% FC-72

Figure 5.13 shows several images of boiling on the heated wire in an emulsion of 0.1% FC-72 by volume in water. Figure 5.14 is the boiling curve for the same experiment. The bulk temperature of the emulsion was 35 °C. This temperature was chosen to bisect the temperatures of the emulsions in Fig. 5.8a, and the heat transfer coefficient generally does fall between the two earlier experiments. In particular,

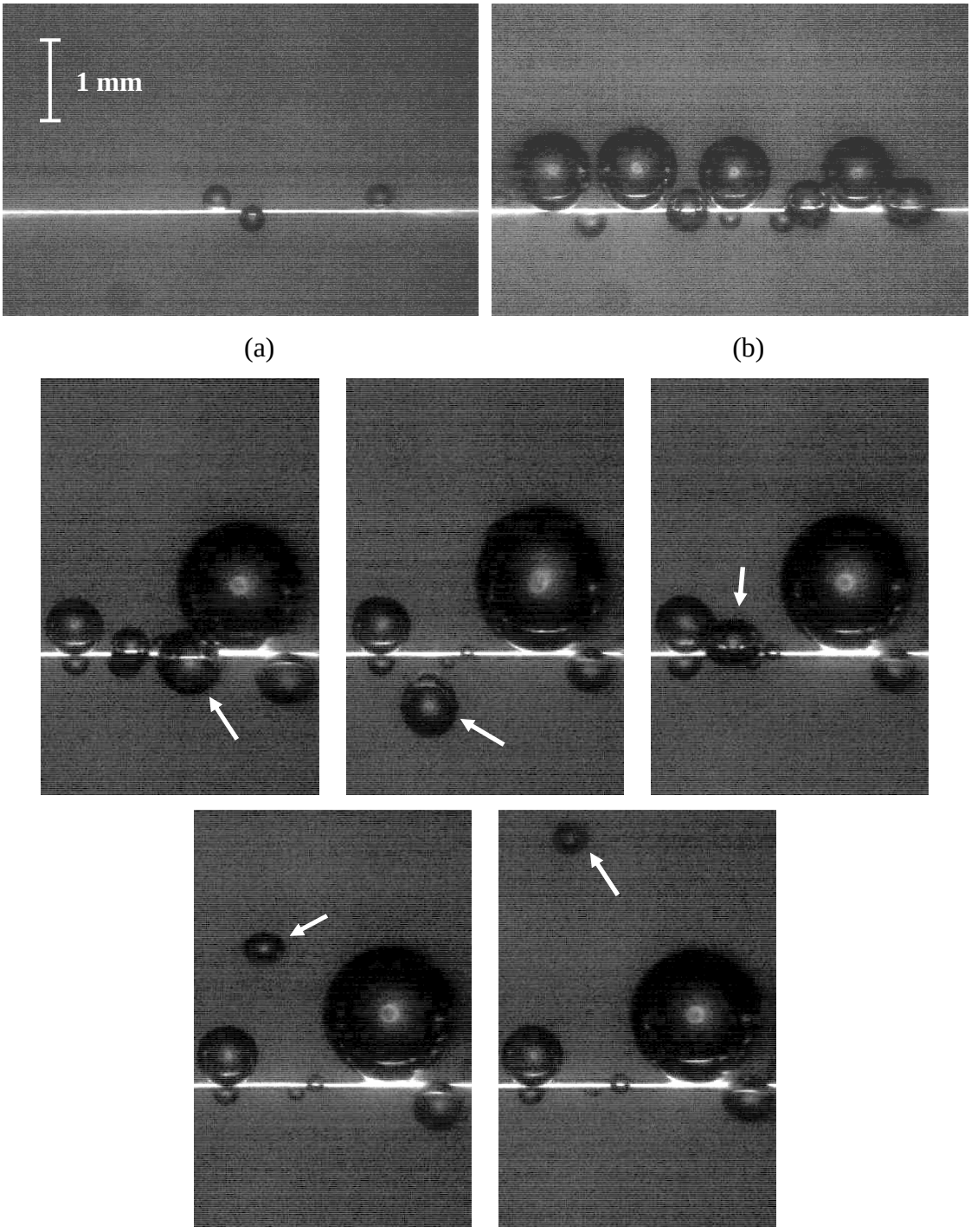

Figure 5.13. Images of heated wire during boiling in FC-72 in water emulsion, 0.1% FC-72 by volume. (a), onset of boiling. (b), attached bubbles at higher heat flux. (c), rapid bubble detachment. (d), boiling at high heat flux, average bubble rise velocity is 0.0087 m/s.

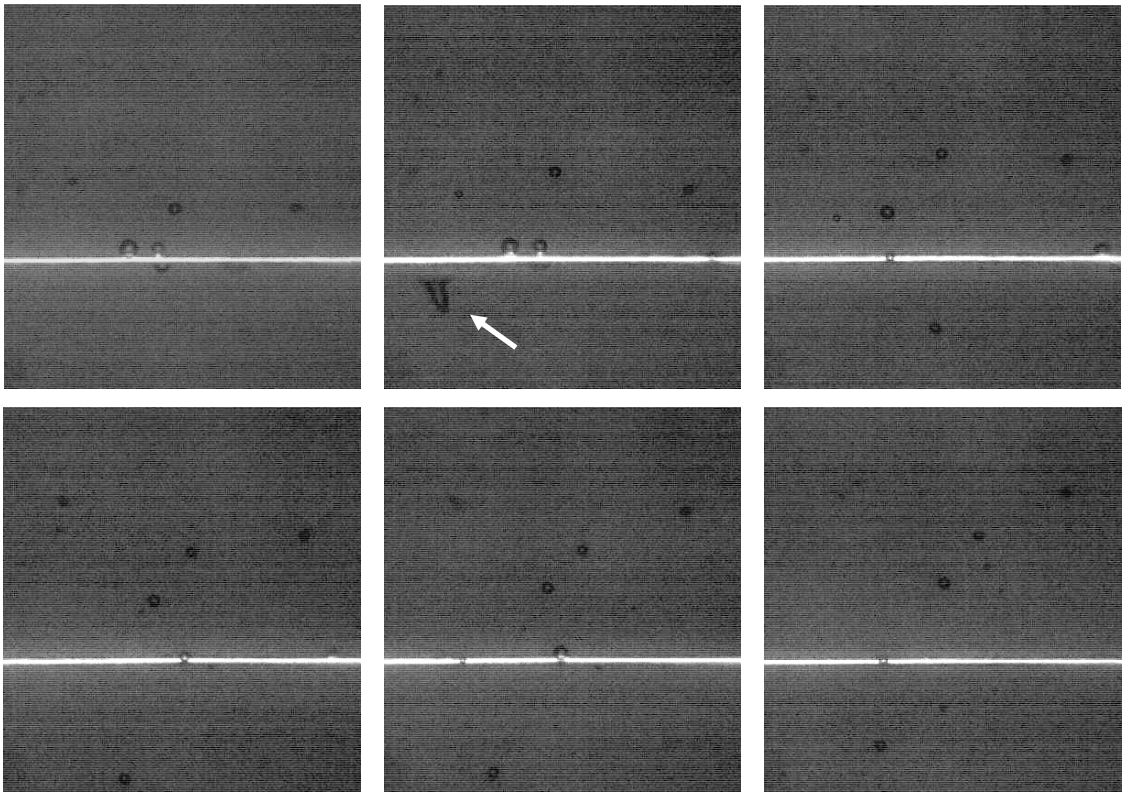

(d)

Figure 5.13 continued.

the rather sudden increase in surface temperature at high heat flux observed in the T_∞ = 45 °C case also occurs here but is less significant.

The images recorded in this experiment bear many similarities to those recorded of boiling water. Bubbles first become visible on the heated wire at the same time that the heat transfer data shows the first sign of boiling (Fig. 5.13a). As heat flux increases more bubbles form, grow larger (Fig 5.13b), and detach from the wire with increasing frequency. One interesting behavior observed in this experiment is that some bubbles depart the wire with significant velocity. Figure 5.13c shows a bubble, initially attached to the near side of the wire, departing from the wire and initially travelling downwards before rising in front of the wire due to buoyancy. The bubble also shrinks visibly due to condensation as it rises out of the frame. This rapid departure of bubbles from the wire is likely responsible for the vibration in the wire noted in Fig. 5.11e.

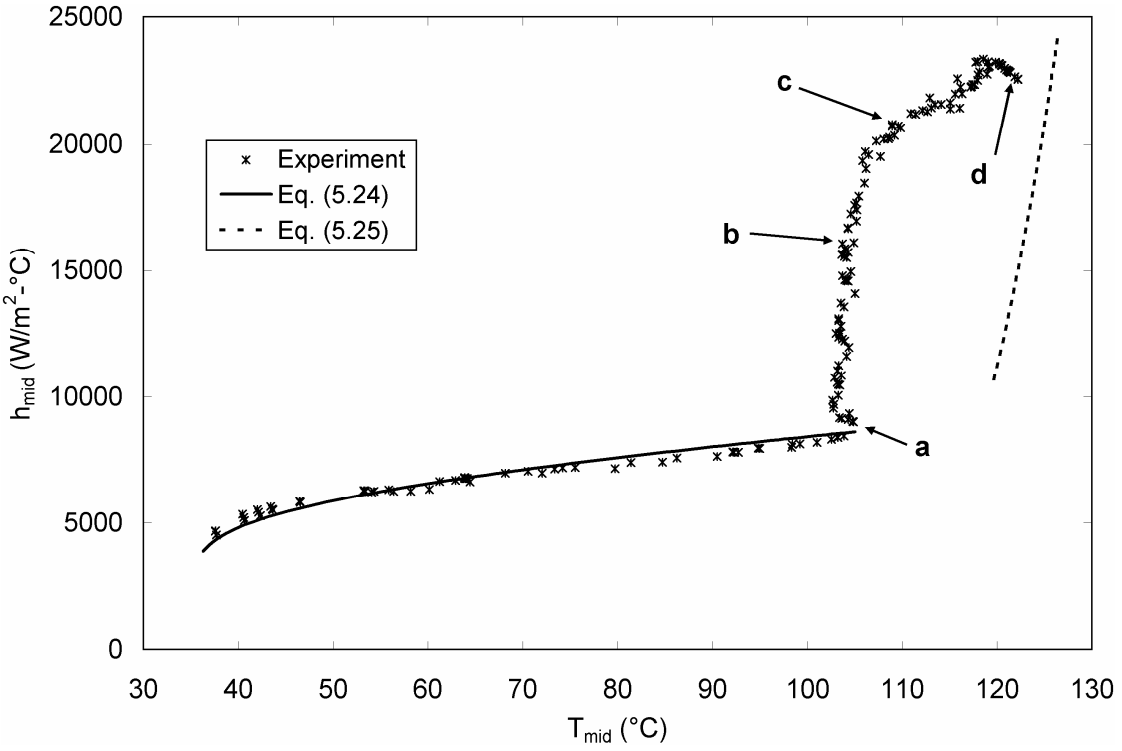

Figure 5.14. Heat transfer coefficient for heated wire to FC-72 in water emulsion, 0.1% FC-72 by volume, T_∞ = 35 °C. Letters denote images in Fig. 5.13. Correlations are calculated for water.

At high heat flux the bubbles that nucleate on the heated wire detach at a much smaller diameter than at lower heat flux (Fig. 5.13d). Due to the high temperature of the wire it is not clear whether the bubbles that nucleate on the wire are FC-72 or water. The detached bubbles visible in Fig. 5.13d have $50 < d_b < 100$ μm, and so could be the result of boiling of individual FC-72 droplets with $10 < d_d < 20$ μm. However, as is seen in the second frame of Fig. 5.13d, some bubbles that nucleate on the wire surface are still propelled downwards from the wire, so the dispersed bubbles seen throughout the frame could be the result of this process instead. (The elongation of the bubble in the second frame is an artifact of the rolling shutter in the image sensor. For this experiment the sensor was oriented such that rows of pixels were recorded top-to-bottom.) In either case, it seems likely that processes are occurring that are too small or too fast for the camera to capture, for the small number of bubbles observed in Fig. 5.13d could not be responsible for such a large change in the heat transfer coefficient.

5.7.3. FC-72 in water emulsion, 0.2% FC-72

Some images of boiling of an emulsion of 0.2% FC-72 in water are shown in Fig. 5.15. Because the opacity of these emulsions increases with the volume fraction of the dispersed component, these images of the 0.2% FC-72 emulsion could only be obtained by moving the heated wire very close to the wall of the test chamber closest to the camera. The proximity of the wall to the heated wire affects the heat transfer data and eventually the wire becomes obscured by bubbles that stick to the wall. However, some observations of boiling at moderate heat flux were made.

As in the previous two experiments, the first appearance of bubbles on the heated wire coincided with the onset of boiling. A unique behavior observed here is that the bubbles did not have steady diameter. In the previous experiments bubbles that formed on the wire soon after boiling began had steady size that increased with the heat flux. In this case, although the trend of increasing bubble size with heat flux held, the bubbles always fluctuated in size as well (Fig. 5.15a). At higher heat flux the bubbles began to detach from the wire with increasing frequency, as in previous experiments. The opacity of the emulsion made observation of the bubbles after departing from the wire impossible, however. In Fig. 5.15b two small bubbles can be observed as they pass in front of the wire but are not visible in either of the preceding or following frames. Thus it is impossible to determine what other boiling behavior may be occurring in the vicinity of the wire. At high heat flux vibration of the wire is observed at ~250 Hz, similar to the boiling water experiment.

5.7.4. Pentane in water emulsion, 0.1% pentane

Figure 5.16 shows several images of the heated wire during boiling of an emulsion of pentane in water with 0.1% pentane by volume. The images are placed in context with the heat transfer data in Fig. 5.17. The emulsions of pentane were generally less cloudy than the emulsions of FC-72, possibly due to the closer match of index of refraction between pentane and water than between FC-72 and water. (At 20 °C the indexes of refraction of water, FC-72, and pentane are 1.333, 1.251, and 1.357, respectively.)

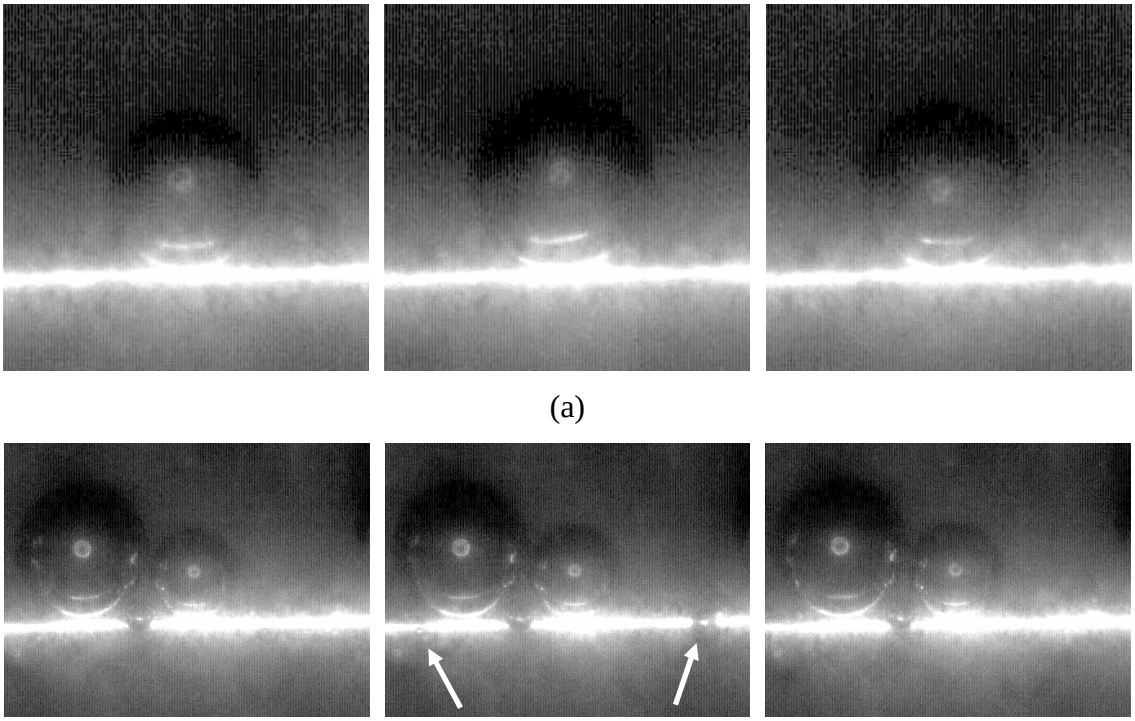

(a)

(b)

Figure 5.15 Images of heated wire during boiling in 0.2% FC-72 in water emulsion. (a), unsteady bubble at low heat flux, field of view is 1 x 1 mm. (b) rapid boiling, field of view is 2 x 1.5 mm.

Many of the behaviors observed in the 0.1 % pentane in water emulsion are similar to those of the 0.1 % FC-72 in water emulsion. The first bubbles become visible on the heated wire at the onset of boiling (Fig. 5.16a). As the heat flux increases, the bubbles grow larger and more bubbles form (Fig. 5.16b). Some oscillation in the size of these large bubbles is observed, but at a lower frequency than was observed in the 0.2 % FC-72 in water experiment (Fig. 5.15a). As the heat flux increases further the bubbles begin to depart from the wire. Bubbles depart with increasing frequency and at smaller sizes as the heat flux increases (Fig. 5.16c). At intermediate heat flux the wire temperature is observed to fluctuate by several degrees around 108 °C with a period of a few seconds. While this temperature fluctuation occurs it is observed that many small bubbles form on the wire and then depart simultaneously (Fig. 5.16d). The temperature fluctuations cease when the bubbles start to depart from the wire individually rather than all at once (Fig. 5.16e).

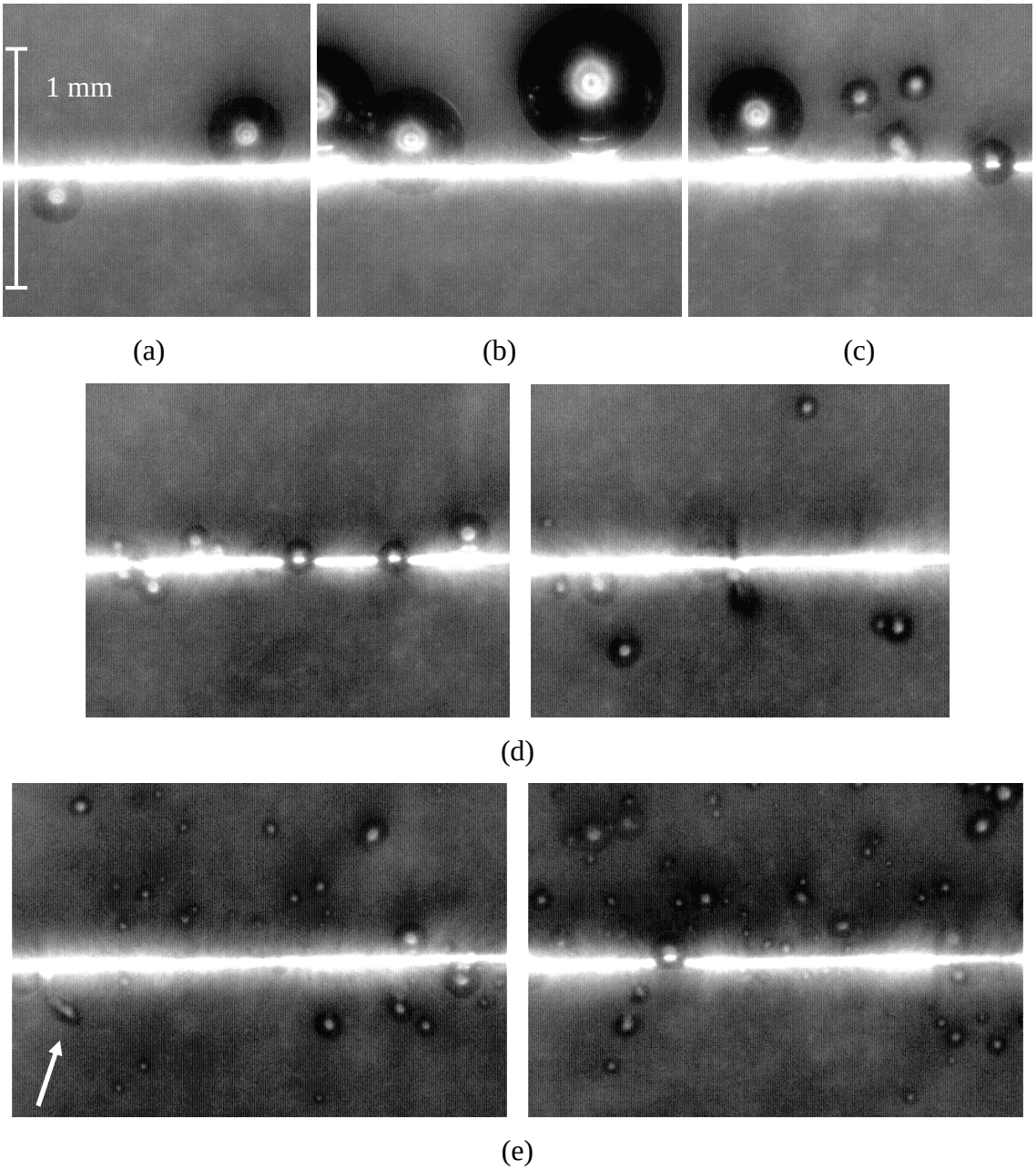

Figure 5.16. Images of heated wire during boiling in 0.1% pentane in water emulsion. (a) and (b), large bubbles attached to wire. (c), departure of bubbles at higher heat flux. (d), simultaneous departure of bubbles, average bubble rise velocity is 0.0076 m/s. (e), boiling at high heat flux, average bubble rise velocity is 0.012 m/s.

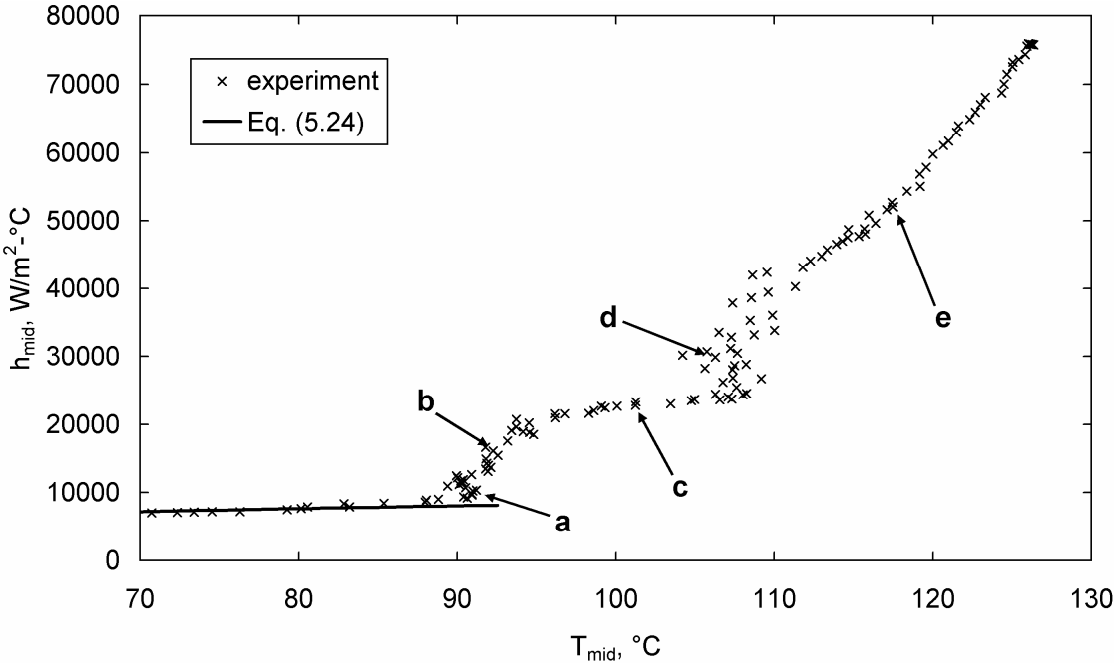

Figure 5.17. Heat transfer coefficient for heated horizontal wire in pentane in water emulsion, 0.1% pentane by volume, T_∞ = 25 °C. Letters denote images in Fig. 5.16. Equation (5.24) calculated using properties of water.

At high heat flux (q" > 4 MW/m^2) bubbles with 25 < d_b < 200 μm can be observed attached to the wire as well as in the liquid surrounding it (Fig. 5.16e). The smallest visible bubbles, if they contain only pentane, contain the same amount of pentane as a droplet with d_d = 5 μm and therefore could be the result of individual droplets boiling. At the high surface temperatures that accompany these conditions, however, the bubbles could also contain steam. On the other hand, the water in the emulsion is subcooled to such a great extent (~75 °C) that it seems unlikely that steam bubbles could exist at any great distance from the wire. The visual data is certainly ambiguous. Some bubbles are observed below the heated wire in Fig. 5.16e, but a bubble can also be observed in the lower-left corner of the first frame moving downwards rapidly, so the bubbles below the wire could all be due to bubble being propelled off of the wire downwards as was observed in the FC-72 in water emulsions (Fig. 5.13d).

5.7.5. Pentane in water emulsion, 0.2%

Figures 5.18 and 5.19 show several images of the heated wire and heat transfer data for boiling in an emulsion of 0.2% pentane in water. The behaviors observed in this

experiment were generally similar to the previous experiments. The large bubbles that formed on the wire at the inception of boiling tended to grow and shrink erratically, similar to the 0.2% FC-72 in water emulsion, but at a slower rate. In addition, small bubbles continually formed and collapsed again on the heated wire (Fig. 5.18a). It is not known whether the bubbles collapsed entirely or merely became too small to observe against the heated wire. The disappearance of the bubbles could not be caused by their departure, for the velocity of the emulsion was not high enough to transport the bubbles out of the field of view between frames.

As the heat flux increased, bubbles began to depart from the heated wire at increasing frequency and at smaller diameters. In some cases bubbles apparently briefly formed small clusters without coalescing (Fig. 5.18b, c). At high heat flux the emulsion near the heated wire appears similar to the 0.1% pentane experiment (Fig. 5.18e), although the number density of bubbles is higher, which is to be expected if the bubbles form from pentane droplets. The range of bubble sizes in Fig. 5.18e is essentially the same as in Fig. 5.16e.

5.8. Discussion

The wide range of behaviors of the emulsions described in the previous sections defies easy, detailed explanation. However, some trends in the data can be identified that lend some insight into the physical processes that occur in heat transfer to dilute emulsions.

5.8.1. Single phase behavior

In the single phase portion of the experiments it is apparent that the presence of the dispersed component hinders natural convection heat transfer significantly. As Fig. 5.20 illustrates, there is a trend towards lower heat transfer coefficient with increasing disperse phase volume fraction, although there is some scatter in the data for pentane in water emulsions. Some decrease in the heat transfer rate is expected because pentane and FC-72 both have much lower thermal conductivity than water (at 25 °C, k = 0.595, 0.117, and 0.056 W/m-°C for water, pentane, and FC-72 respectively). However, according to the effective medium theory of Maxwell (1904), at a dispersed phase volume fraction of 1% the effective conductivity of the emulsion should be no more

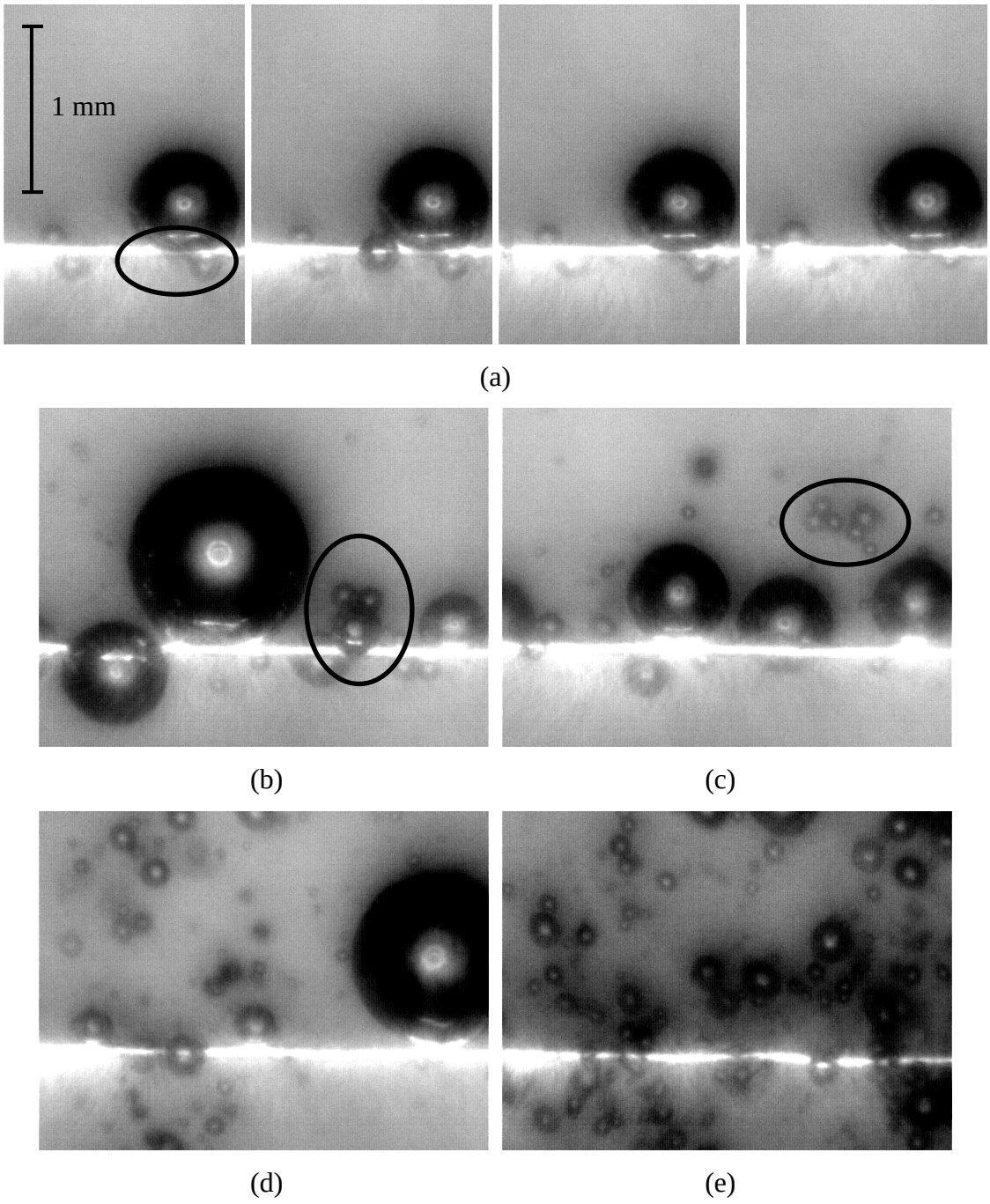

Figure 5.18. Images of heated wire during boiling in pentane in water emulsion, 0.2 % pentane by volume. (a), onset of boiling. (b) – (e), boiling at increasing heat flux. Average rise velocity of bubbles is (b) 0.0052 m/s, (c) 0.0065 m/s, (d) 0.0086 m/s.

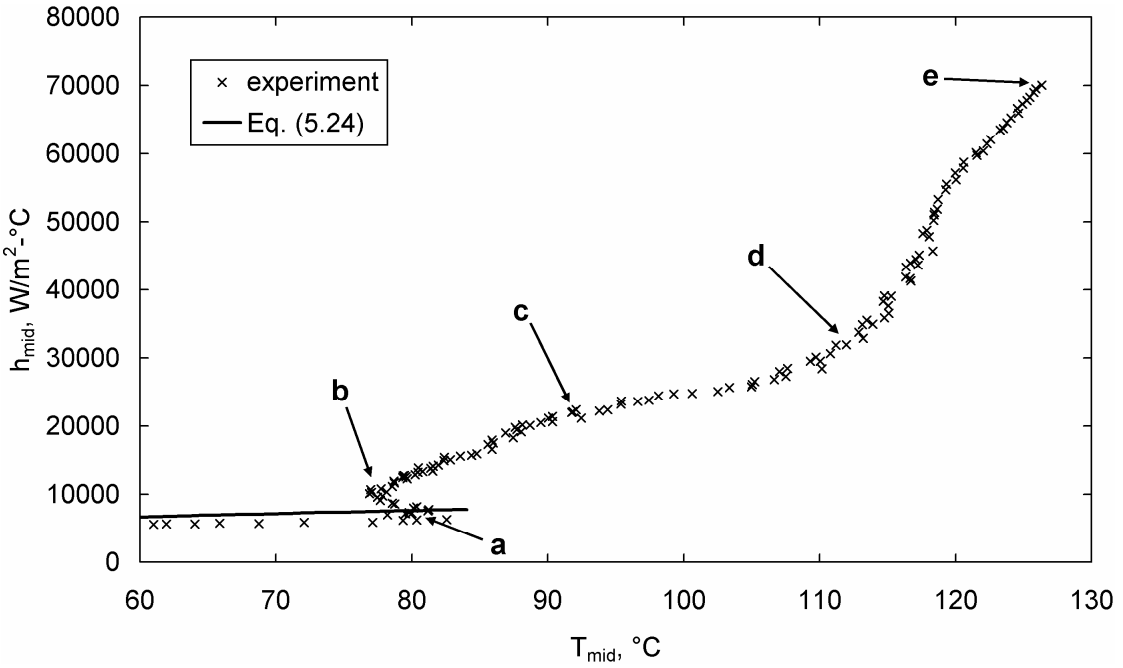

Figure 5.19. Heat transfer coefficient for heated horizontal wire in pentane in water emulsion, 0.2% pentane by volume, T_∞ = 23.5 °C. Letters denote images in Fig. 5.19. Equation (5.24) calculated using properties of water.

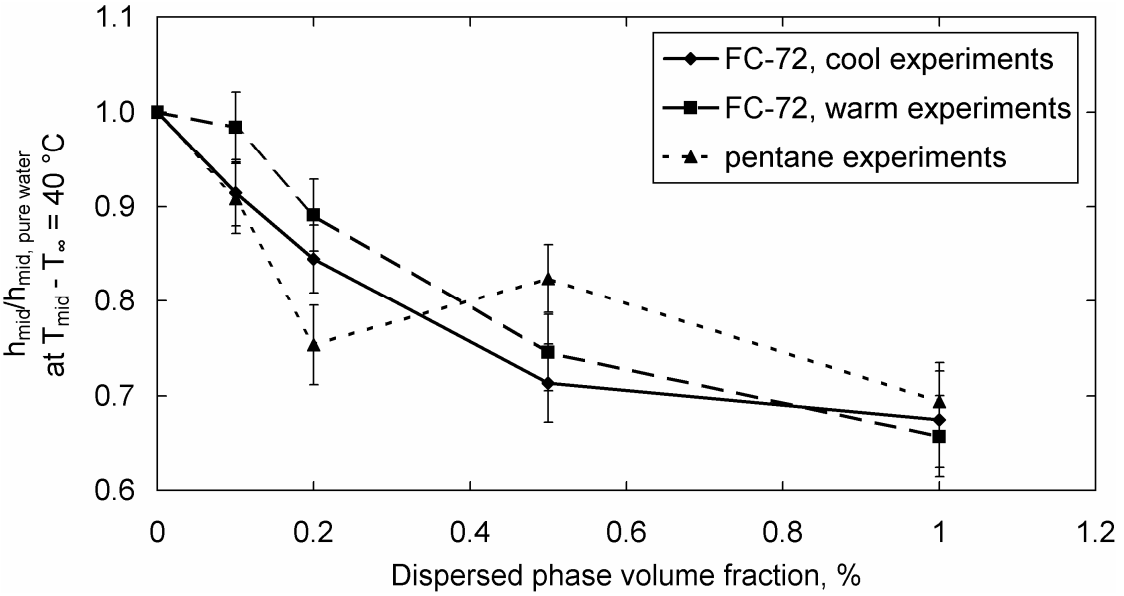

Figure 5.20. Decrease in single-phase free convection heat transfer coefficient for emulsions.

than 1.5% lower, even if the dispersed phase is a perfect insulator. The effect of the dispersed component on the viscosity of the mixture is similarly small (Taylor, 1932). The large decrease in the single-phase heat transfer coefficient, then, is strong evidence that droplets of the dispersed component collect on the surface of the heated wire. If the dispersed liquid forms a uniform layer on the wire surface, the layer need only be a few microns thick to cause the observed decrease in heat transfer. It is not possible to determine, with the instruments used in this study, how much of the surface of the wire is covered or whether the droplets coalesce into a continuous layer of liquid on the wire.

5.8.2. Dispersed component boiling vs. enhanced continuous component boiling

As noted in Section 5.6.3, emulsions of FC-72 in water are observed to begin boiling close to the saturation temperature of water, so that it is difficult to separate the effects of boiling FC-72 droplets alone from evaporation of the water. In contrast, the boiling curves for emulsions of pentane in water have two distinct regions. At surface temperatures below ~105 °C only the pentane is boiling and the boiling curves show similar behavior to that reported by Bulanov et al. (Fig. 5.10). At higher surface temperatures it is likely that the water boils as well, which is enhanced by the presence of pentane bubbles. For the 0.1, 0.2, and 0.5% volume fraction cases there is a distinct jump in surface temperature between these two regions.

5.8.3. Similarity in the dispersed component boiling regime for FC-72 and pentane

Having noted the two distinct boiling regimes for pentane in water emulsions, it is reasonable to return to the FC-72 emulsion data and look for similarities. Figure 5.21 compares the pentane emulsion and FC-72 emulsion boiling curves as a function of the degree of superheat of the dispersed component. The figure contains the warm FC-72 runs only, as the degree of subcooling of the dispersed component in those experiments was similar to that of the pentane emulsion experiments. When compared on this basis, the boiling curves for 0.2, 0.5, and 1.0% dispersed component volume fraction emulsions in the $40 < T_{mid} - T_{sat} < 50$ °C range are remarkably similar. The only exception is the 0.1% case, in which the behavior of the FC-72 in water emulsion has already been noted as being anomalous. The boiling curves are expected to diverge for $T_{mid} - T_{sat} > 50$ °C because, for the FC-72 in water emulsions, this temperature range

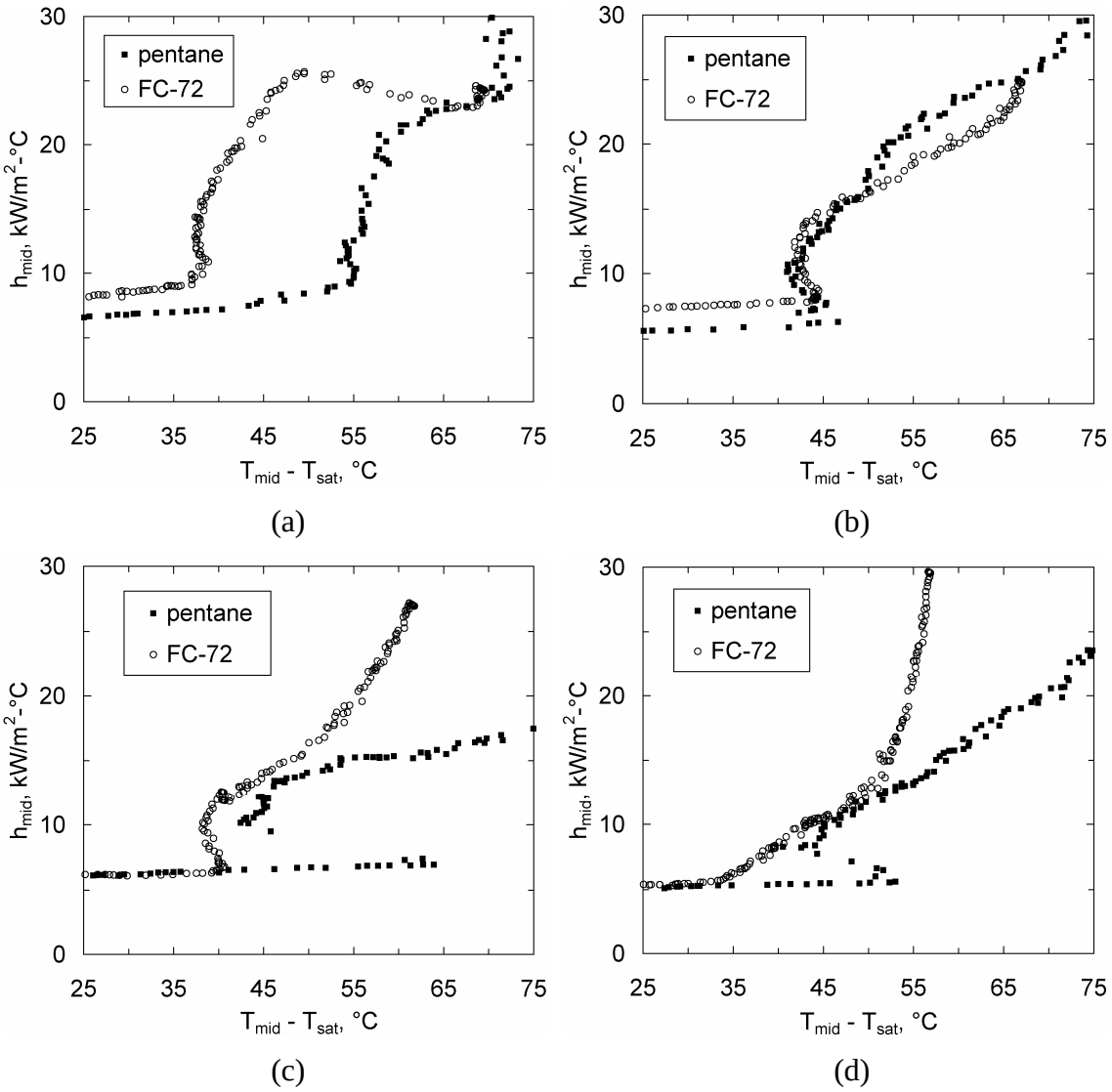

Figure 5.21. Comparison of pentane in water emulsions to FC-72 in water emulsions with small sub-cooling. Emulsions are (a) 0.1%, (b) 0.2%, (c) 0.5%, and (d) 1.0% dispersed component by volume.

corresponds to surface temperatures high enough to cause the water to begin boiling as well. This result suggests that the most significant effects of the bubbles of the dispersed component are caused by their mere presence, and the properties of the vapor in the bubbles are unimportant.

5.8.4. Surface temperature overshoot

One striking difference between pentane and FC-72 emulsions in Fig. 5.21c and d is the large temperature overshoot that occurs before the pentane emulsions begin boiling.

In fact, such overshoots occur inconsistently throughout the experiments. No correlation with degree of subcooling of the emulsion or the dispersed component volume fraction is apparent. One clear distinction is that the largest temperature overshoots are seen in the pentane in water emulsion data, and those cases the temperature of the wire drops suddenly after the inception of boiling rather than gradually as heat flux increases. The inconsistent data suggests that the temperature overshoots are linked to some aspect of the preparation of the emulsions that was not adequately controlled.

One likely source of variability in the emulsions is in the degree to which they were degassed. As noted in Section 5.2, the water used in the emulsions was first degassed by boiling but the dispersed component was not degassed separately. Additionally, after degassing the water was cooled to room temperature and handled further in the course of producing the emulsion. This procedure provided opportunities for the water to re-absorb atmospheric gasses. The large degree of superheat required to initiate boiling in the water experiments (Fig. 5.7) suggests that the emulsions remained at least partially degassed, but differences in the handling of each batch of emulsion could have resulted in different amounts of dissolved gasses in each experiment. It is noteworthy that none of the previous investigators of boiling in emulsions (Bulanov et al., Mori et al., and Ostrovskiy) mention degassing procedures in any of their experiments. In fact, Bulanov's theory of chain boiling depends on the presence of dissolved atmospheric gases in the dispersed component. The data suggests that dissolved gases play a role in the initiation of boiling but do not impact the boiling heat transfer coefficient.

5.8.5. Attached bubbles

The visual observations reported in Section 5.7 are surprising. Both Bulanov's model of boiling emulsions and the model developed in Chapter 3 rely on boiling of individual droplets of the dispersed component in the thermal boundary layer around a heated surface and not on the surface itself. The droplets of the emulsions used in these experiments have $4 < d_d < 22$ μm and, if they boil individually, would produce bubbles with $20 < d_b < 130$ μm. The images obtained of boiling emulsions at high heat flux (Figs. 5.18b-e, 5.16e, and 5.13d) show that the camera system used in these experiments

is capable of capturing bubbles with diameters as small as ~ 25 μm. Therefore, while individual droplets cannot be seen, most bubbles that result from boiling droplets should be visible. However, it is quite clear from the images that at low heat flux there are no small bubbles in the emulsion around the heated wire.

Instead of dispersed bubbles, at low heat flux large bubbles form on the wire and remain attached to it. The first appearance of the bubbles in the recorded video coincides with the inception of boiling in the heat transfer data, and it is reasonable to conclude that the former cause the latter. These large bubbles merit further consideration. The bubbles are observed to grow from the wire, so they probably formed at nucleation sites on the wire that were wetted by the droplets that had collected on the wire. Further growth of the bubbles might be enabled by coalescence of droplets that flow past the wire with the bubbles.

The bubbles contact only a small fraction of the wire's total surface area and yet cause a large rise in the heat transfer coefficient. The presence of the bubbles certainly changes the flow field around the wire, but because the bubbles are mostly stationary and located above the wire (while the emulsion rises past the wire from below), it is not likely that the bubbles themselves would cause significant disruption of the thermal boundary layer around the wire. Phase change and circulation inside the bubbles might account for the improved heat transfer, however. Each bubble contains vapor of the dispersed component, which condenses at the top of the bubble surface where the temperature of the emulsion is less than the saturation temperature of the dispersed component. A film of the dispersed component liquid therefore grows on the surface of the bubble, and this film flows down the sides of the bubble. When the liquid reaches the vicinity of the wire it evaporates again, and the vapor circulates back to the top of the bubble. Thus the bubbles might function as small heat pipes to increase the rate of thermal energy transport out of the thermal boundary layer surrounding the wire. This explanation, it must be noted, is speculation at this point.

Clearly, any model based on boiling of individual droplets around the heated surface is at best incomplete. It does appear, however, that for the pentane in water emulsions the small dispersed bubbles start forming at a lower surface temperature in the 0.2%

dispersed volume fraction case than in the 0.1% volume fraction case. If that trend continues at higher dispersed component fractions (where video cannot be obtained), then boiling of dispersed droplets would be an important boiling mechanism for higher dispersed component fraction emulsions. For the 0.2% pentane in water emulsion, many small dispersed bubbles are observed at wire temperatures below 100 °C, so they must indeed be pentane. It is tempting to attribute the higher boiling heat transfer coefficient of the 0.2% pentane in water emulsion as compared to the 0.1% emulsion for $T_{mid} < 100$ °C (Fig. 5.10) to the presence of these dispersed bubbles, which should improve heat transfer as described in Chapter 3. However, this explanation does not account for the fact that the heat transfer coefficients for the 0.5 and 1.0% pentane emulsions are lower in the same temperature range. Further study of interaction between the large attached bubbles and the dispersed phases is merited.

5.8.6. Pressure jump due to interfacial tension

It is important to note the effect of interfacial tension on the saturation temperature of the droplets. Because of interfacial tension between the droplets and the continuous component, the pressure in the droplets is higher than ambient pressure by $2\sigma_{dc}/r_d$. This pressure jump causes the saturation temperature of the droplets to be higher than expected based upon the ambient pressure.

In order to evaluate the change in saturation temperature, the interfacial tension between the droplets and continuous component must be known. At 22 °C, the interfacial tension between pentane and water is .051 N/m, which falls between the surface tension of water and pentane (.072 and .0158 N/m, respectively) (Goebel and Lunkenheimer, 1997). Similar data is not available for FC-72 and water, but because the surface tension of FC-72 is also much lower than that of water (.0115 N/m at 20 °C), it is reasonable to assume that the interfacial tension between FC-72 and water is also lower than the surface tension of water. The surface tension of water may be used to estimate an upper bound on the increase of saturation temperature of the droplets.

The FC-72 droplets in this study were measured to have $4 \leq d_d \leq 22$ μm. Using the surface tension of water at 80 °C (.063 N/m), the pressure jump in the droplets is between 11 and 63 kPa. In both FC-72 and pentane this pressure rise causes an increase

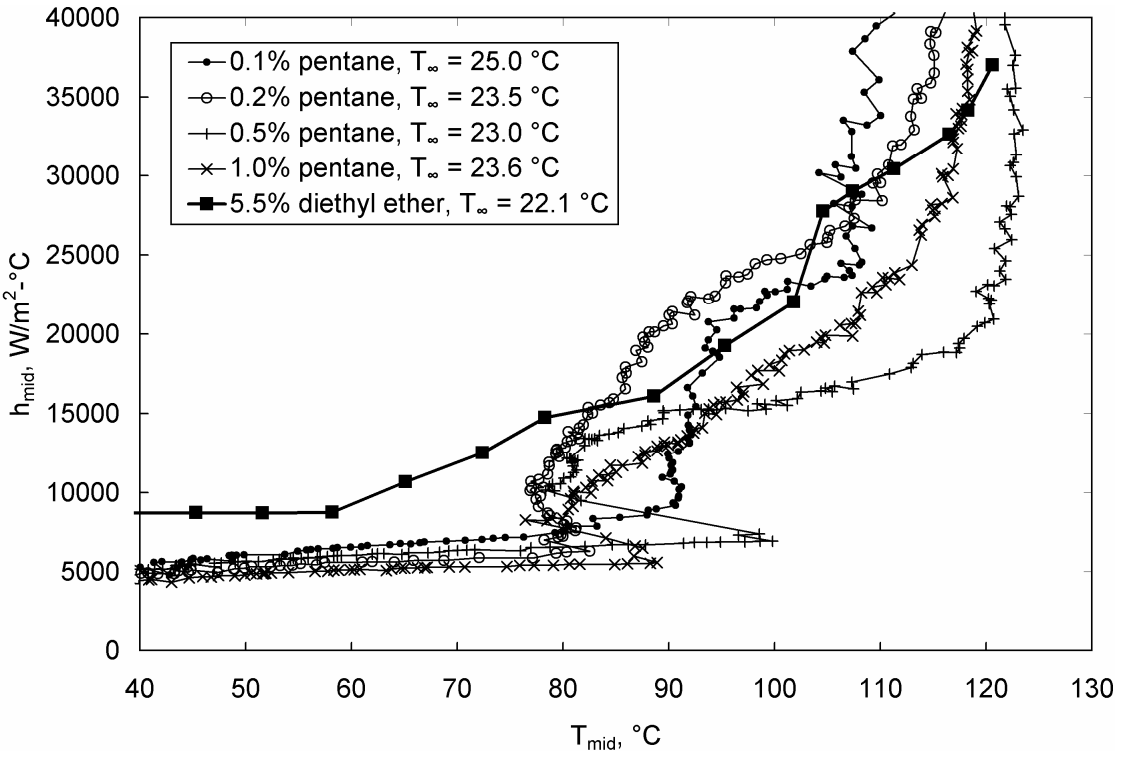

Figure 5.22. Comparison of pentane in water emulsion heat transfer of this study to that for diethyl ether in water emulsion (Bulanov et al., 2006).

in saturation temperature of 3 to 15 °C. Thus all of the droplets in the emulsions are superheated well before any boiling is observed.

5.8.7. Comparison to literature

The results of this experimental study can be compared to those of Bulanov et al. (2006). They measure boiling heat transfer coefficients for emulsions of several combinations of fluids on heated horizontal and vertical wires. The most comparable experiments to the present study are for emulsions of diethyl ether in water and R-113 in water.

Figure 5.22 compares heat transfer coefficients for pentane in water emulsions of this study and an emulsion of diethyl ether in water. The data from Bulanov et al. are for a horizontal heated platinum wire with 50 μm diameter and 36 mm length. The emulsion contained 5.5% diethyl ether by volume with no surfactants and had an average droplet diameter of 60 μm. The experiment was performed at 1 atm pressure, where diethyl ether has a saturation temperature of 34.6 °C. The bulk temperature of

the emulsion was 22.1 °C. The dispersed component in this experiment by Bulanov et al. therefore has a saturation temperature and degree of subcooling very close to that of the pentane used in the current study. Bulanov et al. do not make any mention of degassing their emulsions.

The emulsion of diethyl ether has much higher single phase heat transfer coefficient than the pentane emulsions because of the difference in wire diameters in the two experiments. The diethyl ether emulsion begins boiling at a much lower surface temperature, ~60 °C, than the pentane emulsions, but for wire temperatures above ~85 °C the heat transfer coefficients are comparable. There are several differences between the two experiments that could explain the much lower boiling inception temperature for the diethyl ether experiments. There is insufficient data to distinguish the effects of different wire diameter, droplet size, degassing, dispersed fluid, and dispersed component volume fraction.

Figure 5.23 compares the pentane emulsion data of this study to emulsions of R-113 in water (Bulanov et al., 2006). The experiments with the R-113 emulsions were performed using a vertical platinum wire with diameter 50 μm and 46 mm. The average droplet size was again 60 μm. The saturation temperature of R-113 at atmospheric pressure is 48 °C.

The single phase heat transfer coefficient is again higher for the smaller wire used by Bulanov et al. Interestingly, their data also shows a decrease in the single phase heat transfer coefficient with increasing dispersed component volume fraction. The effect is much less pronounced for the R-113 emulsions, perhaps because the vertical orientation of the wire gives droplets less opportunity to collide with the wire. After boiling inception, the data for R-113 emulsions and pentane emulsions are quite similar in a fairly narrow range of surface temperatures, 80 to 90 °C. This correlation may merely be coincidence, however, as the two fluids have very different saturation temperatures.

A fairer comparison may be made between the FC-72 emulsions and R-113 emulsions on the basis of superheat of the dispersed component, shown in Fig. 5.24. It can be seen that the R-113 and the FC-72 begin boiling at similar degrees of superheat.

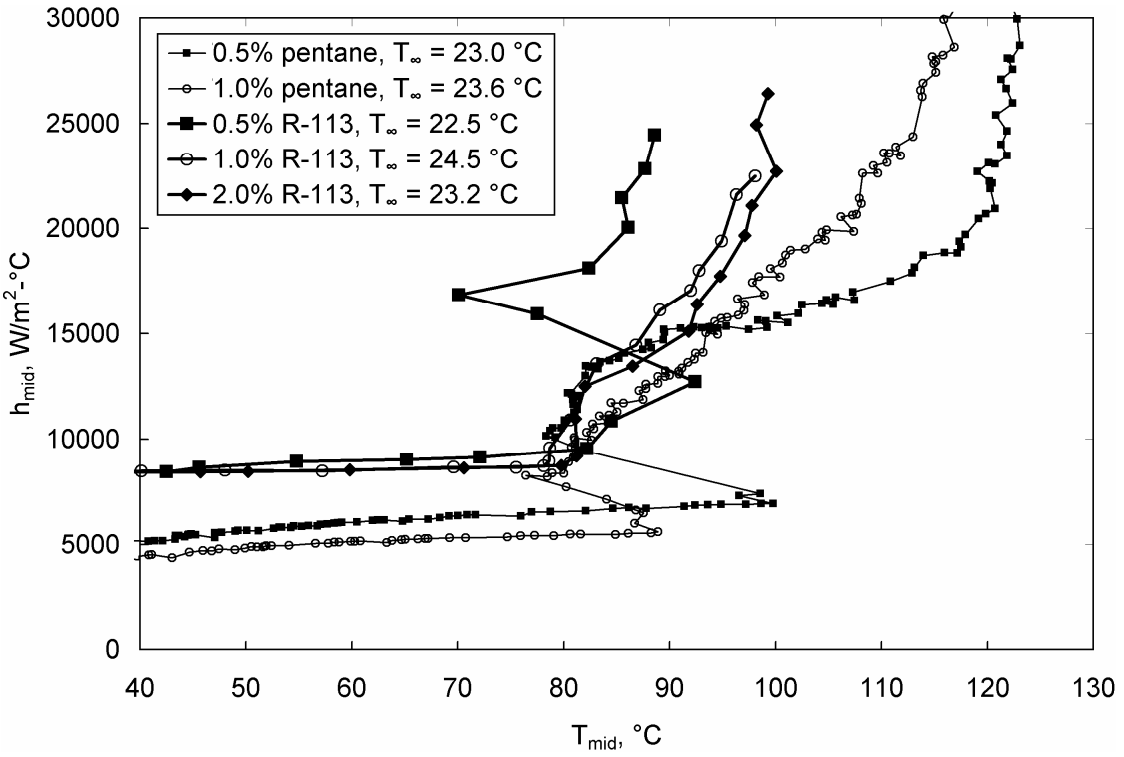

Figure 5.23. Comparison of pentane in water emulsion heat transfer of this study to that for R-113 in water emulsion (Bulanov et al., 2006).[6]

The R-113 emulsions have consistently higher heat transfer coefficients for both single phase and boiling heat transfer.

5.9. Numerical simulation results

5.9.1. Conditions

Simulations were performed using the algorithm described in Chapter 4 in the domain illustrated in Fig. 5.25a. It was assumed that flow around the heated wire is symmetrical, so the simulation domain consists of only half of the flow field around the wire with a symmetry boundary condition imposed at the vertical axis that passes through the centerline of the wire. A no-slip boundary condition is imposed at the wire surface as well as at the outer edge of the simulation domain. The temperature at the

[6] Bulanov et al. (2006) also include data for more dilute emulsions of R-113 in water. However, the data are duplicated and labeled as both .001% and .1% R-113. The reported heat transfer data for these two cases is also very different from the other cases included above. It is not clear which, if either, label is correct, so the data are not included here. (Similar duplications are seen in other tables in the paper for water in oil emulsions.)

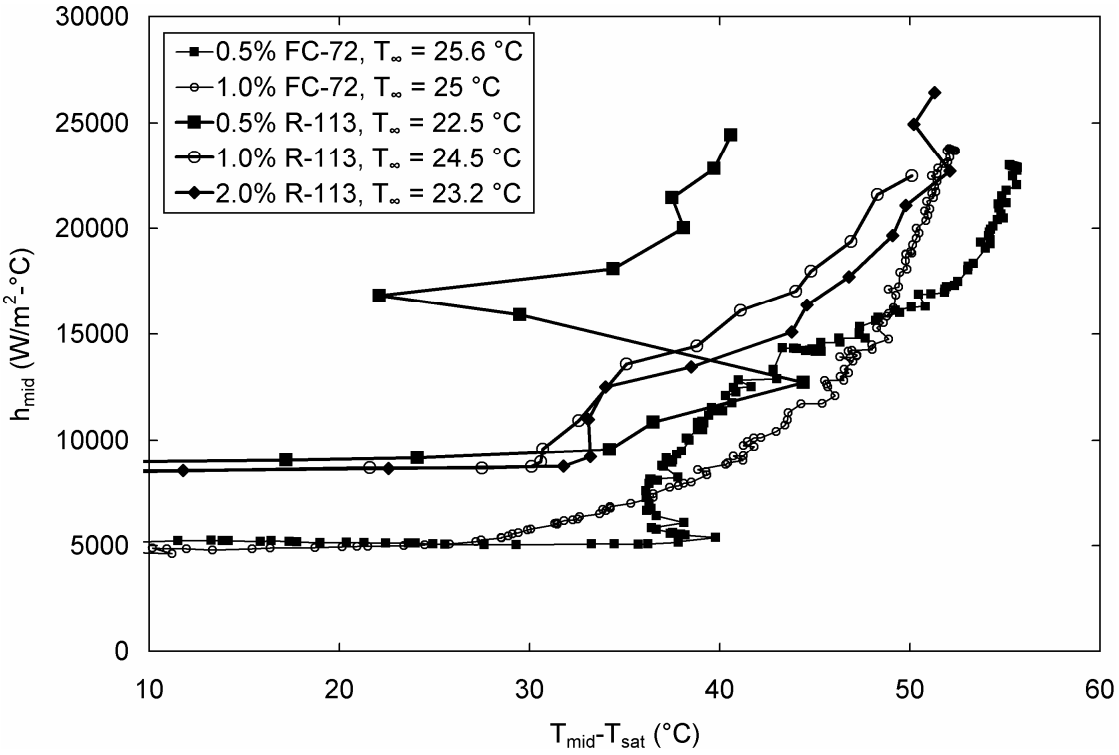

Figure 5.24. Comparison of cool FC-72 in water emulsion data of this study to that for R-113 in water emulsion (Bulanov et al., 2006).

wire was held at constant temperature, and the temperature at the outer edge was fixed at T_∞. For each simulation, the initial temperature field was uniform at T_∞ and the initial velocity for each phase was uniform at zero. The initial bubble volume fraction was zero and the initial droplet volume fraction was set equal to the average dispersed component volume fraction for the emulsion.

This domain was split into a mesh of hexahedral cells. There were 125 cells in the radial direction and 32 cells in the angular direction. The simulations were performed in two dimensions, so the number of cells along the axis of the wire was one. The cells were clustered in the axial direction by a factor of 167. That is, the cells adjacent to the outer boundary of the domain had a radial length 167 times larger than the cells adjacent to the wire. No clustering was imposed in the angular direction (Fig. 5.25b). The mesh was generated using the standard meshing utility of OpenFOAM™.

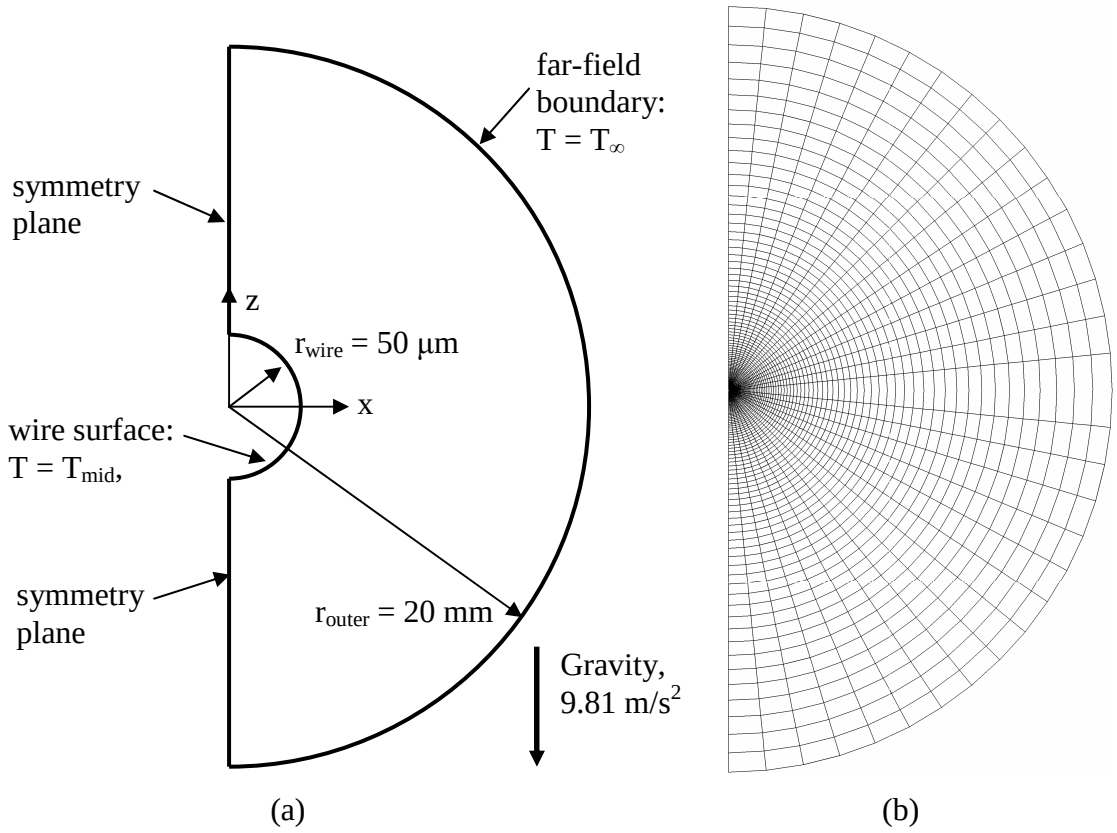

Figure 5.25. Simulation domain, (a) geometry and boundary conditions (not to scale), and (b) mesh.

Meshes with different resolutions were tested to ensure that grid independence was achieved. Reducing the number of cells by 25% in each direction (to 96 by 24 cells) resulted in changed the heat transfer coefficient by ~1%, while increasing the number of cells by 25% changed the heat transfer coefficient by less than .2%. These tests were carried out under conditions that produced the strongest temperature and volume fraction gradients in the emulsion. Thus all of the simulation results reported here are independent of the mesh resolution.

The duration of each simulation was between four and ten seconds. Simulations with a small temperature difference between T_{mid} and T_∞ required the longer duration to reach steady state. For all simulations, a plume of fluid rises from the heated wire and eventually reaches the top of the domain and begins to circulate back down towards the wire. Once the plume reaches the top of the domain, the size of the domain begins to

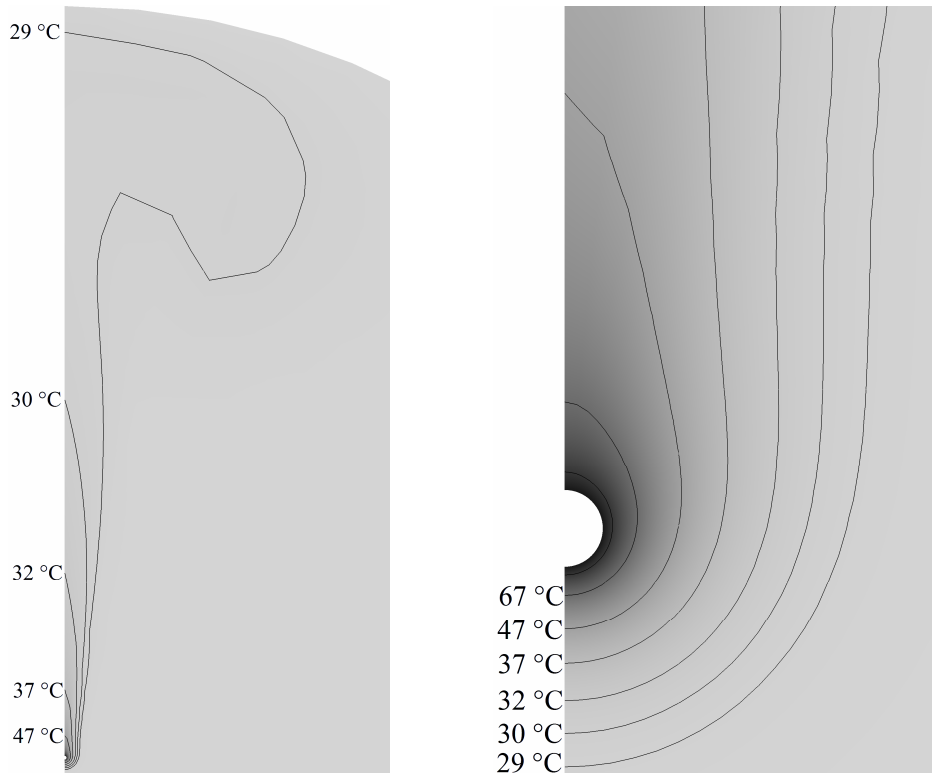

Figure 5.26. Temperature contours for horizontal wire in water, T_{mid} = 98 °C, T_{∞} = 28 °C, ε_d = 0. (a), top half of domain, (b) vicinity of the wire.

have an effect on the heat transfer from the wire and the results are no longer considered indicative of the behavior of the emulsion around the wire alone. For large temperature differences this occurs after approximately four seconds (Fig. 5.26a). For all simulations this duration was sufficient for the heat transfer from the wire to reach a steady value.

Simulations were performed for water as well as emulsions of FC-72 in water. Average FC-72 volume fractions of 0.1, 0.2, 0.5, 1.0, and 2.0% were simulated. Simulations were performed for two bulk temperatures, 28 and 43 °C, and 48 < T_{wire} < 108 °C. Fluid properties were evaluated at the film temperature for each simulation. The effects of varying parameters such as the collision efficiency and the pseudo-turbulent viscosity and thermal conductivity (Eqs. 3.17, 3.26, 3.27) were investigated as well.

5.9.2. Water

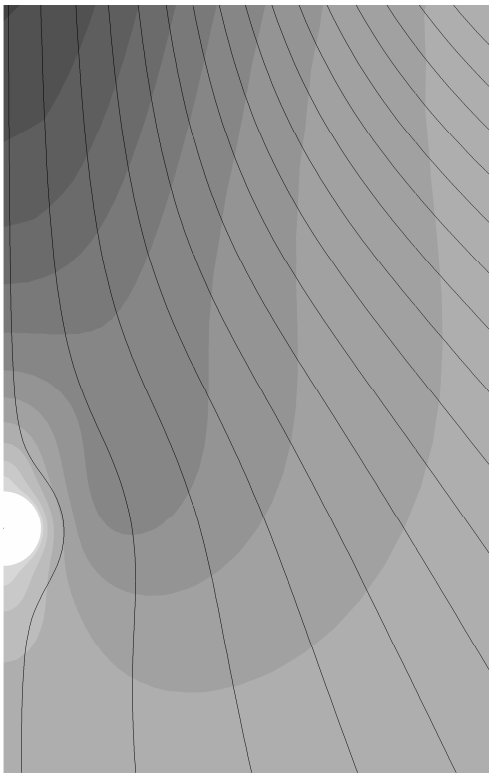

Figure 5.27. Streamlines in vicinity of wire, T_{mid} = 98 °C, T_{∞} = 28 °C, ε_d = 0. Shading indicates velocity magnitude; the maximum velocity is 0.0077 m/s at upper-left corner.

Typical results for the temperature field and velocity field for water are shown in Figs. 5.26 and 5.27. The results shown are for the end of the simulation, at t = 4 s. At this time the plume of heated water has just reached the top of the domain, but the temperature and velocity fields in the vicinity of the wire have been virtually unchanged since t = 1 s. The water velocity near the wire is low and there is no indication of detached vortices or vortex shedding from the wire, so the assumption that the flow field is symmetrical around the wire is reasonable. Two stagnation points exist at the expected locations, the top and bottom of the wire.

As each simulation progresses, the heat flux from the wire surface is calculated from the temperature gradient at the surface. The average heat transfer coefficient for the wire is then obtained. The evolution of the heat transfer coefficient over time takes the same form regardless of the overall temperature difference (Fig. 5.28). The very high

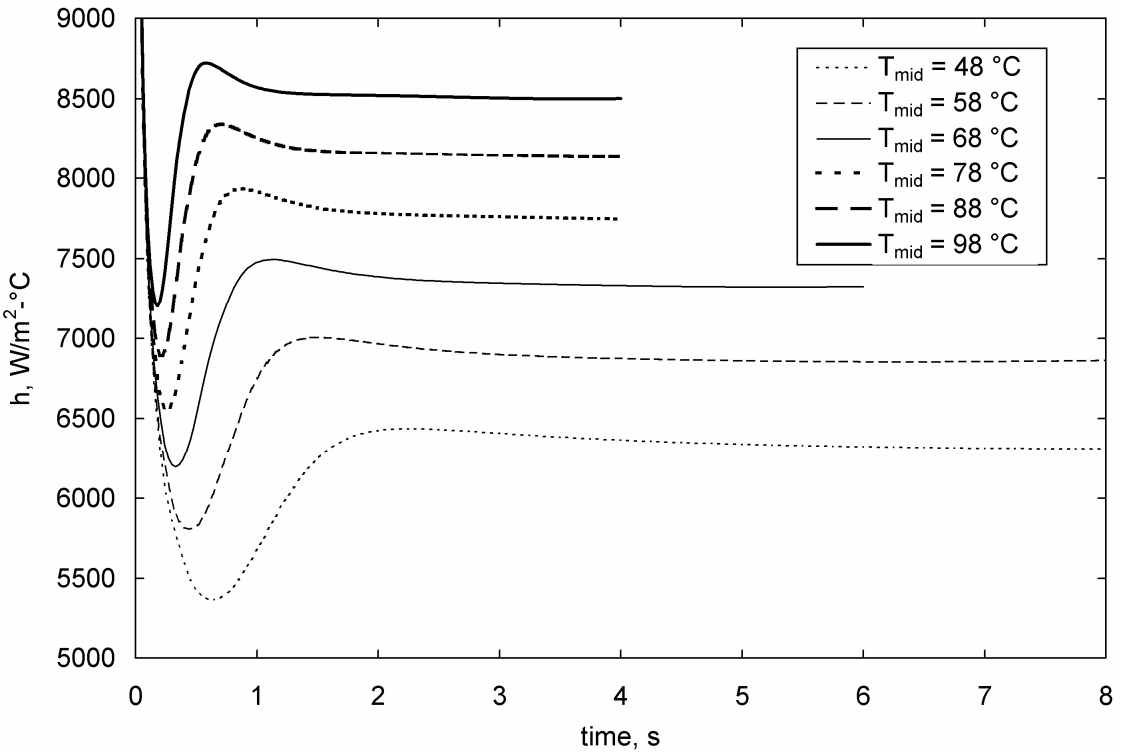

Figure 5.28. Time evolution of the heat transfer coefficient for heated wire in water.

initial heat transfer rate is a result of the initial conditions, in which the water has uniform temperature T_∞, so there is a strong temperature gradient at the heated wire. As energy diffuses into the water the heat transfer rate decreases, until the buoyancy of the heated water causes it to start to rise away from the wire. The heat transfer rate then increases again, and finally settles to its steady value.

Figure 5.29 compares the steady-state results of the simulations to the experimental data as well as Morgan's correlation (Eq. 5.24). The agreement between simulation and experiment is quite good, with the simulation results generally falling within the scatter of the experimental data. This very close match is actually somewhat surprising, as it has been found that the constant-property assumption can lead to significant errors in simulations of flow and heat transfer in water (Kumar, Gupta, and Nigam, 2007).

5.9.3. FC-72 in water emulsions

Results of simulations of emulsions of FC-72 in water are shown in Fig. 5.30. It is immediately apparent that the simulation results do not resemble the experimental

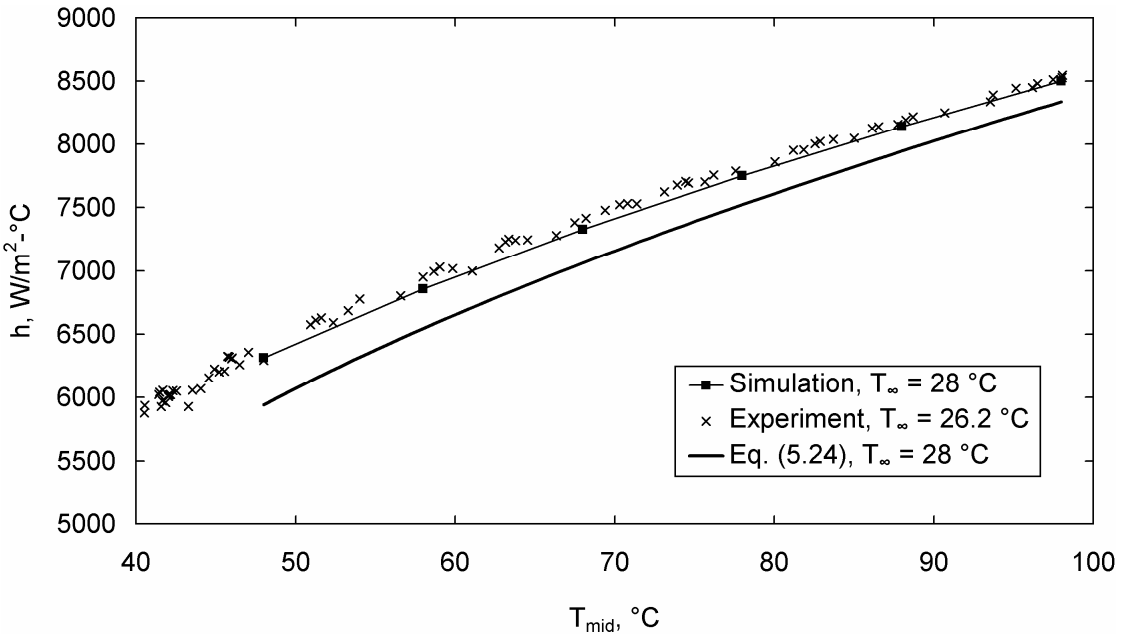

Figure 5.29. Comparison of heat transfer coefficients for heated horizontal wire in water for simulation, experiment, and Eq. (5.24).

results discussed in Section 5.6. The results of 0.1, 0.2, and 0.5% emulsions are indistinguishable from those of water. The 1% emulsion shows only a slight improvement in heat transfer, while the 2% emulsion has a lower heat transfer coefficient than water. In all cases the effects of the emulsified FC-72 are more pronounced when the bulk of the emulsion has less subcooling.

The reasons for this behavior can be discerned by examining the temperature and volume fraction fields around the heated wire. Shown in Fig. 5.31 and 5.32 are the volume fraction of bubbles and droplets, respectively, in the region around the heated wire. Figure 5.33 shows the mass transfer rate near the heated wire. The solid line in the figures is the isotherm T = 56.3 °C, the saturation temperature of FC-72. The figures show that in all cases except for the 2% FC-72 emulsion, not much boiling of the dispersed component actually occurs. The FC-72 droplets tend to settle downwards onto the top half of the wire surface, where some of them boil. Some droplets accumulate at the stagnation point at the top of the wire, and the rate of boiling due to wall contact is highest there. For emulsions with 0.2% or less FC-72, the area immediately above the wire is the only location where any boiling is observed. For

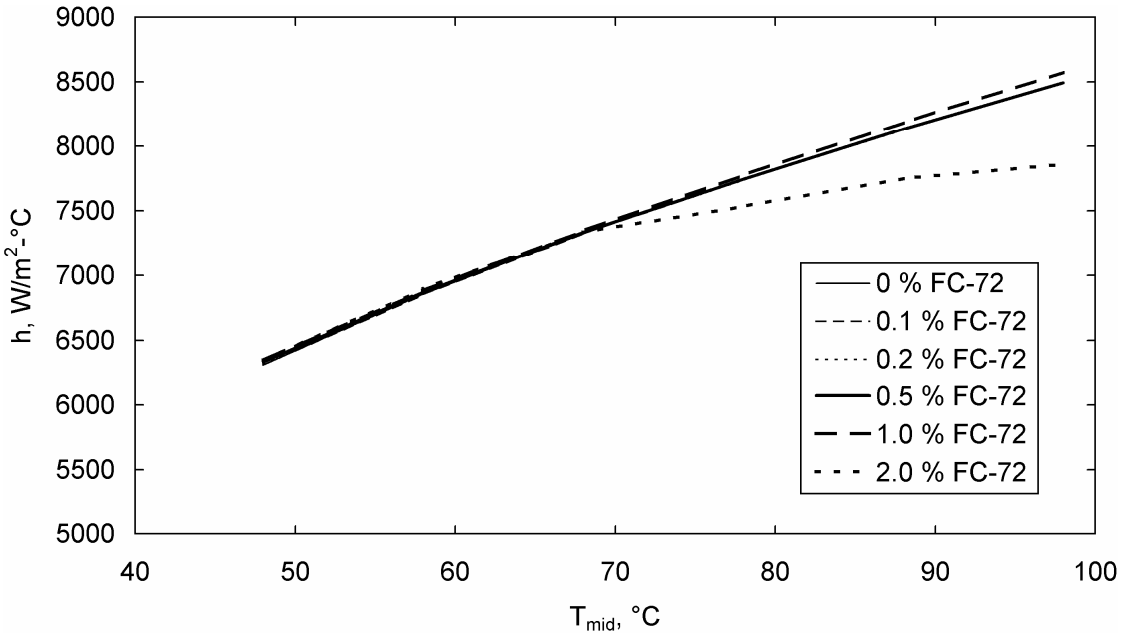

(a)

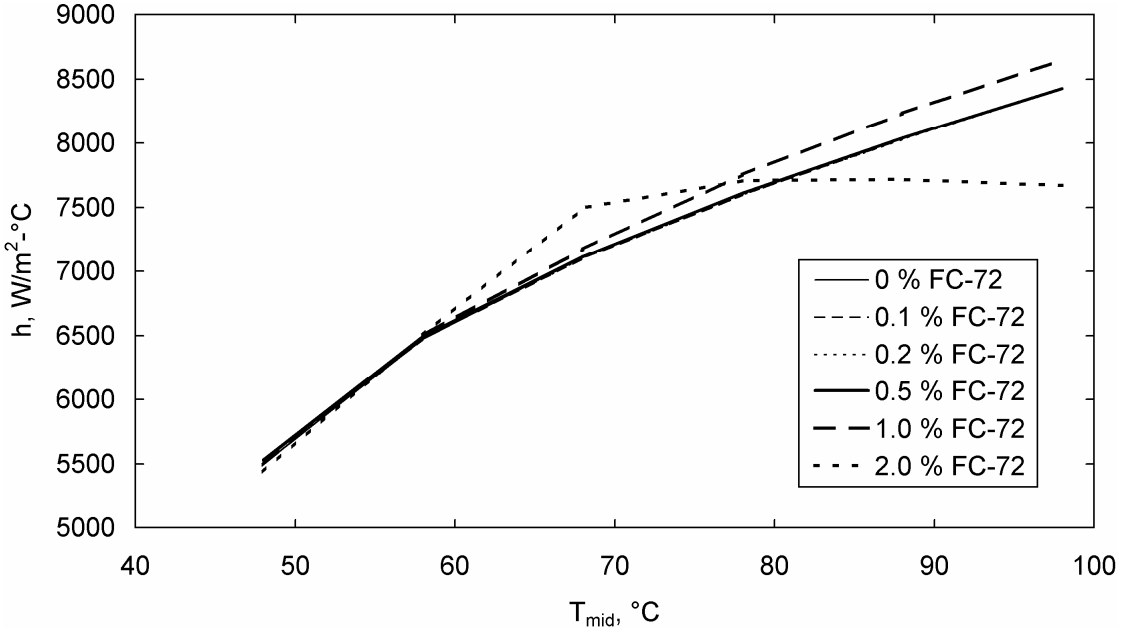

(b)

Figure 5.30. Simulation results for emulsions of FC-72 in water, (a) T_∞ = 28 °C, (b) T_∞ = 43 °C.

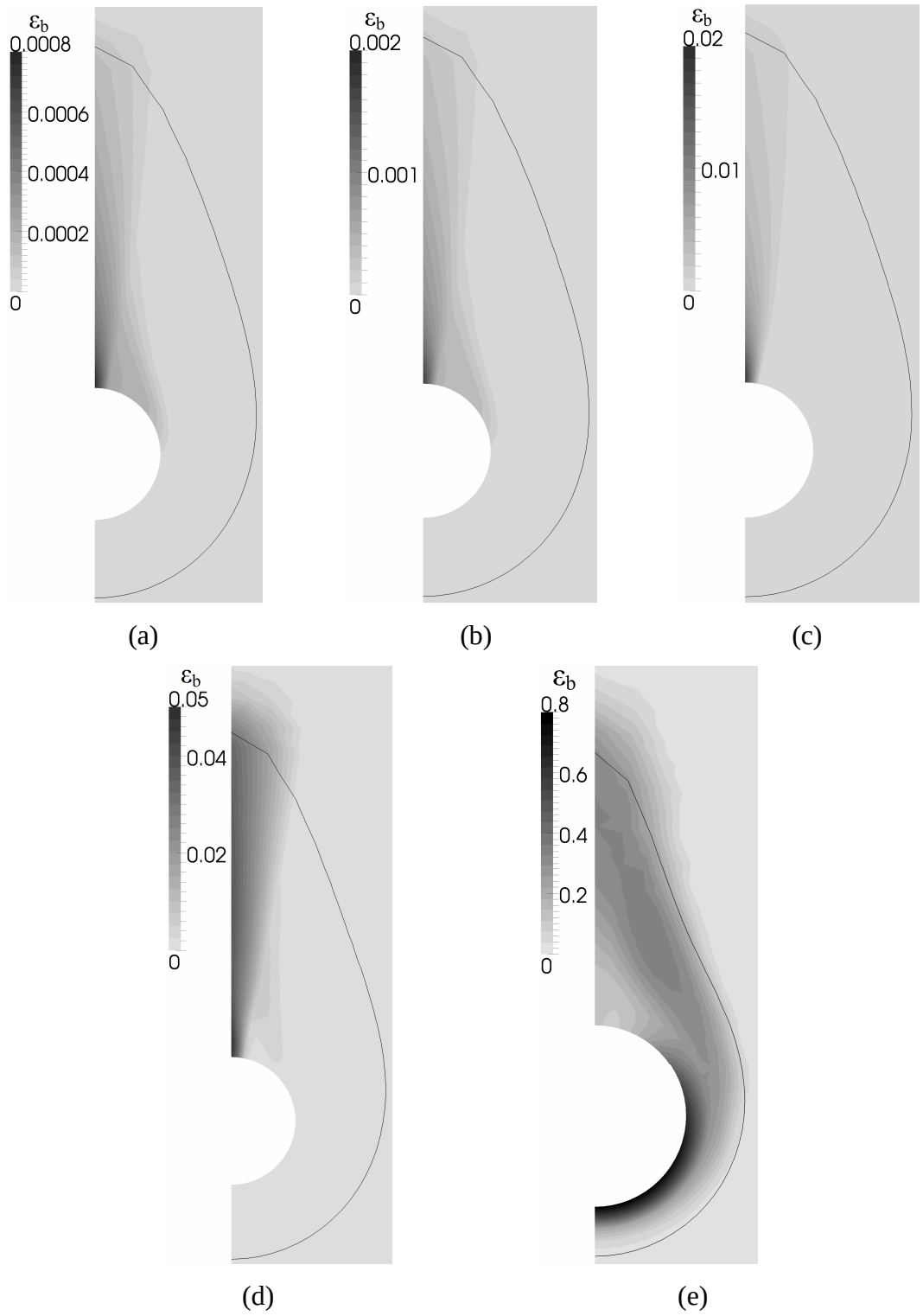

Figure 5.31. Simulated ε_b for emulsions of (a) 0.1%, (b) 0.2%, (c) 0.5%, (d) 1.0%, (e) 2.0% FC-72 by volume in water. T_∞ = 28 °C, T_{mid} = 98 °C, line is the T = 56.3 °C isotherm.

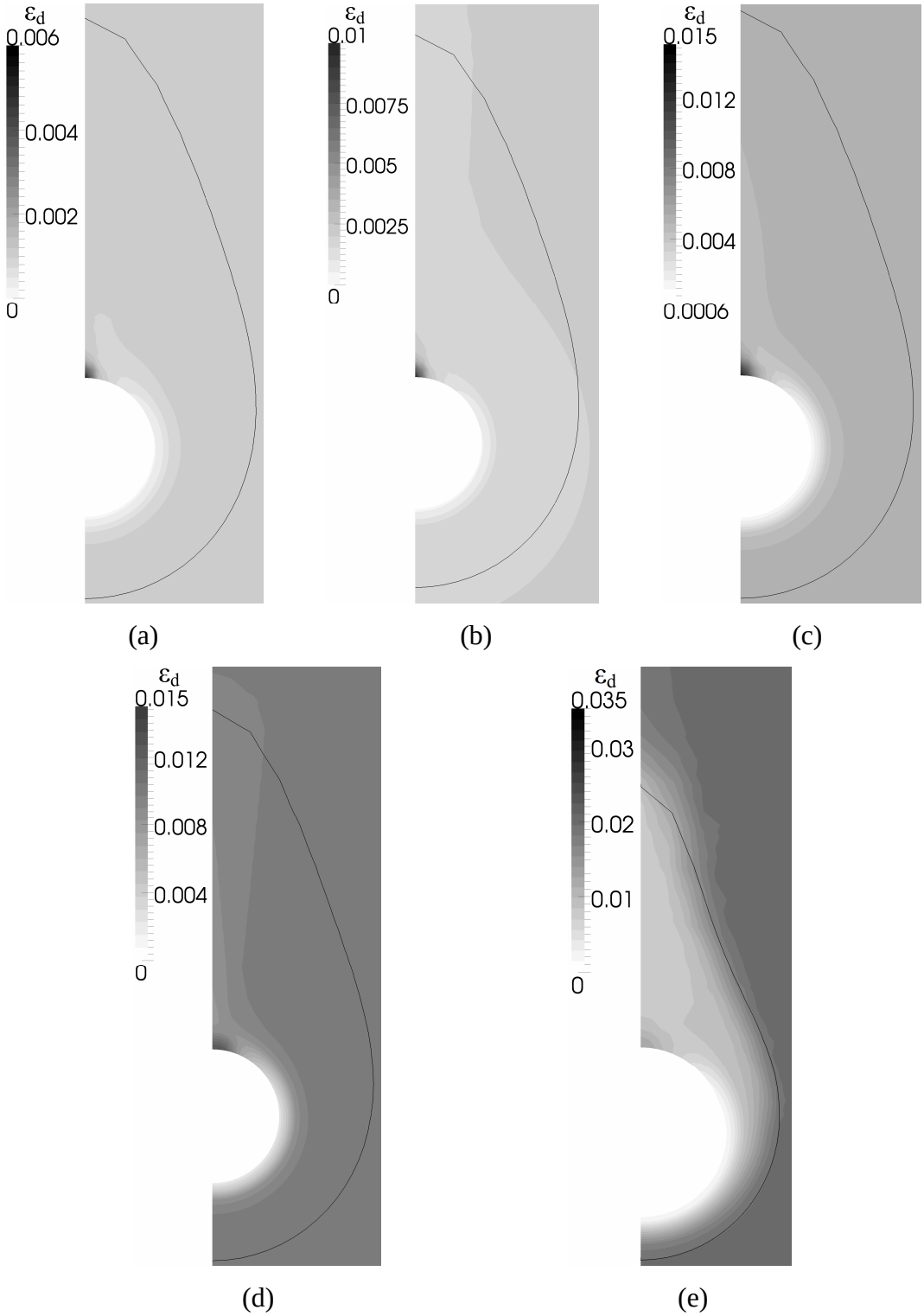

Figure 5.32. Simulated ε_d for emulsions of (a) 0.1%, (b) 0.2%, (c) 0.5%, (d) 1.0%, (e) 2.0% FC-72 by volume in water. T_∞ = 28 °C, T_{mid} = 98 °C, line is the T = 56.3 °C isotherm.

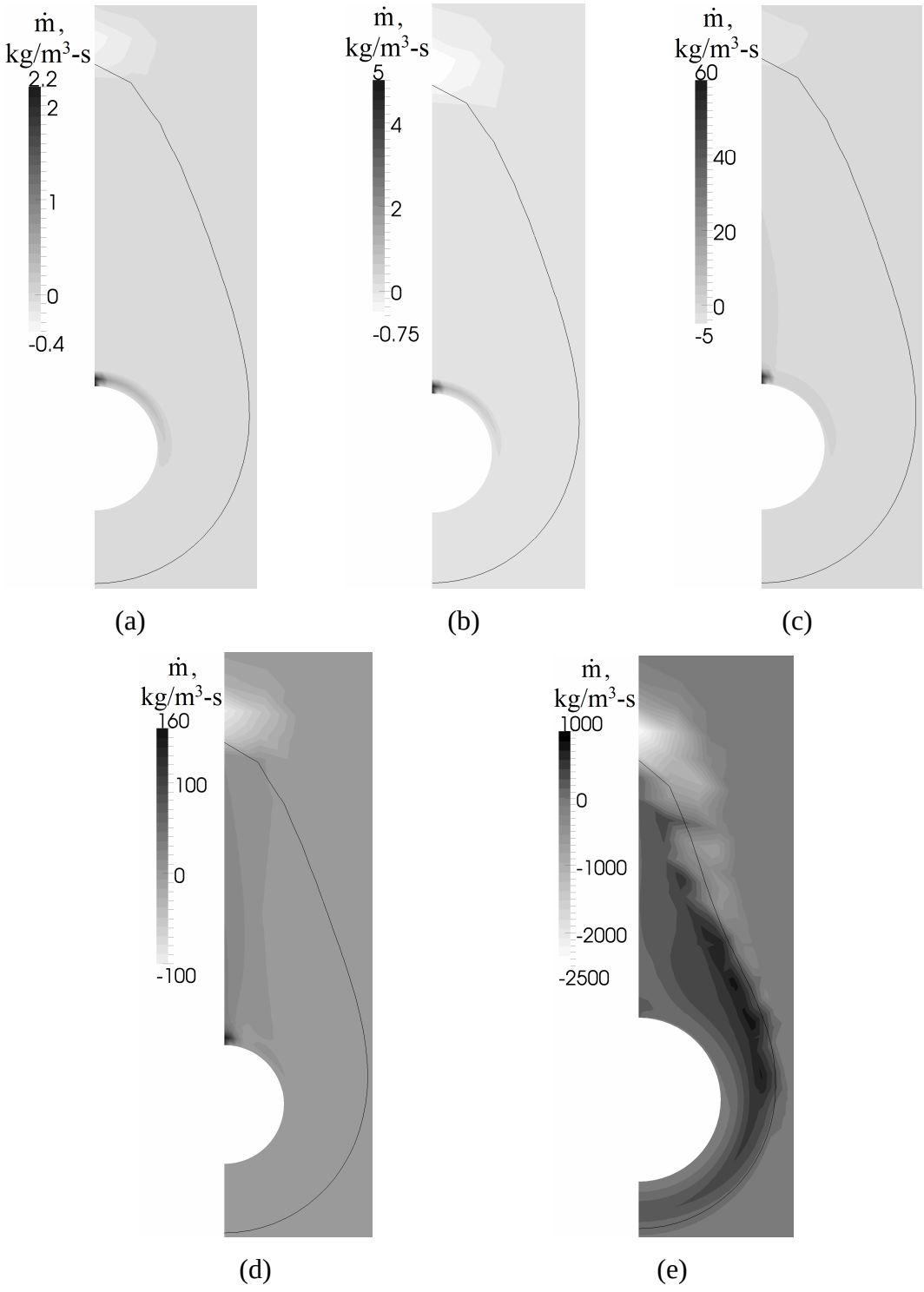

Figure 5.33. Simulated $\dot{m}$ for emulsions of (a) 0.1%, (b) 0.2%, (c) 0.5%, (d) 1.0%, (e) 2.0% FC-72 by volume in water. T_∞ = 28 °C, T_{mid} = 98 °C, line is the T = 56.3 °C isotherm.

emulsions with 0.5% or more FC-72, some additional boiling due to collisions between bubbles and droplets occurs in the plume above the wire as the bubbles rise through the boundary layer. However, the rate of boiling due to collisions is a very strong function of the droplet volume fraction and a strong function of the bubble volume fraction (Eqs. 3.14, 3.18). The boiling that occurs in the plume above the heated wire is far from the wire and has little effect on the overall heat transfer from the wire.

Only for emulsions of 2% FC-72 is rapid boiling seen all around the wire surface (Figs. 3.31e, 3.32e, 3.33e). In this case the droplet volume fraction is high enough to sustain boiling around the bottom half of the wire, even though no droplets settle onto the wire to cause boiling by wall contact in this region. Boiling occurs throughout the region where $T > T_{sat,FC-72}$, and the most rapid boiling occurs near the outer edge of that region, rather than at the wire surface as at lower FC-72 volume fractions. The volume fraction of FC-72 droplets within the thermal boundary layer is depleted significantly. However, as Fig. 5.30 shows, this rapid boiling does not improve the heat transfer coefficient. Instead, the high volume fraction of bubbles around the wire reduces the thermal conductivity of the emulsion (Eq. 3.31), effectively insulating the wire in a manner similar to film boiling. This effect overwhelms the increase in thermal conductivity due to agitation of the emulsion predicted by Eq. (3.27).

It is worth mentioning also that some of the underlying assumptions of the model break down in the 2% FC-72 emulsion case. The bubble volume fraction is as high as 0.75 around the bottom surface of the wire, which is high enough that the bubbles in this region would rapidly coalesce into larger bubbles. On the other hand, the layer below the wire with very high bubble volume fraction is no thicker than the diameter of a single bubble, so individual bubbles would be in the region only very briefly.

Although not shown in detail here, the ε_b, ε_d, and $\dot{m}$ fields around the heated wire are very similar for the simulations performed with higher bulk temperature. The most significant difference between the two cases is that when the emulsion is not as subcooled, the region in which $T > T_{sat}$ above the wire is larger. No qualitative differences between the $T_b = 28$ °C and the $T_b = 43$ °C cases were observed.

Although the heat transfer predicted by the model without modifications does not compare well with the experimentally determined heat transfer coefficients, the simulations agree in some respects with the visualization data. The simulations predict that the rate of dispersed boiling depends strongly on the dispersed component volume fraction and that little boiling occurs at low volume fraction. The visualizations agree that very little dispersed boiling occurs at 0.1% dispersed component volume fraction (Figs. 5.13 and 5.16), and most of the dispersed bubbles seen in those experiments were observed in the enhanced continuous component boiling regime. For the 0.2% pentane emulsion many more dispersed bubbles are observed, and at lower temperatures than for the 0.1% emulsions. Thus the simulations and the visualizations agree regarding the dependence of the rate of dispersed droplet boiling on dispersed component volume fraction.

5.9.4. Parameter variation

The results of the previous section indicate that the model developed in this thesis will predict an improvement in heat transfer in boiling emulsions only in a narrow range of dispersed component volume fractions. When too little of the dispersed component is present, no significant boiling takes place, and too much of the dispersed component leads to film-boiling-like behavior. However, it should be kept in mind that some of the correlations used to provide closure for the balance equations in Chapter 3 are rather speculative. Below, the effects of varying the pseudo-turbulent effects and the collision efficiency are explored.

5.9.4.1 Pseudo-turbulent effects

It has long been argued that the heat transfer enhancement in boiling emulsions is due, at least in part, to agitation of the continuous component by rapid boiling of the dispersed droplets. In Section 3.3 a model was suggested for quantifying the effects of this agitation. The model, as described in Section 3.3, is based upon the displacement of the liquid surrounding a boiling droplet due to its expansion. The model considers only the displacement of the liquid due to a droplet growing from its original size to the maximum size achieved by the bubble during the boiling process.

However, as the study in Appendix A shows, after a highly-superheated droplet boils the resulting bubble oscillates for some time. Although the study neglects acoustic damping, for bubbles in water thermal damping (which is included in the study) is more significant than acoustic damping (Plesset and Prosperetti, 1977). Figure A.6 illustrates that the bubble undergoes many, possibly hundreds, of oscillations. The liquid around a boiling droplet therefore undergoes many repeated displacements inwards and outwards. It follows that the agitation of the emulsion is more significant than the model in Section 3.3 predicts.

The effects of bubble oscillation on the pseudo-turbulent effects in the model of boiling emulsions can be explored by modifying Eqs. (3.26) and (3.27) to include an additional factor,

$$\mu_{c,T} = 0.1 K_T \dot{m} \frac{\rho_c}{\rho_b} R_b{}^2, \tag{5.26}$$

$$k_T = 0.1 K_T \dot{m} c_{p,c} \frac{\rho_c}{\rho_b} R_b{}^2. \tag{5.27}$$

Simulations were performed with K_T = 10, 100, 300, and 1000, and the resulting boiling curves are shown in Figs. 5.34 - 37. Results for emulsions of 0.1, 0.2, and 0.5% FC-72 are not shown because the results are indistinguishable from those for water, just as in the previous section. Results for 2.0 % FC-72 and K_T = 1000 are not shown because of difficulty in achieving stability in the simulations.

These results show that an improvement in heat transfer can be achieved if the agitation of the emulsion is more effective than predicted by the model in Section 3.3. The behavior of the emulsion is still a very strong function of the volume fraction of the dispersed component however, which does not agree with the experimental results. The simulations show an improvement in heat transfer starting at a much lower temperature than in the experiments, but this is simply the result of assuming that droplets will boil upon contact with any surface where $T > T_{sat}$. Use of a correlation to predict the

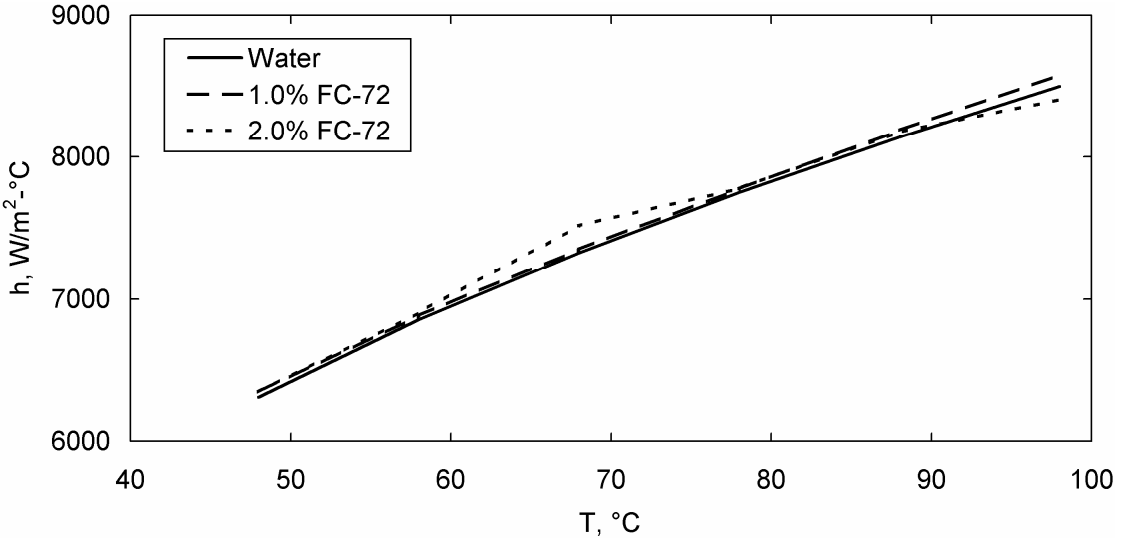

(a)

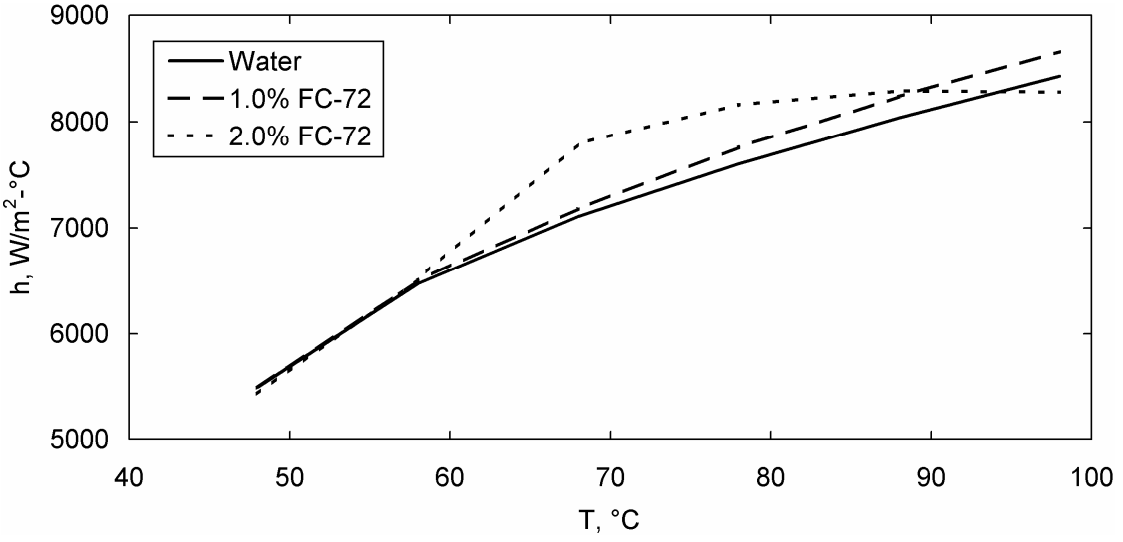

(b)

Figure 5.34. Simulation results for heated wire in FC-72 in water emulsions for K_T = 10, T_∞ = (a) 28 °C and (b) 43 °C.

nucleation temperature of the droplet liquid on the heated surface would bring that aspect of the simulation results into agreement with the experimental results. In fact, the simulations would then predict the sudden jump in heat transfer coefficient observed in some experiments (Fig. 5.8c, for example).

5.9.4.2 Collision efficiency

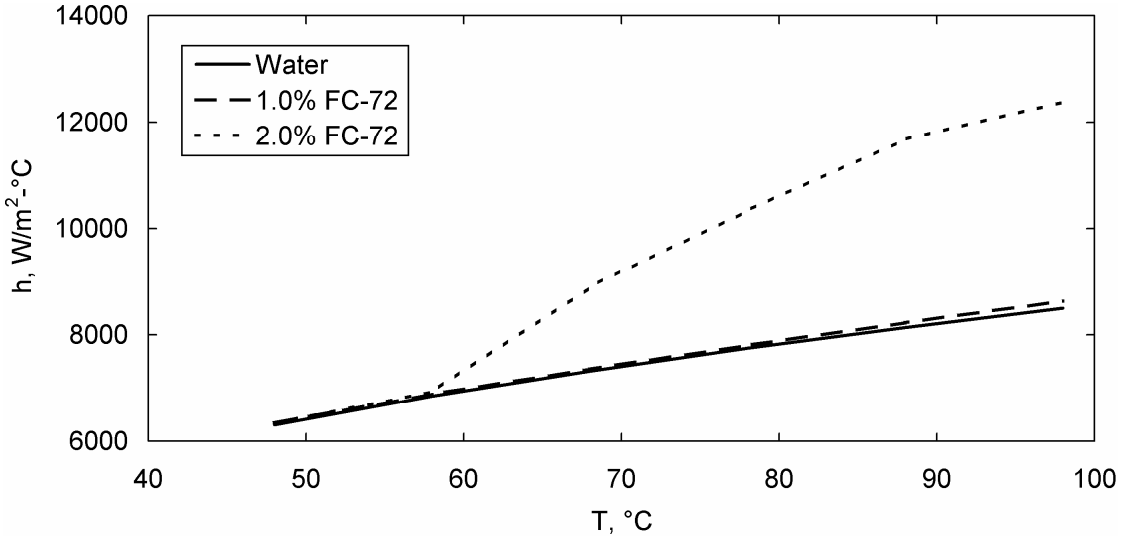

(a)

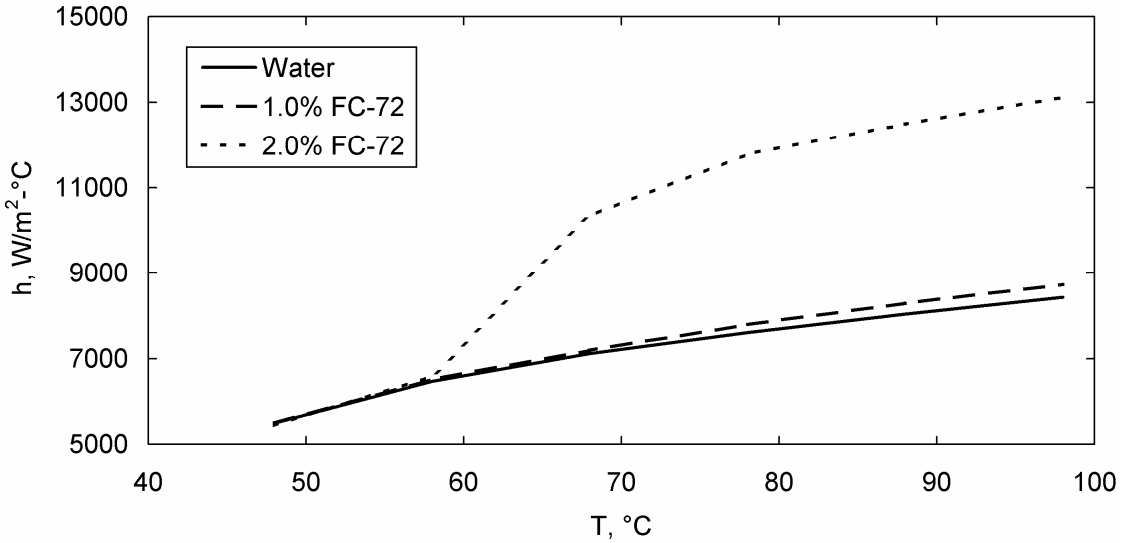

(b)

Figure 5.35. Simulation results for heated wire in FC-72 in water emulsions for K_T = 100, T_∞ = (a) 28 °C and (b) 43 °C.

The correlation given for collision efficiency in Chapter 3 (Eq. 3.17) was interpolated from data from a study of two solid spheres moving past each other in quiescent fluid. The conditions in boiling emulsions are different because droplets and bubbles moving past each other have finite viscosity and internal circulation. The

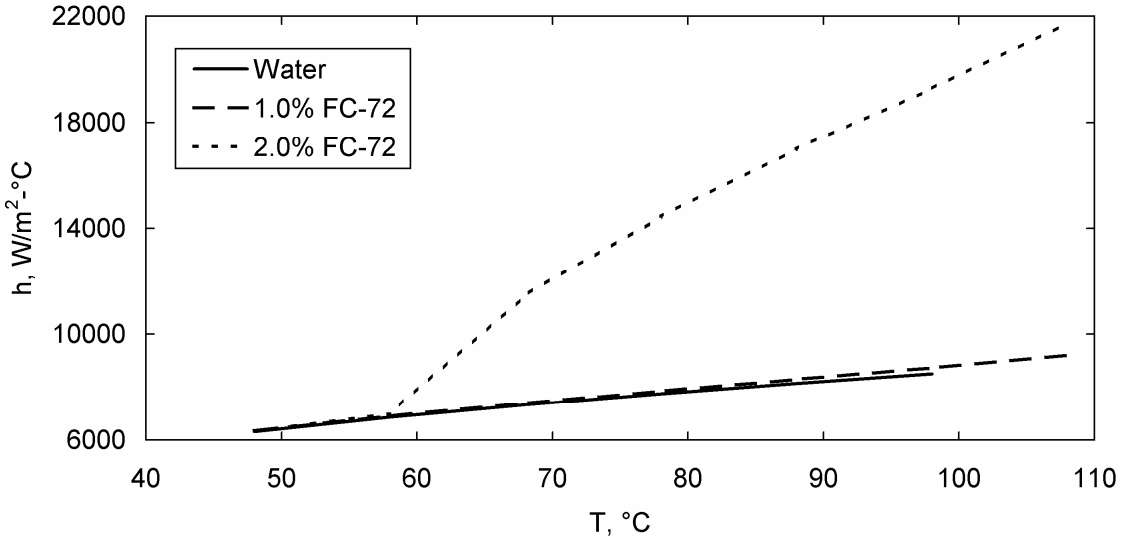

(a)

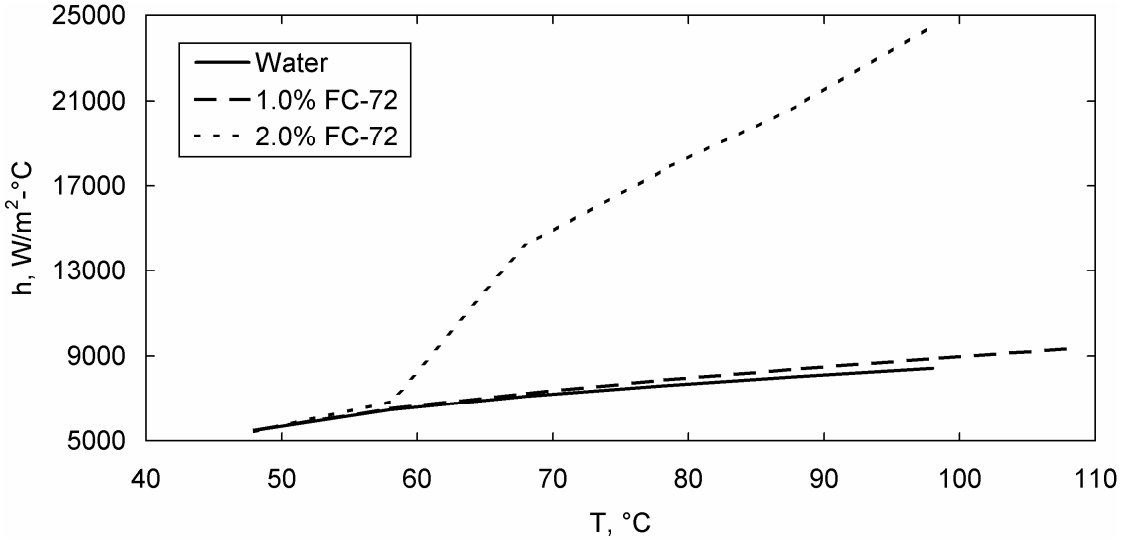

(b)

Figure 5.36. Simulation results for heated wire in FC-72 in water emulsions for K_T = 300, T_∞ = (a) 28 °C and (b) 43 °C.

emulsion is not quiescent either, especially if many droplets are boiling. Accordingly, an adjustment parameter was added to Eq. (3.17) as well,

$$\eta = K_\eta \left[0.00051 \left(\frac{R_b}{R_d} \right)^2 - 0.00738 \left(\frac{R_b}{R_d} \right) + 0.03165 \right]. \tag{5.28}$$

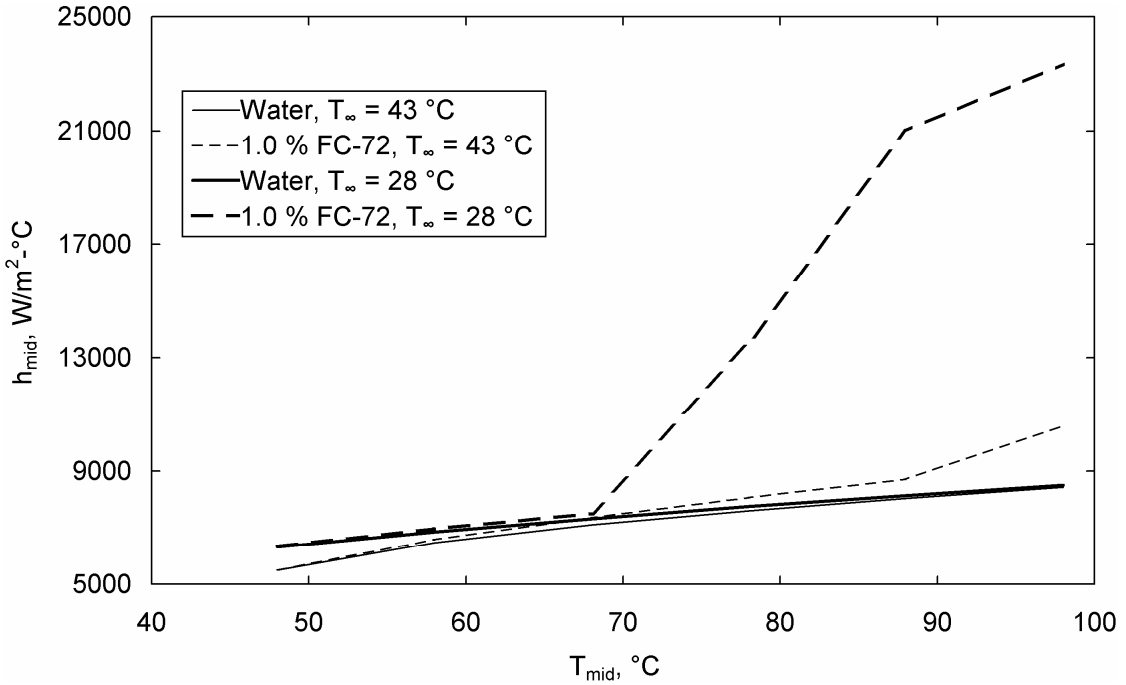

Figure 5.37. Simulation results for heated wire in FC-72 in water emulsions for K_T = 1000.

Simulations were carried out with K_T = 100 and K_η = 3, 10, and 30. The results are shown in Figs. 5.38 - 40. Results for emulsions with 0.1 and 0.2% FC-72 are not shown, as the results are indistinguishable from water.

Increasing the collision efficiency increases the rate of boiling, as expected, but does not necessarily improve the heat transfer coefficient. For 2% emulsions, which already experienced significant boiling when K_η = 1, increasing the collision efficiency causes droplets to boil sooner after entering the thermal boundary layer. The droplets thus tend to boil near the outside of the boundary layer, where the boiling has little impact on the heat transfer at the wire surface. As a result of this rapid boiling, the interior of the thermal boundary layer has high bubble volume fraction, which also tends to impede heat transfer. These effects are most pronounced at high surface temperature and low subcooling, when the thickness of the region around the wire where $T > T_{sat}$ is greater. Thus Fig. 5-40 shows that as K_η increases the heat transfer coefficient increases slightly at low surface temperature while it decreases significantly at high surface temperature.

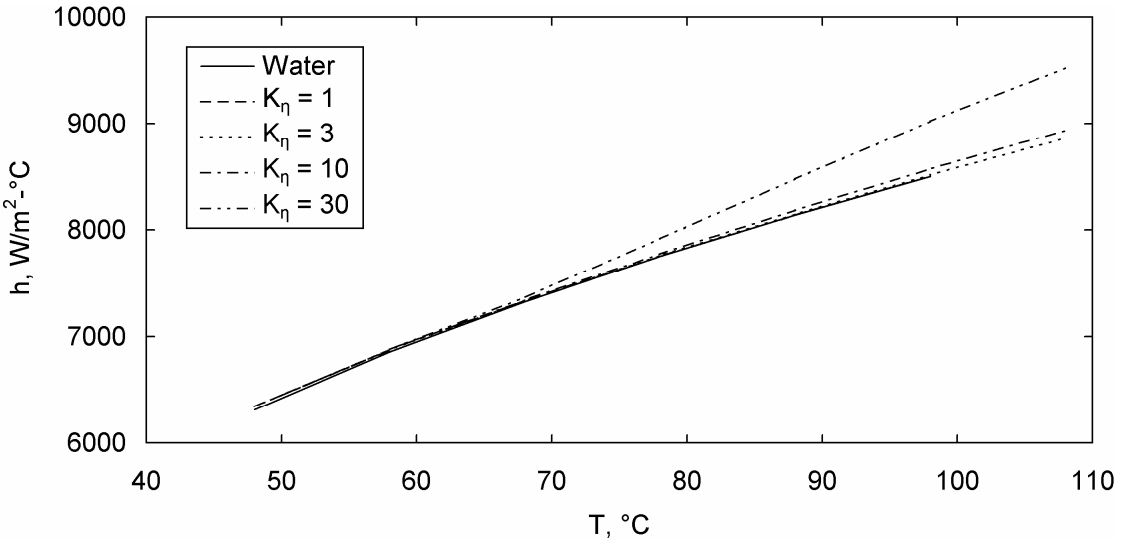

(a)

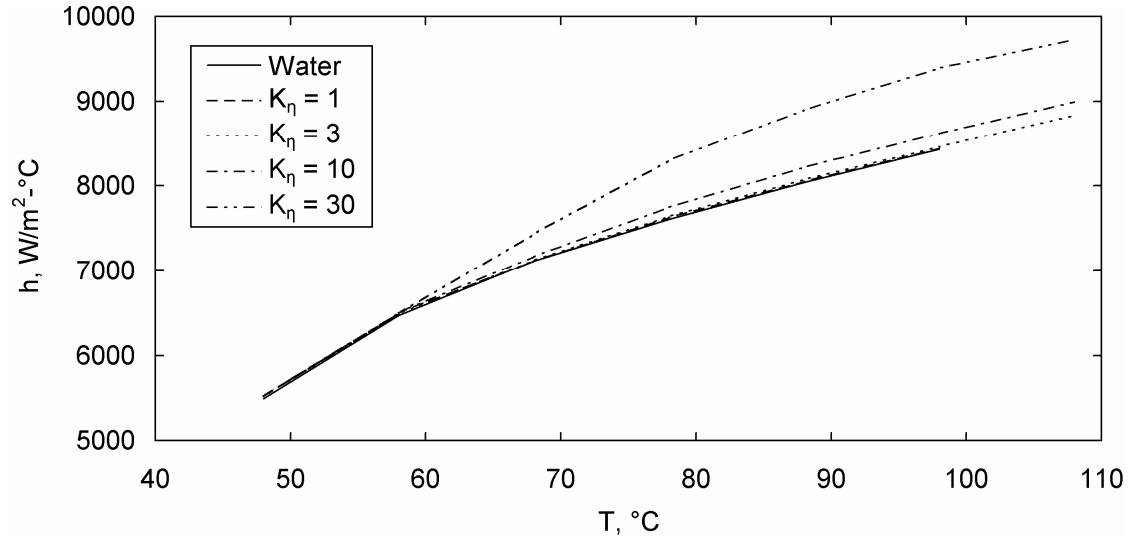

(b)

Figure 5.38. Simulation results for heated wire in FC-72 in water emulsions for K_T = 100, ε_d = 0.5%, T_∞ = (a) 28 °C and (b) 43 °C.

For emulsions of 0.5 and 1% FC-72, increasing the collision efficiency does provide an improvement in the heat transfer coefficient. As in the higher volume fraction case, the effects are more pronounced at higher surface temperature and for lower subcooling. At the highest collision efficiency, the heat transfer coefficient for the 1.0% FC-72 emulsion begins to decrease in the same manner as for the 2% FC-72 emulsion.

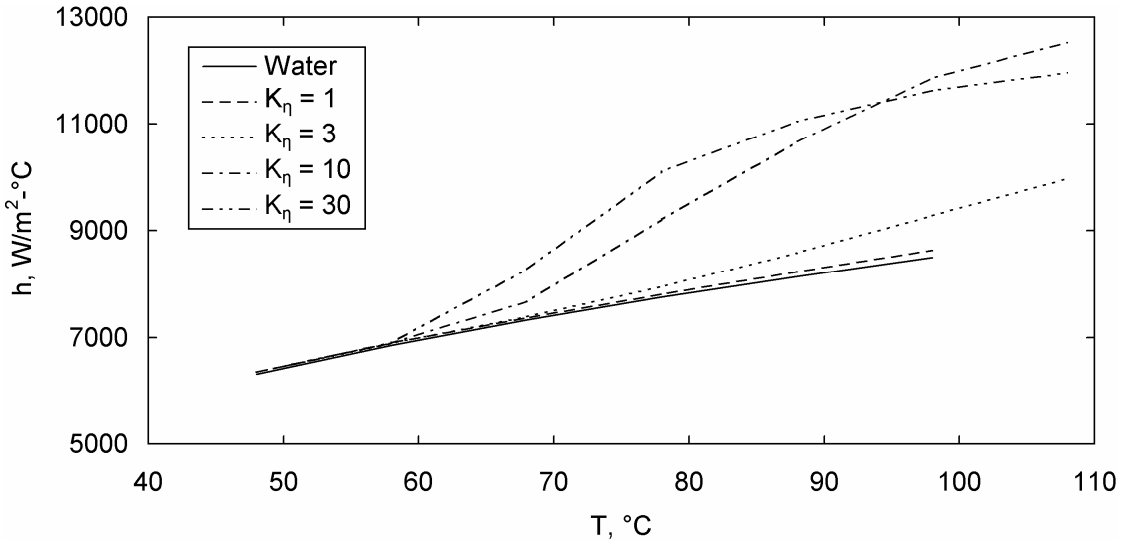

(a)

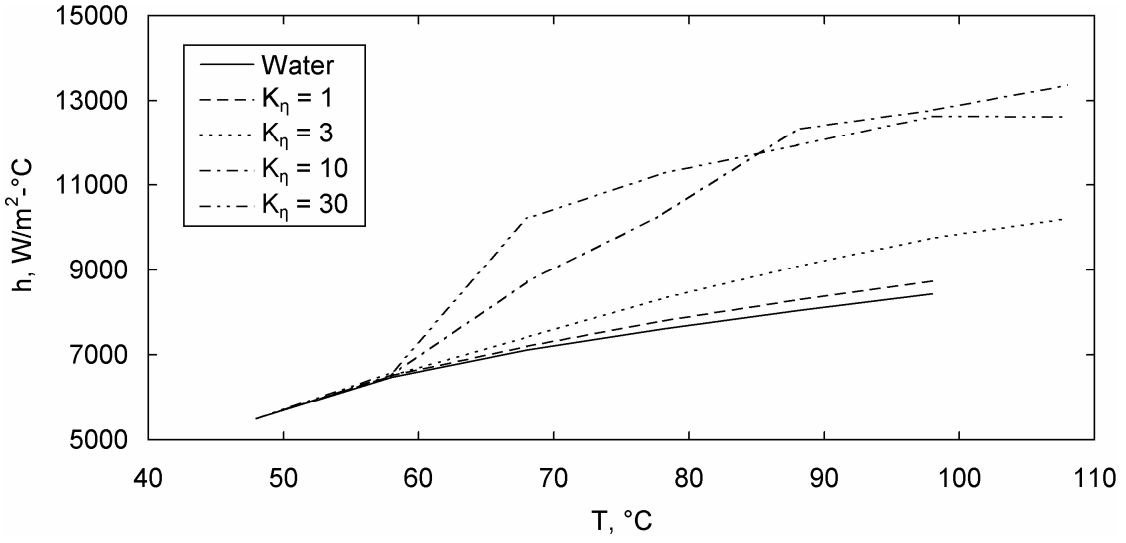

(b)

Figure 5.39. Simulation results for heated wire in FC-72 in water emulsions for K_T = 100, ε_d = 1.0%, T_∞ = (a) 28 °C and (b) 43 °C.

The variables K_T and T_η therefore have rather different effects on the behavior of the simulations. Increasing K_T always increases the heat transfer coefficient, but the heat transfer coefficient remains a very strong function of the dispersed component volume fraction. For a fixed value of K_T, increasing K_η does not significantly increase the maximum heat transfer coefficient that can be achieved by an emulsion. Instead,

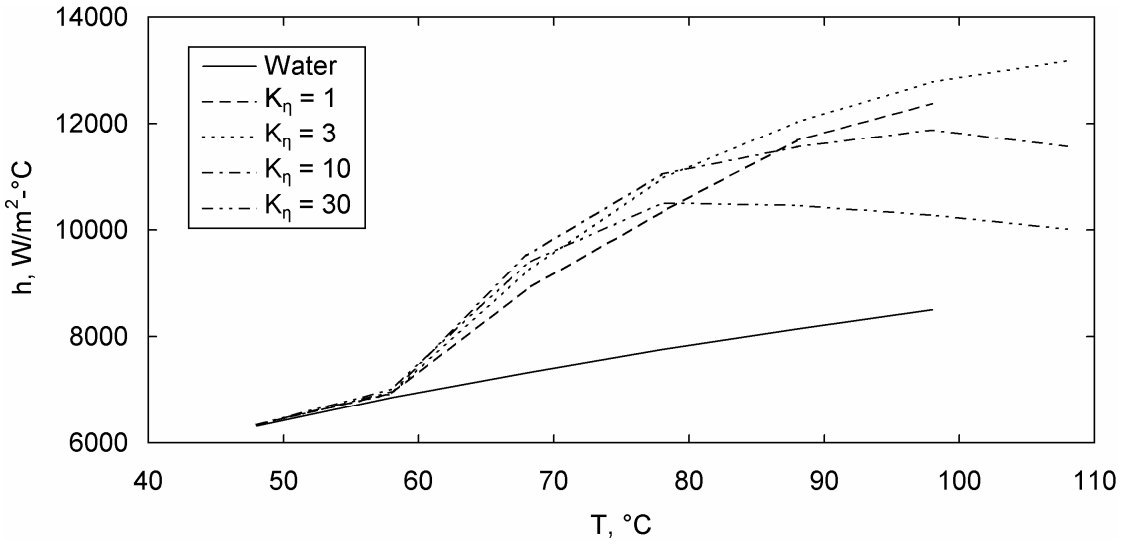

(a)

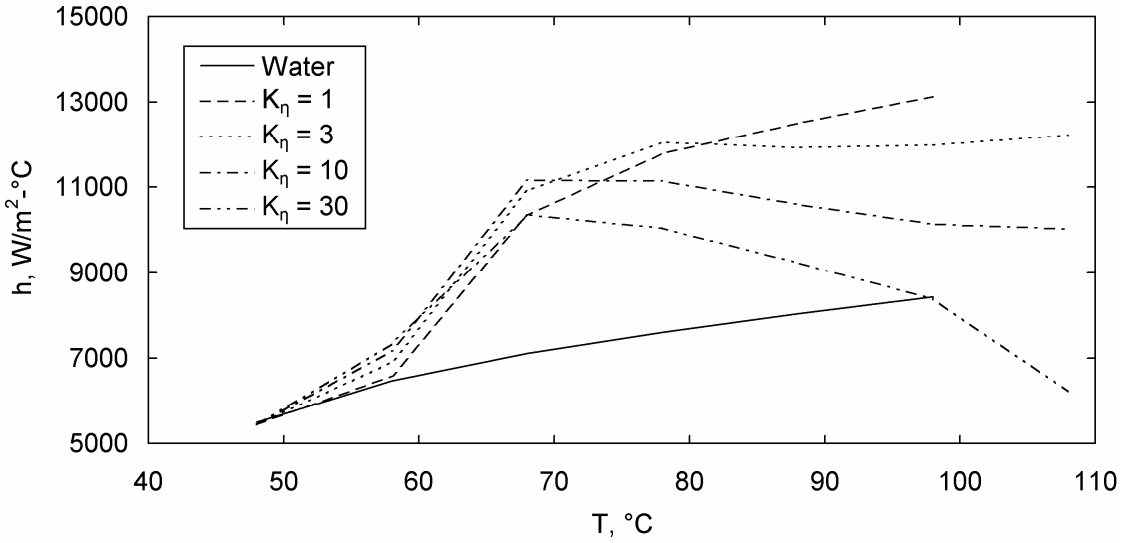

(b)

Figure 5.40. Simulation results for heated wire in FC-72 in water emulsions for K_T = 100, ε_d = 2.0%, T_∞ = (a) 28 °C and (b) 43 °C.

heat transfer is enhanced over a wider range of surface temperatures and dispersed component volume fractions.

5.9.5. Interfacial force scaling

In Section 2.2 a number of interfacial forces were discussed, including drag, virtual mass, lift, and rotational forces. In Section 3.3.1 it was assumed that only drag forces are significant in boiling emulsions. This assumption was evaluated using the

simulation results. A simulation was performed in which the lift, drag, virtual mass, and rotational forces were calculated using Eqs. (2.10) through (2.13) with $C_{vm} = 0.5$ and $C_L = C_R = 0.25$. The simulation conditions were $T_\infty = 28$ °C, $T_{wire} = 98$ °C, $\varepsilon_d = 0.02$, $K_\eta = 1$, and $K_T = 100$.

The simulation results show that the assumption made in Chapter 3 is justified (Fig. 5.41). The lift, rotational, and virtual mass forces are always smaller than the drag forces. Of the three neglected forces, only the virtual mass force for the bubbles is within an order of magnitude of the drag force, and that occurs only near a region of rapid condensation of the bubbles above the thermal boundary layer. None of the neglected forces are significant within the boundary layer. Thus, they would have little effect on heat transfer from the heated wire.

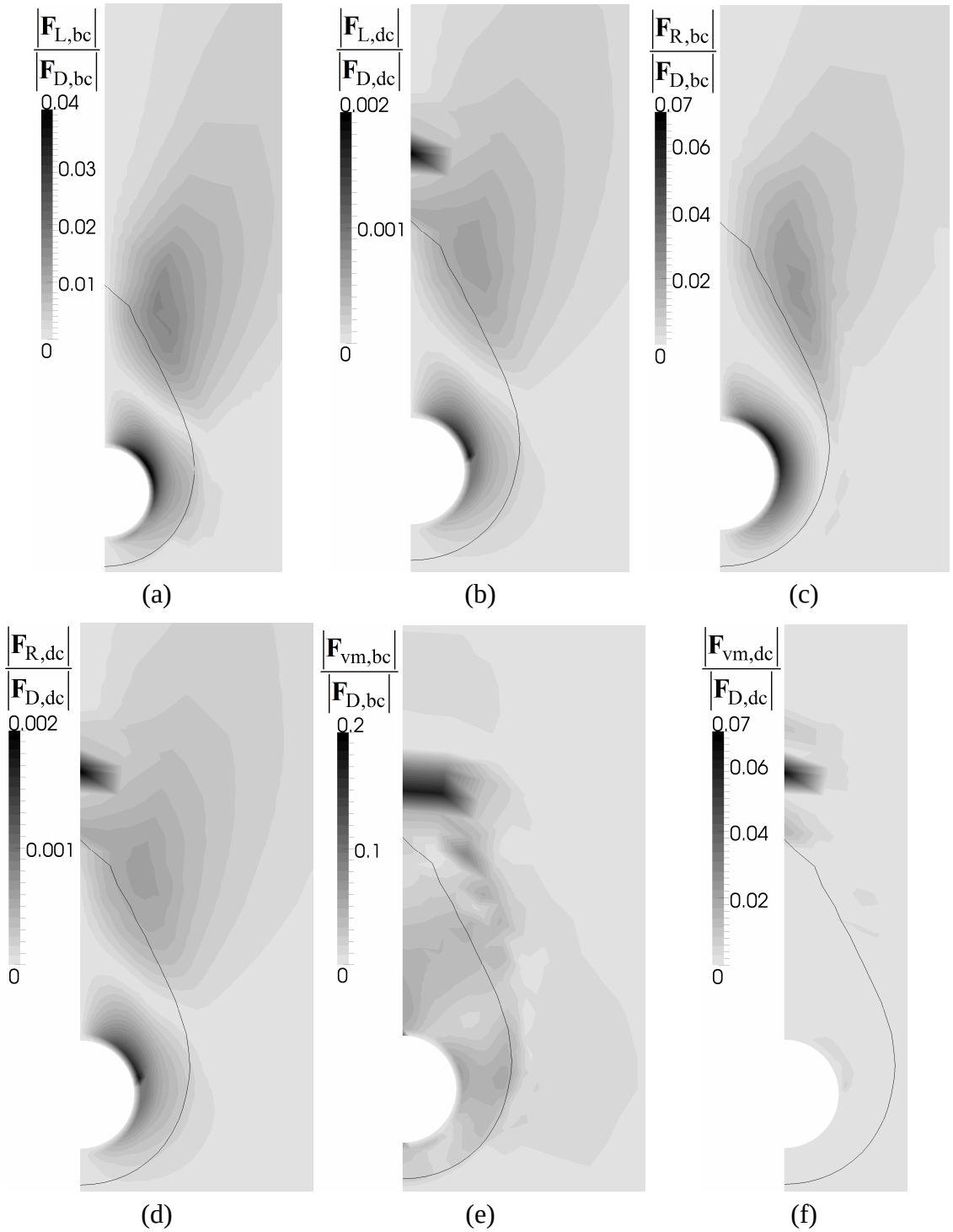

Figure 5.41. Forces near the heated wire, T_{wire} = 98 °C, T_{∞} = 28 °C. (a), (b) Lift to drag force ratio, (c), (d) rotational to drag force ratio, (e), (f) virtual mass to drag force ratio, (g) ε_b, (h) ε_d, (i) $\dot{m}$. Solid line is the T = 56.3 °C isotherm.

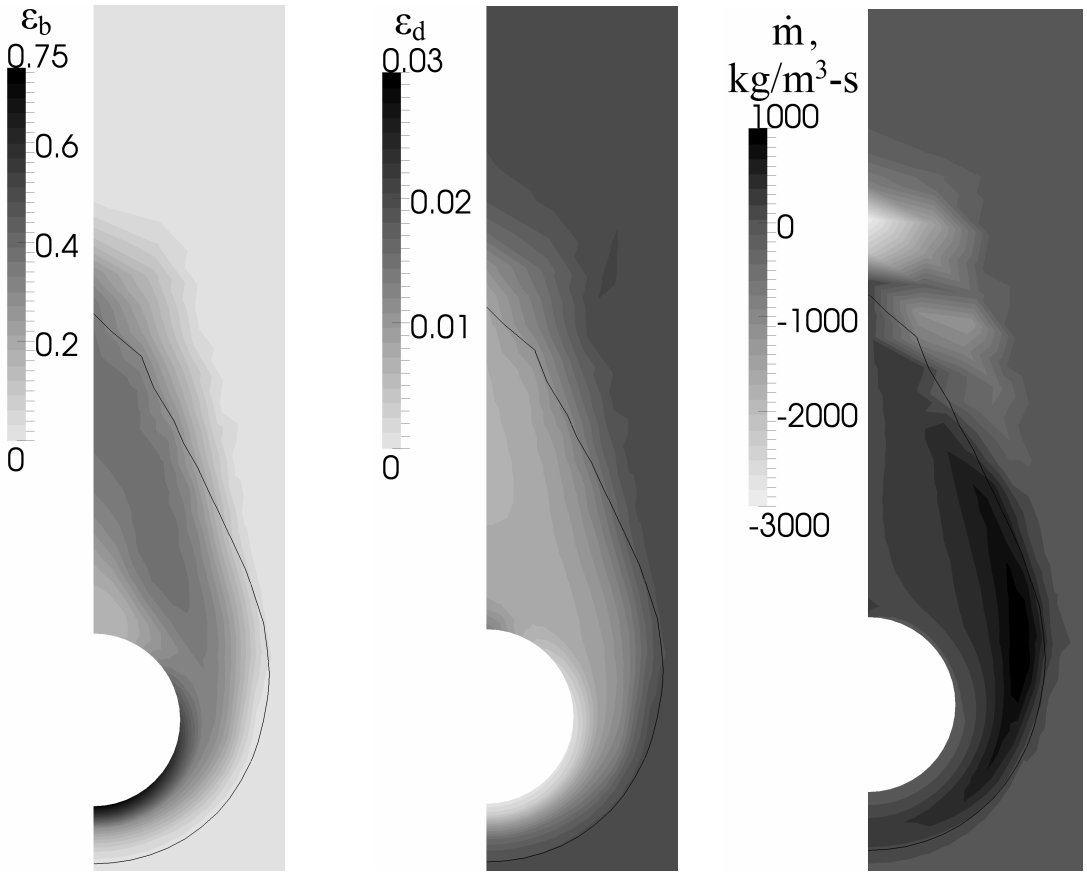

(g) (h) (i)

Figure 5.41 continued.

6. Closure

6.1. Conclusions

The results of the experimental and numerical work are discussed in detail in the previous chapter. Here, the contributions of the present work are summarized, and based on them, future research is suggested.

6.1.1. Experimental work

Enhancement of heat transfer in dilute emulsions by boiling of the low boiling point dispersed component has been demonstrated experimentally by Bulanov and co-workers, but the subject has not otherwise received much attention, and experimental data in the literature is essentially limited to those reported by Bulanov and co-workers. An experimental study was performed to expand the experimental database. Additionally, video was recorded to illuminate the fundamental processes of boiling in dilute emulsions.

Experiments were carried out with emulsions of pentane in water and FC-72 in water, two fluid combinations that have not previously been studied. These fluid combinations have properties closer to emulsions that would have practical use in high heat flux electronics cooling applications than the water in oil and oil in oil emulsions that have been the primary subjects of previous studies. Heat transfer was measured from a heated horizontal wire in a still pool of emulsion, which allows comparison with previous studies that used similar configurations.

Unlike previous studies that looked only at boiling of the dispersed component of the emulsion, the experiments in the present study were extended to surface temperatures higher than the saturation temperature of the continuous component as well. Two distinct boiling heat transfer regimes were observed. At low temperatures boiling of the dispersed component was observed while at high temperatures there was enhanced boiling of the continuous component. The transition between the two regimes occurred at ~ 5 to 15 °C above the saturation temperature of the continuous component. During boiling of the dispersed component, the heat transfer coefficient for the emulsion increases roughly linearly with surface temperature, sometimes after an initial

overshoot in surface temperature. This behavior is similar to previously reported results. When compared on the basis of superheat of the dispersed component, the data for FC-72 in water emulsions and pentane in water emulsions are very similar in the dispersed component boiling region. This result suggests that, aside from saturation temperature, the presence of the dispersed component is more important than its material properties.

During enhanced boiling of the continuous component, the heat transfer coefficient increases much more rapidly with temperature and either parallels or slowly converges towards the behavior predicted by the Rohsenow correlation, $q'' \propto (T - T_{sat})^3$. However, the 0.1% FC-72 emulsion was anomalous in this regard.

The most remarkable result of the visualization experiments is the presence of large attached bubbles on the heated wire. The formation of the bubbles coincides with the inception of boiling as seen in the heat transfer data. Also remarkable is the absence of any visual evidence of individual droplet boiling at very low dispersed component fractions and low temperatures. The large attached bubbles represent an additional boiling mode that has not been reported by previous workers and, when few individual droplets boil, it represents the dominant mode of boiling heat transfer.

6.1.2. Theoretical work

Earlier studies of boiling emulsions have mostly been limited to reporting experimental results and trends in the data. The only previous attempt at formulating a model of the mechanisms at play in boiling dilute emulsions was put forward by Bulanov. However, his model contains several questionable assumptions, some of which are incompatible with each other. Consequently, in the current work a new model was developed that is on more solid physical footing.

First, a one-dimensional model of a single boiling droplet in superheated liquid was developed and used to simulate the behavior of droplets under the conditions found in the thermal boundary layer of a boiling dilute emulsion. The simulations revealed that the droplet boils very quickly so that the resulting bubble overshoots its equilibrium diameter and oscillates for some time. The droplet does not boil rapidly enough to

create a shockwave. The data and insight gained from these simulations were used in the larger model of boiling emulsions.

A model of boiling dilute emulsions was developed based upon the Euler-Euler model of multiphase flows. The general balance equations as developed by Drew and Passman (1999) were applied to the present situation, thus providing a rigorous and physically consistent framework. The model contains three phases, representing the continuous component, liquid droplets of the dispersed component, and bubbles that result from boiling of individual droplets. Mass, momentum, and energy transfer between the phases were modeled based upon the behavior of, and interaction between, individual elements of the dispersed phases.

Boiling mechanisms were modeled based upon the behavior of individual droplets and bubbles, rather than processes at the nanometer scale that are fundamentally unobservable, as in the previous model. Droplet boiling is assumed to occur when a droplet contacts a heated surface with $T > T_{sat}$ or a vapor bubble in a region where $T > T_{sat}$. Collision efficiency between droplets and bubbles and chain-boiling of closely-spaced droplets were considered.

The model is meant to describe the behavior of emulsions in the dispersed component boiling regime, thus it does not account for phase change of the continuous component. The model also does not include the large attached bubbles that were observed in experiments. However, these effects can be added and represent possible avenues of further theoretical work. In fact, the model is extensible in many directions and represents a solid platform for exploration of other geometries and conditions.

6.2. Future work

Boiling in dilute emulsions is a complex phenomenon that has previously received little attention. The main contribution of this work is to place the field on a firm physical foundation. However, many open questions remain and the present work may be extended in several directions. Some significant avenues for further work include,

- The large attached bubbles of the dispersed component are a new discovery and are not included in the present model. The bubbles appear to be the dominant boiling heat transfer mechanism under some circumstances, and therefore deserve closer

study. It is hypothesized that the bubbles enhance heat transfer primarily by circulation within each bubble. That is, vapor condenses in cool surroundings at the top of the bubble and then flows down the side of the bubble in a thin liquid film. The liquid film evaporates at the base of the bubbles (the heated surface), and the vapor circulates back to the top. Analytical work is required to quantify this effect. Direct observation of the flow field around the bubbles, perhaps by particle image velocimetry (PIV), would also be useful to search for other effects of the bubbles.

- The present model takes a rather simplistic view of the agitation of the emulsion by the boiling of droplets, as evidenced by the need for the empirical parameter K_T. One troubling consequence of this view, although not explored in this study, is that the agitation is predicted to be a strong function of the droplet size (Eq. 3.25 and 3.26). In contrast, previous studies that have investigated droplet size have not noted a strong link between the droplet size and heat transfer. An extension of the work in Appendix A to simulate boiling droplets in shear flow or in the presence of other boiling droplets would be beneficial.
- The current model does not include a turbulence model, and therefore is only practical for use in laminar flows. (Direct numerical simulation of turbulence is still possible with the present model, but simulations would probably require more computing resources than is practical.) Work has been done by Rusche (2002) and others on integrating the k-epsilon turbulence model into Euler-Euler models of multiphase flow. Such a turbulence model, if adapted to the present model of boiling emulsions, would also have a benefit for the previous suggestion. It may be possible to directly link the kinetic energy possessed by a boiling droplet to the rate of generation of turbulence kinetic energy.
- The current model uses a correlation for collision efficiency based upon simulations of collisions between two solid spheres. However, in boiling emulsions, droplets, bubbles, and the continuous component all have different viscosities. An analysis or series of simulations of collisions between droplets and bubbles would be beneficial. Additionally, the effects of shear or agitation in the continuous liquid on the collision efficiency should be explored.

- Another aspect of collisions that deserves further attention is the outcome of collisions. In the present model it is assumed that a collision between a droplet and bubble results in the droplet boiling. It is likely, however, that in such a case the droplet would coalesce with the bubble and result in the bubble growing larger. There will also be droplet-droplet and bubble-bubble collisions that can result in coalescence. Accounting for these behaviors would require tracking size distributions for both droplet and bubble phases, which was deemed an unnecessary complication in the present model. These behaviors could also be accounted for by abandoning the Euler-Euler model and developing an Euler-Lagrange model of the emulsion. Such a model would only be usable in very small domains due to the large number density of droplets, even in very dilute emulsions. Such a model may be useful in situations such as microchannels, however.
- Additions to the current model could be made to address the effects of surfactants. Surfactants would impact the outcomes of collisions discussed in the previous suggestion. Surfactants would also change the behavior of the dispersed component at the heated surface. With the discovery of the large attached bubble boiling mechanism, additional experimental work with emulsions with surfactants, especially visual observations of the attached bubbles, would be beneficial.
- Previous experimental studies have found some effects of suspended particles in the dispersed component, which were explained in the context of nucleation within the dispersed droplets. These effects should be explainable within the framework of the current model as well. The behavior of the particles in the large attached bubbles requires investigation as well.
- Finally, this study, as well as most previous experimental studies, focused on heat transfer from thin heated wires. The advantage of this configuration is in the simplicity of the experimental apparatus. However, practical applications of boiling emulsions would involve free convection from flat surfaces or forced convection in small diameter channels. Further study of these configurations is required, both experimental and analytical. It should be confirmed that the behaviors observed for boiling on thin wires also occur in other configurations.

References

Agostini, B., Fabbri, M., Park, J. E., Wojtan, L., Thome, J. R., and Michel, B. (2007), "State of the art of high heat flux cooling technologies," *Heat Transfer Engineering*, **28**(4), pp. 258-281.

Apfel, R. E. (1970), "The role of impurities in cavitation-threshold determination," *Journal of the Acoustical Society of America*, **48**(5), pp. 1179-1186.

Arpaci, V. S. (1991), *Conduction Heat Transfer*, Boston: Pearson Custom Publishing.

Battya, P., Raghavan, V. R., and Seetharamu, K. N. (1984), "Parametric studies on direct contact evaporation of a drop in an immiscible liquid," *International Journal of Heat and Mass Transfer*, **27**(2), pp. 263-272.

Beard, K. V. (1976), "Terminal velocity and shape of cloud and precipitation drops aloft," *Journal of the Atmospheric Sciences*, **33**(5), pp. 851-864.

Beattie, D. R. H. and Whalley, P. B. (1982), "A simple two-phase frictional pressure drop calculation method," *International Journal of Multiphase Flow*, **8**(1), pp. 83-87.

Behzadi, A., Issa, R. I., and Rusche, H. (2004), "Modelling of dispersed bubble and droplet flow at high phase fractions," *Chemical Engineering Science*, **59**(4), pp. 759-770.

Blander, M. and Katz, J. L. (1975), "Bubble Nucleation in Liquids," *AlChE Journal*, **21**(5), pp. 833-848.

Bouré, J. A. and Delhaye, J. M. (1982), "General equations and two-phase flow modeling" in *Handbook of Multiphase Systems*, ed. G. Hetsroni, pp. 1-36 – 1-95, Washington D.C.: Hemisphere Publishing Corporation.

Brennen, C. E. (1995), *Cavitation and Bubble Dynamics*, New York: Oxford University Press.

Buivid, M. G. and Sussman, M. V. (1978), "Superheated liquids containing suspended particles," *Nature*, **275**, pp. 203-205.

Bulanov, N. V. (2001), "An analysis of the heat flux density under conditions of boiling internal phase of emulsion," *High Temperature*, **39**(3), pp. 462-469.

Bulanov, N. V. and Gasanov, B. M. (2005), "Experimental setup for studying the chain activation of low-temperature boiling sites in superheated liquid droplets," *Colloid Journal*, **67**(5), pp. 531-536.

Bulanov, N. V. and Gasanov, B. M. (2006), "Characteristic features of the boiling of emulsions having a low-boiling dispersed phase," *Journal of Engineering Physics and Thermophysics*, **79**(6), pp. 1130-1133.

Bulanov, N. V. and Gasanov, B. M. (2007), "Special features of boiling of emulsions with a low-boiling dispersed phase," *Heat Transfer Research*, **38**(3), pp. 259-273.

Bulanov, N. V. and Gasanov, B. M. (2008), "Peculiarities of boiling of emulsions with a low-boiling disperse phase," *International Journal of Heat and Mass Transfer*, **51**, pp. 1628-1632.

Bulanov, N. V., Gasanov, B. M., and Turchaninova, E. A. (2006), "Results of experimental investigation of heat transfer with emulsions with low-boiling disperse phase," *High Temperature*, **44**(2), pp. 267-282.

Bulanov, N. V., Skripov, V. P., Gasanov, B. M., and Baidakov, V. G. (1996), "Boiling of emulsions with a low-boiling dispersed phase," *Heat Transfer Research*, **27**(5), pp. 312-315.

Bulanov, N. V., Skripov, V. P., and Khmylnik, V. A. (1993), "Heat transfer to emulsion with a low-boiling disperse phase," *Heat Transfer Research*, **25**(6), pp. 786-789.

Bulanov, N. V., Skripov, V. P., and Khmyl'nin, V. A. (1984), "Heat transfer to emulsion with superheating of its disperse phase," *Journal of Engineering Physics*, **46**(1), pp. 1-3.

Buyevich, Yu. A. (1992), "Heat and mass transfer in disperse media – II. Constitutive equations," *International Journal of Heat and Mass Transfer*, **35**(10), pp. 2453-2463.

Chen, T., Klausner, J. F., Garimella, S. V., and Chung, J, N. (2006), "Subcooled boiling incipience on a highly smooth microheater," *International Journal of Heat and Mass Transfer*, **49**, pp. 4399-4406.

Drew, D. A. and Passman, S. L (1999), *Theory of Multicomponent Fluids*, New York: Springer.

Frost, D. and Sturtevant, B. (1986), "Effects of ambient pressure on the instability of a liquid boiling explosively at the superheat limit," *Transactions of the ASME: Journal of Heat Transfer*, **108**(2), pp. 418-424.

Gidaspow, D. (1994), *Multiphase Flow and Fluidization*, Boston, MA: Academic Press.

Goebel, A. and Lunkenheimer, K. (1997), "Interfacial tension of the water/n-alkane interface," *Langmuir*, **13**(2), pp. 369-372.

Gosman, A. D., Lekakou, C., Politis, S., Issa, R. I., and Looney, M. K. (1992), "Multidimensional modeling of turbulent two-phase flow in stirred vessels," *AIChE Journal*, **38**(12), pp. 1946-1956.

Haber, S. and Hetsroni, G. (1971). "The dynamics of a deformable drop suspended in an unbounded Stokes flow," *Journal of Fluid Mechanics*, 49, pp. 257-277.

Hao, Y. L. and Tao, Y. X. (2003). "Non-thermal equilibrium melting of granular packed bed in horizontal forced convection. Part I: experiment," *International Journal of Heat and Mass Transfer*, 46(26), pp. 5017-5030.

Hao, Y. L. and Tao, Y. X. (2003). "Non-thermal equilibrium melting of granular packed bed in horizontal forced convection. Part II: numerical simulation," *International Journal of Heat and Mass Transfer*, 46(26), pp. 5031-5044.

Hao, Y. L. and Tao, Y. X. (2004). "A numerical model for phase-change suspension flow in microchannels," *Numerical Heat Transfer, Part A: Applications*, 46(1), pp. 55-77.

Hill, D. P. (1998), "The computer simulation of dispersed two-phase flows," Ph.D. Thesis, University of London, London.

Iida, Y., Okuyama, K., and Sakurai, K. (1994), "Boiling nucleation on a very small film heater subjected to extremely rapid heating," *International Journal of Heat and Mass Transfer*, **37**(17), pp. 2771-2780.

Ishii, M. and Zuber, N. (1979), "Drag coefficient and relative velocity in bubbly, droplet or particulate flows," *AIChE Journal*, **25**(5), pp. 843-855.

Kagan, Yu. (1960), "The Kinetics of boiling of a pure liquid," *Russian Journal of Physical Chemistry*, **34**(1), pp. 42-46.

Kandlikar, S. G. and Grande, W. J. (2004), "Evaluation of single phase flow in microchannels for high heat flux chip cooling – thermohydraulic performance enhancement and fabrication technology," *Heat Transfer Engineering*, **25**(8), pp. 5-16.

Katz, J. L. and Blander, M. (1973), "Condensation and boiling: corrections to homogeneous nucleation theory for nonideal gases," *Journal of Colloid and Interface Science*, **42**(3), pp. 496-502.

Katz, J. L., Saltsburg, H., and Reiss, H. (1966), "Nucleation in associated vapors," *Journal of Colloid and Interface Science*, **21**, pp. 560-568.

Kays, W. M., Crawford, M. E., and Weigand, B. (2005), *Convective Heat and Mass Transfer, 4th Ed.*, Boston, MA: McGraw-Hill.

Kenrick, F. B., Gilbert, C. S., and Wismer, K. L. (1924), "The superheating of liquids," *Journal of Physical Chemistry*, **28**, pp. 1297-1307.

Kumar, V., Gupta, P., and Nigam, K. D. P. (2007), "Fluid flow and heat transfer in curved tubes with temperature-dependent properties," *Industrial and Engineering Chemistry Research*, **46**, pp. 3226-3236.

Kwak, HY., Oh, SD., and Park, CH. (1995), "Bubble dynamics on the evolving bubble formed from the droplet at the superheat limit," *International Journal of Heat and Mass Transfer*, **38**(9), pp. 1709-1718.

Lee, H. S. and Merte, H. (1996), "Spherical vapor bubble growth in uniformly superheated liquids," *International Journal of Heat and Mass Transfer*, **39**(12), pp. 2427-2447.

Lee, H. S. and Merte, H. (2005), "Explosive vapor bubble growth in uniformly superheated liquids: R-113 and mercury," *International Journal of Heat and Mass Transfer*, **48**, pp. 2593-2600.

Lide, D. R. (2010), "Electrical Resistivity of Pure Metals," in *CRC Handbook of Chemistry and Physics*, 90th Ed. (Internet Version 2010), CRC Press/Taylor and Francis, Boca Raton, FL.

Lien, Y.-C. (1969), "Bubble Growth Rates at Reduced Pressure," Ph.D. Thesis, Massachusetts Institute of Technology, Cambridge, Massachusetts.

Lienhard, J. H. IV and Lienhard, J. H. V (2008), *A Heat Transfer Textbook, 3rd Ed.*, Cambridge, MA: Phlogiston Press. Online version 1.31 retrieved November 13, 2009 from http://web.mit.edu/lienhard/www/ahtt.html.

Mahood, H. B. (2008), "Direct-contact heat transfer of a single volatile liquid drop evaporation in an immiscible liquid," *Desalination*, **222**, pp. 656-665.

Maxwell, J. C. (1904), *A Treatise on Electricity and Magnetism, 3rd Ed.*, Oxford UK: Clarendon Press.

Mikic, B. B., Rohsenow, W. M., and Griffith, P. (1970), "On bubble growth rates," *International Journal of Heat and Mass Transfer*, **13**(4), pp. 657-666.

Moore, G. R. (1959), "Vaporization of superheated drops in liquid," *AIChE Journal*, **5**(4), pp. 458-466.

Morgan, V. T. (1975), "The overall convective heat transfer from smooth circular cylinders," in *Advances in Heat Transfer*, **11**, pp. .

Mori, Y. H., Inui, E., and Komotori, K. (1978), "Pool boiling heat transfer to emulsions," *Transactions of the ASME Journal of Heat Transfer*, **100**(4), pp. 613-617.

OpenCFD Ltd. (2009), *OpenFOAM: The Open Source CFD Toolbox – Programmer's Guide*, version 1.6, http://www.openfoam.com/docs/, retrieved February 6, 2010.

OpenCFD Ltd. (2009), *OpenFOAM: The Open Source CFD Toolbox – User Guide*, version 1.6, http://www.openfoam.com/docs/, retrieved February 6, 2010.

Ostrovskiy, N. Yu. (1988), "Free-convection heat transfer in the boiling of emulsions," *Heat Transfer-Soviet Research*, **20**(2), pp. 147-153.

Panton, R. L. (2005), *Incompressible Flow, 3rd Edition*, Hoboken, NJ: John Wiley and Sons.

Park, HC., Byun, KT., and Kwak, HY. (2005), "Explosive boiling of liquid droplets at their superheat limits," *Chemical Engineering Science*, **60**, pp. 1809-1821.

Patankar, S. V. (1980), *Numerical Heat Transfer and Fluid Flow*, New York: McGraw-Hill.

Pavlov, P. A and Skripov, V. P. (1970), "Explosive boiling of liquids and fluctuation nucleus formation," *High Temperature*, **8**(4), pp. 833-839.

Peskin, R. L. (1982), "Turbulent fluid-particle interaction" in *Handbook of Multiphase Systems*, ed. G. Hetsroni, pp. 1-184 – 1-204, Washington D.C.: Hemisphere Publishing Corporation.

Pinksy, M., Khain, A., and Shapiro, M. (2001), "Collision efficiency of drops in a wide range of Reynolds numbers: Effects of pressure on spectrum evolution," *Journal of the Atmospheric Sciences*, **58**, pp. 742-764.

Plesset, M. S. and Prosperetti, A. (1977), "Bubble dynamics and cavitation," *Annual Review of Fluid Mechanics*, **9**, pp. 148-185.

Plesset, M. S. and Zwick, S. A. (1954), "The growth of vapor bubbles in superheated liquids," *Journal of Applied Physics*, **25**(4), pp. 493-500.

Pope, S. B. (2000), *Turbulent Flows*, Cambridge, UK: Cambridge University Press.

Raina, G. K. and Grover, P. D. (1985), "Direct contact heat transfer with change of phase: Theoretical model incorporating sloshing effects," *AIChE Journal*, **31**(3), pp. 507-510.

Rayleigh (1917), "On the pressure developed in a liquid during the collapse of a spherical cavity," *London, Edinburgh, and Dublin Philosophical Magazine and Journal of Science*, **34** (sixth series), pp. 94-98.

Roesle, M. L. and Kulacki, F. A. (2008), "Characteristics of Two-Component Two-Phase Flow and Heat Transfer in a Flat Microchannel," *Proceedings of the 2008 ASME Summer Heat Transfer Conference*, New York: ASME.

Rohsenow, W. M. (1952), "A method of correlating heat transfer data for surface boiling of liquids," *Transactions of the ASME*, **74**(6), pp. 969-975.

Rusche, H. (2002), "Computation fluid dynamics of dispersed two-phase flows at high phase fractions," Ph.D. Thesis, University of London, London.

Rusche, H. and Issa, R. I. (2000), "The effect of voidage on the drag force on particles, droplets, and bubbles in dispersed two-phase flow," *Japanese European Two-Phase Flow Meeting*, Tsukuba, Japan.

Shepherd, J. E. and Sturtevant, B. (1982), "Rapid evaporation at the superheat limit," *Journal of Fluid Mechanics*, **121**, pp. 379-402.

Sideman, S. and Taitel, Y. (1964), "Direct-contact heat transfer with change of phase: Evaporation of drops in an immiscible liquid medium," *International Journal of Heat and Mass Transfer*, **7**, pp. 1273-1289.

Silva, L. F. L. R. and Lage, P. L. C., "Implementation of an eulerian multi-phase model in OpenFOAM and its application to polydisperse two-phase flows," *Proceedings of the OpenFOAM International Conference*, 2007, http://www.opensourcecfd.com/conference2008/2007/index.php?option=com_content&task=view&id=3&Itemid=30, retrieved February 6, 2010.

Skripov, V. P. (1974), *Metastable Liquids*, New York: John Wiley and Sons.

Soo, S. L. (1967), *Fluid Dynamics of Multiphase Systems*, Blaisdell Publishing, Waltham, Massachusetts.

Steinke, M. E. and Kandlikar, S. G. (2004), "Single-phase heat transfer enhancement techniques in microchannel and minichannel flows," *Proceedings of the Second International Conference on Microchannels and Minichannels*, ASME, New York.

Strasberg, M. (1959), "Onset of ultrasonic cavitation in tap water," Journal of the Acoustical Society of America, **31**(2), pp. 163-176.

Sung, M. K. and Mudawar, I. (2009), "CHF determination for high-heat flux phase change cooling system incorporating both micro-channel flow and jet impingement," *International Journal of Heat and Mass Transfer*, **52**, pp. 610-619.

Taylor, G. I. (1932), "The viscosity of a fluid containing small drops of another fluid," *Proceedings of the Royal Society of London, Series A*, **138**(834), pp. 41-48.

Theofanous, T. G. and Patel, P. D. (1976), "Universal relations for bubble growth," *International Journal of Heat and Mass Transfer*, **19**, pp. 425-429.

Thome, J. R. (2006), "The new frontier in heat transfer: Microscale and nanoscale technologies," *Heat Transfer Engineering*, **27**(9), pp. 1-3.

Tochitani, Y., Mori, Y. H., and Komotori, K. (1977), "Vaporization of single liquid drops in an immiscible liquid part 1: Forms and motions of vaporizing drops," *Wärme- und Stoffübertragung*, **10**, p. 51-59.

Tochitani, Y., Nakagawa, T., Mori, Y.H., and Komotori, K. (1977), "Vaporization of single liquid drops in an immiscible liquid part 2: Heat transfer characteristics," *Wärme- und Stoffübertragung*, **10**, p. 71-79.

Topping, J. (1962), *Errors of Observation and Their Treatment, 3rd Ed*, Chapman and Hall, London

Tuckerman, D. B. and Pease, R. F. W. (1981), "High-performance heat sinking for VLSI," *IEEE Electron Device Letters*, **2**(5), pp. 126-129.

Vuong, S. T. and Sadhal, S. S. (1989), "Growth and translation of a liquid-vapour compound drop in a second liquid, Part 1: Fluid mechanics," *Journal of Fluid Mechanics*, **209**, pp. 617-637.

Vuong, S. T. and Sadhal, S. S. (1989), "Growth and translation of a liquid-vapour compound drop in a second liquid, Part 2: Heat transfer," *Journal of Fluid Mechanics*, **209**, pp. 639-660.

Wakeshima, H. and Takata, K. (1958), "On the limit of superheat," *Journal of the Physical Society of Japan*, **13**(11), pp. 1398-1403.

Wallis, G. B. (1969), *One-dimensional Two-phase Flow*, McGraw-Hill, New York.

Wismer, K. L. (1922), "The pressure-volume relation of superheated liquids," *Journal of Physical Chemistry*, **22**(4), pp. 301-315.

Wohak, M. G. and Beer, H. (1998), "Numerical simulation of direct-contact evaporation of a drop rising in a hot, less volatile immiscible liquid of higher density – possibilities and limits of the SOLA-VOF/CSF algorithm," *Numerical Heat Transfer, Part A: Applications*, **33**, pp. 561-582.

Wojtan, L., Revellin, R., and Thome, J. R. (2006), "Investigation of saturated critical heat flux in a single, uniformly heated microchannel," *Experimental Thermal and Fluid Science*, **30**, pp. 765-774.

Xing, K. Q., Tao, Y. X., and Hao, Y. L. (2006), "Slurry viscosity study and its influence on heat transfer enhancement effect of PCM slurry flow in micro/mini channels," *Proceedings of the 2006 ASME International Mechanical Engineering Congress and Exposition*, New York: ASME.

Zhang, H., Mudawar, I., and Hasan, M. H. (2007), "Assessment of dimensionless CHF correlations for subcooled flow boiling in microgravity and Earth gravity," *International Journal of Heat and Mass Transfer*, **50**, pp. 4568-4580.

Appendix A.

Simulation of boiling droplets

To understand the behavior of boiling emulsions, it is helpful to first understand what happens when a small, highly-superheated droplet boils. Some key questions are how long the boiling process takes, how the bubble behaves after all the liquid in the droplet has evaporated, and what effect the boiling process has on the surrounding liquid.

The growth of vapor bubbles in liquid has been the subject of intense study for several decades. Early studies examined the expansion of vapor bubbles in an infinite domain of uniformly superheated liquid. In these studies the bubble is generally assumed to be stationary in the surrounding liquid and spherical. Expansion of the bubble is initially limited by the inertia of the liquid and later by thermal diffusion to the bubble surface. More recently boiling in suspended droplets has received increasing attention. Typically the droplets under study have d_d ~1 mm, as are found in direct contact heat exchangers. Buoyancy becomes important in these cases because the growing vapor bubble rises through the liquid with the evaporating droplet suspended from the bottom of the bubble. The rate of boiling in these cases is determined by convection to the bubble-droplet pair as they rise through the surrounding liquid.

The droplets that make up the emulsions studied in this thesis are two to three orders of magnitude smaller than those found in direct contact heat exchangers, and so their behavior during boiling is also quite different. Such small droplets have insignificant drift velocity and boil so quickly that gravitational effects are negligible. And unlike the bubble expanding in superheated liquid, the heat transfer properties of the liquid around the droplet are important in the later stages of boiling. The behavior of the bubble after the droplet has completely evaporated also merits examination. A better understanding of how boiling occurs in such small droplets is important to understanding the overall behavior of a boiling dilute emulsion.

Because studies of boiling droplets for direct contact heat exchangers generally do not address these issues, a numerical study of boiling droplets has been performed. A

one-dimensional model of a boiling droplet that includes both the momentum and thermal energy equations has been developed, and a series of simulations performed for conditions typical of those found in boiling emulsions.

A.1. Prior work

The growth of vapor bubbles in a superheated liquid is a complicated phenomenon and involves the effects of thermal diffusion and inertia in the surrounding liquid, and surface tension at the surface of the bubble. Different effects are dominant at different times and under different conditions and accurate modeling of all stages of bubble growth has only been accomplished with numerical simulations. Boiling of large suspended droplets is more complex still, as buoyancy causes the droplet and bubble to move through the surrounding liquid and lose spherical symmetry.

Generally, a vapor bubble that forms in superheated liquid undergoes three phases of growth. The bubble starts with the same temperature as the surrounding liquid and its growth is driven by the difference between the vapor pressure inside the bubble and the ambient pressure. Immediately after the bubble first forms, this driving pressure difference is nearly balanced by the surface tension of the bubble and the bubble experiences surface tension dominated growth (Fig. A.1a). The pressure jump due to surface tension varies with the inverse of the bubble diameter so that the effect of surface tension quickly becomes negligible as the bubble size increases. After the pressure jump due to surface tension becomes small the rate of bubble growth is limited by the inertia of the surrounding liquid (Fig. A.1b). As the bubble continues to expand, evaporation at the bubble surface causes its temperature to decrease. The vapor pressure in the bubble decreases until eventually there is zero driving force due to pressure difference. From this point on the bubble growth is limited by the rate of heat diffusion to the bubble surface (Fig. A.1c). For a bubble growing in uniformly-superheated liquid, this phase of growth continues indefinitely (Lee and Merte, 1996).

Mikic, Rohsenow, and Griffith (1970) developed an analytical solution for vapor bubbles growing in uniformly superheated liquid, valid in both the inertia and thermal diffusion dominated phases. They find a set of scaled coordinates,

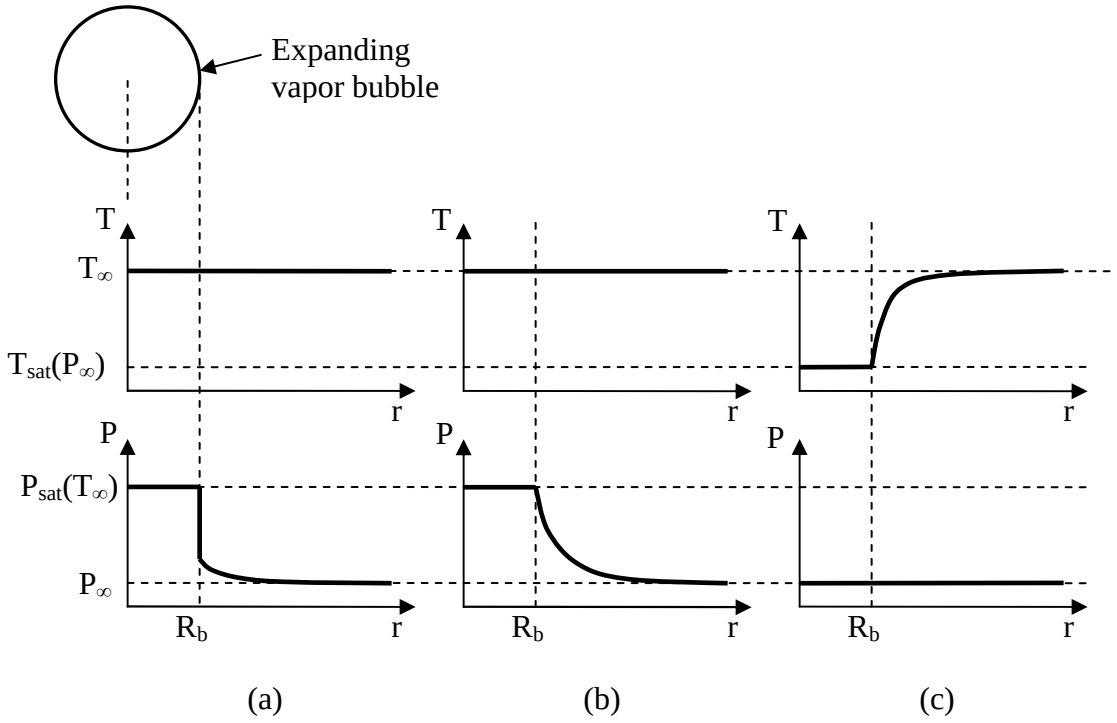

Figure A.1. Pressure and temperature fields in and around vapor bubbles for (a) surface tension-dominated growth, (b), inertia-dominated growth, and (c) thermal diffusion-dominated growth.

$$R^+ = \frac{\pi}{12}\sqrt{\frac{2i_{fg}\rho_v\Delta T}{3\rho_f T_{sat}}}\,\frac{R}{Ja^2\alpha_f}, \tag{A.1a}$$

$$t^+ = \frac{\pi}{18}\,\frac{h_{fg}\rho_v\Delta T}{\rho_f T_{sat}}\,\frac{t}{Ja^2\alpha_f}, \tag{A.1b}$$

for which bubble growth is described by,

$$R^+ = \frac{2}{3}\left[\left(t^+ + 1\right)^{3/2} - \left(t^+\right)^{3/2} - 1\right]. \tag{A.2}$$

Like most analytical solutions, this one neglects surface tension. This equation approaches the solution of Plesset and Zwick (1954) for thermal diffusion dominated growth at large t^+ ($R^+ \approx (t^+)^{1/2}$). At small t^+, the bubble radius increases linearly with time ($R^+ \approx t^+$), similar to the Rayleigh solution for inertia dominated growth (Rayleigh, 1917). Unlike the Rayleigh solution however, Eq. (A.1) does not contain the driving pressure difference. Instead the pressure difference is replaced with the driving temperature difference ΔT through the use of a linear approximation of the Clausius-Clapeyron equation. The approximation can result in under prediction of the bubble growth rate for large degrees of superheat (Theofanous and Patel, 1976), Eq. (A.2) is found to agree well with experimental data for moderate superheat (Lien, 1969). The quantity ΔT is the difference between the ambient temperature T_∞ and the saturation temperature at the ambient pressure, $T_{sat}(P_\infty)$.

Analytical solutions are generally not possible when more accurate models of fluid properties or the thermal boundary layer are utilized. A numerical study by Lee and Merte (1996) uses accurate models of fluid properties and simulates the temperature field surrounding the bubble. They also include the surface tension of the bubble in their model. They begin their simulations with a bubble radius very close to the critical bubble radius, R_{cr},

$$R_{cr} = \frac{2\sigma}{P_{sat}(T_\infty) - P_\infty}. \qquad \text{(A.3)}$$

Because a bubble at the critical radius is in unstable equilibrium, a small perturbation in the bubble radius is required to cause the bubble to expand. Lee and Merte show that for small perturbations, the magnitude of the perturbation has no effect on the subsequent expansion of the bubble aside from a small change in the time that elapses before the bubble begins to expand rapidly. Their simulations show good agreement with experimental studies for a wide range of fluids, ambient pressures, and degrees of superheat. They also find that the earlier model of Mikic et al. is accurate in many

cases except for the earliest stage of bubble growth where surface tension plays a significant role.

These studies of bubbles in uniformly superheated liquid have limited applicability to suspended droplets because they do not consider the interaction between the bubble, droplet, and the surrounding liquid, as well as the loss of spherical symmetry that occurs due to buoyancy. Sideman and Taitel (1964) study evaporating droplets of superheated pentane and butane with $1.9 < d_d < 3.9$ mm. They develop an analytical model and find a relation between the Nusselt and the Péclet numbers of the evaporating droplet. They assume that the bubble is spherical with the droplet forming a layer around the bottom portion of the bubble and steady potential flow around the bubble and droplet as they rise due to buoyancy. They find the rate of heat transfer to the droplet and compare it to experimental results obtained by photographing droplets undergoing boiling while rising through water. Tochitani and co-workers (Tochitani, Mori, and Komotori, 1977; Tochitani, Nakagawa, Mori, and Komotori, 1977) also develop an analytical model of heat transfer to a boiling droplet using a geometric model of the droplet similar to that of Sideman and Taitel, but assume that the flow around the droplet is Stokes flow rather than potential flow. They also find a relationship between the Nusselt and the Péclet numbers and find that it matches experimental results for $0.8 < d_d < 1.4$ mm and $Re < 1$. Battya, Raghavan, and Seetharamu (1984) re-examine the data of Sideman and Taitel and find that the Nusselt number also depends on the Jakob number. The correlations of Sideman and Taitel, Tochitani et al., and Battya et al. all predict that $Nu \rightarrow 0$ as $Pe \rightarrow 0$, and thus none of them are appropriate for very small droplets that have negligible velocity relative to the surrounding liquid.

Other researchers have examined boiling droplets using more sophisticated models of the geometry of the bubble and droplet (Vuong and Sadhal, 1989a, 1989b). Raina and Grover (1985) study the effects of sloshing of the droplet around the bubble. Mahoud (2008) performs numerical simulations of boiling droplets in which the bubble and droplet are concentric, and Wohak and Beer (1998) perform axisymmetric simulations of a boiling deformable droplet. All of these studies examine droplets with

d_d ~ 1 mm that boil in time scales of milliseconds to seconds. Therefore they address a different set of processes and forces than are dominant in boiling of very small droplets.

Shepherd and Sturtevant (1982) address rapid boiling of a superheated droplet. They observe boiling in droplets near their limit of superheat and compare the rate of expansion to the classical models of inertia dominated growth and thermal diffusion dominated growth for $0.5 < d_d < 1$ mm. They find that the vapor bubble grows more rapidly than predicted for thermal diffusion growth when the bubble reaches approximately the original size of the droplet. They attribute this deviation from theory to instabilities that roughen the bubble surface. They also observe oscillation of the resulting vapor bubble and instabilities that occur there as well. Thus, although this study observes bubble growth on a time scale close to that of droplets boiling in emulsions, it is principally concerned with instability that occurs at much larger length scales. Lee and Merte (2005) and Frost and Sturtevant (1986) also address instability of large boiling droplets near the superheat limit.

Kwak, Oh, and Park (1995) study the oscillating bubble that results from a droplet boiling at its superheat limit. They develop coupled differential equations for the evolution over time of the bubble pressure, temperature, radius and velocity, and the thickness of the thermal boundary layer:

$$\frac{dP_b}{dt} = -\frac{3\gamma P_b}{R_b}\frac{dR_b}{dt} - \frac{6(\gamma-1)k_c(T_b - T_\infty)}{\delta_t R_b}, \tag{A.4}$$

$$\frac{dT_b}{dt} = -\frac{3(\gamma-1)T_b}{R_b}\frac{dR_b}{dt} - \frac{6(\gamma-1)k_c T_b(T_b - T_\infty)}{\delta_t R_b P_b}, \tag{A.5}$$

$$R_b\frac{du}{dt} + \frac{3}{2}u^2 = \frac{1}{\rho_c}(P_b - P_\infty), \tag{A.6}$$

$$u = \frac{dR_b}{dt}, \tag{A.7}$$

$$\left[1+\frac{\delta_t}{R_b}+\frac{3}{10}\left(\frac{\delta_t}{R_b}\right)^2\right]\frac{d\delta_t}{dt}=\frac{6\alpha_c}{\delta_t}-\left[\frac{2\delta_t}{R_b}+\frac{1}{2}\left(\frac{\delta_t}{R_b}\right)^2\right]\frac{dR_b}{dt}-$$
$$\delta_t\left[1+\frac{\delta_t}{2R_b}+\frac{1}{10}\left(\frac{\delta_t}{R_b}\right)^2\right]\frac{1}{(T_b-T_\infty)}\frac{dT_b}{dt}. \quad \text{(A.8)}$$

They assume a quadratic temperature profile in the boundary layer. Because the last term of Eq. (A.8) contains the temperature difference ($T_b - T_\infty$) in the denominator, they artificially set $d\delta_t/dt = 0$ when $|T_b - T_\infty| < 0.21°C$. This restriction ensures that the boundary layer thickness remains small compared to the bubble radius. They do not address in detail the boiling process that leads to the oscillating bubble. Park, Byun, and Kwak (2005) compare this model to experimental results for droplets of different hydrocarbons with $d_d \sim 1$ mm boiling at their superheat limit, and also develop a model for the pressure field far from the droplet during boiling. Park et al. add viscous and surface tension terms to Eq. (A.6) although, for the size of the bubble they simulate, surface tension effects should be negligible and there should be no viscous forces for radially symmetric motion of the bubble.

A.2. Boiling model

In order to gain an accurate picture of all stages of the boiling process in very small suspended droplets, a series of numerical simulations were performed for various droplet sizes, degrees of superheat, and combinations of fluid parameters for the droplet and surrounding liquid. The simulations include thermal diffusion through the liquid surrounding the vapor bubble and the momentum of the liquid. A key simplifying assumption is that the bubble nucleus forms, and remains, at the center of the spherical droplet so that spherical symmetry is maintained (Fig A.2a). Furthermore, the liquids are assumed to be incompressible and have constant properties, although the droplet and the surrounding liquid may have different properties. The vapor in the bubble is assumed to obey the ideal gas law, and the temperature and pressure are assumed to be uniform throughout the bubble.

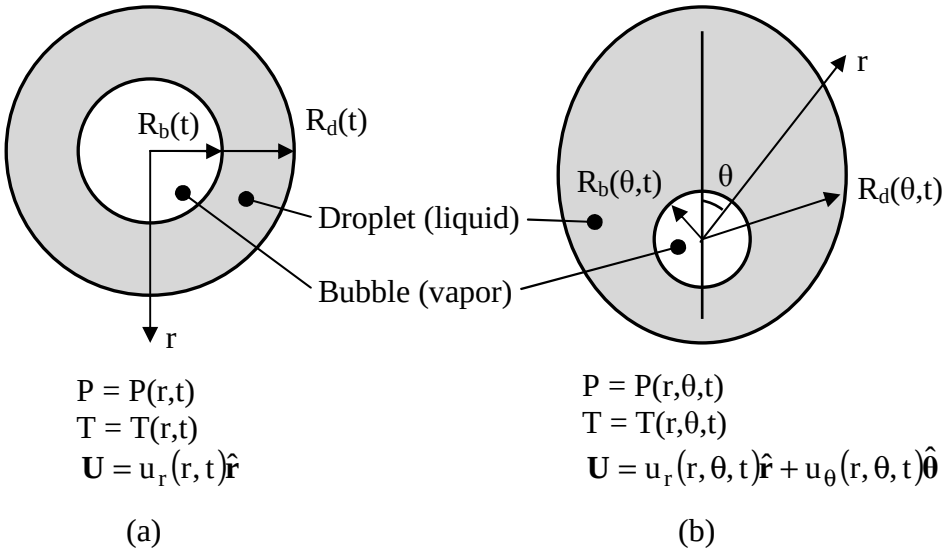

Figure A.2. Models of a boiling droplet. (a) Spherically symmetric one-dimensional model. (b) Axisymmetric two-dimensional model.

A more realistic model would allow for departures from spherical symmetry if the bubble nucleus forms at some point away from the center of the droplet (Fig. A.2b). In this case the droplet retains radial symmetry around an axis defined by the centers of the bubble and the droplet. This axisymmetric model is much more complex than the one-dimensional model, and the one-dimensional model used in this study is expected to be reasonably accurate. An early analytical model of vapor bubble growth in uniformly superheated liquid found that the departure from symmetry caused by the presence of a solid wall adjacent to the bubble actually had little impact on bubble growth, slowing the rate of growth by about one third but not changing the form of the resulting equations (Mikic et al., 1970). It is assumed that departures from spherical symmetry in small droplets would have similarly small impact.

The boiling process can be divided into two time domains based on the presence of droplet liquid. In the first time domain, the growth of the vapor bubble is accompanied by evaporation of the droplet liquid at the bubble surface. During this period the vapor in the bubble is assumed to be saturated, and the rate of evaporation of liquid at the droplet surface must be taken into account. The second time domain begins when the liquid has completely evaporated. During this period the mass of the vapor bubble

remains constant and is no longer assumed to be saturated. Further, expansion is assumed to be uniform and thus the liquid velocity surrounding the bubble has only a radial component. The state of the vapor in the bubble is determined using the ideal gas law and the Clausius-Clapeyron equation.

A.2.1. Momentum balance

Recalling that the problem has spherical symmetry and that the liquids around the bubble are incompressible, the velocity in the liquid can be expressed as,

$$u(r,t)=\frac{F(t)}{r^2}. \tag{A.9}$$

Thus, if the velocity of the liquid can be found at any location at a given time step, the velocity everywhere in the liquid is known. When this equation for velocity is inserted into the momentum equation the result is,

$$\frac{\partial P}{\partial r}=\rho\left(\frac{2}{r}u^2-\frac{1}{r^2}\frac{dF(t)}{dt}\right). \tag{A.10}$$

The result is given as Eq. (A.11), which also includes a term for the pressure jump at the bubble surface due to surface tension. It is assumed that the droplet radius is large enough that the pressure jump at the droplet surface is negligible. The pressure jump at each surface due to viscosity is also assumed to be negligible. Equation (A.11) also accounts for differing densities in the droplet and the surrounding liquid,

$$0=(P_b-P_\infty)-\frac{2\sigma}{R_b}+\frac{F(t)^2}{2}\left(\frac{\rho_d}{R_b^4}+\frac{\rho_c-\rho_d}{R_d^4}\right)+\frac{dF(t)}{dt}\left(-\frac{\rho_d}{R_b}+\frac{\rho_d-\rho_c}{R_d}\right). \tag{A.11}$$

The pressure in the bubble is obtained at any time using the equation of state of the vapor in the bubble. Therefore, Eq. (A.11) may be used to find the evolution of F(t) over time.

A.2.2. Thermal energy balance

The thermal energy balance equation in the liquid is,

$$\frac{\partial T}{\partial t} + u\frac{\partial T}{\partial r} = \alpha\left(\frac{\partial^2 T}{\partial r^2} + \frac{2}{r}\frac{\partial T}{\partial r}\right). \tag{A.12}$$

The temperature is assumed to be uniform inside the vapor bubble, and during the first time domain it is assumed that the vapor is saturated because it is in contact with its own liquid at the bubble surface. The saturation pressure and temperature are linked by the Clausius-Clapeyron equation, assuming that the latent heat of vaporization is constant,

$$\frac{P_{sat}}{P_{sat,0}} = \exp\left[\frac{i_{fg}}{R_G}\left(\frac{1}{T_{sat,0}} - \frac{1}{T_{sat}}\right)\right]. \tag{A.13}$$

After the droplet has completely evaporated, the temperature in the bubble is determined using the energy balance of the bubble. The energy balance includes the work done by the expanding bubble and heat diffusion to the bubble from the surrounding liquid,

$$\frac{dT_b}{dt} = \frac{4\pi R_b^2}{m_b c_{v,b}}\left(k\frac{\partial T}{\partial r}\bigg|_{r=R_b} - P_b\frac{dR_b}{dt}\right). \tag{A.14}$$

During the first time domain the mass of vapor in the bubble increases due to evaporation according to,

$$\frac{dm_b}{dt} = \frac{4\pi R_b^2 k_d}{i_{fg}}\frac{\partial T}{\partial r}\bigg|_{r=R_b}. \tag{A.15}$$

Evaporation at the bubble surface also results in a relative velocity between the bubble surface and the liquid adjacent to the surface equal to,

$$\frac{dR_b}{dt} - u\Big|_{r=R_b} = \frac{1}{4\pi R_b^2 \rho_d}\frac{dm_b}{dt}. \qquad (A.16)$$

A summary of the variables, initial and boundary conditions, and governing equations is given in Table A.1. Two sets of governing equations are given. The first set is for the first time domain in which evaporation occurs. The second set applies when the droplet is completely evaporated and the bubble is superheated, in which case no phase change occurs. The equations for the first time domain also apply to any time after the complete evaporation of the droplet in which the vapor in the bubble becomes saturated again and recondensation occurs at the bubble surface.

A.2.3. Initial and boundary conditions

In all simulations the bubble begins at rest with an initial radius 0.1% larger than the critical radius, Eq. (3). The initial temperature is uniform and equal to the ambient temperature. The ambient temperature and pressure are held constant throughout each simulation. Simulations are performed at different ambient temperatures, while in all cases the ambient pressure is held at one atmosphere.

A.3. Solution method

The simulations represent the temperature field in the liquid around the bubble by a one-dimensional array of nodes. The first node is located at the surface of the bubble and represents the temperature of the bubble. It is assumed that there is no temperature jump at the bubble surface. The last node has temperature fixed at the ambient temperature. Simulations are performed with a total of sixty nodes that are spaced to span a distance of 40 μm from the bubble surface. Using an approach similar to that of Lee and Merte (1996), the nodes are clustered near the bubble surface according to,

$$r_i = R_b + (40\mu m)\left(\frac{i}{N-1}\right)^{2.2}, \qquad (A.17)$$

Table A.1. Quantities and formulas in the one-dimensional model of a boiling droplet.

Quantity	Initial / boundary conditions	Governing equation	
		with phase change	without phase change
$T(r,t)$	$T(r,0) = T_\infty$ $T(R_b,t) = T_b$	(A.12)	(A.12)
$F(t)$	$F(0) = 0$	(A.11)	(A.11)
$m_b(t)$	$m_b(0) = \frac{4}{3}\pi R_b^3(0)\frac{P_\infty}{R_G T_\infty}$	(A.15)	$m_b = m_d$
$R_b(t)$	$R_b(0) = \frac{1.001 \cdot 2\sigma}{P_{sat}(T_\infty) - P_\infty}$	(A.16)	$\frac{dR_b}{dt} = u\big\|_{r=R_b}$
$R_d(t)$	N/A	$R_d = \left(R_b^3 + \frac{m_d - m_b}{4/3\pi\rho_d} \right)^{1/3}$	$R_d = R_b$
$T_b(t)$	$T_b(0) = T_\infty$	$T_b = T_{sat}$	(A.14)
$P_b(t)$	N/A	$P_b = P_{sat} = \rho R_G T_b$	$P_b = \rho R_G T_b$

where i is the node number, $0 \le i \le N\text{-}1$. As the simulation progresses the nodes move outwards with uniform velocity equal to that of the bubble surface. The first node is therefore always located at the bubble surface and the spacing between nodes remains constant.

The equations are solved by an iterative, fully implicit method. The discretized form of Eq. (A.12) is,

$$T_i = \frac{a_{i,1}T_{i-1} + a_{i,2}T_{i+1} + a_i^t T_i^{old}}{a_{i,1} + a_{i,2} + a_i^t}. \qquad (A.18)$$

The coefficients $a_{i,1}$ and $a_{i,2}$ account for energy transfer through the inner and outer surfaces, respectively, of node i and are defined as follows. These equations take into account the motion of the nodes themselves as well as that of the liquid.

$$a_{i,1} = k\frac{(r_i + r_{i-1})^2}{(r_i - r_{i-1})} + \rho c\left[2F - \frac{R_b - R_b^{old}}{2(\Delta t)}(r_i + r_{i-1})^2\right] \tag{A.19}$$

$$a_{i,2} = k\frac{(r_{i+1} + r_i)^2}{(r_{i+1} - r_i)} + \rho c\left[\frac{R_b - R_b^{old}}{2(\Delta t)}(r_{i+1} + r_i)^2 - 2F\right]. \tag{A.20}$$

The coefficient a_i^t accounts for temperature change within node i and is defined as,

$$a_i^t = \frac{\rho c}{6(\Delta t)}\left[(r_{i+1} + r_i)^3 - (r_i + r_{i-1})^3\right] \tag{A.21}$$

Defining k, ρ, and c in Eqs. (A.19 – 21) requires some care for any nodes adjacent to the boundary between the droplet and surrounding liquid. In Eqs. (A.19) and (A.20), ρ and c are set equal to the properties of the liquid present at the inner and outer surface of the node. On the other hand, k is a weighted average of k_c and k_d that accounts for conduction through the droplet liquid and surrounding liquid in series. In Eq. (A.21), ρc is a weighted average of the droplet and surrounding liquid values based on the fraction of the node occupied by each liquid. The averages are linear averages based on radii. This approach ignores the curvature of the nodes, but the effect of this approximation is small as long as the distance between nodes is small compared to the radius of each node.

All of the differential equations are solved implicitly in time so iteration at each time step is required. The number of iterations is typically set at fifteen, and the equations are under-relaxed using a relaxation parameter between 0.6 and 0.7. The initial time step size is typically set to 1 ns, and is increased somewhat as the simulation progresses. Simulation durations are between 50 μs and 1 ms. Care is taken to halt the simulations before the thermal boundary layer grows to the outer edge of the simulated region of liquid. The droplets typically take between 10 and 100 μs to boil.

A.4. Results

A.4.1. Conditions

Simulations are performed for various combinations of fluids and for a range of droplet sizes and degrees of superheat. Droplet radii are chosen in the range $2 \leq R_d \leq 15$ μm. Three combinations of fluids are simulated. Droplets of water in mineral oil are simulated to investigate configurations in which the droplet liquid has much higher thermal conductivity than the surrounding liquid. For this combination of fluids superheats of 40 and 80 °C are considered, corresponding to temperatures over which boiling of water in oil emulsions has been observed experimentally (Mori et al., 1978).

Simulations are performed with droplets of two liquids, pentane and FC-72, suspended in water. In these cases the surrounding liquid has higher thermal conductivity and specific heat than the droplet. For these configurations smaller degrees of superheat, 20 to 60 °C, are considered. For all three pairs of fluids, properties are evaluated at the saturation temperature of the more volatile liquid and are assumed to be constant. In all cases the ambient pressure is equal to one atmosphere.

A.4.2. Initial bubble growth

The initial behavior of the vapor bubble is qualitatively similar to that observed by Lee and Merte (1996). As described in Section A.1, the bubble growth accelerates as it transitions from surface tension dominated growth to inertia dominated growth, where the bubble radius increases at a constant rate (Fig. A.3). A novel result here is that the rate of expansion of the bubble depends on the droplet size. Equation (A.11) shows that a difference in density between the droplet liquid and the surrounding liquid can impact the rate of growth of the bubble, but only when the bubble and droplet radii are comparable. When $R_b << R_d$ the inertial effects of any difference in density is negligible. Therefore, for water in mineral oil ($\rho_d/\rho_c = 1.17$) the rate of expansion is nearly independent of the droplet size, while for pentane in water ($\rho_d/\rho_c = 0.614$) the rate of expansion is significantly greater in larger droplets. For FC-72 in water ($\rho_d/\rho_c = 1.63$) the opposite trend is observed (Figs. 2(a) – (c)).

A.4.3. Final bubble growth

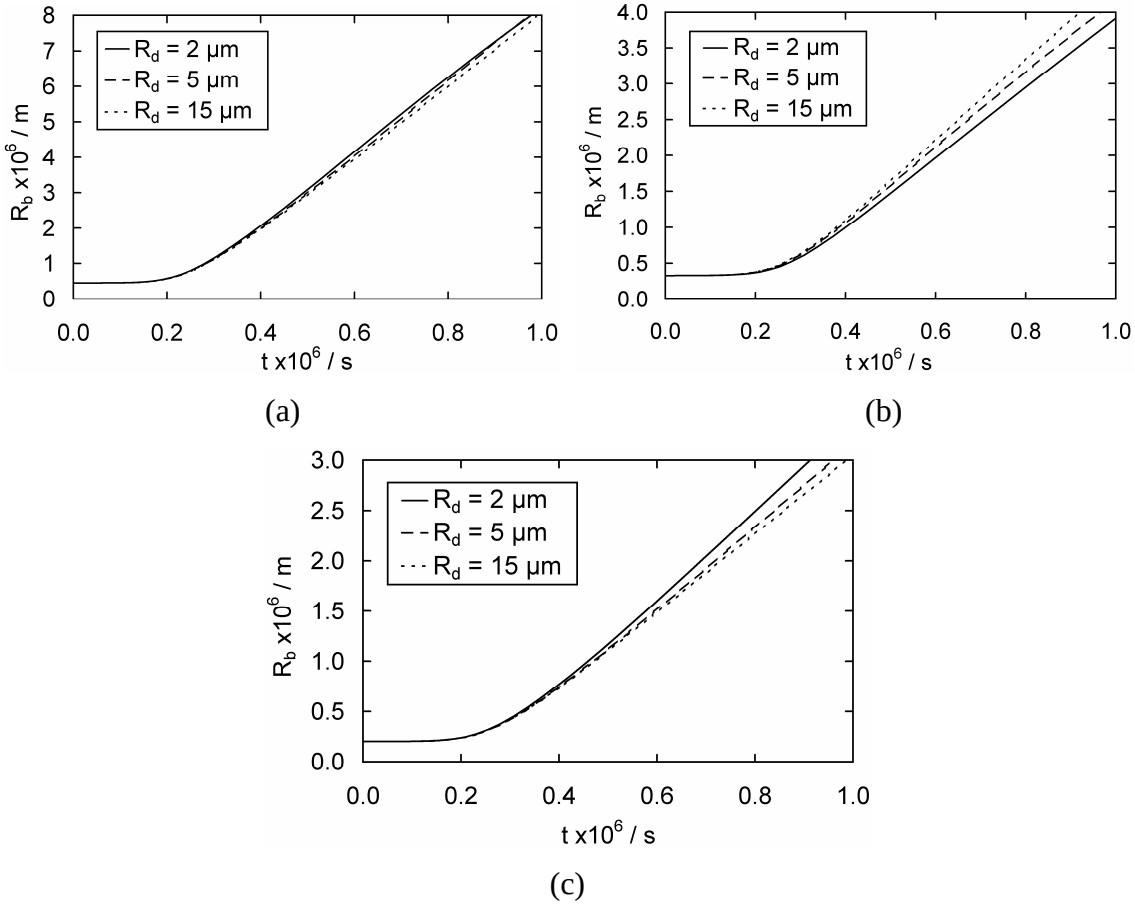

Figure A.3. Initial bubble growth for (a) water droplets in oil with ΔT = 40 °C, (b) pentane droplets in water with ΔT = 20 °C, and (c) FC-72 droplets in water with ΔT = 20 °C.

After the initial inertia dominated growth, bubble growth approaches the analytical solution of Mikic et al. (1970) until the droplet is mostly evaporated (Fig. A.4 – A.6). For water in oil and FC-72 in water (fluid combinations for which $\rho_d > \rho_c$) the simulated bubble growth is generally faster than predicted by Eq. (A.2), while the opposite is true for pentane in water ($\rho_d < \rho_c$). This result is explained by the deviation in the rate of bubble growth during the momentum dominated growth described in the previous section. The simulated bubble growth also tends to run faster than Eq. (A.2) for larger ΔT. This discrepancy is most likely due to the relation used in this study for the

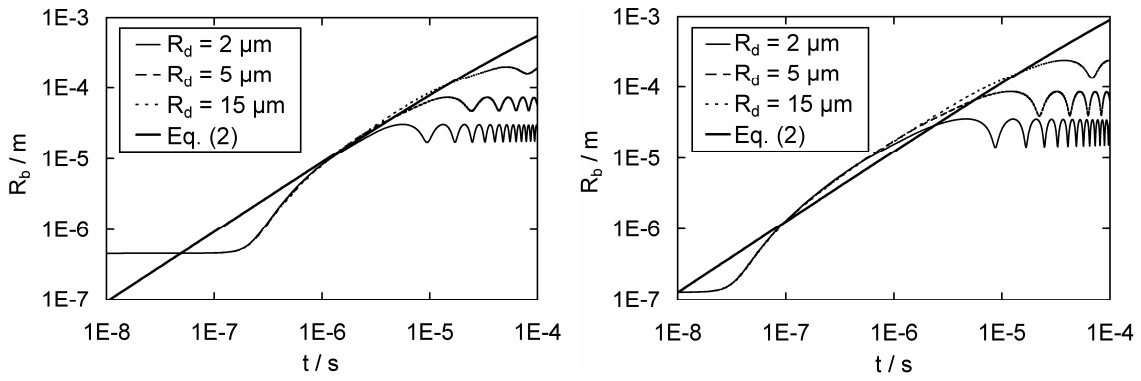

Figure A.4. Bubble growth for water droplets suspended in mineral oil with (a) ΔT = 40 °C and (b) ΔT = 80 °C. Equation (A.2) calculated using properties of water.

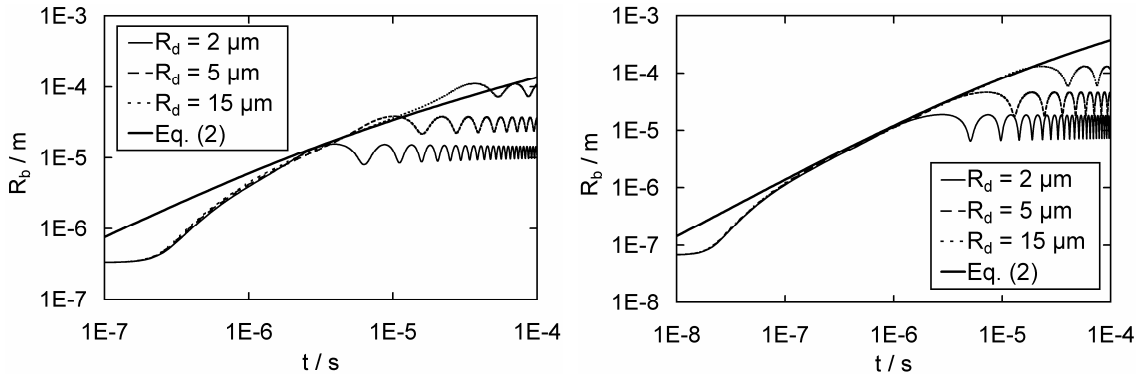

Figure A.5. Bubble growth for pentane droplets suspended in water with (a) ΔT = 20 °C and (b) ΔT = 60 °C. Equation (A.2) calculated using properties of pentane.

saturation pressure (Eq. A.13) which results in a larger initial driving pressure than the relation used by Mikic et al. (1970).

As the bubble continues to expand, the layer of droplet liquid surrounding the bubble becomes thinner and eventually evaporates completely. Therefore the thermal boundary layer around the bubble grows progressively into the liquid that surrounds the droplet. For the water in oil case, the oil has lower thermal conductivity, specific heat,

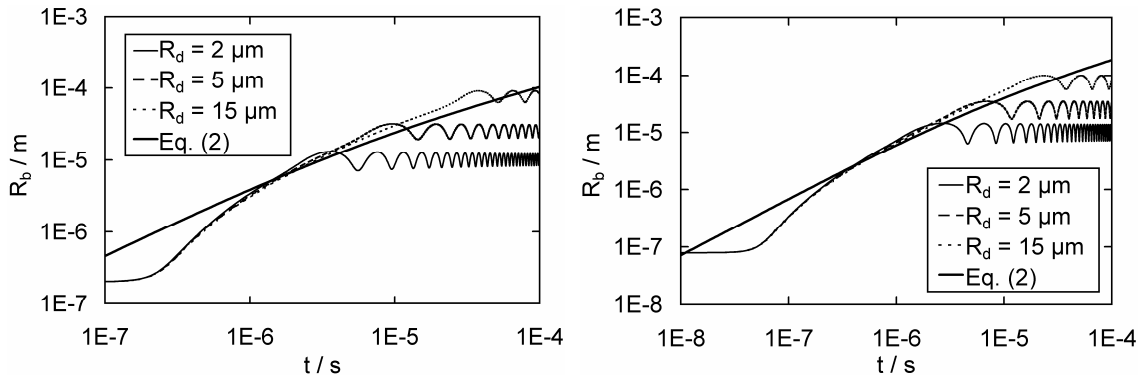

Figure A.6. Bubble growth for FC-72 droplets suspended in water with (a) $\Delta T = 20$ °C and (b) $\Delta T = 40$ °C. Equation (A.2) calculated using properties of FC-72.

and density than the water. All three factors contribute to reducing the rate at which heat diffuses to the bubble surface, which reduces the rate of bubble expansion in the later stages of boiling. For water in oil, the thermal properties of the oil begin to influence the rate of bubble expansion when the bubble reaches approximately one third of its equilibrium radius. For pentane in water and FC-72 in water, the surrounding liquid has much higher thermal conductivity and higher specific heat than the droplet liquid, so the bubble accelerates near the end of the boiling process.

For all combinations of fluids considered here, these effects at the end of the boiling process are most pronounced for larger droplets and for lower ΔT. The model of Mikic et al. (1970) shows that thermal diffusion dominated growth occurs later in the boiling process, so the dependence on droplet size is expected. Equation (A.2) also shows that the region of inertia dominated growth grows with increasing ΔT.

A.4.4. Bubble oscillation

Eventually the bubble must come to rest at its equilibrium radius. Ignoring surface tension this radius is,

$$R_{b,0} = R_{d,0}\left(\frac{\rho_d R_G T_\infty}{P_\infty}\right)^{1/3}. \qquad (A.22)$$

However, when the droplet completely evaporates the liquid around the bubble still has considerable velocity and so the bubble oscillates for some time. The oscillations decay as a result of thermal and acoustic damping (Plesset and Prosperetti, 1977). These simulations are not expected to accurately predict the decay of the oscillations because acoustic damping, which depends on the compressibility of the liquid, is not modeled. Neglecting surface tension, small-amplitude oscillations of a spherical vapor bubble are sinusoidal at the Minnaert frequency (Brennen, 1995),

$$f_M = \frac{1}{2\pi R_{b,0}} \sqrt{\frac{3\kappa P_\infty}{\rho_c}}. \tag{A.23}$$

For an isothermal bubble the polytropic coefficient $\kappa = 1$, and for an adiabatic bubble $\kappa = c_p/c_v$. When heat transfer between the bubble and surrounding liquid occurs, κ is expected to fall somewhere between these two extremes (Plesset and Prosperetti, 1977).

As Fig. (A.7) illustrates, the oscillations of the smaller water vapor bubbles in this study are neither small amplitude nor exactly sinusoidal, and therefore the analytical solutions for small oscillations are not expected to be precisely correct. For all three combinations of fluids the frequency of oscillation falls close to the Minnaert frequency for an isothermal bubble. The polytropic coefficient varies from a minimum of 0.95 for $R_d = 5$ μm in the pentane in water case, to a maximum of 1.06 for $R_d = 2$ μm in the water in oil case, suggesting that the bubble is close to isothermal during oscillations in all cases.

Figure (A.7) also shows that the dependence of the magnitude of the bubble oscillations on the initial droplet size is much more significant for the water in oil case than for the pentane and FC-72 in water cases. This behavior is a result of the deceleration or acceleration of the bubble expansion when the droplet is mostly evaporated, as discussed in the previous section. The high thermal conductivity of water also results in much faster decrease in the magnitude of the oscillations due to thermal damping than in the water in oil case.

A.4.5. Bubble temperature variation

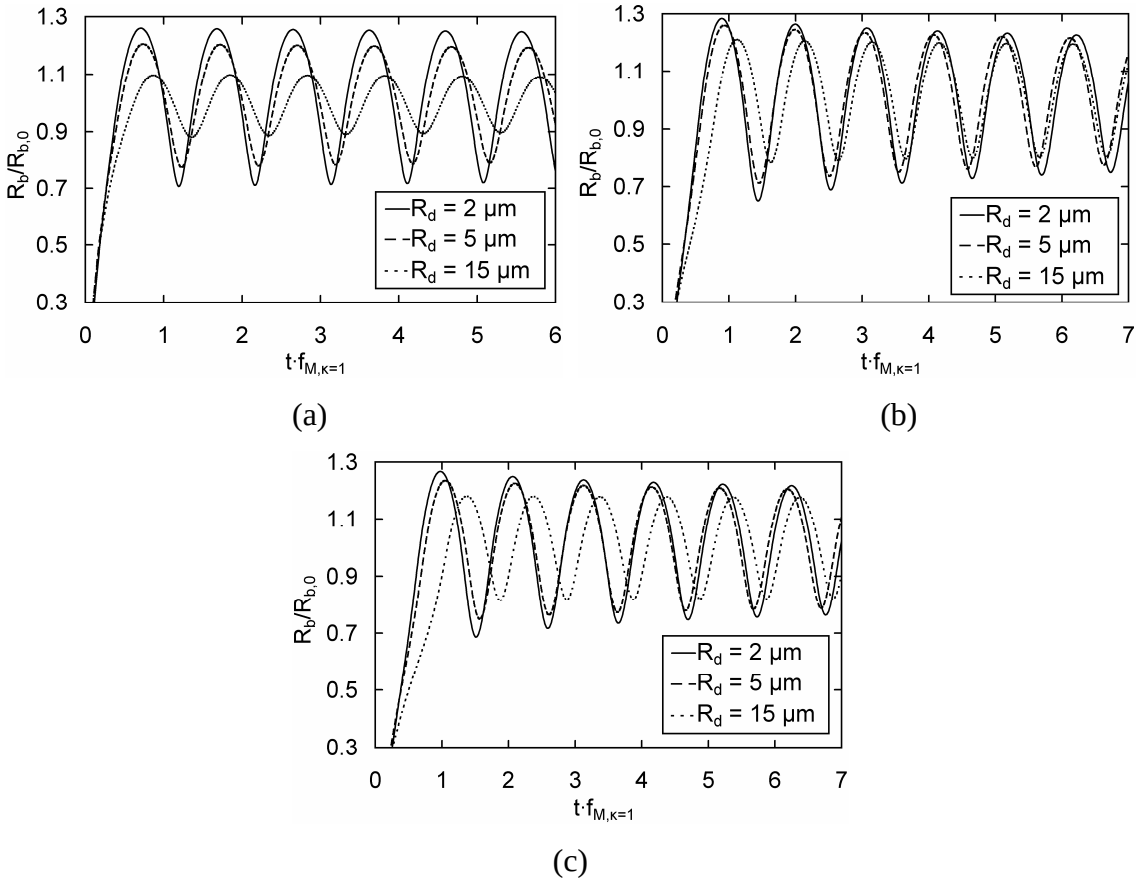

Figure A.7. Oscillation of (a) water vapor bubble in mineral oil, ΔT = 40 °C, (b) pentane vapor bubble in water, ΔT = 20 °C, and (c) FC-72 vapor bubble in water, ΔT = 20 °C.

Figures A.8 and A.9 show the evolution of the bubble temperature over time for the water in oil and FC-72 in water cases. Figure A.8 illustrates the decrease in bubble temperature during the early expansion of the bubble. In all cases the initial decrease in bubble temperature is nearly independent of the droplet radius, which is consistent with the observation that the initial bubble expansion is also nearly independent of the droplet radius. Figure A.8b shows that for the smaller water droplets in oil, there is a second stage of rapid cooling of the bubble that occurs after the initial expansion begins. This behavior is a result of the thermal boundary layer growing into the oil around the water droplet. As discussed in Section A.4.3, as this occurs the rate of heat transfer to the bubble surface decreases. The rate of evaporation therefore decreases,

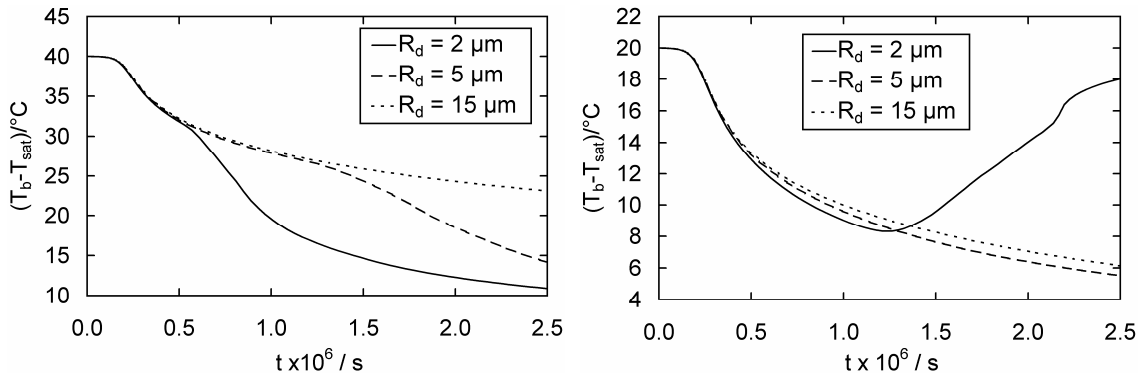

Figure A.8. Temperature at bubble surface during initial expansion for (a) water in oil, ΔT = 40 °C and (b) FC-72 in water, ΔT = 20 °C.

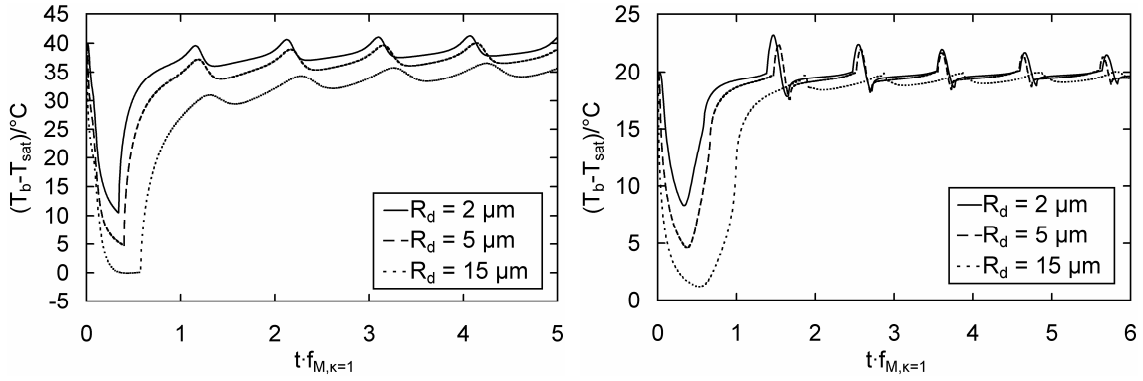

Figure A.9. Temperature at bubble surface for (a) water in oil, ΔT = 40 °C and (b) FC-72 in water, ΔT = 20 °C.

but the inertia of the surrounding liquid prevents the rate of expansion of the bubble from changing instantly. Therefore the specific volume of the vapor in the bubble rises and the temperature decreases. The FC-72 droplet in water has the opposite behavior, where the temperature in the bubble begins to rise shortly before the droplet evaporates completely due to the increase in the rate of heat transfer as the layer of liquid FC-72 around the bubble becomes thin.

Figure A.9 shows the variation in bubble temperature during the entire boiling process and the first few oscillations of the bubble. Figure A.9a shows that only for the

largest water droplet in oil does the bubble temperature ever reach T_{sat}, so that the bubble experiences purely thermal diffusion limited growth. The figure also shows that the bubbles are indeed close to isothermal when oscillating, as the results discussed in the preceding section implied. The rather sharp changes in the FC-72 bubble temperature (Fig. A.9b) occur near the minimum radius in each oscillation and are caused by FC-72 vapor briefly becoming saturated. A small amount of FC-72 condenses onto the surface of the bubble, and acts as thermal insulation for the bubble due to its poor thermal conductivity. As the bubble expands in the next cycle of oscillation the FC-72 evaporates again.

This intermittent re-condensation of the droplet liquid is, perhaps, less physically realistic than the other results. It seems plausible that because the time during which the FC-72 is saturated is so small, it may remain a subcooled vapor rather than condensing at the bubble surface. To investigate the significance of re-condensation additional simulations were performed of FC-72 droplets in water in which condensation was not allowed after the initial vaporization of the droplet. The resulting oscillations of the bubble are not significantly different from the simulations in which condensation occurs. As expected, the variation of the bubble temperature is diminished. The frequency of oscillation of the bubble and the rate of thermal damping of the oscillations are both slightly lower.

A.4.6. Comparison with the Kwak et al. model

The model developed by Kwak et al. (1995) was also applied to the bubbles simulated in this study. Because their model only describes oscillating bubbles, the initial conditions for numerical calculations using Eq. (A.4-8) were taken from the results of the simulations performed for this study at the time when the droplet evaporates completely. The initial thermal boundary layer thickness was set so that the initial heat transfer rate to the bubble was the same as the rate predicted by this study. To ensure that the boundary layer thickness remain small compared to the bubble radius it was necessary to increase the temperature range to $\left|T_b - T_\infty\right| < 1°C$ for which $d\delta_t/dt = 0$. It is not surprising that this more severe restriction on Eq. (A.8) is

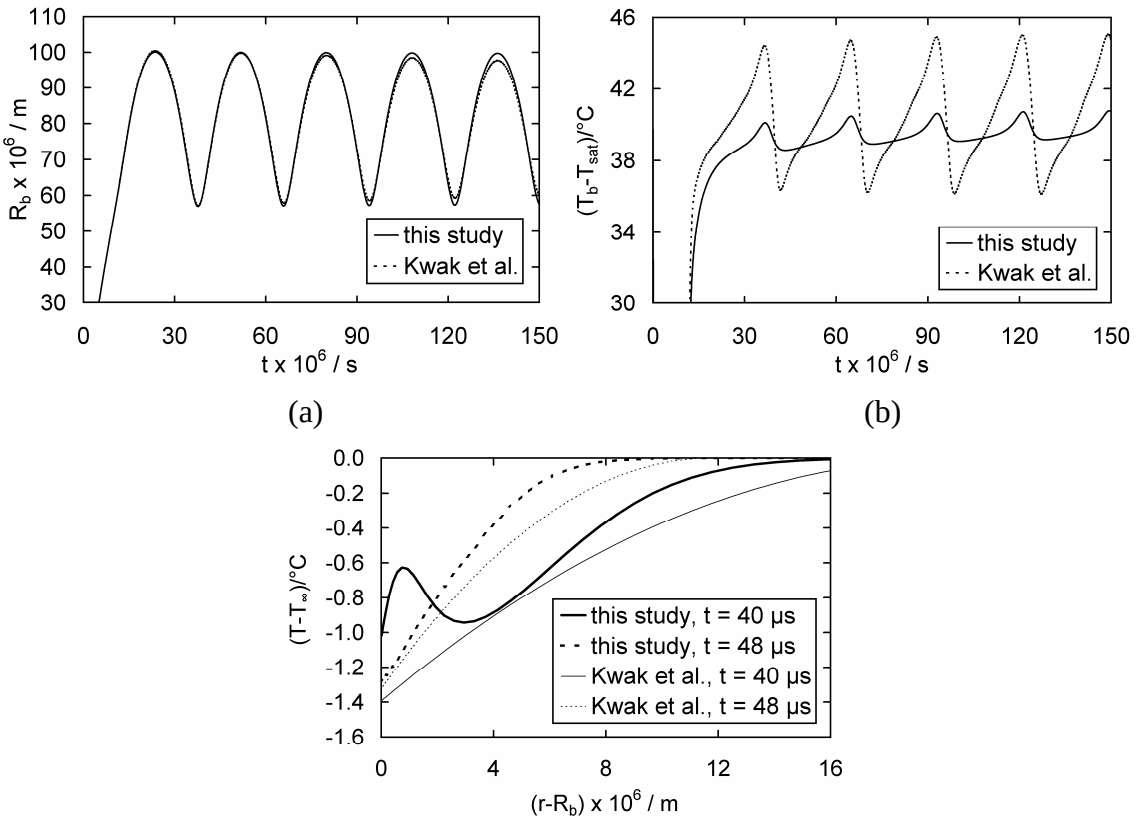

Figure A.10. Predictions of (a) radius and (b) temperature for oscillating FC-72 vapor bubble in water, and (c) boundary layer temperature profile, ΔT = 40 °C and R_d = 15 μm.

necessary, as Kwak et al.'s model was developed for much larger bubbles than the ones in this study.

Figure A.10 compares the results of this study to simulations performed using the Kwak et al. model for the oscillating bubble that results from the boiling of a droplet of FC-72 in water with R_d = 15 μm and ΔT = 40 °C. As Fig. (A.10a) illustrates, the two models are in very close agreement regarding the frequency and initial amplitude of the oscillations. However, the Kwak et al. model predicts significantly larger variation in the bubble temperature, and the variation increases with time as the thermal boundary layer grows (Fig. A.10b). The most likely reason for these discrepancies is the assumption by Kwak et al. of a quadratic temperature profile in the boundary layer. As Fig. (A.10c) illustrates, the model developed in this study predicts that the temperature

profile in the boundary layer can become complex. The shape of the temperature profile predicted by this study at t = 40 μs contains the entire history of the boiling droplet including heat transfer to the droplet during the boiling process and bubble expansion (0 < t < 24 μs), heat transfer from the bubble during its subsequent contraction (24 < t < 38 μs), and finally heat transfer to the bubble again as it begins to expand again (38 μs < t). Any model that assumes a temperature profile in the boundary layer cannot capture this behavior.

A.4.7. Bubble radius overshoot

Additional simulations were performed for $1 \le R_d \le 30$ μm and $4 \le \Delta T \le 45$ °C for FC-72 droplets in water. The primary figure of interest in these simulations is the maximum radius achieved by the bubble as compared to its steady-state radius. The results of these simulations are summarized in Table A.2. The case of $R_d = 30$ μm and $\Delta T = 4$ °C is not simulated because the bubble does not reach its maximum size before 1 ms has elapsed, at which time the thermal boundary layer reaches the outer limit of the simulation domain.

The information represented by Table A.2 is needed to describe the rate of chain boiling introduced in Section 3.3. For the purposes of performing numerical simulations of boiling emulsions, it would be useful to find a function to represent the data in the table. An examination of the data shows that the ratio of maximum to steady-state bubble radius decays roughly exponentially with droplet radius and increases logarithmically with the degree of superheat. A function that accounts for both trends and fits the data in Table A.2 with RMS error of 0.0026 is given in Eq. (A.24),

$$\frac{R_{b,max}}{R_b} = 1.74\times10^{-6}\left(\frac{\Delta T}{°C}\right)^3 - 1.97\times10^{-4}\left(\frac{\Delta T}{°C}\right)^2 + 0.011\frac{\Delta T}{°C} + 0.9767 + \left[0.04\ln\left(\frac{\Delta T}{°C}\right) - 0.00322\right]\exp\left(-.0839\frac{R_d}{\mu m} + 0.3004\right). \quad \text{(A.24)}$$

There is a decrease in the ratio of bubble radii that occurs at the smallest values of droplet radius and superheat. Equation (A.24) does not account for this deviation away from the overall trends of the data. However, fine-grained emulsions require larger degrees of superheat to initiate boiling (Bulanov and Gasanov, 2008). It is therefore unlikely that much boiling will occur under these conditions in any simulation, and so the decreased accuracy of Eq. (A.24) under these conditions is not significant.

Table A.2. Ratio of $R_{b,max}$ to steady-state bubble radius for various values of droplet radius and superheat.

R_d (μm)	ΔT (°C) 4	6	8	11	15	20	25	30	35	40	45
1	1.0736	1.1157	1.1489	1.1893	1.2327	1.2766	1.3129	1.3438	1.3709	1.3949	1.4167
1.5	1.0782	1.1178	1.1492	1.1878	1.2296	1.2721	1.3072	1.3373	1.3637	1.3868	1.4075
2	1.0776	1.1156	1.1461	1.1836	1.2243	1.2658	1.3002	1.3297	1.3554	1.3781	1.3985
3	1.0729	1.1089	1.1380	1.1741	1.2132	1.2531	1.2865	1.3151	1.3401	1.3624	1.3827
4.5	1.0652	1.0991	1.1269	1.1614	1.1988	1.2371	1.2692	1.2969	1.3213	1.3434	1.3634
6	1.0587	1.0909	1.1176	1.1511	1.1874	1.2243	1.2555	1.2820	1.3065	1.3293	1.3502
9	1.0489	1.0785	1.1036	1.1351	1.1696	1.2042	1.2335	1.2589	1.2832	1.3050	1.3268
13	1.0401	1.0671	1.0903	1.1199	1.1526	1.1854	1.2172	1.2365	1.2602	1.2806	1.3011
18	1.0327	1.0571	1.0787	1.1062	1.1372	1.1686	1.1946	1.2181	1.2399	1.2595	1.2814
24	1.0268	1.0488	1.0686	1.0945	1.1235	1.1536	1.1793	1.2008	1.2203	1.2392	1.2610
30	---	1.0428	1.0612	1.0855	1.1128	1.1415	1.1664	1.1854	1.2039	1.2246	1.2472

Appendix B.

Apparatus drawings

The following pages contain detail drawings of the test cell components, bus bar assembly, and power supply. The test cell is made of clear acrylic. Two end plates, two side plates, and four flanges are assembled into a permanent subassembly in the configuration shown in Fig. 5.1 using solvent bonding. The side subassembly is fastened to the base using ¼-20 UNC hardware. The bus bar subassembly is fastened together using #4-40 UNC hardware.

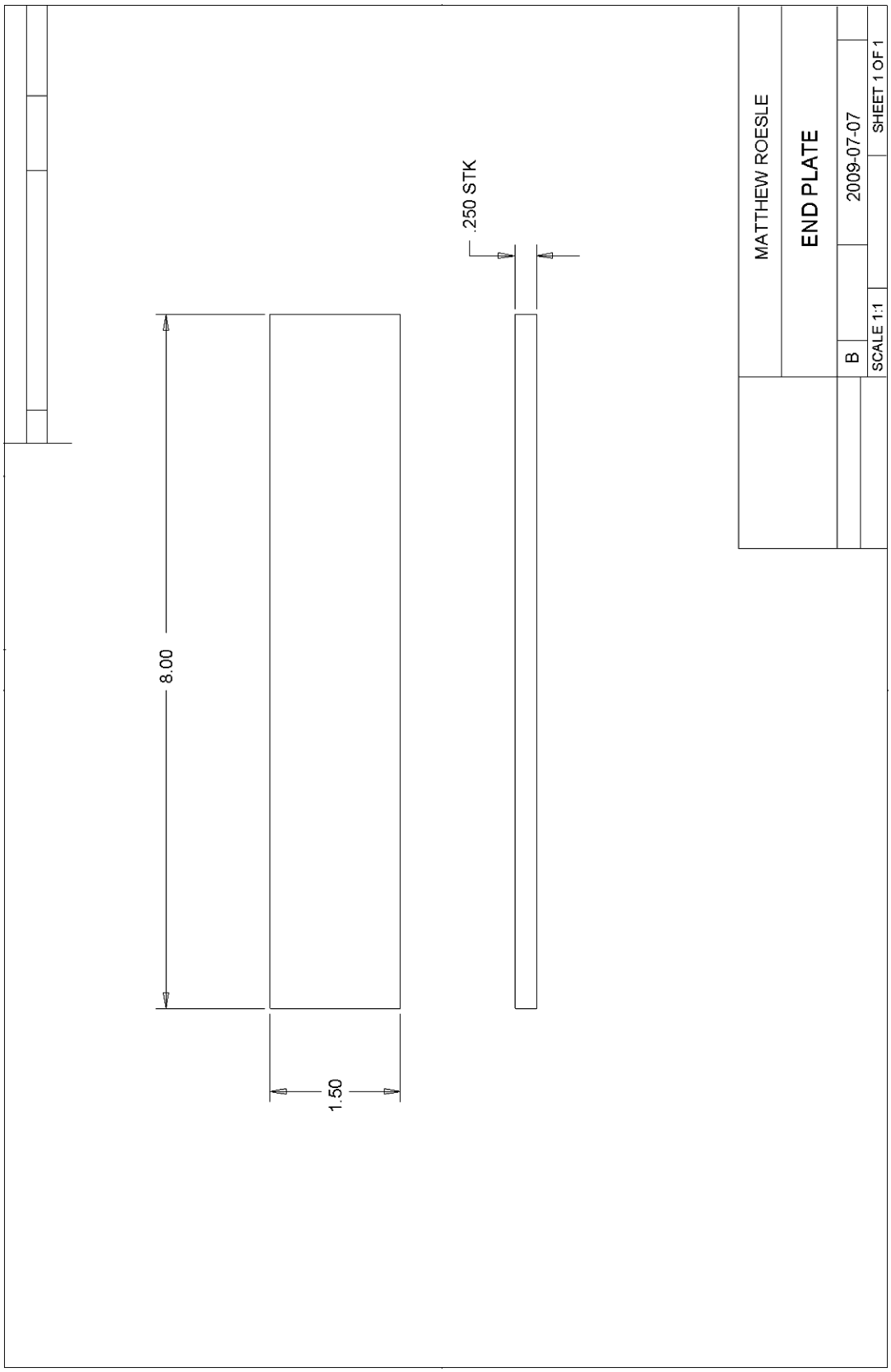
.250 STK
8.00
1.50
MATTHEW ROESLE
END PLATE
B
2009-07-07
SCALE 1:1
SHEET 1 OF 1

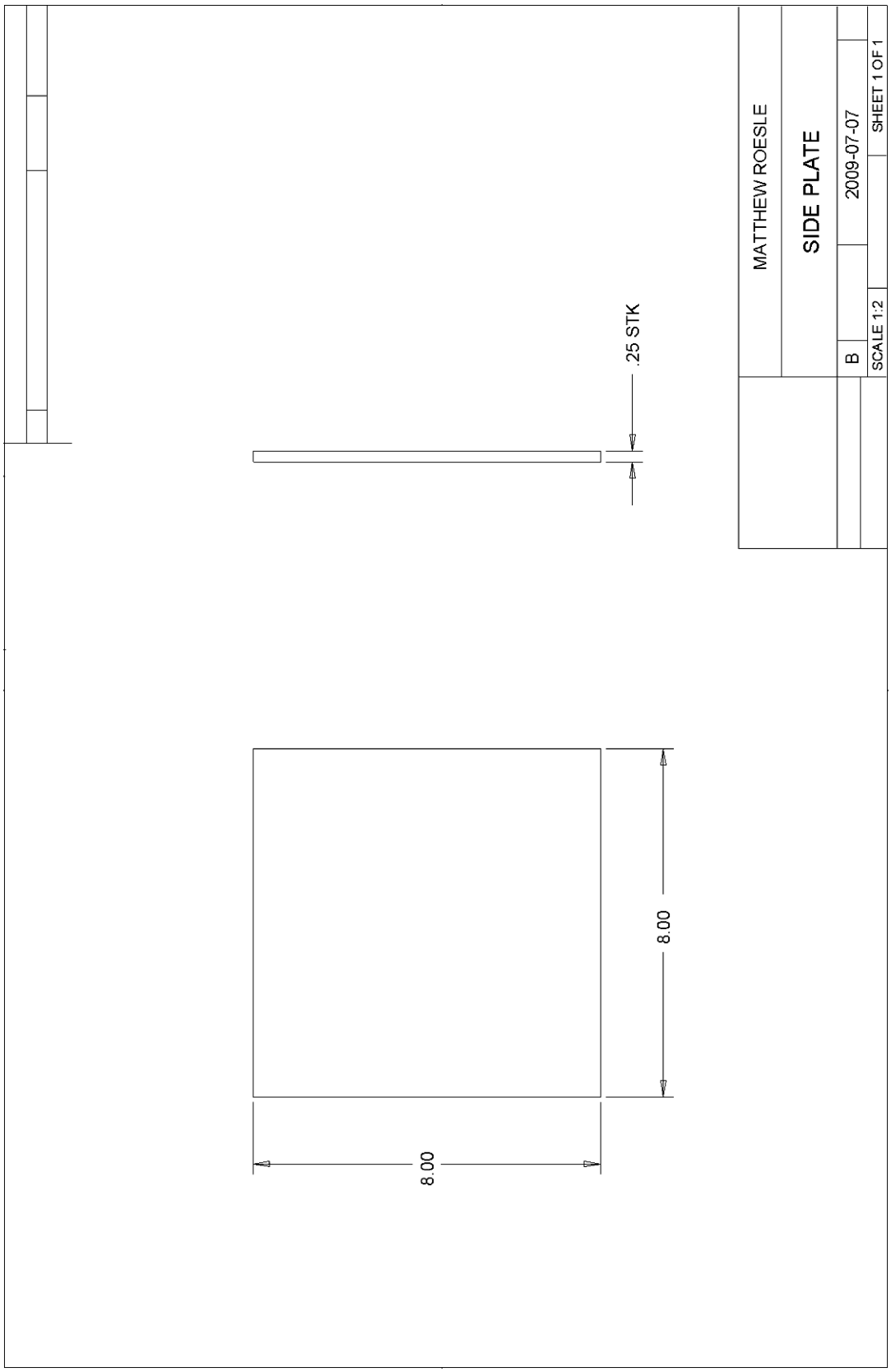
.25 STK
8.00
8.00
MATTHEW ROESLE
SIDE PLATE
B
2009-07-07
SCALE 1:2
SHEET 1 OF 1

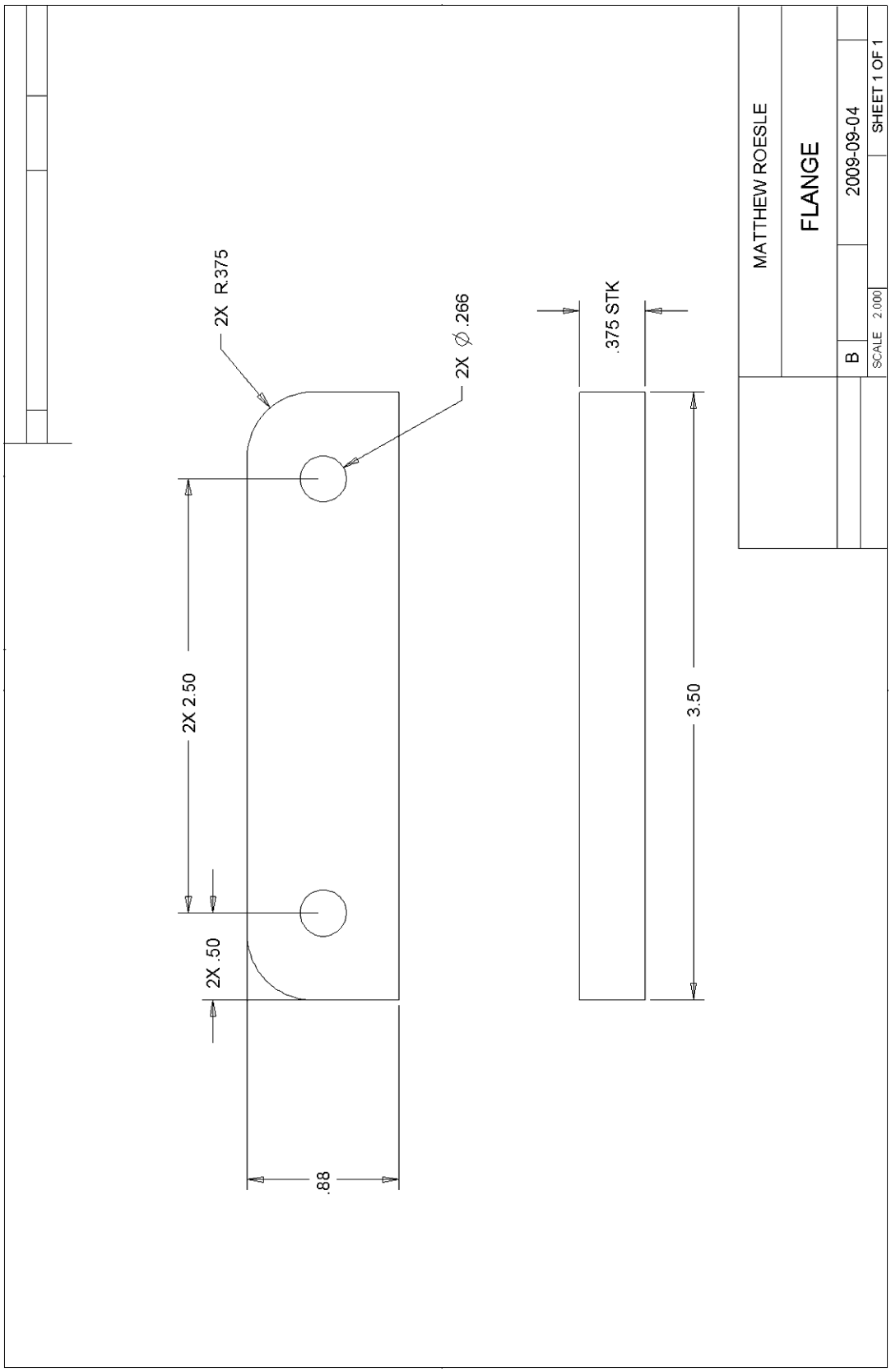
2X R.375
2X ∅.266
2X 2.50
2X .50
.88
.375 STK
3.50
MATTHEW ROESLE
FLANGE
B
2009-09-04
SCALE 2.000
SHEET 1 OF 1

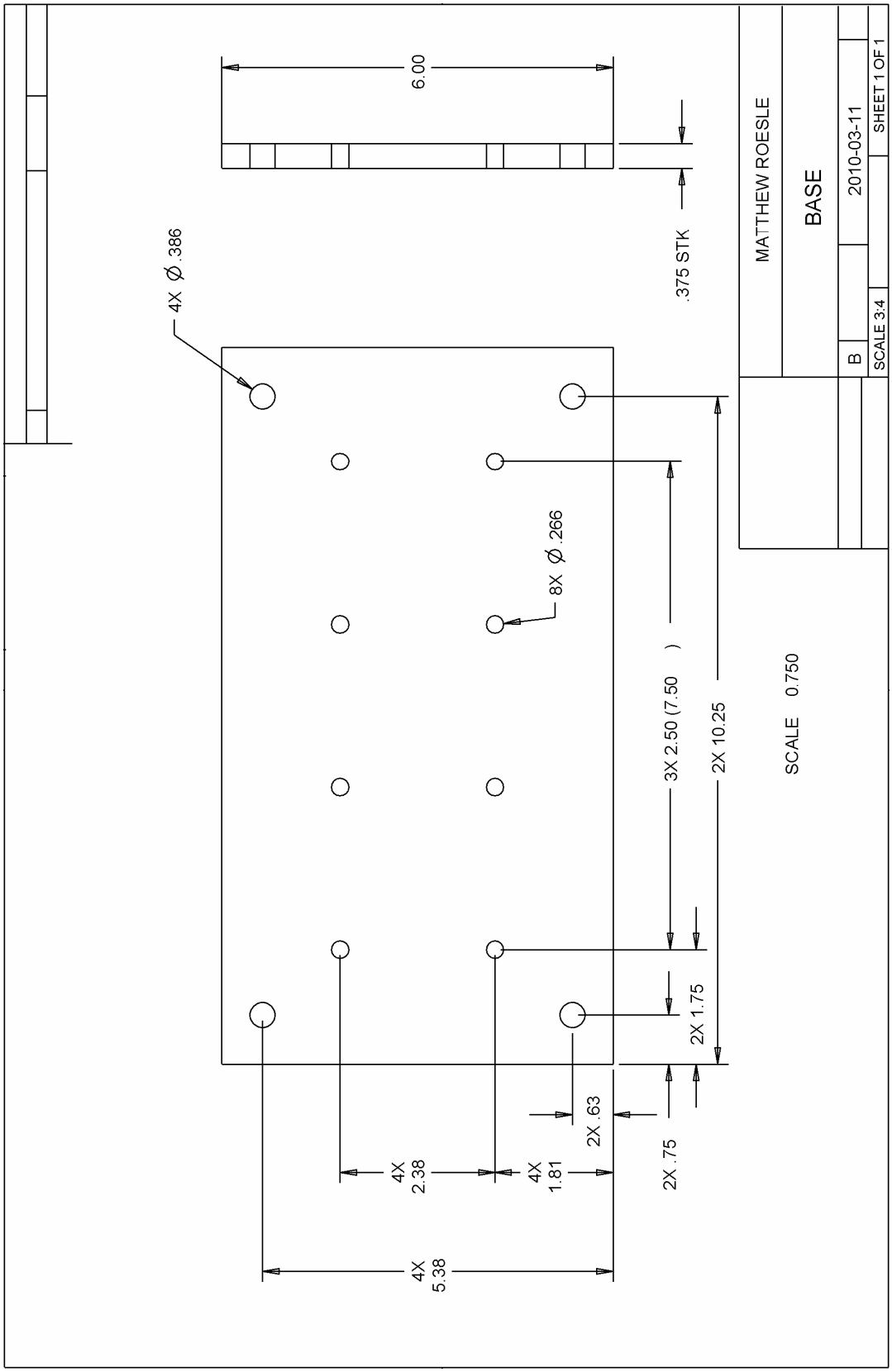
6.00
.375 STK
4X Ø .386
8X Ø .266
3X 2.50 (7.50)
2X 10.25
2X 1.75
2X .63
2X .75
4X 2.38
4X 1.81
4X 5.38
SCALE 0.750
MATTHEW ROESLE
BASE
B
2010-03-11
SCALE 3:4
SHEET 1 OF 1

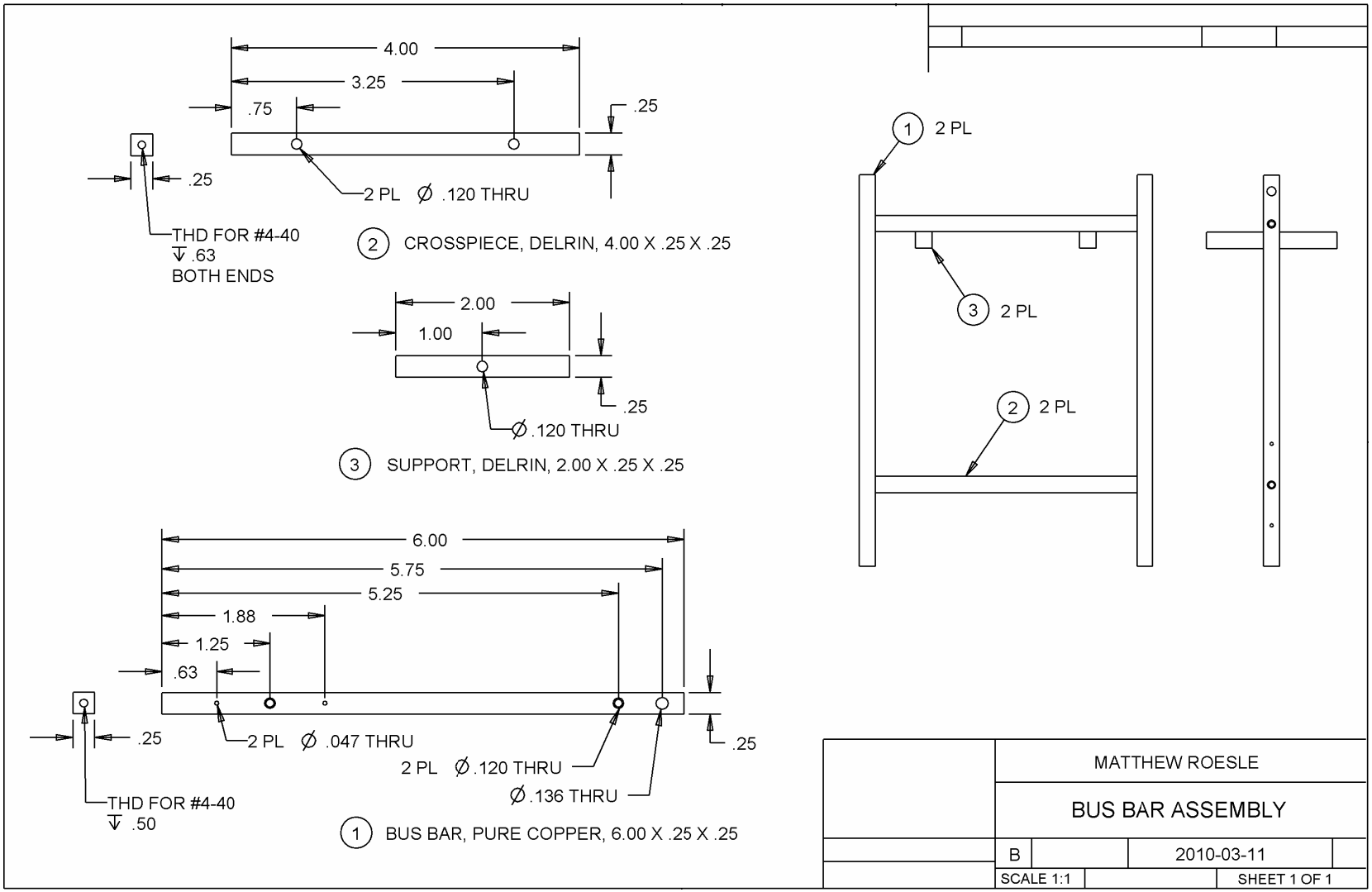
4.00
3.25
.75
.25
.25
2 PL Ø .120 THRU
THD FOR #4-40
↧ .63
BOTH ENDS
2 CROSSPIECE, DELRIN, 4.00 X .25 X .25
2.00
1.00
.25
Ø .120 THRU
3 SUPPORT, DELRIN, 2.00 X .25 X .25
6.00
5.75
5.25
1.88
1.25
.63
.25
2 PL Ø .047 THRU
2 PL Ø .120 THRU
Ø .136 THRU
.25
THD FOR #4-40
↧ .50
1 BUS BAR, PURE COPPER, 6.00 X .25 X .25
1 2 PL
3 2 PL
2 2 PL
MATTHEW ROESLE
BUS BAR ASSEMBLY
B
2010-03-11
SCALE 1:1
SHEET 1 OF 1

Power supply:

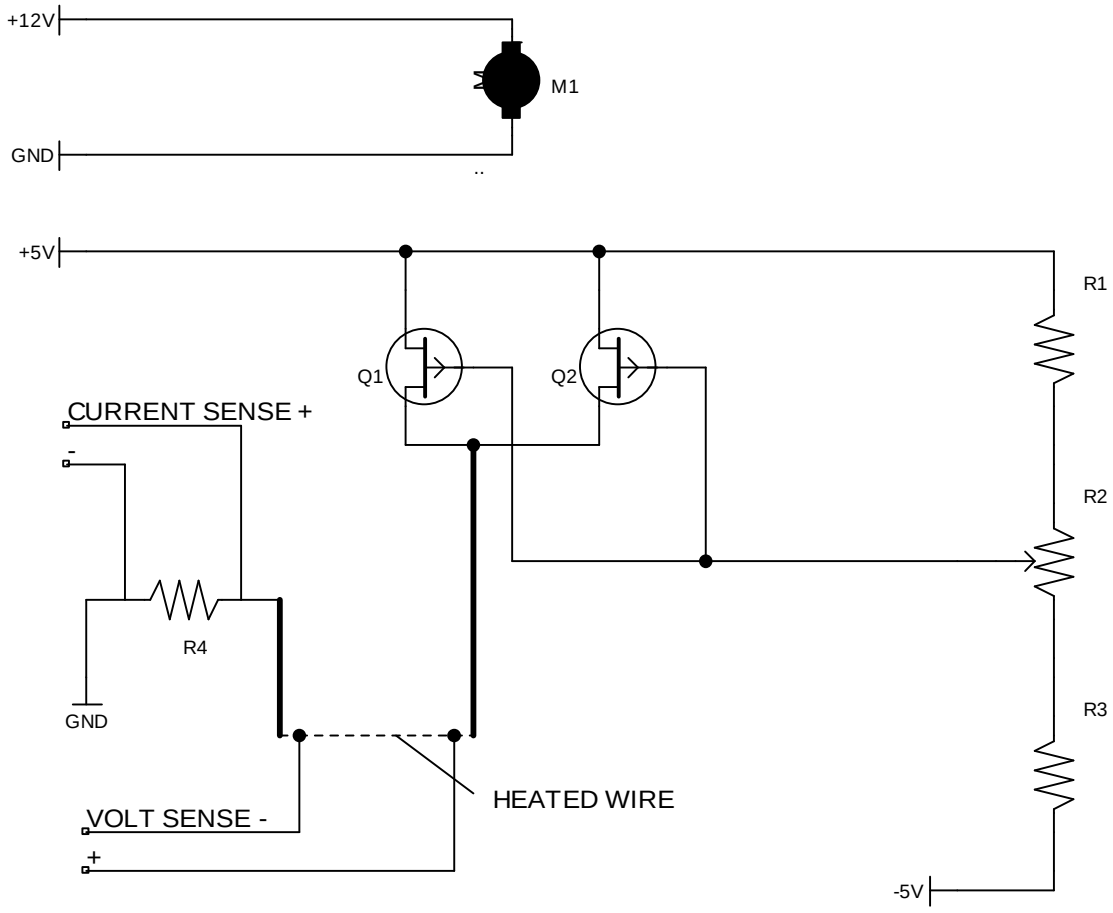

Parts list:

R1	5.6 kΩ, ¼ Watt, 5 % tolerance
R2	10 kΩ, ¼ Watt, 10 % tolerance
R3	3.9 kΩ, ¼ Watt, 5 % tolerance
R4	0.005 Ω, 4 Watt, 1 % tolerance
Q1, Q2	P-channel MOSFET, part number IRF4905
M1	Muffin fan, 120 mm, 12 V, 0.6 A

Notes:

1. Q1 and Q2 are mounted on heat sinks, air flow from fan M1 is directed over them
2. Voltage sense wires contact the heated wire immediately adjacent to the bus bars

Appendix C.

Averaged balance equations

Table C.1. Variables in the generic conservation equation (Eq. C.1).

Conservation principle	Ψ	$\boldsymbol{\gamma}$	ζ
Mass	1	0	0
Momentum	$\mathbf{U}$	$\mathbf{T}$	$\mathbf{b}$
Energy	$e + \frac{1}{2}\lvert\mathbf{U}\rvert^2$	$\mathbf{T}\cdot\mathbf{U} - \mathbf{q}$	$\mathbf{b}\cdot\mathbf{U} + S$

As described in Section 2.2, multiple approaches have been used historically to derive the averaged balance equations for multiphase flows from the local equations of motion (Bouré and Delhaye, 1982, Hill, 1998, Wallis, 1969). In this section the conditional averaging approach as used by Drew and Passman (1999) will be described. Key features of this approach are the use of ensemble averaging to achieve the averaged equations in a single averaging operation, and the use of a phase indicator function to isolate each phase in the mixture.

C.1. Exact balance equations

The averaging process begins with the local, instantaneous balance equations for mass, momentum, and energy. These equations can be expressed as a generic balance equation,

$$\frac{\partial \rho\Psi}{\partial t} + \nabla\cdot\rho\Psi\mathbf{U} = \nabla\cdot\boldsymbol{\gamma} + \rho\zeta, \qquad \text{(C.1)}$$

where values for Ψ, $\boldsymbol{\gamma}$, and ζ are given in Table C.1 (Drew and Passman, 1999). For multiphase flows, these balance equations, plus appropriate jump conditions at interfaces between the phases and constitutive relations for each fluid, form a complete description of the flow. These equations are typically not used directly in numerical simulations because the computing resources required to resolve all the interfaces is prohibitive.

C.2. Phase indicator function

A basic tool used to develop the conditional averaged balance equations is the phase indicator function X_i, defined as,

$$X_i(\mathbf{x}, t) = \begin{cases} 1 & \text{if phase i is present at } (\mathbf{x}, t) \\ 0 & \text{otherwise} \end{cases}. \tag{C.2}$$

This function has the effect of picking out one phase of a multiphase mixture (Drew and Passman, 1999). The phase indicator function is used to condition Eq. (C.1) so that balance equations may be obtained for each phase individually.

The phase indicator function is thus constant except at the interface, so the gradient of X_i may be used to pick out the interfaces of phase i. Drew and Passman (1999) express ∇X_i in terms of the Dirac delta function $\delta(\mathbf{x},t)$,

$$\nabla X_i = \mathbf{n}_i \delta(\mathbf{x} - \mathbf{x}_I, t), \tag{C.3}$$

where $\mathbf{n}_i$ is the unit normal vector pointing towards phase i and $\mathbf{x}_i$ is the location of the interface. Another important property of the phase indicator function is the topological equation,

$$\frac{\partial X_i}{\partial t} + \mathbf{U}_I \cdot \nabla X_i = 0, \tag{C.4}$$

which can be interpreted physically to mean simply that the interface travels with the velocity of the interface, $\mathbf{U}_I$ (Hill, 1998).

C.3. Conditional averaging

To obtain averaged balance equations for each phase of a multiphase mixture, the exact balance equation (Eq. C.1) is first multiplied by the phase indicator function. The first three terms of the resulting equation can be expanded to obtain,

$$\frac{\partial X_i \rho \Psi}{\partial t} + \nabla \cdot X_i \rho \Psi U = \nabla \cdot X_i \boldsymbol{\gamma} + X_i \rho \zeta + \rho \Psi \left(\frac{\partial X_i}{\partial t} + \mathbf{U} \cdot \nabla X_i \right) - \boldsymbol{\gamma} \cdot \nabla X_i \,. \tag{C.5}$$

Next, the velocity on the right hand side of Eq. (C.5) is expanded to $\mathbf{U}_I$ + ($\mathbf{U}$ - $\mathbf{U}_I$) and the topological equation is applied,

$$\frac{\partial X_i \rho \Psi}{\partial t} + \nabla \cdot X_i \rho \Psi \mathbf{U} = \nabla \cdot X_i \boldsymbol{\gamma} + X_i \rho \zeta + \left(\rho \Psi \left(\mathbf{U} - \mathbf{U}_I \right) - \boldsymbol{\gamma} \right) \cdot \nabla X_i \,. \tag{C.6}$$

The last term on the right hand side represents the transfer of the quantity Ψ to phase i across its interfaces by mass transfer and by diffusive flux. The conditioned balance equation can then be averaged using ensemble averaging,

$$\frac{\partial \overline{X_i \rho}}{\partial t} + \nabla \cdot \overline{X_i \rho \mathbf{U}} = \overline{\rho \left(\mathbf{U} - \mathbf{U}_I \right) \cdot \nabla X_i} \,, \tag{C.7}$$

$$\frac{\partial \overline{X_i \rho \mathbf{U}}}{\partial t} + \nabla \cdot \overline{X_i \rho \mathbf{U} \mathbf{U}} = \nabla \cdot \overline{X_i \mathbf{T}} + \overline{X_i \rho \mathbf{b}} + \overline{\left[\rho \mathbf{U} \left(\mathbf{U} - \mathbf{U}_I \right) - \mathbf{T} \right] \cdot \nabla X_i} \,, \tag{C.8}$$

$$\begin{aligned} &\frac{\partial \overline{X_i \rho \left(e + \frac{1}{2} |\mathbf{U}|^2 \right)}}{\partial t} + \nabla \cdot \overline{X_i \rho \left(e + \frac{1}{2} |\mathbf{U}|^2 \right) \mathbf{U}} = \nabla \cdot \overline{X_i \left(\mathbf{T} \cdot \mathbf{U} - \mathbf{q} \right)} + \overline{X_i \rho \left(\mathbf{b} \cdot \mathbf{U} + S \right)} \\ &+ \overline{\left[\rho \left(e + \frac{1}{2} |\mathbf{U}|^2 \right) \left(\mathbf{U} - \mathbf{U}_I \right) - \left(\mathbf{T} \cdot \mathbf{U} - \mathbf{q} \right) \right] \cdot \nabla X_i} . \end{aligned} \tag{C.9}$$

An averaged balance equation for the internal energy may be obtained from Eq. (C.8) and (C.9),

$$\frac{\partial \overline{X_i \rho e}}{\partial t} + \nabla \cdot \overline{X_i \rho e \mathbf{U}} = -\nabla \cdot \overline{X_i \mathbf{q}} + \overline{X_i \mathbf{T} : \nabla \mathbf{U}} + \overline{X_i \rho S} + \overline{\left[\rho e \left(\mathbf{U} - \mathbf{U}_I \right) + \mathbf{q} \right] \cdot \nabla X_i} \,. \tag{C.10}$$

A number of manipulations are now required to cast these equations into the more familiar forms given in Section 2.2 (Eqs. 2.5-2.7). First, averaged equations are defined as follows. The phase fraction is simply the average of the phase indicator function,

$$\varepsilon_i = \overline{X_i} \,. \tag{C.11}$$

As noted by Drew and Passman (1999), ε_i is often called the volume fraction of phase i, which implies volume averaging. By the definition given here, however, the volume fraction is a result of ensemble averaging and so is defined even as the volume approaches zero. As noted in Section 2.2, density and the diffusive and fluctuation fluxes are averaged using component averages,

$$\bar{\rho}_i = \frac{\overline{X_i \rho}}{\varepsilon_i}, \tag{C.12}$$

$$\overline{\mathbf{T}}_i = \frac{\overline{X_i \mathbf{T}}}{\varepsilon_i}, \tag{C.13}$$

$$\bar{\mathbf{q}}_i = \frac{\overline{X_i \mathbf{q}}}{\varepsilon_i}, \tag{C.14}$$

$$\mathbf{T}_i^{\mathrm{Re}} = -\frac{\overline{X_i \rho \mathbf{U}_i' \mathbf{U}_i'}}{\varepsilon_i}, \tag{C.15}$$

$$\mathbf{q}_i^{\mathrm{Re}} = \frac{\overline{X_i \rho \mathbf{U}_i' e_i'}}{\varepsilon_i} + \frac{\overline{X_i \rho \mathbf{U}_i' \frac{1}{2}\left|\mathbf{U}_i'\right|^2}}{\varepsilon_i} - \frac{\overline{X_i \mathbf{T} \cdot \mathbf{U}_i'}}{\varepsilon_i}. \tag{C.16}$$

The fluctuation heat flux contains fluctuation internal energy flux, fluctuation kinetic energy flux, and fluctuation shear working terms. Other quantities are Favré (mass-weighted) averaged, including velocity, internal energy, and body sources $\mathbf{b}_i$ and S_i,

$$\bar{\mathbf{U}}_i = \frac{\overline{X_i \rho \mathbf{U}}}{\bar{\varepsilon}_i \bar{\rho}_i}, \tag{C.17}$$

$$\bar{e}_i = \frac{\overline{X_i \rho e}}{\bar{\varepsilon}_i \bar{\rho}_i}, \tag{C.18}$$

$$\bar{\mathbf{b}}_i = \frac{\overline{X_i \rho \mathbf{b}}}{\bar{\varepsilon}_i \bar{\rho}_i}, \tag{C.19}$$

$$\bar{S}_i = \frac{\overline{X_i \rho S}}{\bar{\varepsilon}_i \bar{\rho}_i}. \tag{C.20}$$

Equations (C.7), (C.8), and (C.10) can be can be put in terms of these averaged variables by expressing each exact variable as the sum of its average and a fluctuating component, and then applying the Reynolds averaging rules. For example, Drew and Passman (1999) expand the momentum flux term in Eq. (C.8),

$$\overline{X_i \rho \mathbf{U}\mathbf{U}} = \overline{X_i \rho \left(\bar{\mathbf{U}}_i + \mathbf{U}_i'\right)\left(\bar{\mathbf{U}}_i + \mathbf{U}_i'\right)} = \overline{X_i}\rho \bar{\mathbf{U}}_i \bar{\mathbf{U}}_i + \overline{X_i \rho \mathbf{U}_i' \mathbf{U}_i'} = \varepsilon_i \bar{\rho}_i \bar{\mathbf{U}}_i \bar{\mathbf{U}}_i - \varepsilon_i \mathbf{T}_i^{\mathrm{Re}}. \tag{C.21}$$

The choices of variable weightings made by Drew and Passman simplify this process considerably. In the limit of incompressible flows the distinction between component weighting and mass weighting vanishes. Other terms are handled similarly, and the results are given as Eq. (2.5)-(2.7),

$$\frac{\partial \varepsilon_i \bar{\rho}_i}{\partial t} + \nabla \cdot \left(\varepsilon_i \bar{\rho}_i \overline{\mathbf{U}}_i \right) = \Gamma_i , \tag{2.5}$$

$$\frac{\partial \varepsilon_i \bar{\rho}_i \overline{\mathbf{U}}_i}{\partial t} + \nabla \cdot \left(\varepsilon_i \bar{\rho}_i \overline{\mathbf{U}}_i \overline{\mathbf{U}}_i \right) = \nabla \cdot \left[\varepsilon_i \left(\overline{\mathbf{T}}_i + \mathbf{T}_i^{Re} \right) \right] + \varepsilon_i \bar{\rho}_i \bar{\mathbf{b}}_i + \mathbf{F}_i + \mathbf{U}_{i,I} \Gamma_i , \tag{2.6}$$

$$\begin{aligned} \frac{\partial \varepsilon_i \bar{\rho}_i \bar{e}_i}{\partial t} + \nabla \cdot \left(\varepsilon_i \bar{\rho}_i \overline{\mathbf{U}}_i \bar{e}_i \right) = \varepsilon_i \overline{\mathbf{T}}_i : \nabla \overline{\mathbf{U}}_i - \nabla \cdot \left[\varepsilon_i \left(\bar{\mathbf{q}}_i + \mathbf{q}_i^{Re} \right) \right] + \\ \varepsilon_i \bar{\rho}_i \bar{S}_i + \varepsilon_i D_i + E_i + e_{i,I} \Gamma_i . \end{aligned} \tag{2.7}$$

The final term in Eq. (2.5) represents mass transfer between phases. The last two terms in Eq. (2.6) and (2.7) represent diffusive and convective transport between phases, respectively. These averaged quantities are conditioned with the gradient of the phase indicator function (Drew and Passman, 1999),

$$\mathbf{F}_i = -\overline{\mathbf{T} \cdot \nabla X_i} , \tag{C.22}$$

$$E_i = \overline{\mathbf{q} \cdot \nabla X_i} , \tag{C.23}$$

$$\Gamma_i = \overline{\rho (\mathbf{U} - \mathbf{U}_I) \cdot \nabla X_i} , \tag{C.24}$$

$$\mathbf{U}_{i,I} \Gamma_i = \overline{\rho \mathbf{U} (\mathbf{U} - \mathbf{U}_I) \cdot \nabla X_i} , \tag{C.25}$$

$$e_{i,I} \Gamma_i = \overline{\rho e (\mathbf{U} - \mathbf{U}_I) \cdot \nabla X_i} . \tag{C.26}$$

Considerable modeling effort has gone into finding expressions for the diffusive flux terms (Hao and Tao, 2003b,; Hill, 1998;Rusche, 2002; Drew and Passman, 1999). The convective flux terms are often neglected (Hill, 1998; Rusche, 2002), but because phase change is important in the current study, proper handling of these terms is crucial.